Damage formation and annealing studies of low energy ion implants in silicon using medium energy ion scattering.

Matthew Werner

Institute for Materials Research (IMR)
School of Computing, Science and Engineering (CSE)
The University of Salford, UK.

Submitted in partial fulfilment of the requirements of the degree of Doctor of Philosophy, March 2006.

Contents

List of Tables

List of Figures

Acknowledgements

There are many people who I need to thank and acknowledge for their contribution towards this PhD. Firstly I need to thank my supervisor Professor Jaap van den Berg for his help and support throughout the entire time we've worked together.

Many days and nights have been spent carrying out MEIS experiments and I am grateful to all the staff at Daresbury who have helped along the way, Dr Paul Bailey, Dr Tim Noakes, Dr Kevin Connell, Mark Pendleton, Paul Morrell and Brian Blackwell.

I am grateful to everybody who I worked with on the IMPULSE project. In particular to Dr Thomas Feudal, Marc Herden and Daniel Gehre of AMD who provided many implanted samples. The two collaborations that proved to be the most fruitful and enjoyable were with Damiano Giubertoni and Massimo Bersani of ITC – IRST who carried out many of the SIMS measurements presented here, and with Dr Luciana Capello and Dr Till Metzger of the ESRF who carried out the X-ray studies presented here. In addition L. Ottaviano, C. Bongiorno and Dr G. Mannino provided the EFTEM images. Outside of the IMPULSE project Eric Collard and Dr Richard Goldberg of Applied Materials provided Sb implanted samples. Dr Wilfred Vandervorst of IMEC carried out some SIMS experiments. Salvatore Gennaro and Damiano Giubertoni of ITC – IRST have provided the results of Hall effect measurements.

I need to thank other PhD students at Salford who I've had a lot of fun working with. Andy Wooding, Mike Reading and Jiri Fiala have been a real help, particularly helping out with many late night MEIS/DVD sessions. Phil Edmondson has carried out the XTEM work presented here and has been helpful throughout the PhD in many discussions, as has Kerry Abrams. I am especially grateful to my brother Dave Werner for invaluable help in writing the code for the depth scale program.

Professor Dave Armour and Professor Peer Zalm have been very helpful in discussions throughout the project, and have assisted with proof reading the thesis. Dr George Wolstenholme has provided technical assistance and Professor George Carter has made helpful suggestions. Dr Reza Valizeda has helped by carrying out some RBS measurements.

Finally I need to thank some friends and my family for many things, including encouragement, support and pretending to be interested in silicon implants. In no particular order, Pete and Lesley Daniel, Mike and Lorna Smith, Matt and Sarah Stuart, Hannah "Cushion" Groves, Melanie Shaw, Dr June Lashley, Clayre Fontaine, Chris Morriss, Mum, Dad and Chloe "Pufa Fish" Werner.

Abbreviations and Symbols

a/c	amorphous / crystalline
As_nV	As vacancy cluster
BOX	buried oxide
CMOS	complimentary metal oxide semiconductors
Cz Si	Czochalski grown Si
E_{act}	activation energy
E_d	displacement energy
EFTEM	energy filtered transmission electron microscopy
EOR	end of range
Epi	epitaxially grown Si
FDL	faulted dislocation loops
FWHM	full width half maximum
GI-DXS	grazing incidence – diffuse x-ray scattering
IC	integrated circuit
ITRS	international technology roadmap for semiconductors
MEIS	medium energy ions scattering
ML	monolayer
MOSFET	metal oxide field effect transistor
NMOS	n-channel metal oxide semiconductor
PAI	pre-amorphising implant
PDL	perfect dislocation loop
PMOS	p-channel metal oxide semiconductor
RBS	Rutherford backscattering spectrometry
RBS/C	channelling Rutherford backscattering spectrometry
RNG	random nucleation and growth
R_p	mean projected range
R_s	sheet resistance
RTA	rapid thermal annealing
RTP	rapid thermal processing
SA	spike annealing
SDE	source / drain extensions
SIMS	secondary ion mass spectrometry
SOI	silicon on insulator
SPER	solid phase epitaxial regrowth
SR	specular reflectivity
SRIM	stopping and range of ions in matter
TED	transient enhanced diffusion
TEM	transmission electron microscopy
TRIM	transport and range of ions in matter
TRR	time resolved reflectivity
UHV	ultra high vacuum
ULE	ultra low energy
ULSI	ultra large scale integrated technology
USJ	ultra shallow junctions
USJ	ultra shallow junction
V_D	drain voltage
V_g	gate voltage
V_H	Hall voltage
V_t	threshold voltage

X_j	junction depth
XRD	X-ray diffraction
XRF	X-ray fluorescence
XTEM	cross-section transmission electron microscopy

Abstract

The work described in this thesis concerns studies of damage and annealing processes in ion implanted Si, relevant for the formation of source / drain extensions in sub 100 nm CMOS devices. Implants were carried out using 1-3 keV As, BF_2 and Sb ions and implanted samples were annealed at temperatures between 550 °C and 1130 °C.

The principal analysis technique used was Medium energy ion scattering (MEIS), which yields quantitative depth profiles of displaced Si atoms and implanted dopants. The results obtained have been related to comparative analyses using SIMS, TEM and X-ray techniques.

Heavy ion damage evolution and the concomitant dopant redistribution as a function of ion dose was investigated using As and Sb implantation into Si. It was found that for low doses the damage build up does not follow the energy deposition function. Instead a ~4 nm wide amorphous layer is formed initially under the oxide that grows inwards into the bulk with increasing dose. For low doses As is seen to have migrated into the damaged regions near the surface, where it appears to be more readily accommodated. Both effects are ascribed to the migration of interstitials.

Various annealing studies have been carried out to investigate the regrowth behaviour of the damaged Si and the redistribution of the dopant. Effects of recrystallisation, dopant movement into substitutional positions, dopant segregation and diffusion are observed. Annealing studies of implanted Silicon on Insulator (SOI) wafers have shown a regrowth that has a wavy a/c interface unlike the layer by layer mode that is typical in solid phase epitaxial regrowth. This effect is ascribed to localised damage accumulation at the buried oxide layer.

Following a BF_2 implant into Si, pre-amorphised by a Xe bombardment, an interaction between Xe, F and B has been observed to occur upon annealing during which the implanted species conglomerate at depths related to the end of range of the BF_2 implant in the amorphous Si.

Publications

The results presented and discussed in the following results chapters of this thesis have been published in the following journals and proceedings.

Chapter 5.

1 M. Werner, J.A. van den Berg, D.G. Armour, W. Vandervorst, E.H.J. Collart, R.D. Goldberg, P. Bailey d, T.C.Q. Noakes. Nucl. Instr. and Meth. B 216 (2004) 67–74
Damage accumulation and dopant migration during shallow As and Sb implantation into Si.

Chapter 6

2 J.A. van den Berg, D Armour, S Zhang, S Whelan, M Werner, E.H.J. Collart, R.D. Goldberg, P. Bailey, T.C.Q. Noakes. MRS proceeding 2002 vol. 717, P303 – 308.
Damage and dopant profiles produced by ultra shallow B and As ion implants into Si at different temperatures characterised by medium energy ion scattering.

3 J A van den Berg, D G Armour, M Werner, S Whelan, W Vandervorst and T Clarysse, E H J Collart and R D Goldberg, P Bailey and T C Q Noakes, Proc. Int. Conf. on Ion Implantation Technology, ITT2002, September 2002, p597
High depth resolution characterization of the damage and annealing behaviour of ultra shallow As implants in Si.

4 L. Capello, T. H. Metzger, M. Werner, J. A. van den Berg, M. Servidori, M. Herden, T. Feudel Mat. Sci. and Eng. B **124-125** (2005) 200 – 204.
Solid-Phase Epitaxial Regrowth of a shallow amorphised Si layer studied by x-ray and medium energy ion scattering.

Chapter 7

5 M. Werner, J.A. van den Berg, D.G. Armour, G. Carter, T. Feudel, M. Herden, M. Bersani, D. Giubertoni, P. Bailey, T.C.Q. Noakes. Materials Science and Engineering B 114–115 (2004) 198–202.
The interaction between Xe and F in Si (100) pre-amorphised with 20 keV Xe and implanted with low energy BF_2.

6 M. Werner, J.A. van den Berg, D.G. Armour, G. Carter, T. Feudel, M. Herden, M. Bersani, D. Giubertoni, L. Ottaviano, C. Bongiorno, and G. Mannino, P. Bailey, T.C.Q. Noakes. Applied Physics Letters, Volume 86, 2005, P 151904.
Shallow BF_2 implants in Xe-bombardment-preamorphized Si: The interaction between Xe and F.

Chapter 1 Introduction

1.1 Introduction

Low energy ion implantation is a key processing step for the production of integrated circuits (IC's) in ultra large scale integrated technology (ULSI). It is the most widely used method for introducing dopant atoms into silicon wafers to produce electrically active n – type and p – type doped regions in complementary metal oxide semiconductor (CMOS) transistors, as well as other types of devices. The main reason for this is the technique's ability to control the depth and dose of the implanted dopant atoms with the necessary level of accuracy and reproducibility for volume production (1).

An unavoidable consequence of energetic ion bombardment is the displacement of lattice atoms. The work described in this thesis is a study of the behaviour of the damage growth and dopant accumulation during ultra low energy implantation, as well as damage dissolution and dopant redistribution effects during annealing. Studies were carried out in collaboration with Advanced Micro Devices (AMD), the world's second largest processor manufacturer. The implantation conditions studied in this thesis are relevant to current and future device production. A brief description of transistors and the current state of the technology is made within this introduction to set the context for the later work.

1.2 CMOS Devices

The most important transistors in IC's are metal oxide semiconductor field effect transistors (MOSFET) (2). These can be either n-channel (NMOS) or p-channel (PMOS) transistors. CMOS, which dominates IC technology, utilises both NMOS and PMOS transistors. A schematic of an enhancement mode NMOS or PMOS transistor is shown in Figure 1.1a). The physical structure of both transistors is essentially the same and they consist of two highly doped regions, the source and drain, which are oppositely doped with respect to the surrounding region. The Fermi level (the energy level at which the probability of occupation by an electron is 0.5 (7)) has to be continuous across a junction of n and p regions at equilibrium, therefore electrons and holes migrate across the junction, creating positive and negative space charge regions which forms a depletion region at the junction. Between the source and drain is the channel. A polysilicon gate terminal placed over the channel is separated from the channel by an insulating SiO_2 layer. In an ideal device, when a bias voltage is applied to the gate

terminal (V_g), current cannot flow from the gate because of the insulating layer. (However in reality some gate leakage can occur.) The electric field due to an applied voltage, affects electrons and/or holes in channel region.

In the absence of a bias voltage on the gate, relative to the substrate (which is usually at earth potential along with the source), the source and drain regions form two back to back semiconductor junction diodes. No current can flow from the source to drain irrespective of the voltage applied between them and the transistor is termed to be in the "off" state (although some reverse gate leakage current can occur in this state). An NMOS transistor has an n-doped source and drain and is p-doped under the gate. Applying a positive voltage to the gate will create an n-channel inversion layer, by first repelling holes and then attracting electrons into that region. The n – type source and drain are then connected by a surface n – channel, enabling the flow of current from the source to drain, if a voltage is applied to the drain (V_D). Electrons form the majority charge carriers. The opposite is true for PMOS transistors, which consist of p – type source and drains and an n – doped channel. When a negative voltage is applied to the gate, a p – channel inversion layer is formed in which holes form the majority charge carriers (2-7).

The threshold voltage (V_t) is the gate voltage for which the channel region becomes strongly inverted and current can start to flow from source to drain. In this state the transistor is said to be "on" (2-7). The threshold voltage (V_t) is of great importance and can be adjusted by one or more threshold adjust implants in the device. A threshold voltage adjust implant places dopants just under the gate oxide (8).

The gate voltage determines the width of the conducting channel and hence the current that can flow in the channel from source to drain can be modulated by varying the gate voltage (2-7). For increasing drain voltages, the drain current quickly reaches a saturated point determined by the gate voltage.

The source / drain extensions (SDE) extend underneath the gate and consist of more lightly doped regions than the source and drain. They provide a gradual dopant concentration gradient between the S/D and the channel region which reduces the maximum electric field and hence reduces the threshold voltage (5). Smaller electric fields are required in order to avoid hot carrier effects. A large electric field can accelerate the carriers, usually electrons because of their higher mobility, to high energies. The energetic, termed hot, electrons can be accelerated into the gate oxide. Excess charge building in the oxide will change the device operating characteristics over time (7).

The enhancement mode transistor described is the type most commonly used. In comparison a depletion mode transistor is engineered to normally conduct by creating a thin doped layer of the same type as the source and drain underneath the gate. Applying a gate voltage which is opposite in polarity to the voltage applied in enhancement mode devices makes conduction stop. In all cases silicide or metal contacts allow the terminals to be connected to other devices by metal interconnects. The above is in fact a very simplified description of a transistor. Many implantations and processing steps are required to make a device.

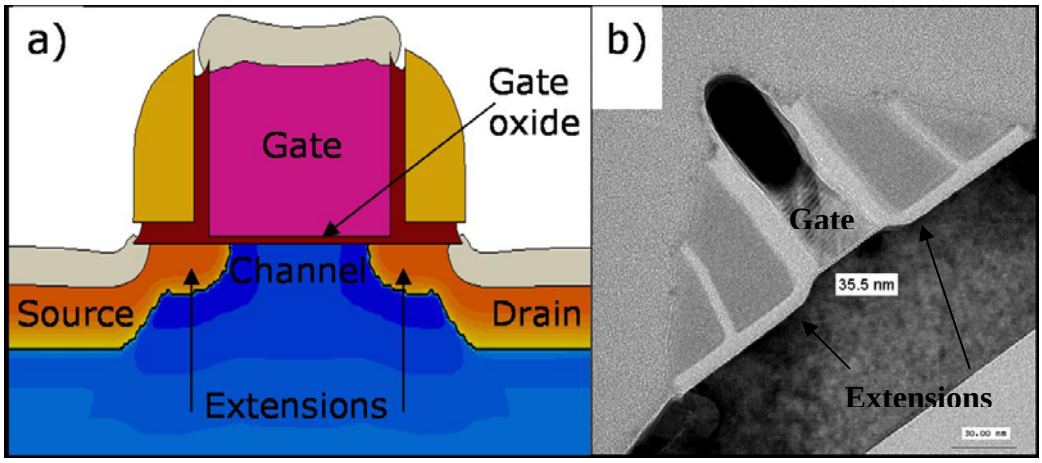

Figure 1.1 a) Schematic of a MOS transistor. b) XTEM image of an AMD optimised transistor with a gate length of 35 nm, modified from (16).

In CMOS both NMOS and PMOS transistors are manufactured on a single wafer by first forming wells doped oppositely to the wafer in which to build the transistor in. Usually an n-type well is formed in a p-type wafer to form a PMOS device. The main advantage of CMOS over NMOS and bipolar technology is the much smaller power dissipation. Theoretically a CMOS circuit has almost no static power dissipation and power is only dissipated when the circuit switches (3).

Two important physical parameters that affect transistor performance are the gate length L_g, and the SDE junction depth, X_j. The gate length has an important bearing on the speed of operation of a device, as the velocity of electron motion in Si is limited, therefore the time for the current to travel the distance from source to drain depends on the distance of travel. The junction depth has to be related to the gate length, as discussed below. From an analysis point of view X_j is often somewhat arbitrarily taken to be the depth where the concentration of dopants in the extension is 1E18 cm^{-3}.

This is an approximate average level for the concentration of dopant in a Si wafer, therefore the junction occurs at the depth of the change over point. The electrical characteristics, i.e. the sheet resistance, of the doped regions are also of extreme importance for the power consumption of the device.

From a simplistic point of view, reducing the dimensions of transistors produces several obvious means of improvement in IC performance. The first is that reduced size allows faster switching speeds, due to a shorter duration for current to cross a shorter channel. The second reason for an improvement is that smaller transistors allow for more dense packing and hence an increase in the number of transistors on a chip allowing the chip to perform more operations. Modern processors contain millions of transistors on a single chip, for example in 2004 the leading AMD processor, the Opteron contained 205 million transistors on an area of approximately 2 cm^2 (9). A cross sectional transmission electron microscopy (XTEM) image of a transistor from this processor is shown in Figure 1.1b). The gate length in this case is 35 nm.

In 1965 Gordon Moore, co-founder of Intel, observed that the number of transistors on IC's doubled every 12 months and predicted that it was likely to continue to do so (10). In 1975 Moore revised that to every two years (11). These predictions have since become known as "Moore's Law", with the timeframe between 1 and 2 years for doubling the number of devices. The semiconductor industry has strived to follow "Moore's law" and has sustained the rate of improvements to devices ever since (12). This improvement is illustrated in Figure 1.2 where the number of transistors on Intel processors is plotted against the year of its production (12). This is likely to continue for some while, although there are some serious potential "showstoppers" ahead, discussed later (13).

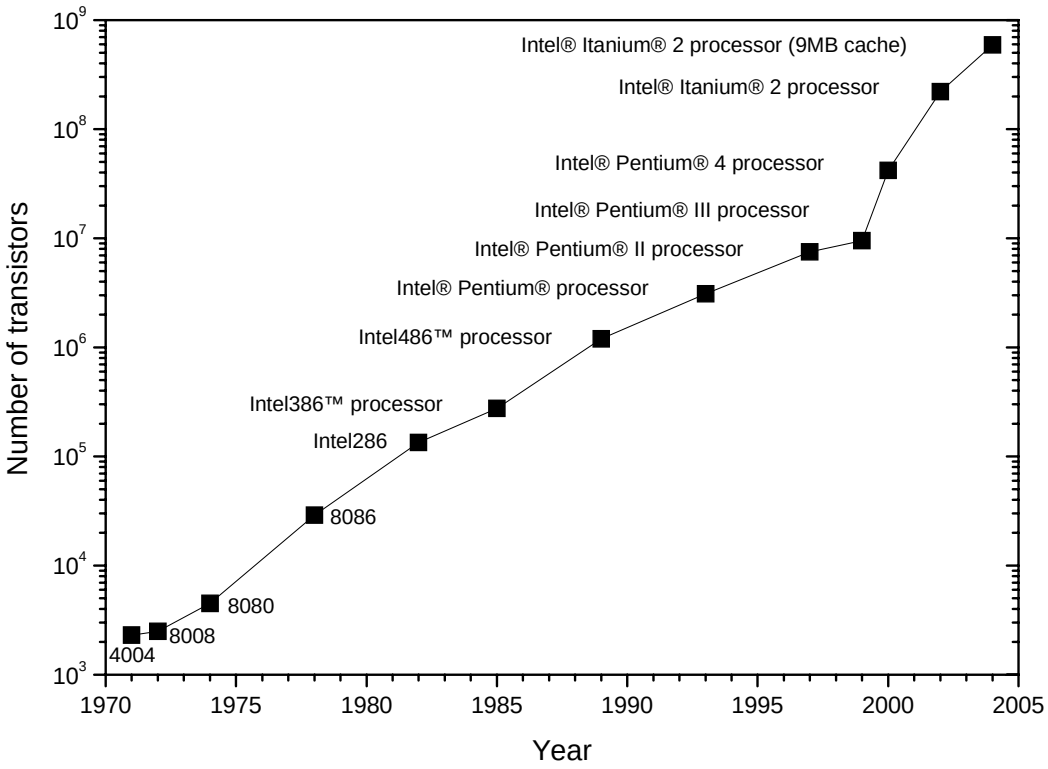

Figure 1.2 Number of transistors on Intel Microprocessors. Values from (12)

To continually achieve this rate of improvement, aggressive targets for the performance of all aspects of devices, including the gate length, junction depth, and sheet resistance, as well as production methods have been laid out as a guide in the International Technology Roadmap for Semiconductors (ITRS) (13). This states performance criteria and designates technology nodes, determined by the repeat spacing of devices, which are considered necessary for the industry to be able to achieve on an annual basis in order to sustain the rate of progress of "Moores Law". The roadmap pushes research and development to achieve these criteria, particularly where no manufacturable solutions are known. The current version of the roadmap contains detailed short term goals till 2009 and longer term projections till 2018.

Simply reducing the gate length alone would produce short channel effects. This situation arises when the depletion widths of the source and drain become comparable to the channel length and merge, known as "punch through", and the device no longer operates with MOSFET characteristics. This behaviour can short the channel and increase subthreshold leakage currents from the source to the drain (2-4). For this reason transistor dimensions have to be generally reduced by scaling down all dimensions and keeping the same transistor shape. 'Halo' or 'pocket' implants place dopants just below

the active channel, adjacent to the source and drain to precisely tailor the background doping there (5). They can help to prevent expansion of the drain depletion region into the lightly doped channel to reduce short channel effects. However, classical transistor scaling theory requires reduced source drain extension depth with reduced transistor gate length, ($X_j \approx 0.55\ L_g$) (2, 13). The projected junction depth requirements in the ITRS are therefore based on the gate length. Sheet resistance R_s values for both NMOS and PMOS are also given in the roadmap. As a guide to the rate of development, in 2001, technology was in the 130 nm node and in 2004 it was in the 90 nm node. The projection for 2007 is to be in the 65 nm node. Some values from the 2003 ITRS (13) relevant to this PhD project are shown in table 1.1 and have not been changed in the 2004 revision (13). Besides the existence of a general roadmap, manufacturers tend to follow their own modified roadmap. Figure 1.3 shows the trend for size reduction of CMOS transistors at AMD along with XTEM images of test structures.

Year	**2003**	**2004**	**2005**	**2006**	**2007**
Technology node		90			65
L_g (nm)	45	37	32	28	25
X_j extension (nm)	24.8	20.4	17.6	15.4	13.8
Max extension Rs P/N (Ω/□)	545/255	663/310	767/358	833/389	884/412

Table 1.1 Parameters from 2003 ITRS. From (13).

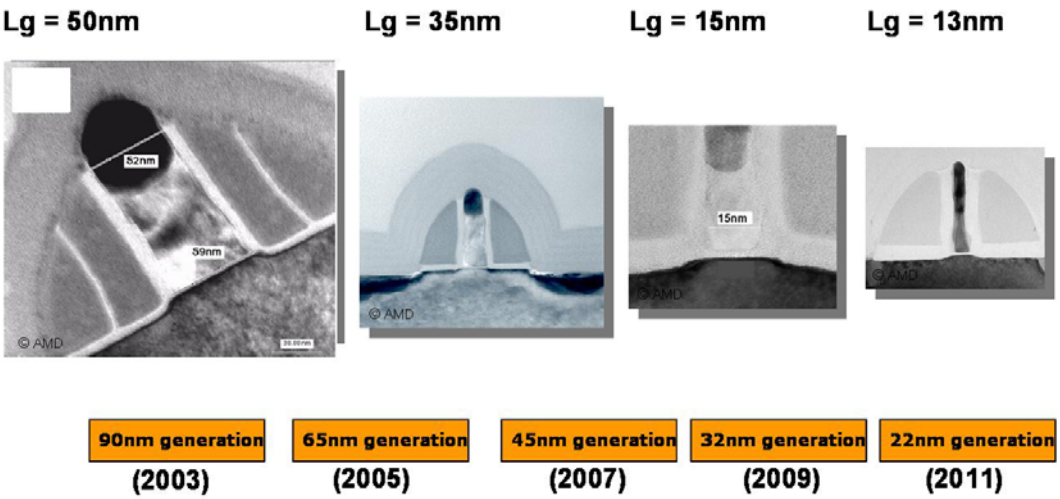

Figure 1.3 Roadmap for device shrinkage at AMD with XTEM of test structures. Modified from (9).

It has been noted that the rate of improvement cannot continue by merely reduced scaling alone due to the existence of fundamental material limits. For example, the gate oxide and L_g scaling is reaching its limit, because for much thinner oxides, gate oxide leakage current would dominate and high-k materials are not yet mature enough for high volume manufacturing (14, 15). The oxide layers in production have a thickness of around 1.2 nm but by the time scaling has reduced the required oxide layer to a thickness of 0.7 nm, this will correspond to just two atomic layers and is probably the ultimate manufacturing limit of bulk silicon oxide (32). The limit in downscaling must ultimately be related to the spacing between the atoms in the Si crystal, i.e. approximately 0.3 nm (33). In much the same way, with continued downscaling a point will be reached where there will so few dopant atoms in the channel region (down to as few as 100), that any small statistical variations in the number would have dramatic consequences on the device operation. It is not known if the number of dopant atoms could be controlled with the required accuracy (26).

There is a complicated relationship between many transistor parameters. It is therefore extremely important to carefully optimise all parameters for the best overall performance and reliability of the device and the production costs (14, 16, 17). For example it has been observed that simply reducing the SDE junction depth does not specifically lead to an improvement in overall device performance. Variation in X_j did not produce an observable variation in the threshold voltage characteristics (16).

To continue to improve devices there is a growing need to better understand all the mechanisms involved to fully exploit all the possibilities for improvement. The work in this thesis is concerned with understanding some of the mechanisms involved.

There is also a growing need to introduce novel methods of improving device performance. Advanced structures have to be considered as well introducing new ways to improve performance using the current device structure (5, 14, 32). The introduction of strain in devices is now actively pursued as one way to improve performance. In strained Si there can be higher carrier mobility (18). Devices may be created either through using strained SiGe or by using highly stressed overlayer films that are selectively formed over the NMOS and PMOS regions (14). Tensile films are used for NMOS and compressive ones for PMOS.

Another method to improve the operation of the transistor has been the introduction into volume production, within the last two years, of devices created on silicon on insulator (SOI) wafers for an improvement in the area of device latch – up, i.e. better isolation of the devices from the bulk substrate so that capacitance effects do not cause one transistor to interfere with the operation of surrounding transistors (3). Partially depleted devices have a similar construction to the standard CMOS devices, the source and drain do not extend to the depth of the buried oxide layer. These devices are already in production. Fully depleted devices are formed on narrow Si layers and the source and drain extend down to the buried oxide. A move to this sort of transistor is expected within a few years (9, 13). Further benefits and differences of SOI transistors are beyond the scope of this thesis. Because of the growing importance of SOI substrates a description of work comparing the regrowth behaviour of SOI and bulk Si substrates is included in Chapter 6 of this thesis.

1.3 Ion implantation

Ion implantation is carried out in an ion implanter in which dopant atoms are ionised in an ion source plasma. Positively charged ions are extracted from the source and accelerated in an electrostatic lens that forms them into a beam, mass analysed in a magnetic field (and occasionally focused in electric fields), and accelerated or decelerated, before impinging on the wafer (5). Since all practical implant energies exceed the threshold for lattice atom displacement, the process of ion implantation inevitably produces damage to the Si crystal lattice structure through collisions of the dopant ions with the Si atoms and the accommodation of the implanted ions within the matrix (19).

At the implant energies currently of interest for device production i.e. 1 – 5 keV, energy will be transferred mainly through nuclear interactions (elastic collisions), from the energetic ions to the initially stationary target atoms. A collision results in an ion being scattered and loss of energy through which the projectile slows down. Eventually after a series of collisions with different target atoms an ion will come to rest at some range within the Si once it has lost all its energy. For a given implant species the lower the implant energy, the shorter the range will be. The statistical nature of the slowing down process produces a distribution of the implanted ions within the Si about some mean depth. The implanted ion distribution is approximately a Gaussian distribution, or more accurately, a Pearson distribution. Driven by the relentless reduction of device dimensions the trend has been to use increasingly lower implant energies.

Si atoms that gain sufficient energy during a collision to overcome the binding energy are displaced from their lattice site, leaving behind a vacancy, i.e. an empty lattice site. Si atoms and implanted dopant ions stopped on a non lattice site are termed interstitials. Both structures are irregularities in the Si lattice and are referred to as point defects. Conglomerations of two or more point defects, referred to as extended defects, are also produced by ion implantation. Point defects can migrate depending on the temperature. Regions such as the surface or internal interfaces can act as a sink to trap migrating point defects (21).

Energetic recoil Si atoms produced by collisions with the incoming dopant ions will also collide with other Si atoms and if sufficient energy is transferred they in turn will be displaced. This process continues resulting in a collision cascade. The collision cascade produced by single heavy implanted ions, such as As, Sb, and Xe, tends to produce small amorphous zones. Once a certain implant concentration has been exceeded these zones will spatially overlap forming a continuous amorphous layer. Implanted light ions such as B create less damage to the Si lattice, but damage will build up until a certain critical concentration of defects exists when the crystal structure can collapse into an amorphous structure (20). It is difficult to produce an amorphous layer with light ions and will require substantially higher implant doses to achieve compared to heavy ions.

1.4 Annealing

To produce electrically active doped regions the implanted material must be annealed to restore the crystal lattice and locate the implanted atoms onto substitutional sites where they can become electrically active. Upon annealing, fully amorphised Si

produces a device quality regrown layer. On the other hand highly damaged Si layers, even after annealing to very high temperatures, always contain residual defects (22). This is one reason for using a pre-amorphising implantation (PAI) step prior to implanting the dopant. It is energetically more favourable for Si to be in a crystal structure rather than a damaged / amorphous state. Solid phase epitaxial regrowth (SPER) can proceed from the interface of the crystal and amorphous region in a layer-by-layer fashion upon annealing at temperatures of 550 °C and above (22). The regrowth rate is temperature dependant and increases with increasing anneal temperature. The regrowth rate also varies with the crystal orientation, (100) Si regrows faster than (110) Si, which in turn is faster than (111) orientated Si. This is one reason for the majority of devices being made on (100) Si. (100) Si is also the easiest orientation to grow. During the regrowth of amorphous layers the implanted dopant can take up substitutional lattice positions depending on concentration (22). For high dopant concentrations some dopant may not be able to be accommodated in the regrown layers and will be swept in front of the interface between the amorphous / crystalline interface, forming a segregated layer at the surface (23, chapter 6) or form clusters.

High anneal temperatures of > 1000 °C are typically preferred as they can result in fewer defects and higher levels of activated dopant. The thermal budget is the integral of the anneal temperature and time, which gives a measure of the total heat energy. However higher thermal budgets allow for more diffusion of the dopant, adversely affecting both the junction depth and abruptness. It is therefore favourable to optimise the thermal budget to produce shallower junctions with high levels of activation (1). This has led to the development of spike annealing, in which the wafers are heated to some higher temperature (usually > 1000 °C) but are not held at this maximum temperature. Fast ramp up and ramp down rates are used. This reduces diffusion as opposed to the more conventional rapid thermal processing (RTP), in which the wafer is held at the maximum anneal temperature for some duration, usually of the order of seconds.

At the end of the range of an amorphising implant will be a region essentially crystalline but containing a substantial number of defects. This interstitial rich defect region is termed the end of range (EOR) and the defects in this area have an important effect on the behaviour of the dopant ions during annealing (24, 25). These defects evolve during annealing and form extended defects. The dissociation of these extended defects at high anneal temperatures leads to the release of interstitials which sweep through the lattice and interact with the dopant atoms. This results in a burst of

enhanced diffusion of the implanted dopant ions, many orders of magnitude higher than standard Fickian diffusion called transient enhanced diffusion (TED). Diffusion can limit the shallowness of the transistor junction produced and consequently has important implications for device production.

Pre-amorphisation is also carried out to minimise channelling of implanted dopant ions (26). Traditionally amorphisation has been carried out using Ge implants but in the studies in this thesis Xe has been predominantly used. Using a deeper pre-amorphising implant (PAI) can spatially separate the end of range damage from the junction depth.

1.5 Objective, preparation, analysis techniques and equipment

The objective of the studies reported in this thesis was to investigate near surface damage formation and regrowth processes as well as the behaviour of dopant ions implanted into silicon during ultra low energy ion implantation and annealing. The focus was to study conditions typical for forming ultra shallow junctions (USJ's), for source / drains and extensions. Implant and annealing conditions are similar to those used in actual device production (i.e. 3keV BF_2 and As). However a particular interest was to gain a better understanding of the mechanisms involved using detailed structural characterisation of the as-implanted and annealed Si. For this reason there is special emphasis on using lower annealing temperatures to capture the various stages of regrowth which cannot be identified under production annealing conditions. The work formed part of a European project, IMPULSE (27), the project aims of which were to get a complete physical and electrical characterisation of implants and to identify the optimum implantation and anneal process conditions for the latest generation transistors. The work was performed in close collaboration with Advanced Micro Devices (AMD) in Dresden, Germany.

Additional work has been carried out in close collaboration with Applied Materials Implant Division, part of one of the largest equipment manufacturers in the semiconductor industry.

Implanted and annealed samples used in this project have been produced at The University of Salford using the Ultra Low Energy Implanter (28), by AMD, in Dresden as part of the IMPULSE project (27), and by Applied Materials Ltd. Both AMD and Applied Materials used Applied Materials Quantum LEAP implanters (29).

The main analysis technique used for the characterisation of the samples was medium energy ions scattering (MEIS). In essence a high resolution variation of the

technique of channelling Rutherford Backscattering Spectrometry (RBS/C), MEIS is able to provide depth profiles of both the dopant and the damaged Si with sub nm depth resolution. Experiments were carried out at the CCLRC facility at Daresbury Laboratory (30). Additionally, secondary ion mass spectrometry (SIMS) measurements were carried out for a comparison with MEIS experiments, forming the basis of the analysis.

1.6 Scope of the project

A review of atomic collisions in solids is contained in chapter 2. Chapter 3 reviews damage formation and annealing in ion implanted Si. Chapter 4 reviews the analysis techniques, primarily focusing on MEIS. It also includes information on sample production including information regarding the implantation and annealing equipment.

In chapter 5 the results of the Si damage build up and dopant migration during implantation with increasing implant doses are discussed. These studies were carried out using As and Sb ions. Damage was found to build up in a narrow layer underneath the oxide layer, with increasing implant dose. This would grow to slightly greater depths until a narrow amorphous layer was formed. The width of the amorphous layer would be subsequently increased for increased implantation dose. The location of the implanted dopant was closely related to the depth of the damaged layer. The dopant appeared to be more easily accommodated within the damaged layer. This effect is attributed to mobile interstitials being trapped at the surface sink.

Chapter 6 is concerned with aspects of Si regrowth and dopant behaviour following annealing. The studies involved mainly As implants, along with the use of Xe as a pre-amorphising implant. Different types of annealing method, i.e. standard furnace annealing, rapid thermal annealing and spike annealing (31) have been carried out. The studies are focused on using annealing conditions that are typically used in production and lower temperatures in the range 550 °C to 700 °C to study SPER. A study is also included comparing SPER on bulk Si with silicon on insulator (SOI) substrates.

An intriguing interaction between Xe, used to pre-amorphise the Si, and F and B from the BF_2 implant is described in chapter 7. Some of the implanted X, F and B have been observed to accumulate at depths of around the end of range of the BF_2 implant into the amorphous Si.

References

1 Chason et al. J. Appl. Phys., Vol 81, No 10, 15 May 1997, p 6513 – 6561.

2 Physics of Semiconductor devices, Second edition, S.M. Sze, John Wiley and Sons, New York, 1981.

3 Modern Semiconductor Device Physics, Edited S.M. Sze, John Wiley and Sons, New York, 1998.

4 Semiconductor devices physics and technology, S.M. Sze, John Wiley and Sons, New York, 1985.

5 Ion Implantation Science and Technology. 2000 Edition. Edited by J. F. Ziegler, Ion Implantation Company, 2000.

6 Electronic Materials Science For Integrated Circuits in Si and GaAs. J.W. Mayer, S.S. Lau. Macmillian Publishing Company, 1990.

7 Introductory Semiconductor Device Physics. G. Parker, Prentice Hall, 1994.

8 Wolf S., Silicon Processing for the VLSI Era, Volume 2 – Process integration, Chapter 5, Lattice Press, 1990.

9 T. Feudel, M. Horstman, D. Greenlaw, *Advanced annealing for* μ*P Technologies*, oral presentation at IMPULSE project meeting, 11th October 2004, Dresden, DE.

10 Electronics, Volume 38, Number 8, April 19, 1965

11 G. E. Moore, "Progress in Digital Integrated Electronics." IEEE Technical Digest 1975. International Electron Devices Meeting, IEEE, 1975, pp. 11-13.

12 http://www.intel.com/technology/silicon/mooreslaw/ and pages within (accessed 14/2/05).

13 http://public.itrs.net/ (accessed 18/2/05)

14 M. Horstman et al. Mat. Sci. Eng. B 114 – 115 (2004) p3 – 8.

15 T. Ghani, et al., VLSI Tech. Digest (2000).

16 T. Feudel, M. Horstmann, M. Gerhardt, M. Herden, L. Herrmann, D. Gehre, C. Krueger, D. Greenlaw, M. Raab, Mater. Sci. Semicond. Proces., **7**, (2004), 369.

17 A. Erebach, T. Feudal, A. Schenk, C. Zechner. Mat. Sci. Eng. B 114 – 115 (2004) p15 – 19.

18 K. Rim, et al., IEDM Tech. Digest (2003) 49.

19 Ion Implantation of Semiconductors, G. Carter, W.A. Grant, Arnold, 1976.

20 L. Pelaz, L.A. Marqués, J. Barbolla, Journal of Appl. Phys. 96 (2004) 5947.

21 P.M. Fahey, P.B. Griffin, J.D. Plummer, Rev. Mod. Phys. 61 (1989) 289.

22 J.S Williams. Solid Phase Recrystallisation process in Silicon. Chapter 5, p 133, in Surface modification and alloying by laser, ion and electron beams, Editors J.M. Poate, G. Forti and D.C. Jacobson, Plenum, 1983.

23 J A van den Berg, D G Armour, M Werner, S Whelan, W Vandervorst and T Clarysse, E H J Collart and R D Goldberg, P Bailey and T C Q Noakes, Proc. Int. Conf. on Ion Implantation Technology, ITT2002, September 2002, p597

24 A. Claverie, L.F. Giles, M. Omri, B. de Maudit, G. Ben Assayag, D. Mathiot. Nucl. Inst. Meth. **B 147** (1999) 1.

25 C. Bonafos, D. Mathiot, A. Claverie, Journal of Appl. Phys. **83** (1998) 3008.

26 E.C. Jones, E. Ishida, Mat. Sci. and Eng. R24 (1998) 1.

27 http://www.imm.cnr.it/imm/progetti/projects/impulse/impulse_home.html (Accessed 01/12/03)

28 R. D. Goldberg et al. Rev Sci Instrum. Vol 71, Number 2, Feb 2000 p1032.

29 http://www.amat.com/products/quantum.html (Accessed 03/06/03)

30 www.dl.ac.uk/MEIS (accessed 10/12/03)

31 Rapid Thermal Processing of Semiconductors. V. E. Borisenko, P. Hesketh. Plenum Press, 1997.

32 H. Wong, H. Iwai, Physics World, Vol 18, No 9, Sept 2005, p 40.

33 H. Iwai, Solid State Electronics, **48** (2004) 497.

Chapter 2 Atomic collision in solids

2.1 Introduction

Ion implantation is a process of injecting energetic ions into solids. Removal of an electron from an atom leaves a positively charged ion that can be accelerated in an electric field, and deflected in both electric and magnetic fields. The interaction of energetic ions with atoms in solids is of fundamental importance for understanding the behaviour of the implanted dopant ions as well as for the MEIS analysis technique. In this chapter a review of the relevant ion / solid interactions is carried out. The review concentrates on the atomic physics relevant to the specific energy regions associated with low energy implantation and MEIS. It is not intended to be an exhaustive review of ion – solid interactions. The topic is considerably more complex than the description here. The MEIS analysis technique is discussed further in chapter 4.

Much of the understanding of the theory of particles travelling through matter began with the work of Bohr (1, 2). As an energetic ion (or atom) moves through a solid, it interacts and collides with lattice atoms. This interaction is due to the force of repulsion between the two nuclei and between the two electrons clouds; and attraction between nuclei and electrons. It is usually described in terms of an interatomic potential, the precise form of which depends on the degree to which the nuclei penetrate the electron screen. For both the areas of present interest, the overall scattering can be described in terms of simple binary collisions or sequences of such collisions. However in addition to losing energy via such collisions the incident particle loses energy directly to the electrons in the solid and particularly for high energy light ions, the latter is the dominant process. As a simple rule of thumb, when the energy in keV is less than the ion mass in amu ($E < M$) then elastic energy loss dominates. When the energy is greater than the ion mass ($E > M$), inelastic energy loss dominates (14).

In the context of the present study, for low energy implantation, the theoretical interest is in the calculation of the depth distributions of the implanted ions and defects, while for MEIS the dependence of the energy of the scattered projectile ions on scattering angle and the depth at which the scattering centre is located is the primary interest. Essentially the relevant theory is required to relate the yield of the detected scattered ions as a function of energy at a reference scattering angle to the density and depth distribution of the different scattering atoms. It is necessary therefore, to consider the theory of elastic scattering processes in order to determine the energy loss per collision as a function of the scattering angle and the masses of the colliding particles

and the probability of scattering through a specific angle – the differential scattering cross section. In principle this information enables the range of the projectile particle to be calculated and the distribution of displaced target atoms to be determined. The statistical nature of the overall bombardment process has led to the development of highly effective computer codes such as SRIM (3) that enable the necessary calculations to be carried out with acceptable accuracy. Because inelastic processes play a significant role for the bombardment conditions relevant to MEIS, these processes too need to be discussed in some detail.

2.2 Elastic energy loss / Nuclear Stopping

The simplest approach when describing collisions of particles is to treat each interaction as a binary collision, i.e. a moving incident ion (or atom) and a stationary target atom, with no external restraints. This approximation is valid due to the limited range of interaction of the nuclei and hence no other nuclei will be involved. Total energy will be conserved, so the energy lost by the incident ion will be gained by the target atom.

It is a convenient approximation to describe the interacting particles as point masses, which is reasonable in view of the nucleus size. There are forces of attraction between nuclei and electrons, and repulsion between nuclei, and between electrons. The interaction is governed by the potential between the two particles, which is the sum of the potentials of interaction for each individual electron and the nuclei from the two particles. A useful simplification is to treat the potential for interaction as simply the potential between the two nuclei, with the electrons serving only to screen the positive nuclear charges from each other hence reducing the effective positive charges.

For small atomic separations r, $0 < r << a_0$, where a_0 is the radius of the Bohr orbit in hydrogen (= 0.53Å) there are no electrons between nuclei and the potential is purely repulsive and can be described by a Coulomb potential. This can occur with high energy, light particles in solids, e.g. MeV H and He in Si. This situation is the so-called Rutherford scattering situation. The Coulomb potential is given by;

$$V(r) = \frac{Z_{1,\mathrm{eff}} Z_{2,\mathrm{eff}} e^2}{4\pi\varepsilon_0 r} \qquad (2.1)$$

where $Z_{1,\mathrm{eff}}$ and $Z_{2,\mathrm{eff}}$ are the reduced values of the nuclear charges. The force of repulsion is;

$$F(r) = \frac{Z_{1,\mathrm{eff}} Z_{2,\mathrm{eff}} e^2}{4\pi\varepsilon_0 r^2} \qquad (2.2)$$

Equations 2.1 and 2.2 show that the force and the potential decrease rapidly with increasing atomic separation. Collisions leading to deflections occur over a relatively small range of distances, the closest being about 10^{-11} m and obviously the most distant collisions occur at a distance no greater than half the interatomic spacing.

This situation is not changed significantly when screening functions are introduced and the entire collision sequences associated with ion implantation over the energy range of present interest can be described in terms of successive binary collisions. An additional justification for this approximation is that over the major part of the highly energetic interaction, the energy transferred in the collisions significantly exceeds the binding energies of the target atoms in the solid. Hence there is no need to adjust the mass of the target atoms to compensate for binding effects.

When the distance between the two atoms is of the order of a_0, e.g. for 10 – 200 keV H and He in Si, the Coulomb potential is no longer valid, because the positive charges are likely to be reduced by the presence of inner shell electrons in the region between the two nuclei. Several analytical and empirical approximations have been developed to calculate the effects of electron screening which leads to a screened Coulomb potential, where the Coulomb potential is multiplied by a screening function

$$V(r) = \frac{Z_1 Z_2}{4\pi\varepsilon_0 r} \exp\left(\frac{-r}{a}\right) \qquad (2.3)$$

where r is the separation distance and a is the screening radius, or parameter. This screening parameter is an important concept. It moderates the effect of the nuclear positive charge on the electrons because the inner electrons shield some of the nuclear charge. Bohr suggested an empirical exponential form (4). More complicated potentials were derived based on analytical results, such as those developed by Firsov (5), given in equation 2.4, Moliere (6), and Lindhard (7), all of which are based on the Thomas – Fermi free electron gas model (8).

$$a = \frac{a_0}{(Z_1^{1/3} + Z_2^{1/3})^{2/3}} \qquad (2.4)$$

For MEIS using 100 – 200 keV H or He ions it is generally accepted that a screening function as expressed in the Molière potential (6) or a modified form of it is a good screening function to use (9, 10). The implications for MEIS are discussed further in chapter 4.

A universal potential (11, 12, 13) developed by Biersack and Ziegler, again based on treatment of the Thomas – Fermi model (free electron gas) has been shown to give a good description for intermediate separations ($0 < r < a_0$) which are of vital

importance for many atomic collision problems, such as that of radiation damage in solids. The purpose was to find a way of calculating the potential for any ion – target combination. Using a calculation of the interatomic potential for about 500 ion – target combinations, a function for the average potential could be produced.

2.2.1 Scattering cross section

The precise trajectories of the colliding particles depend on the impact parameter and the interaction potential. This forms the basis of the quantitative calculation of the probability of scattering through a specific angle and the rate of elastic energy loss as the projectile particle passes through the solid target. The quantity of interest for both these calculations is the so – called scattering cross – section (14, 15, 16). It is used as a quantitative measure of the probability that an incident particle will be scattered by a target atom at an angle θ into a solid angle Ω and comes from the work of Rutherford in explaining the results of Geiger and Marsden on the scattering of alpha particles.

If a uniform parallel flux of ions is incident upon a stationary atom, ions at a certain p will be scattered into a cone of half angle θ as shown in Figure 2.1. The plane area defined by radii p and p + δp defines atoms that are scattered between angles θ and θ + δθ. This area 2πpδp is known as the differential scattering cross section (dσ) for scattering between impact parameter limits p and p + δp and scattering angles θ and θ + δθ. However the solid angle (dΩ) included by the cones of half angle θ and θ + δθ is equal to 2π sinθ δθ. The differential scattering cross section for scattering into unit solid angle becomes:

$$\sigma(\theta) = \frac{\mathrm{d}\sigma}{\mathrm{d}\Omega} = \frac{\mathrm{p}\delta\mathrm{p}}{\sin\theta\delta\theta} \tag{2.5}$$

The value of the differential scattering cross section is given by:

$$\sigma = \frac{\mathrm{d}\sigma}{\mathrm{d}\Omega} = \mathrm{F}\left[\frac{\mathrm{Z_1 Z_2 e^2}}{4\mathrm{E}\sin^2(\theta/2)}\right]^2 \mathrm{g}(\theta, \mathrm{M_1}, \mathrm{M_2}) \tag{2.6}$$

where F is a function derived from the Moliere potential, given by (9, 10):

$$\mathrm{F} = 1 - \frac{0.042\mathrm{Z_1 Z_2}^{4/3}}{\mathrm{E}} \tag{2.7}$$

and g is a multiplication factor to account for the transformation from the centre of mass to the lab frame of reference. The scattering yield will vary with the differential scattering cross section. For conditions with a larger σ the scattering yield will therefore also be larger. This has important consequences for MEIS analysis and the rate of

energy deposition. Equation 2.6 shows that significantly σ is proportional to Z_1^2, Z_2^2, E^{-2} and $\sin^{-4}(\theta/2)$. The implications for MEIS analysis are discussed further in section 4.2.2.

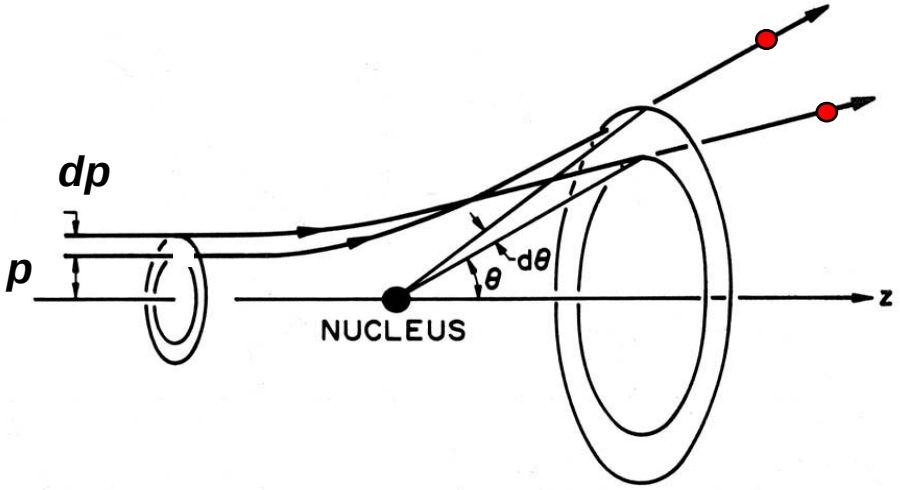

Figure 2.1 Scattering into a solid angle. From (16).

2.2.2 The Kinematic Factor

Using the hard sphere model a collision between an energetic ion and a stationary target atom is illustrated in Figure 2.2. The incident ion (mass M_1) moves towards the target atom (mass M_2), with some perpendicular distance between the line of the centre of the particles, p, called the impact parameter. The centre of the incident ion will approach the centre of the target atom to a distance of the sum of the radii of the two spheres, $2R_0$, where a collision takes place. The incident ion will be scattered and energy will be imparted to the target ion causing it to recoil. Because there are no external constraints total energy and momentum are conserved.

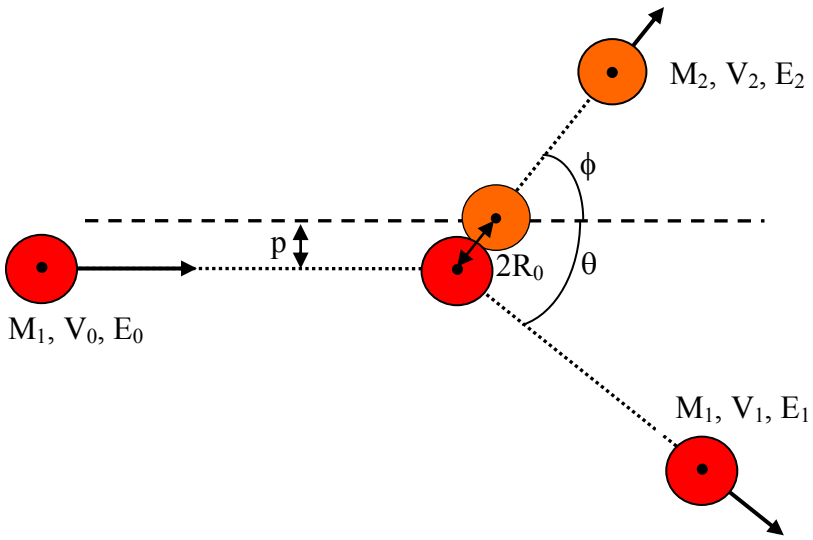

Figure 2.2 Elastic scattering configuration.

The kinematic factor K is defined as the ratio of the energy of an ion after a collision to its energy before a collision, i.e.

$$K \equiv \frac{E_1}{E_0} = \left[\frac{V_1}{V_0}\right]^2 \tag{2.8}$$

It can be shown that

$$\left[\frac{V_1}{V_0}\right] = \left[\frac{\left(M_2^2 - M_1^2 \sin^2\theta\right)^{\frac{1}{2}} + M_1 \cos\theta}{M_2 + M_1}\right] \tag{2.9}$$

where θ is the scattering angle. Therefore the kinematic factor for backscattering, where $M_1 < M_2$ is given by (14, 17),

$$K = \left[\frac{\left(M_2^2 - M_1^2 \sin^2\theta\right)^{\frac{1}{2}} + M_1 \cos\theta}{M_2 + M_1}\right]^2 \tag{2.10}$$

In Chapter 4 it is shown in more detail how this expression allows MEIS analysis to be sensitive to scattering from different masses and hence be sensitive to different elements (9, 10, 17).

2.2.3 Energy transferred in elastic collisions

The amount of energy that can be transferred in an elastic collision is dependent on the masses of the particles and the impact parameter. The maximum energy transfer results from a head on collision and is given by (14):

$$T = \frac{4M_1M_2}{(M_1 + M_2)^2} E_0 \qquad (2.11)$$

The energy transferred will decrease with increasing impact parameter and the average energy transferred is half that of the maximum value. The path of each ion depends on the individual collisions that it encounters and hence the final depth of an implanted ion will be subject to statistical variations. The nuclear stopping power $(dE/dx)_n$ gives an average rate of energy loss of the ions through elastic collisions. The nuclear stopping power can be related to the scattering cross section. The rate of nuclear energy loss affects both the range of an implanted ion, discussed in section 2.4, and the damage to the crystal, discussed in chapter 3.

2.3 Inelastic energy loss / Electronic stopping

The interaction of an energetic ion with the electrons in the target results in inelastic energy loss of the ion. As the ion passes by, each atom will be individually perturbed, leading to electron excitation within each participating atom, in some cases ionisation will occur. Electron excitation and ionisation lead to internal energy consumption in the colliding atom system. The energy absorbed in the excitation process will not generally be restored to the kinetic or potential energy of the system and this leads to inelastic energy loss. An average of the individual interactions gives the rate of inelastic energy loss, called the stopping power or the specific energy loss, termed $(dE/dx)_e$, and in this thesis expressed in units of eV/Å.

As an ion travels through a solid it would undergo many interactions and as such it is not possible to know the precise details of these interactions. Several models exist to describe the interactions and provide estimates for the stopping powers. Only a brief summary of important models is given here. Further explanation is beyond the scope of this thesis. Further details are given in (5, 8, 17). Accurate values for the inelastic energy loss rates as a function of energy are essential for the correct depth scale calibration of the MEIS results. This is discussed further in section 4.2.3.1.

2.3.1 Models for inelastic energy loss

Bohr used classical mechanics to describe the interaction of a charged moving particle with the electrons in the target, (1, 2). The energy loss under these circumstances is based on the classical calculation of the momentum and energy transferred to an electron by the ion in a collision. This simple picture ignores the fact that electrons are bound to atomic nuclei. The ionisation energy required to separate the electron from the atom has to be accounted for and therefore the scattering event becomes inelastic. Bohr showed that the rate of energy loss varies with the ion velocity.

A number of approximations were developed to take into account possible energetic states of an electron in the target and the average population of these states. The work of Bethe (18) and Bloch (19) produced a quantum mechanical approach to the inelastic energy loss. The Bethe – Bloch formula only describes the energy loss well at energies beyond the maximum in the dE/dx curve to near relativistic velocities, i.e. in the region from 10MeV/amu to 2 GeV/amu (see Figure 2.3 later). In this regime there is an increase in the inelastic stopping power for a decrease in velocity.

For lower energies, two models that better describe the inelastic energy loss are that of Firsov (20) and Lindhard (21, 22). Neither model comprehensively takes account of every interaction taking place, but both theories adequately describe the general behaviour of the stopping power with regard to the energy dependence and the magnitude.

Firsov's expression (20) is based on a simple geometric model of momentum exchange between the projectile and the target atom during the interpenetration of the electron clouds surrounding the two colliding atoms. Each binary collision is viewed as leading to an overlap of their electron orbits and the formation of 'quasi molecules' with electrons from both atoms crossing the instantaneous quasi boundary between the atoms, which then take on the momentum of the atom to which they temporarily attach. Electrons transferred either temporarily or permanently from the ion to the atom and vice versa cause a transfer of momentum. Thus electrons from the moving atom lose momentum in transferring to the initially stationary target atom and those from the struck atom gain momentum from the incident particle. This momentum exchange processes leads to energy loss of the incident particle.

Another way to look at the inelastic energy loss is the model of Lindhard and Scharff (21, 22) based on a free electron gas. In the gas, positively charged nuclei are embedded in effectively a plasma. The electrons are no longer considered to be attached to any one atom. The model assumes that the free electron gas consists of electrons at

zero temperature on a fixed uniform positive background with overall charge neutrality. A fast charged particle entering the system brings about a polarisation of the medium which causes energy absorption. The interaction of the charged particle on the homogeneous electron gas is a small perturbation. It is worth mentioning that this work forms part of a comprehensive theory of energetic ions often referred to as LSS theory (23). The electronic stopping power is dependant on the colliding atoms but varies linearly with velocity for low energies. In addition to the electronic stopping power LSS theory gives a universal nuclear stopping power and allows the range to be calculated. A more detailed treatment of LSS theory is beyond the scope of this thesis.

2.3.2 Summary of General trends in the inelastic energy loss curve

The rate of inelastic energy loss is dependant on the ion energy, and can be considered to consist of two different velocity regimes. The maximum of the stopping curve lies in the general vicinity of the 'Thomas – Fermi' velocity given by $Z_1^{2/3}v_0$ (v_0 is the Bohr velocity and, $v_0 = e^2 / \hbar = 2.2x10^8$ cm/s) and is usually somewhat above it. This provides a convenient reference point. Starting with fast moving particles the stopping cross section increases with decreasing velocity because the particle spends more time in the vicinity of the atom. The stopping is found to be inversely proportional to the energy. As the energy decreases towards the maximum $(dE/dx)_e$ increases less rapidly with falling energy E, and eventually turns around and starts to decrease. For low velocities the stopping is found to be proportional to $E^{0.5}$ (24). These aspects are illustrated in Figure 2.3 below for the electronic stopping powers of He and H ions in Si.

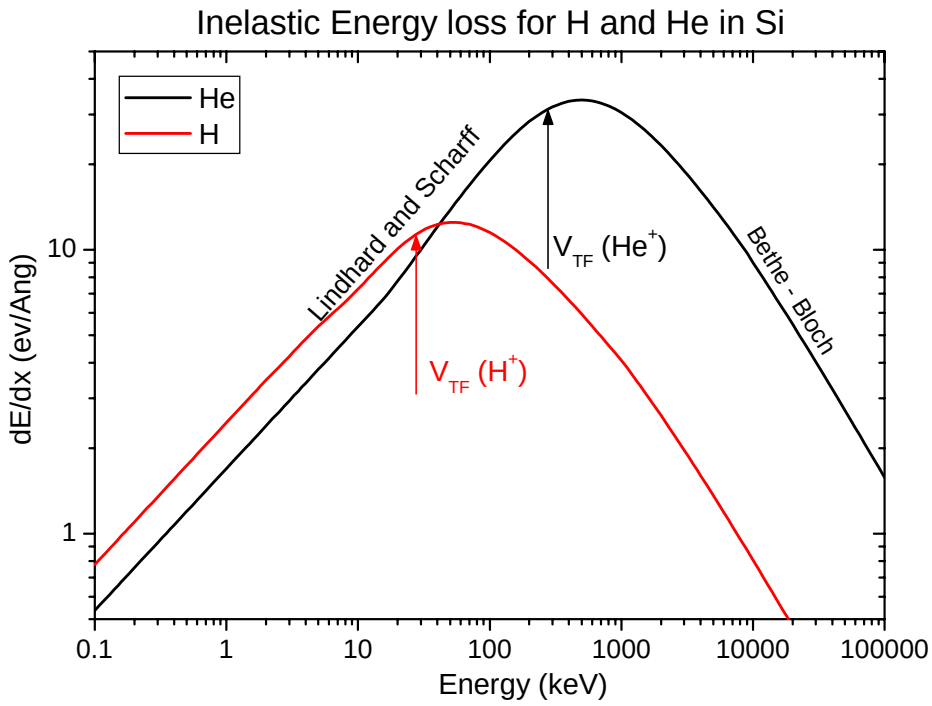

Figure 2.3 Electronic stopping powers for H and He ions in Si. The positions corresponding to the Thomas Fermi velocity are indicated, along with the energy regimes where different models for the stopping powers are applicable.

Electronic stopping depends on the electronic states in the target so that in principle gas, liquid, and solid of the same element must have different stopping cross sections. The nature of the chemical binding also affects the electronic states. Both of these effects however are weak.

2.3.3 Experimentally obtained stopping powers

As well the large amount of theoretical information available on the magnitude of the stopping powers available, experimental measurements can be carried out to determine stopping powers. Averages of the best experimental and theoretical stopping power values have been produced and can be tabulated using the SRIM programs (3, 8). The MEIS analysis in this thesis has used the SRIM values for the inelastic stopping powers.

2.3.4 Difference in stopping powers in open channels

Along the open crystal channels the electron densities are reduced. This has the effect of reducing the rate of inelastic energy loss compared to a random direction (25). R is defined as the ratio of the energy loss in an open channel to the energy loss in a

random direction. For He it has been found that R is energy dependant and has a maximum near the maximum in the dE/dx curve. The crystal orientation also has a strong influence on R. For He in Si <111> R is ≈ 0.93 near to the maximum. This is reduced to ~ 0.9 in the energy range 100 – 200 keV. For the Si <110> directions R is ≈ 0.83 at the maximum (25).

2.3.5 Correlation between stopping and screening

As the electronic and nuclear stopping occurs at the same time in close collisions and the screening of the nucleus is due to the electrons it would appear that there should be some correlation between the elastic and inelastic energy loss. However it is justifiable to ignore these correlations and regard the electronic stopping as a continuous process (26).

2.3.6 Example of relevant nuclear and electronic stopping powers

In Figure 2.4 the nuclear and electronic stopping powers for He and As in Si are plotted. These values are obtained from SRIM 2003. There is a wide energy range for both, displaying the trends described previously. The relevant energy regimes used for MEIS and low energy implantation are indicated between dashed lines for the He and As plots, respectively. As mentioned previously it is electronic stopping that dominates for the medium energy light He ions. The same is also true for RBS measurements in the 1 – 2 MeV energy range. Nuclear stopping is negligible, apart from the actual backscattering event. On the other hand for low energy heavy ions used for implantation, nuclear stopping dominates.

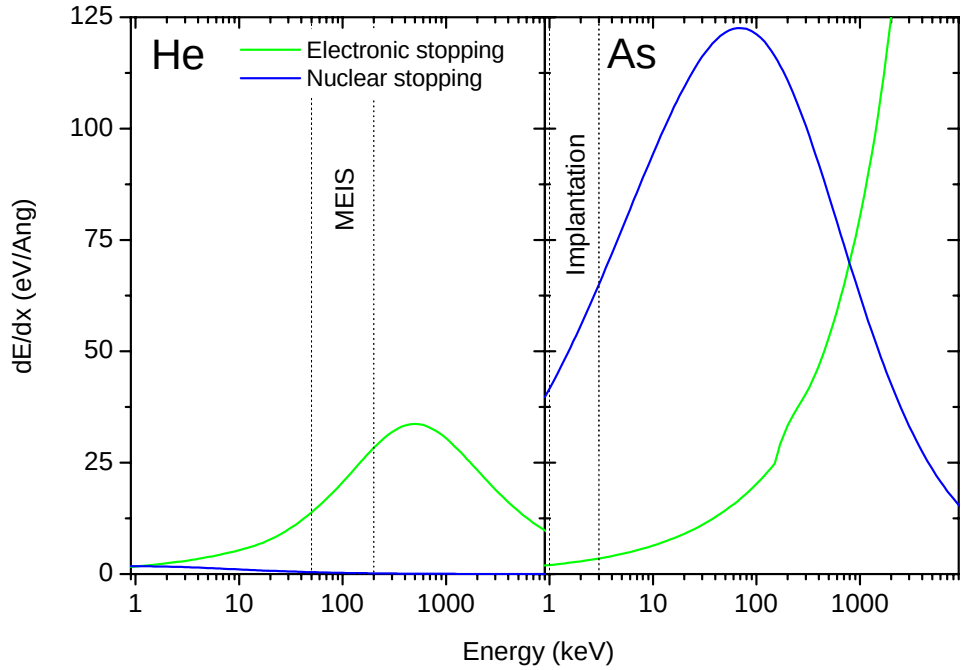

Figure 2.4 Electronic and Nuclear stopping powers for He and As in Si. The energy regimes used in MEIS and for the implants are indicated.

2.4 Ion range

Ions travelling through a solid will undergo collisions with different lattice atoms and as such the path taken by all the implanted ions will vary. The final depth that implanted ions will come to rest at will vary as with any statistical process, and as such will usually follow a Gaussian distribution. The average depth of implanted ions is known as the mean projected range (R_p), and the spread of the implanted ions about the mean depth is known as straggling.

2.4.1 Range calculation

In dealing with the stopping power it is often convenient to define a stopping cross section, S, where;

$$S_e = \frac{1}{n}\left(\frac{dE}{dx}\right)_e \qquad \text{and} \qquad S_n = \frac{1}{n}\left(\frac{dE}{dx}\right)_n \qquad (2.12 \text{ a and b})$$

where N is the density (15). Stopping cross sections are often used in range calculations.

The rate of energy loss of an ion as it travels through a solid is the sum of the nuclear and electric stopping, i.e.:

$$\frac{dE}{dx} = \left(\frac{dE}{dx}\right)_e + \left(\frac{dE}{dx}\right)_n \qquad \text{or} \qquad \frac{dE}{dx} = N\left(S_n(E) + S_e(E)\right) \qquad (2.13)$$

in terms of stopping power and stopping cross section respectively. Knowledge of the stopping power allows the overall slowing down to be described in a quantitative way. It therefore enables calculation of the range. Rearranging equation 2.13 and integrating from the maximum energy E_0 to zero yields the total path length, R(E), of the ion:

$$R(E) = \int_0^{E_0} \frac{dE}{\left(dE/dx\right)_e + \left(dE/dx\right)_n} \quad \text{or} \quad R(E) = \frac{1}{N}\int_0^{E_0} \frac{dE}{S_n(E) + S_e(E)} \qquad (2.14)$$

2.4.2 Simulation of ion implantation (using SRIM)

Several computer simulation codes have been developed to calculate parameters such as the range and straggling of implanted ions. The Stopping and Range of Ions in Matter (SRIM) (3) is a group of programs which calculate the stopping and range of energetic ions into matter using a fit to a full quantum mechanical treatment of ion-atom collisions. The most comprehensive of these programs is the Transport of Ions in Matter (TRIM). The TRIM simulation code is widely used for simulating the effects of ion implantation and has been useful within this study to compare theory to the experimental depth profiles obtained from MEIS. Because of the statistical nature of the paths of implanted ions simulations TRIM uses Monte Carlo methods and a binary collision algorithm to calculate the ion trajectories of many implanted ions. It will accept complex targets made of compound materials, and calculate the final 3D distribution of implanted ions and also all kinetic phenomena associated with the ion's energy loss: target damage, sputtering, ionisation and phonon production. As an example a simulation of the paths of twenty implanted As and B ions into Si with an implant energy of 3 keV, is shown in Figure 2.5 a) and b) respectively. The shallower implantation and smaller amount of straggling seen with As compared to B is due to the higher nuclear stopping power. TRIM works on the basis of an amorphous matrix.

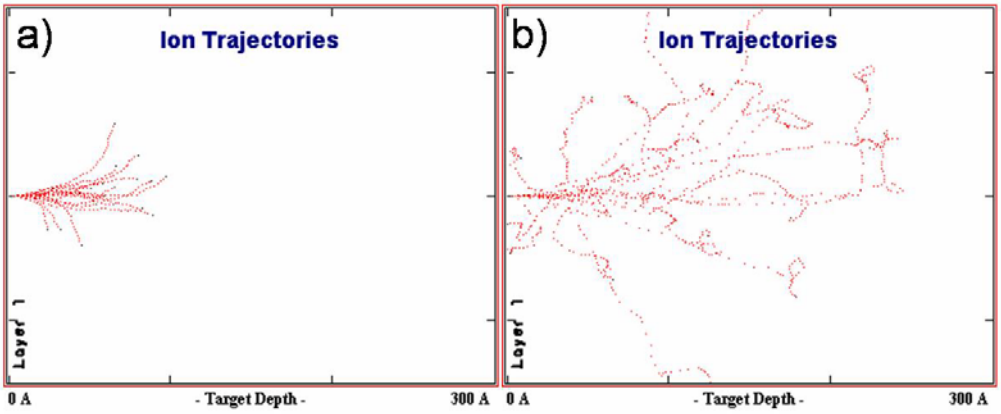

Figure 2.5 Results of TRIM simulations showing the trajectories of 20 a) 3 keV As ions and b) 3 keV B ions, implanted into Si.

2.4.3 Channelling of the ions

As mentioned previously in relation to the inelastic energy loss, in a crystal there are large open channels (25). If implantation is carried out along an axis it can be possible for a small fraction of the ions to be channelled to considerably greater depths. Screening prevents large angle scattering. For ion implantation this is undesirable as shallow junctions are required. Often pre-amorphisation or implantation off axis is carried out to avoid channelling. Channelling is exploited in the MEIS analysis technique to study damaged layers and this is described in section 4.2.1.6.

References

1 N. Bohr, Phil. Mag. **25** 10 (1913)

2 N. Bohr, Phil. Mag., **30** 581 (1915)

3 Ziegler, J. F. SRIM – The Stopping and Range of Ions in Matter. <http://www.srim.org/> (Accessed 07/04)

4 N. Bohr, Kgl. Dansk. Vid. Selsk. Mat. Fys. Medd. 18, No 8, 1948.

5 O. B. Firsov, Sov. Phys. JETP 6, 1958, 534.

6 G. Moliere, Z. Naturforsch. 2a, 1947, 133.

7 L. Lindhard, V. Nielsen, M. Scharff, Det Kong. Dan. Viden. Selskab. Mat. Fys. Medd. 36, 1968, 10.

8 J. F. Ziegler, J. P. Biersack, and U. Littmark, The Stopping and Range of Ions in Solids (Pergamon Press, New York, 1985).

9 Van der Veen, J.F., Surf. Sci. Rep., **5**, Nos. 5/6, 1985.

10 Tromp, R.M. Medium Energy Ion Scattering. In: Briggs D. and Seah P. editors. Practical surface analysis. Volume 2 – Ion and Neutral Spectroscopy. 2nd ed. John Wiley Ltd. 1992.

11 J. P. Biersack, J. F. Ziegler, Nucl. Instrum. Meth. 194, 1982, 93.

12 D. J. O'Connor, J. P. Biersack, Nucl. Instrum. Meth. B 15, 1986, 14.

13 J. P. Biersack, J. F. Ziegler. "The Stopping and Range of Ions in Solids". From Ion implantation techniques, Springer, Berlin, 1982, Eds. H. Ryssel & H. Glaswisching.

14 Ion Implantation of Semiconductors, G. Carter, W.A. Grant, Arnold, 1976.

15 Ion implantation, G. Dearnaley, J. H. Freeman, R. S. Nelson, J. Stephen, North – Holland Publishing Company, Amsterdam, 1973.

16 Fundamentals of surface and thin film analysis, L.C. Feldman, J. Mayer, North-Holland, 1986.

17 Backscattering Spectrometry, W. K. Chu, J. W. Mayer, M. Nicolet, Academic Press, New York, 1978.

18 H. A. Bethe, Ann. Physik, **5**, 325 (1930)

19 F. Bloch, Ann. Physik, **16**, 285 (1933)

20 O. B. Firsov, Sov. Phys. JETP 9, (1959), 1076.

21 J. Lindhard and M. Scharff, Kgl. Danske Vid. Selsk., Matt. – Fys. Medd. **27**, No 15. (1953)

22 J. Lindhard and M. Scharff, Phys. Rev. **124**, 128 (1961)

23 J. Lindhard, M. Scharff, H. E. Schiøtt. Matt. Fys. Medd. Kgl. Danske Vid. Selsk., **33**, (1963) No 14.

24 E. Fermi and E Teller, Phys. Rev., **72**, 399 (1947)

25 Eisen, F. H. G.J. Clark, J. Bøttiger, J.M.Poate, Radiat. Eff. 13, 1972, pp 93

26 Lindhard 1954, Kgl. Danske Vid. Selsk., Matt.-Fys. Medd. **28**, No. 8.

Chapter 3 Damage and Annealing processes

3.1 Introduction

Ion implantation into Si results in the displacement of Si atoms, i.e. damage to the Si lattice. While simple atomic displacement can be described in terms of the atomic theory summarised in Chapter 2, the role of energy deposition density in determining the nature of the damage is more complex. This chapter describes the damage effects produced during implantation and different types of model for damage build up and amorphisation. To produce the electrically active doped regions, post implantation annealing is required to restore the crystal lattice and enable the dopants to take up substitutional lattice sites. The process by which the crystal lattice structure is restored during annealing in most device production, i.e. solid phase epitaxial regrowth (SPER), is described. Defect evolution also occurs during annealing and a brief summary of these aspects is given. Defects still present after annealing can be detrimental to transistor device performance in that they can introduce unwanted leakage currents and decreasing carrier mobility, i.e. the proportionality constant between the electric field and the electron drift velocity (1). Diffusion of the implanted ions to greater depths during annealing needs to be minimised for shallow junction depths (X_j). The evolution of the defects at the end of the range (EOR) of the implant can cause an anomalous enhancement of dopant diffusion called transient enhanced diffusion (TED). The effects discussed in this chapter shows that optimised annealing conditions must be a compromise between conditions that result in high levels of electrical activation with minimal defects and conditions that minimise the dopant diffusion.

3.1.1 Si crystal structure and its properties

The Si crystal lattice has a diamond – type structure. This can be considered to be composed of two interpenetrating fcc lattices offset by a ¼ lattice cell along each of the [100], [010] and [001] axes (2, 3). Each Si atom is covalently bound to four others in a tetrahedral arrangement sharing two valence electrons of the sp^3 shell per bond (3) with a typical bond angle of 109.47° (4). The conventional unit cell contains 8 atoms and has a lattice constant, a, of 5.4 Å (2, 3). The distance of nearest neighbour spacing is $\sqrt{3}/4a = 2.4$ Å and the next nearest neighbour is 3.8 Å (3). The Si unit cell is shown in Figure 3.1. The atomic density of Si is 5.032×10^{22} atoms/cm^3 at room temperature (3). The (100), (110) and (111) planes are shown in Figure 3.2 respectively. Si has three isotopes, ^{28}Si, ^{29}Si and ^{30}Si, with ^{28}Si the most abundant isotope with a natural

abundance of 92.23 % (3). This has a small bearing on the MEIS spectra and is discussed in section 4.2.2.

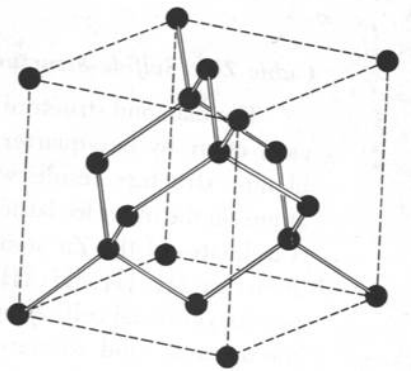

Figure 3.1 Si unit cell. From (2).

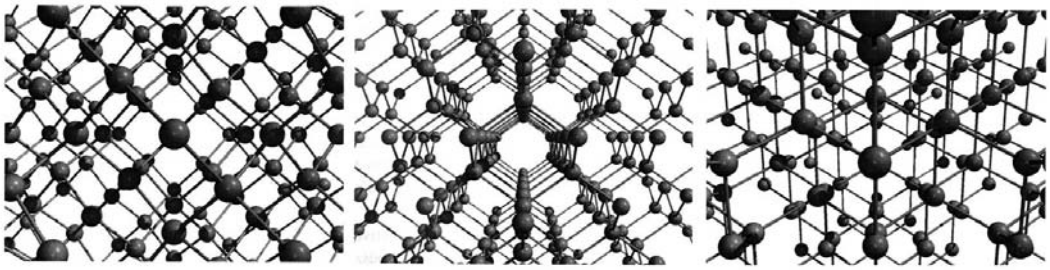

Figure 3.2 Si (100), (110) and (111) planes. From (3)

Intrinsic (undoped) Si has a band gap of 1.1 eV at room temperature and will have an equal (low) concentration of holes and electrons (5). Extrinsic (doped) Si will have an excess of holes or electrons depending on the doping type. Usually doping is with group III and V atoms although group II and VI are also used. To be electrically active these atoms have to replace a Si atom being covalently bound to Si atoms, creating an unsatisfied bond (hole) if a group III ion or with an extra electron not involved in bonding, available of conduction, if group V dopant.

Si oxidises in air to form a native SiO_2 layer. This SiO_2 is amorphous and is an electrical insulator. The native oxide can easily be removed in a HF dip. Thin oxide layers are used as the insulating gate oxide and can easily be grown on the surface of Si to the required thickness. Mechanisms for oxide growth are discussed in (6) and references therein. Oxygen molecules react with surface Si atoms to form SiO_2. Further growth is due to the diffusion of oxygen through the SiO_2 layer which reacts with Si at

the Si/SiO_2 interface, consuming the Si. The ease of removing and growing high quality oxides on Si is one reason for it being the dominant material in semiconductor processing.

3.2 Implantation induced defects, damage build-up and amorphisation

3.2.1.1 Atomic displacement

An energetic ion or atom moving through a solid loses energy in a succession of collisions. The loss must be dissipated to the atoms of the solid increasing their kinetic and potential energies, or to the electrons in excitation and ionisation

Each atom is bound to its equilibrium lattice position by the forces of interaction with its neighbours. If an ion impacts a target atom and imparts an amount of energy large enough to break the bonds holding the atom it will be permanently displaced from its lattice site (7). The amount of energy required to dislodge an atom in this fashion is known as the displacement energy (E_d) and is regarded to be 13 eV for bulk Si (8).

3.2.1.2 Point defects

The smallest defects in Si, i.e. interstitials and vacancies are termed point defects and the main effect of such defects is on their nearest neighbouring atoms in the crystal. Defects of higher dimensionality are classified under the terms extended or secondary defects (3).

Point defects can be separated into two categories. Native defects (9), also known as intrinsic defects (3), consist of only atoms native to the crystal. Impurity related defects (9), also called extrinsic point defects (3), arise from the introduction of foreign impurities into the lattice (9). Native point defects will exist in any pure Si lattice above absolute zero, and obviously will always exist in ion implanted Si.

The main point defects of interest, within the context of this thesis, are the vacancy, interstitial, and also the interstitialcy. A vacancy is an empty lattice site, created when an atom is displaced in a collision, and shown schematically in Figure 3.3a). An interstitial is an atom which is not located on a regular lattice site. Si interstitials are often termed self interstitials, Figure 3.3c), to distinguish them from impurity interstitials, Figure 3.3e). An interstitialcy is proposed to consist of two atoms in non substitutional positions configured around a single lattice site, shown in Figure 3.3d). Often no distinction is made between interstitials and interstitialcies as both essentially consist of one extra atom (9). Differences are proposed for the diffusion mechanisms, discussed in section 3.5. A further defect, the di-vacancy, Figure 3.3 b),

can be formed directly through the dislodgment of two neighbouring atoms or through migration of defects, (discussed later).

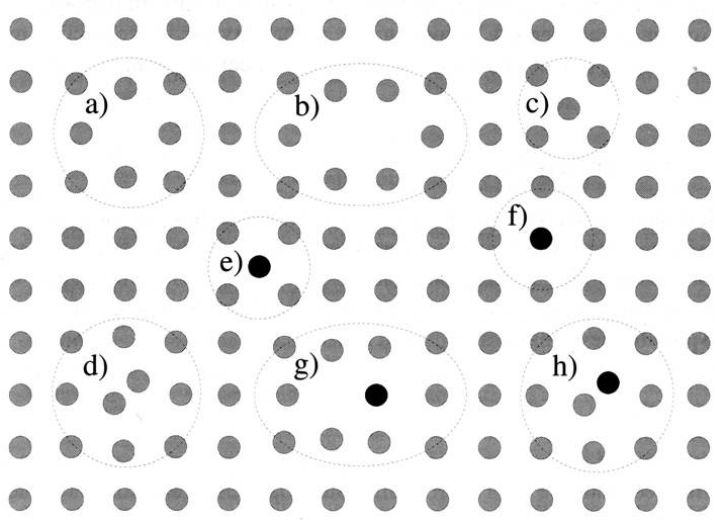

Figure 3.3 Schematic of different defect types, i.e. a) vacancy, b) di-vacancy, c) self interstitial, d) interstitialcy, e) impurity interstitial, f) substitutional impurity, g) impurity vacancy pair, h) impurity self interstitial pair. From (3).

Extrinsic defects involve non – Si (dopant) atoms. They can occur as interstitials, as shown in Figure 3.3 e). When they take up substitutional positions within the lattice, they are called substitutional impurities, as shown in Figure 3.3 f). Such a position would be required for the dopant to become activated. More complex configurations such as the impurity vacancy pair g) and impurity self-interstitial pair h) can be formed. The presence of defects has important consequences for the diffusion of the dopant, discussed later in section 3.5.

A collision producing a displacement leads to the formation of both a vacancy and interstitial simultaneously, called a Frenkel pair. It is possible during the quenching of the cascade for an interstitial to recombine with a vacancy and annihilate both defects.

Point defects introduce lattice strain and cause a local distortion of the matrix, atoms surrounding a vacancy tend to relax towards the vacancy and an interstitial tends to push out the surrounding atoms. Substitutional dopant atoms may also cause some lattice distortion due to differing sizes of the atoms.

Another important defect configuration that occurs for heavy dopants such as As, is the As vacancy cluster, As_nV, where up to 4 As atoms can surround a vacancy (10). Although in this configuration the As atoms are on substitutional lattice sites the As is electrically inactive.

On the basis that by creating an interstitial a vacancy is also created and that when an interstitial and vacancy combine they are annihilated, then there will be an excess of interstitials in the ion implanted Si, due to the number of implanted ions which is known as the plus one model (11). This only holds in damaged crystalline Si. In amorphised Si the plus 1 model holds in the area beyond the amorphous/crystalline interface, with the ions that reach that depth.

Point defects can become electrically active if they accept or lose electrons during their formation and may have electron energy states that fall within the Si band gap. In Si the presence of a vacancy results in the neighbouring atoms having unsatisfied bonds. Unsatisfied bonds reconfigure themselves to accommodate the defect in the lattice. This can create different charge states. Vacancies can have one of 5 charge states V^{2-} V^{-} V^{0} V^{+} V^{2+} (12). They are predominantly double negative in n-type material and neutral in p-type. An interstitial, having valence electrons not involved in bonding, exhibits donor like properties. The lattice reconstruction around a point defect depends on its charge state. Charge states can effect the migration of the defect.

3.2.1.3 Point defect migration and secondary defects formed prior to annealing

Depending on lattice temperature and charge state, point defects become able to migrate at different temperatures. Vacancies and interstitials are mobile at low temperatures, ~ 150K (12). Divacancies are stable up to ~ 500K and therefore are the dominant vacancy complex found in room temperature implants. If a vacancy is bound to an impurity they can become stable to 400 – 500 K (13).

A variety of outcomes are possible with mobile point defects. For example a mobile vacancy could recombine with an interstitial, or vice versa. Bonding to impurity atoms can occur, forming for example an impurity-vacancy pair. Mobile interstitials can be trapped at various defect traps and sinks, for example the SiO_2 – Si interface, the surface, pre-existing damage, amorphous zones, and amorphous/crystalline interfaces. Secondary defects are formed from the agglomeration of several point defects to form clusters. They can be created during the quenching stage of the implantation, or post implantation through the migration of mobile defects, or during annealing. Secondary defects act as precursors for extended defects that are formed during annealing. There is a lower free energy for conglomerations of secondary and extended defects compared to point defects. These issues are discussed further in sections 3.4 and 3.5.

3.2.1.4 Dynamic annealing

A specific consequence of the migration of vacancies and interstitials is that damage can be removed by the annihilation of vacancies and interstitials during the collision cascade caused by implantation. This process is called dynamic annealing and the rate is dependant upon implant parameters, principally the rate of defect generation and the substrate temperature. An increased defect migration at higher implantation temperatures causes correspondingly higher levels of defect annihilation. A high implant temperature could stop amorphous layers forming depending on the implant species and fluence. (See section 3.3 for a description of the amorphisation process.) If however implantation is carried out at liquid nitrogen temperatures the majority of defects will be frozen in. It is worth mentioning there is a careful balance of effects occurring within implantation to the extent that under certain conditions it is possible to re – crystallise amorphous layers by ion implantation (14-16) in a process called ion beam induced epitaxial crystallisation, through the energy supplied in the implantation. There is a delicate balance between crystallisation and the damage formation (14).

3.2.2 Amorphisation

3.2.2.1 Structure of amorphous Si

Amorphous Si differs from crystalline Si by having no long range order or periodicity. It can be described as having a frozen liquid structure or as a continuous random network of Si atoms. Generally each Si atom is four fold coordinated bonded to four other Si atoms but with large average distortion of bond angles and lengths that incorporate 5 and 7 ring structures as well as the 6 ring structure for the crystalline, as shown in Figure 3.4. Additionally amorphous Si has been found to contain defects without four fold coordination, such as dangling bonds and vacancy type defects (4).

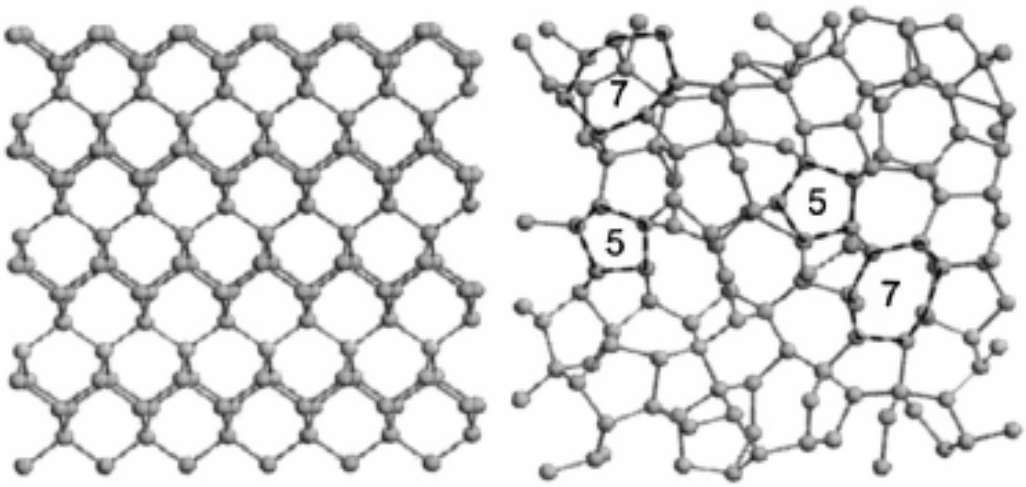

Figure 3.4 Structure of crystalline Si (left) showing the 6 ring structure and amorphous Si (right) where the 5 and 7 ring structure is visible. From (4)

3.2.2.2 Ion implantation amorphisation

Ion implantation of Si can produce amorphous Si layers or a damaged but essentially still crystalline structure depending on implantation conditions (4). For transistor device production there are distinct advantages for using implants that amorphise the Si therefore the focus of this thesis is on amorphising implants. The reasons for amorphising the Si will be discussed in some detail throughout this thesis but as a brief summary the main reasons are the production of higher quality defect free regrown layers compared to the regrowth of highly damaged layers. The junction depth can be spatially separated from the end of range, and channelling of the ions can be suppressed. The experiments carried out in this thesis on the whole use amorphised Si or are concerned with the formation of a continuous amorphous layer.

Amorphous Si layers can also be produced by deposition, e.g. chemical vapour deposition (CVD) or using low energy ion beams. However deposited amorphous Si layers are less well characterised and with less reproducible characteristics than ion implanted amorphous Si (17).

3.2.2.3 Collision Cascades, produced by single heavy and light ions

When an ion is implanted into Si it will probably undergo a hard collision with an atom near the surface. Energy will be transferred in the collision as described in chapter 2 (18). It is likely that the energy transferred will exceed the displacement

energy E_d causing the target atom to be displaced. Any energy transferred exceeding E_d becomes the resulting kinetic energy of this so-called primary recoil atom, which moves away from the ion track into the lattice. Primary recoil atoms with sufficient energy are able to displace further atoms, producing secondary recoil atoms, which in turn can create higher order recoils. This process continues, creating a collision cascade. The ion will continue travelling through the material, creating more primary recoil atoms along its path until all its energy is dissipated.

The energy deposition density is much higher for heavy ions compared to light ones. This difference results in the damage build up proceeding in a very different fashion for heavy and light ions, and is a critical factor for amorphous zone and layer formation. In this section the collision cascades of heavy ions are first described, followed by light ions, highlighting the differences. Different models for amorphisation, i.e. heterogeneous and homogeneous amorphisation, appropriate for heavy and light ions respectively, are described in the following sections, along with a brief summary of other relevant models and damage effects.

The amount of energy transferred in a collision is impact parameter dependent, with maximum transfer for a head on collision, and decreasing with increasing impact parameter. The average energy transfer is dependent on the scattering cross section (18). Heavy ions, with a larger scattering cross section are more likely to undergo collisions, and the average energy transfer is therefore higher for heavy ions (18). The mean free path for an energetic particle between collisions λ_d is given by

$$\lambda_d = 1/N\sigma \qquad (3.1)$$

where N is the atomic lattice density and σ is the scattering cross section, given in equation 2.6. Since σ is proportional to Z_1^2 it follows that the mean free path for a heavy ion is much shorter than for a light ion. It is in fact of the order of an interatomic spacing. A heavy ion therefore generates another displacement almost immediately after the first, causing the energy deposition density to be much higher for heavy ions than with light ones. Since primary recoils are created close together along the ion track, the individual cascades tend to overlap with their neighbours and the final result would be a giant collision cascade containing all the overlapping individual cascades. As the ion energy decreases along its path, its scattering cross section increases causing collisions closer together. The rate of energy deposition increases along the ion path, until towards the end of the ion path where the ion energy is low and correspondingly the total energy transferred to recoils is also low. The resulting collision cascade is therefore ellipsoidal in shape (18), as shown schematically in Figure 3.5 a). A heavy ion, such as As, hitting

a Si atom will suffer little angular deflection in a collision and will continue into the lattice making further collisions with Si atoms along its path. For heavy ions in the energy range of interest, the cascade from a single ion will produce a small amorphous zone.

Considering the behaviour of light ions, such as B, the mean energy transfer will be lower than with a heavy ion. The primary Si recoils produced from light ions will have on average less energy and consequently fewer secondary recoils will be produced. Secondary cascades will be small and may consist of only a few displaced atoms. For a light ion, the collision cross section σ is much lower. From equations 3.1 (and 2.6) it is obvious that the mean free path between collisions is much greater with a light ion than a heavy ion. This results in a much lower energy deposition density for light ions. As the small cascades will be created much further apart they will not overlap, so amorphous zones will not be produced (18). As a light ion travels a substantially greater distance between collisions a higher proportion of its energy will be lost inelastically, than with heavy ions. However this effect is less important at the low energies of interest where electronic stopping is low. A light ion has more likelihood of being deflected through large angles than heavy ions and so it will tend to take a zigzag pathway. The overall effect is that small pockets of damage are formed at locations along the path as shown schematically in Figure 3.5b). A single implanted light ion will not produce an amorphous zone.

In summary the distribution of displacements around an ion track depends strongly on the ion mass. Heavy ions have a much higher energy deposition density resulting in small amorphous zones. A light ion has a much lower energy deposition density resulting in damage which is sparse and created in pockets along a zigzag ion path. Important models of how these damage distributions produce a continuous amorphous layer are described in the following sections. The models are described with reference to the type of ion which is most appropriate.

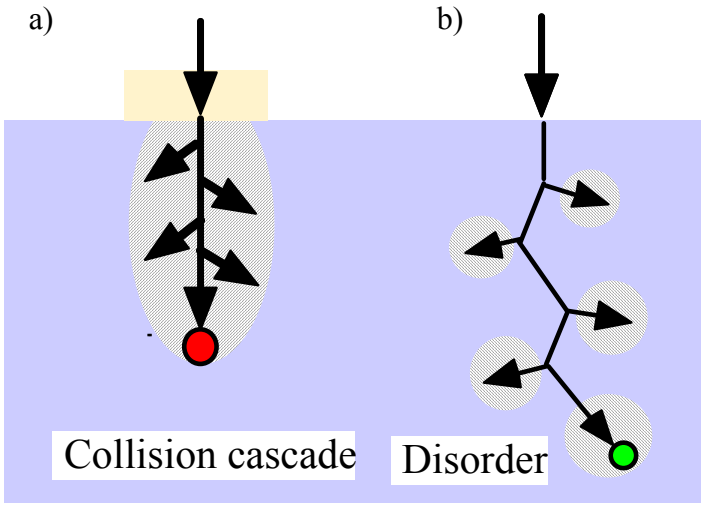

Figure 3.5 Illustration of location of damage formed by a) heavy and b) light ions

3.2.2.4 Heterogeneous amorphisation (overlap model)

The first model views the production of a continuous amorphous layer in ion implanted Si as being due to the overlapping of the locally amorphised zones, produced by heavy ion bombardment (19). This overlapping cascade model is called heterogeneous amorphisation because it assumes that locally amorphous zones are generated heterogeneously by the incident ions within the cascade. As ion fluence increases, these amorphous zones accumulate and overlap to produce a continuous amorphous layer (19). Observations of heavy ion implant are consistent with the heterogeneous formation of an amorphous phase along a single ion track (20). The amorphous fraction increases linearly with dose for the heavy ions, but for light ions a phase change occurs over a small variation of dose once a high dose has been implanted (4). As such this heterogeneous model is more commonly associated with the build-up of damage from heavy ions. The ion energy primarily determines the width of the layer (21), with the dose having a secondary effect. Once an amorphous layer is produced, further implantation can push the depth of the amorphous layer to greater depths.

To apply this model to light ions, the number of overlapping ion tracks necessary to form an amorphous zone would need to be considered. Light ions with small cascades would require many overlapping ion tracks to produce the amorphous zones that act as a precursor for the formation of an amorphous layer (4). In comparison heavy ion implants can result in the creation of amorphous zones with no overlap necessary (4).

3.2.2.5 Homogeneous model (Critical defects model)

The second model is based on ion irradiation causing a build up of defects within the lattice (22-25). Once a certain critical defect density has been reached the damaged crystal lattice collapses into an amorphous state. This is energetically favourable because the free energy of amorphous Si is lower than that of highly damaged crystalline Si. The number of defects increases with increasing fluence until a point where the free energy of the defective crystalline phase exceeds that of amorphous Si and a phase transformation into the amorphous state occurs.

This model for amorphisation is known as homogeneous amorphisation because the amorphous Si is thought to nucleate as a result of an interaction among sufficient number of defects produced within different collision cascades and distributed homogeneously throughout the irradiated region. Homogeneous amorphisation is more appropriate where irradiation produces low density cascades and simple defects, as is the case with light ions at room or higher temperatures (24). The onset of amorphisation would be expected to occur abruptly over a narrow range in dose, as has been found experimentally (4). The transformation occurs when the defect concentration exceeds about 1.15×10^{22} cm^{-3} (4). The effect of dynamic annealing is to reduce the defect density present compared to the number of defects produced and an increased implantation dose would be required to for amorphisation at, for example, room temperature compared to liquid nitrogen temperature where defects are frozen in (4).

3.2.2.6 Other models

A two stage nucleation limited model, is suggested because amorphisation occurs preferentially at pre existing amorphous defects (26) or a/c interfaces (27-30). This nucleation and growth (31) operates by the production of suitable amorphisation sites, via the accumulation of residual defects to reach a certain type or density, which then act as sinks for simple defects and produce the growth of the amorphous phase.

An energy spike is a term used to describe two similar types of collective effect, i.e. displacement and thermal spikes. The production of interstitial – vacancy pairs, i.e. the number of displaced atoms per cascade can be described using a modified version of the Kinchin – Pease relationship (7, 32) using more realistic potentials (33)

$$\nu(E) = \frac{kf(E)}{E_d} \qquad (3.2)$$

where υ(E) is the production yield, f(E) is the energy deposited in elastic collision process, E_d is the energy required to permanently displace an atom and k is a constant (=0.42). This relationship is valid in the linear cascade regime where collisions are considered to occur only between moving and stationary atoms. However discrepancies exist between the predictions of simple cascade theory and experimental results (34). The concept of energy spikes is introduced to explain the data. When the energy deposition into a region is large, all of the atoms within the collision cascade will be moving, with the deposited energy distributed amongst them. When the nuclear energy deposition per atomic plane exceeds the displacement energy a continuous array of displacements will occur, called a displacement spike. Alternatively if a sufficient number of moving atoms exist in the volume, Maxwell – Boltzmann statistics will apply and a temperature can be attributed to the region called a thermal spike. If the energy shared amongst atoms in a spike exceeds the latent heat of melting or sublimation of the material, large scale damage will result or the crystal may become amorphous (34, 13). The number of atoms receiving energy exceeding E_d will be fewer than those receiving the energy required to melt and therefore thermal and displacement spikes are distinguishable. A thermal spike can be viewed as a remnant after the propagation of a displacement spike since the energy remaining in the displacement spike ($<E_d$) will be distributed to the lattice as heat.

Defect based models for amorphisation attempted to identify specific defects that can that can act as amorphous embryos, i.e. the specific defect types that can cause the 5 and 7 membered rings characteristic of amorphous Si. A more comprehensive review of these defect specific models is given in (4).

3.2.3 Other implantation effects

3.2.3.1 Sputtering

Sputtering is a process in which atoms from the near surface region are ejected. It occurs when a moving atom reaches the surface in an outgoing direction with energy exceeding the surface binding energy. For Si a value of 2.3 eV for the surface binding energy can be used (35).

3.2.3.2 Atomic mixing

Atomic mixing is a process of rearrangement of atoms in the vicinity of the ion implantation due to collisions rearranging the location of the atoms. For example O atoms from the SiO_2 layer could be redistributed to greater depths during implantation.

Sputtering and atomic mixing play an important role in SIMS analysis, discussed in chapter 4, in the sense that the former is the basis of the technique and the latter places an undesirable limit on the resolution.

3.2.3.3 Range shortening

As the implanted ion concentration increases during an implantation, the stopping power of Si changes slightly from being the stopping in pure Si to the combination of stopping powers of the Si and dopant, as determined by Braggs rule (see section 4.2.1.2). An increased stopping power leads to a concept called range shortening whereby the range of an implant reduces slightly with increasing fluence. This is most applicable with a high concentration of implanted dopants.

3.3 Annealing

3.3.1 Introduction

Following ion implantation it is necessary to anneal the damaged wafers to restore the crystal lattice structure and electrically activate the implanted dopant ions. The dopant ions must be located on regular substitutional lattice sites. Traditionally furnace annealing was used for this with temperatures from approximately 600 °C upwards, with timescales of minutes or hours. Furnace annealing in the region of 600 °C would leave behind a large number of defects and require a second higher temperature anneal to remove them.

Rapid thermal annealing (RTA), using for example arc or halogen lamps, has more recently been employed. Far higher temperatures, e.g. >1000 °C and shorter anneal durations, e.g. seconds, are common. Spike annealing (SA) is a variant, applied to minimise diffusion, carried out using the same type of RTA equipment. SA has a "zero" dwell time at the maximum temperature and uses rapid ramp up and down rates, e.g. 200 $°Cs^{-1}$ and 70 $°Cs^{-1}$ respectively are typical.

All these types of annealing operate in the heat balance regime, which is where equilibrium between deposited and lost power is established and results in a steady state heat balance throughout the wafer. The timescales involved in this regime are $t>10^{-2}$ s (36).

Other types of annealing include flash annealing, where a short duration pulse ($10^{-6} < t < 10^{-2}$ s) from flash lamps will rapidly raise the temperature, creating a temperature gradient through the wafer. This is the thermal flux regime.

Pulsed lasers can produce rapid heating of the surface layers, with times of 10^{-11} to 10^{-6} s. This is known as the adiabatic regime, and affects only the near surface. It is possible with pulsed lasers to either regrow the surface region through liquid phase epitaxy or through solid phase epitaxy in the sub melt region (36).

In device production it is currently most common to use RTA or SA but as the need for shallower junctions becomes greater, different types of annealing methods, including laser annealing, are being increasingly considered (37).

The annealing of ion implanted amorphous Si produces a variety of effects, depending strongly on the initial state of the implanted region. Effects include epitaxial crystallisation, random nucleation and growth, dopant segregation and defect enhanced diffusion, which are described in this chapter. Regrown layers contain fewer defects when the starting point is amorphous Si compared to initially highly damaged layers.

3.3.2 Solid phase epitaxial regrowth (SPER)

Solid phase epitaxial regrowth (SPER) is a process whereby amorphised Si is recrystallised upon thermal annealing from temperatures above half that of the melting temperature of the crystal, i.e. for Si from approximately 500 °C, to approximately 1350 °C. The underlying Si crystal acts as a template for the amorphised Si to be arranged upon (epitaxy). This occurs while the Si is still a solid, hence the term solid phase epitaxial regrowth (14, 38, 39).

During SPER the amorphous Si rearranges itself on the underlying crystalline substrate starting from the amorphous / crystalline (a/c) interface and proceeds to the surface in a layer-by-layer fashion. Since crystalline Si has lower free energy there is always a driving force towards rearrangement to the crystal structure. During SPER, the implanted dopants take up substitutional lattice sites as the crystal-amorphous interface passes through their location. Time resolved reflectivity (TRR) (38) is the main technique that has been used for measuring SPER rates. It has been observed that impurities (dopants) affect the regrowth behaviour and the rate of SPER. Intrinsic (undoped) Si will be described first and then the addition of impurities is considered.

3.3.2.1 Intrinsic Si

It has been shown for intrinsic amorphous layers, produced by self ion implantation, that the regrowth velocity is temperature and orientation dependant. The orientation dependence is related to the density of atomic packing on the different planes. The regrowth rate on (100) Si is approximately 2.5 times greater than (110) Si

and is approximately 25 times faster than (111) Si (40). Regrown (111) substrates have been observed to contain high levels of defects compared to (100) and (110) orientated substrates. In this thesis all experiments were carried out on (100) Si. A model for recrystallisation shows that bonds can be broken and reformed to produce the crystalline phase. To be considered a part of the crystal each atom should have at least two undistorted bonds to already aligned atoms of the crystal. For the (100) surface, a single atom can simply attach to any other atom of the crystal but for (110) and (111) planes two and three adjacent atoms, respectively, must attach simultaneously, to atoms of the crystal, which is less probable, accounting for the differences in rate and defects observed (39).

The regrowth velocity is also temperature dependent and is shown to follow an Arrhenius type expression.

$$v = v_0 \exp\left(-\frac{E_A}{kT}\right) \ (nms^{-1}) \qquad (3.3)$$

where v is the growth velocity, k is the Boltzmann constant (8.617E-5 eV/K), T the temperature at which regrowth is occurring and E_A the activation energy. v_0 and E_A can both be obtained from a plot of regrowth rates against temperature. Values obtained for intrinsic (100) Si are E_A = 2.68 eV, and $v_0 = 3.07 \times 10^{15}$ nms^{-1} (39), although various studies have produced values for the activation energy from 2.3 to 2.9 eV (41). Doping changes the regrowth rate. For 2×10^{14} cm^{-2} As implanted Si, the values for E_A and v_0 are 2.76 eV and 3.68×10^{15} respectively (39). Figure 3.6 shows the trend in regrowth rate with temperature for ion implanted Si. Values for (110) and (111) have been inferred from the (100) values. Values for SPER rates of intrinsic and doped Si using equation 3.3 are given in Table 3.1 below.

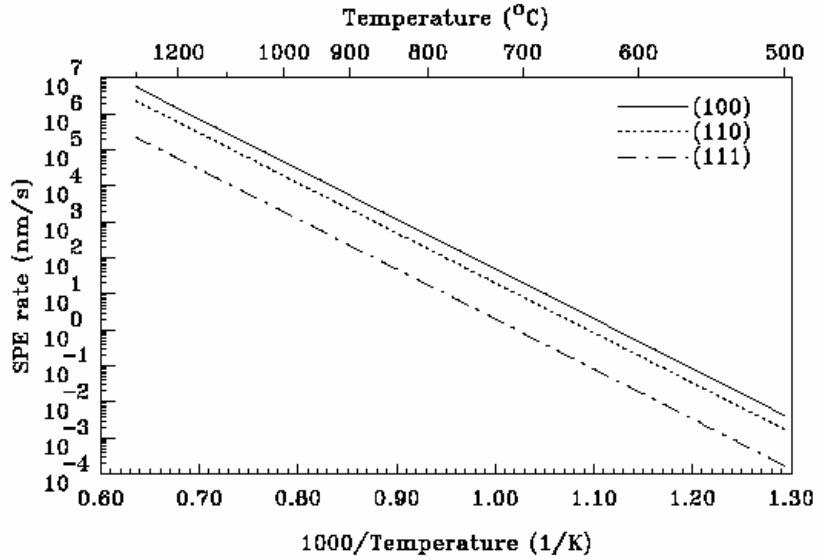

Figure 3.6 SPER rates for Si (100), (110) and (111). From (39).

	SPER rate (nms^{-1})	
Anneal temperature / °C	Intrinsic Si	As doped to 2×10^{21} cm^{-3}
550	0.12	0.047
600	1.04	0.43
650	7.18	3.1
700	40.5	18.7
800	797	402
900	9420	5120
1000	75600	43700

Table 3.1 Regrowth rates for intrinsic and 2×10^{14} cm^{-2} As doped Si, for various temperatures.

3.3.2.2 Dopant and other impurity Atoms

Implanted impurity atoms have been observed to alter the regrowth rate. The effects depend on species and concentration (42). Virtually all non doping impurities (e.g. O, N, F), at moderate to high concentration (0.1 to >1 atom %), have been seen to reduce the SPER rate (43).

For group III and group V dopants such as B and As ions at low concentrations, ~ 1×10^{19} cm^{-3}, an increase in the regrowth rate has been observed (42), with B exhibiting the largest rate enhancing effect. As dopant concentrations are increased, it has been observed that the regrowth rate reaches some maximum value and then slows down for increasing concentration (14) and this is described in more detail for specific

relevant dopants later. For equal concentration of n and p type dopants, the regrowth rate is reduced to that characteristic of intrinsic amorphous Si (38).

For increasing dopant concentrations, of the order 1×10^{20} cm^{-3}, processes such as impurity segregation and precipitation can occur, which alter the crystallisation kinetics. These processes are strongly influenced by the growth temperature and the rate at which dopant diffuse in the amorphous Si layer. Precipitation e.g. dopant clustering has been observed to retard the epitaxy. Segregation or "Push out" of the dopant occurs for slow diffusing species (As, Sb), which do not precipitate prior to epitaxy. Segregation occurs at the a/c interface and the effect is to "snowplough" excess dopant in front of the advancing a/c interface (14, 38). Segregation is not observed below a certain critical impurity concentration, which is species dependant and is always greater than the equilibrium solid solubility, i.e. the maximum concentration that can be accommodated through diffusion at a particular temperature. Note that the term solid solubility or just solubility is often used to refer to the concentration that can take up substitutional positions during SPER. At concentrations below the solid solubility all dopants present can take up substitutional positions. For higher concentrations above the solid solubility excess dopant segregates. At these concentrations the regrowth rate is observed to appreciably slow down. For much higher dopant concentrations polycrystalline growth has been observed, associated with random nucleation and growth (38), as described in section 3.3.3.

B has the highest solid solubility of the elements in group III (36, 44). For concentrations from 2×10^{19} cm^{-3} to 2×10^{20} cm^{-3} B enhances the SPER rate (42). The amount of enhancement increases with increasing dose within this concentration range. Above 2×10^{20} cm^{-3} a saturation in rate occurs. The saturation level can be increased with increasing annealing temperature. This effect is believed to be due to the limited solid solubility of B in Si, and the assumption that only dissolved B increases the SPER rate.

BF_2 is most commonly used to implant B. BF_2 contains both rate enhancing B and rate retarding F in the same layer. The effect of BF_2 is simply a combination of rate enhancement from B effects and retardation effects from F. F retardation is strongly temperature dependent therefore rate retardation due to F in BF_2 sample should be less pronounced as the temperature is increased. During annealing F has been observed to both segregate to the surface and diffuse to the EOR region (45-48).

When As is present in amorphous Si there is a temperature dependant interplay between processes such as SPER, random crystallisation, impurity diffusion, defect

complex formation, precipitation and segregation. At low annealing temperatures ~ 600 °C crystallisation is strongly dependent on ion fluence. There is not a simple rate enhancement, which tracks the As concentration profile as seen with B. The maximum concentration before retardation occurs is ~ 1.5×10^{21} cm^{-3} (49). The formation of dislocations maybe directly related to As clustering and precipitation. Solubility increases with temperature and therefore fewer defects occur with high temperatures. It is suggested that As vacancy clusters can form at the a/c interface and contribute to the rate retardation (38). Severe retardation of the SPER rate is observed at high concentrations.

During SPER dopants may become substitutional and electrically active in concentrations well exceeding the equilibrium solid solubility (39). Substitutional concentrations incorporated into an amorphous regrowth can exceed the equilibrium solid solubility by as much as 560 times (41). The high substitutional concentration of impurities observed after SPER can be attributed to trapping by the rapidly moving interface (39).

3.3.2.3 Models for SPER

A number of models adopting several differing approaches have been developed to describe the mechanisms of the SPER process. Atomistic models consider how the atoms on the amorphous Si side of the interface are rearranged onto the crystal template. Electric field models consider the electronic properties of the structure at the amorphous / crystalline interface and consider more closely the effects of the dopant on the SPER process. Finally kinematic models attempt to identify the rate limiting step of the SPER process and derive equations that can predict the SPER rate as a function of temperature and dopant concentration (17). The most important models are briefly mentioned here.

Starting with the atomistic approach models, the focus is to consider the behaviour at the a/c interface and the structure of the amorphous Si, which can be described by a continuous random network (CRN). Consideration is made as to how atoms from the amorphous side might reorder themselves onto the crystalline template. A model was first created for Si (111) (50). The a/c interface is viewed to be fully coordinated, i.e. there are no free bonds, so it would be in the lowest energy configuration. The difference in energy between amorphous and crystalline Si is due to bond angle distortion (50, 51). In the model, crystallisation is viewed as a simple bond rearrangement process which starts with the breaking of a single bond and continues as the defect propagates along a crystal ledge to minimise bond angle distortion and

nearest neighbour distance (52). By doing this, the five and seven membered ring structure can be restored to the crystalline state. This model was extended to Si (100) and the activation energy for SPER was identified with the sum of the energy to break a bond at the interface and the increase in distortion energy accompanying bond rearrangement (51). It was suggested that SPER proceeds through the propagation of [110] ledges on {111} planes and ledges (53). The energy to break every bond was not required for recrystallisation to occur. It was found to be possible to make major readjustments with the breaking of just one bond and propagating the loose ends through the structure. The shortcomings of this type of model are that they do not account for the differences observed in the SPER rate with implanted group III and V dopant and other impurities.

Electric field models based on electronic processes make a much better attempt to explain the SPER rate dependence on dopant concentration. Several different models exist and the crux of these arguments is to identify specific defects that give rise to the bond breaking process. An important model of this type extended the models using crystallisation along kink sites, to incorporate doping effects (14). It was proposed that SPER is mediated by the generation and motion of kink like steps along [110] ledges. Here SPER is viewed as a cooperative process in which the motion of a kink is accompanied by crystallisation of many atoms before the kink is annihilated. Addition of a doping impurity can either increase the concentration of charged kinks or reduce the kink migration energy and enhance the SPER rate. Kinks can be pinned by the formation of a strong bond between a Si atom and an impurity atom. This model is illustrated in Figure 3.7. This model describes intrinsic as well as doping enhancement. The growth site of this model can be visualised as some bond breaking defect.

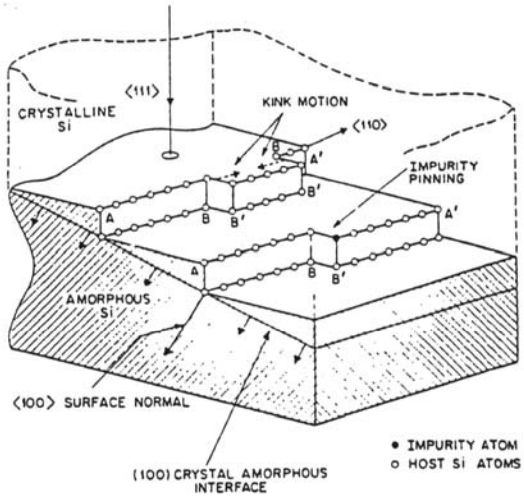

Figure 3.7 Schematic representation of SPER of Si(100) in terms of kink (BB') generation and motion along [110] ledges (AA'). From (14).

Further models are based on effects such as the Fermi level, vacancies or dangling bonds. The models differ in the assumptions on the defect responsible for SPER. Also it is not clear if defects have to migrate from the Si layer or from the amorphous layer to the interface, or whether it can be determined by local concentration at the interface. There is not sufficient experimental evidence to back up any one particular model (39).

3.3.3 Random Nucleation and growth (RNG)

When amorphous Si has no crystalline seed to act as a template for regrowth the behaviour upon annealing is to form random nucleates resulting in polycrystalline Si. Since as mentioned previously the free energy of the crystalline state is lower than that of the amorphous one, upon annealing there is a strong tendency to start to form the four-fold coordination and tetrahedral bond angles of the minimum free energy, which leads to the formation of small recrystallised nuclei from which crystallites grow from. The orientation of the nuclei will not be orientated with respect to other nuclei so a single crystal structure will not form. As the crystallites grow larger eventually all the amorphous material will be converted into crystalline grains. High impurity concentrations that inhibit SPER may also cause RNG (38).

3.3.4 Annealing ambient considerations

Annealing is usually carried out in either an N_2, or N_2 5% O_2 environment. The addition of some O_2 to the environment maintains or leads to growth of the surface oxide layer. This has the effect of trapping any segregated dopant under the oxide, hence all the implanted dopant is retained. The presence of O in Si may also lead to oxygen enhanced diffusion. Annealing in a pure N_2 environment can lead to dopant loss.

3.4 Defects after annealing and evolution during annealing

3.4.1 Classification of Defects

Defects arising during annealing in ion implanted Si are dependent on implantation and annealing conditions and have been classified in five different categories (36, 41). MEIS is not sensitive to the type of individual defects and as such specific defects have not been studied in great detail. The five categories will only be briefly summarised here, taken from the reviews in (36, 41) and important defects will be discussed later. Defect evolution during annealing has an important impact on diffusion of dopants discussed in section 3.5.

Category I defects are produced when the implantation does not produce an amorphous layer. Defects are formed at the depth of approximately the peak of the implant concentration. The defects formed are dependent on the concentration and anneal temperature. Point defects at these depths will be predominately interstitials that coalesce into defects such as {113} rod like defects and stacking faults. At temperatures above 700 °C these defects can dissolve and form dislocation loops.

Category II defects are formed in material when the surface layer is amorphised by the implant. They are formed beyond the depth of the original a/c interface, in the highly damaged but still crystalline material and are called end of range (EOR) defects. Category II defects evolve during annealing, into {113} defects and dislocation loops which are discussed in more detail in sections 3.4.2 and 3.5.

Category III defects are associated with imperfect regrowth of an amorphous layer and are located in the region of the previously amorphous Si. The main types are hairpin dislocations, microtwins and segregation defects. Hairpin dislocations nucleate when the regrowing a/c interface encounters small microcrystalline regions that are slightly misorientated with respect to the bulk crystalline material. As the microcrystalline pocket is incorporated into the single crystal bulk, a hairpin dislocation is nucleated which propagates to the surface forming a 'V' shaped defect. Using a heavier pre – amorphising implant species produces a sharper a/c interface which will contain fewer misorientated microcrystallites. Microtwins are mainly formed on (111) orientated Si. Segregation defects are associated with the rejection of an implanted species by the moving a/c interface. Because of low solubility of some species in the crystalline silicon the ion stays in the amorphous layer as long as possible. At some maximum concentration, the regrowing a/c interface breaks down and defect formation occurs. These defects include misorientated microcrystallites, microtwins, clusters, and small stacking faults.

Category IV defects arise from the regrowth of a buried amorphous layer where the two advancing a/c interfaces meet. The defects are microtwins and hairpins defects. Category II defects are formed at both of the original a/c interfaces.

Category V defects occur when the solubility of the implanted species at the annealing temperature is exceeded around the mean projected range of the implant where the maximum concentration occurs. Precipitates and dislocation loops can be formed during SPER.

The location of these defects within the damage region is illustrated in Figure 3.8.

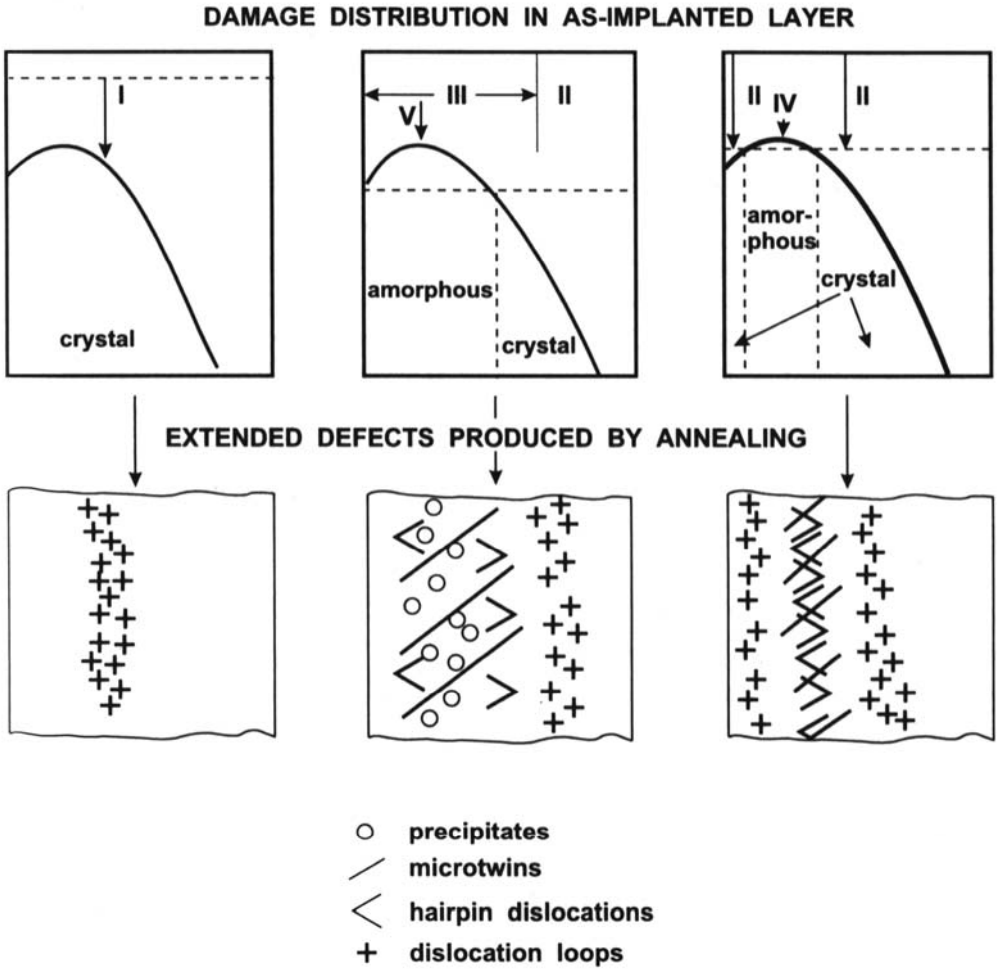

Figure 3.8 The relationship between the damage density distribution (solid lines) and amorphisation threshold (dashed line) leading to the different categories of defect. From (36).

3.4.2 End of Range defects and their evolution upon annealing

Defects formed in the EOR region beyond the original amorphous / crystalline interface (Category II defects), and specifically their evolution, can play an important role in the diffusion of dopant atoms. Five important types of EOR defects are described here, all of which arise because of an excess of interstitials. These defects evolve through a ripening process which is driven by the reduced formation energy of larger defects. Smaller clusters dissociate while the larger defects attract the released interstitials and remain stable up to high temperatures. The effect on diffusion is discussed in section 3.5.

Immediately following implantation and in the early stage of annealing, most of the excess interstitials are stored as di-interstitials (54). These can grow during moderate

thermal annealing (600 – 700 °C and form small aggregates of Si interstitials, with the most stable "magic" clusters being made up of 4 and 8 atoms (55). For longer anneal times and higher temperatures, the excess interstitials condense into extended defects (56). This category of defects consist of {113}'s, perfect dislocation loops (PDL's) and faulted dislocation loops (FDL's) and TEM images of each are shown in Figure 3.9.

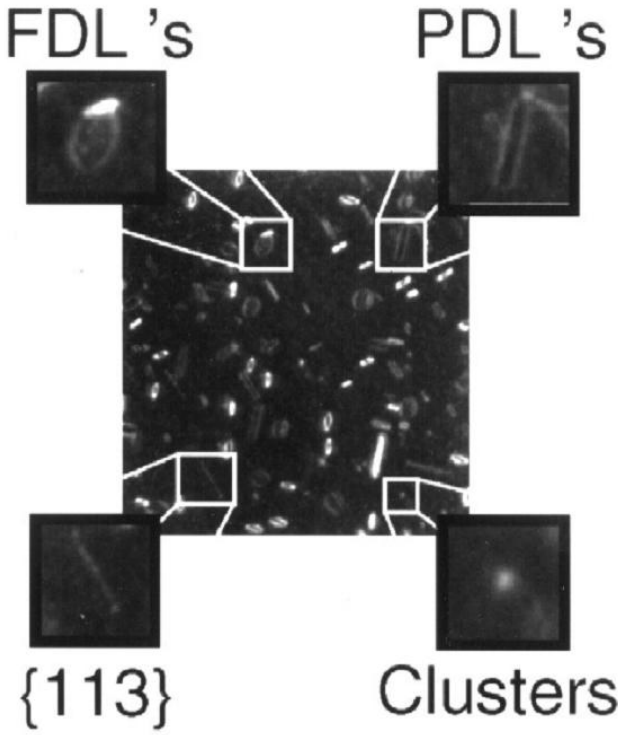

Figure 3.9 TEM images of defects present in the EOR damage area of ion implanted Si. These are clusters, {113}s, PDLs, and FDLs. From (56).

{113} rod like defects are formed from smaller clusters and can become visible in a TEM from lengths of 2 nm (57). The {113} defects are bundles of rows of Si di-interstitials that lie on {113} planes and which are elongated along <110> directions and consist of condensates of interstitials forming five and seven – membered rings (58). This atomic arrangement provides a way to insert planes of self interstitials without dangling bonds (58). They have a constant width of 4 nm. Once {113} defects are formed, further annealing can make the larger {113}'s grow in size at the expense of the smaller ones, thereby reducing the density of {113}'s.

Dislocation loops form in the most densely packed crystal planes for reason of energy minimisation. Typically the loops consist of circular extra {111} planes of Si interstitials with the lattice elongated along <110> directions. Perfect dislocation loops

contain no stacking fault, but faulted dislocation loops have a stacking fault in the {111} plane (59), as illustrated in Figure 3.10.

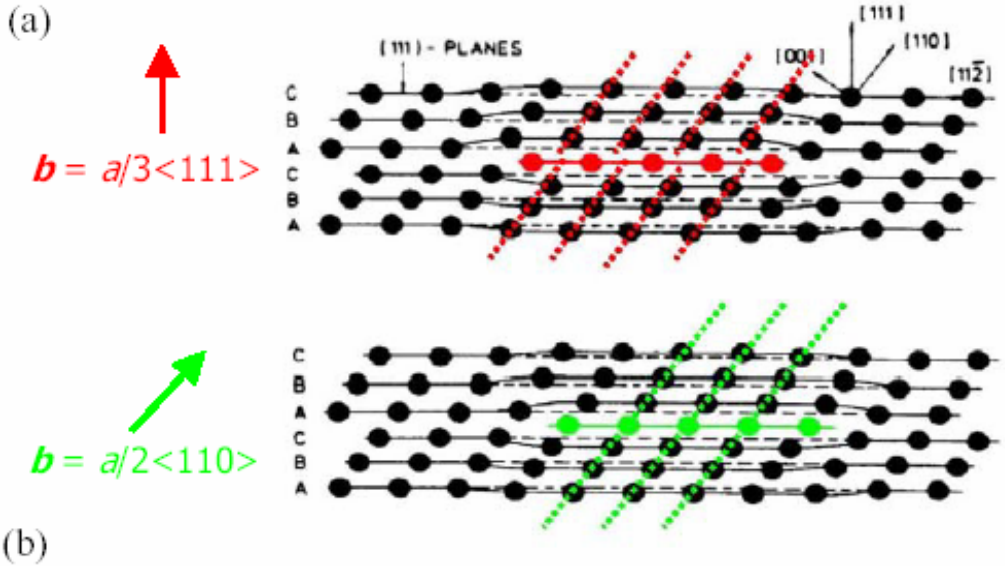

Figure 3.10 Structure of a) faulted dislocation loops and b) perfect dislocation loops. Faulted dislocation loops contain a {111} stacking fault. From (60).

Dislocation loops (perfect and faulted) act as nucleation sites for Si interstitials released from {113} defects during annealing at temperatures of 800 °C and above. This is termed a conservative Ostwald ripening process. The density of the dislocation loops will increase while the density of the {113} defects will decrease by a similar amount (73). For temperatures of 1000 °C and greater, perfect dislocation loops start to dissociate leaving large highly stable faulted dislocation loops that will be stable at 1050 °C. A PDL can act as a sink for a {113} defect and a source for FDL at the same time (57). The dependence of the formation of the different types of defects on the implantation dose is illustrated in Figure 3.11.

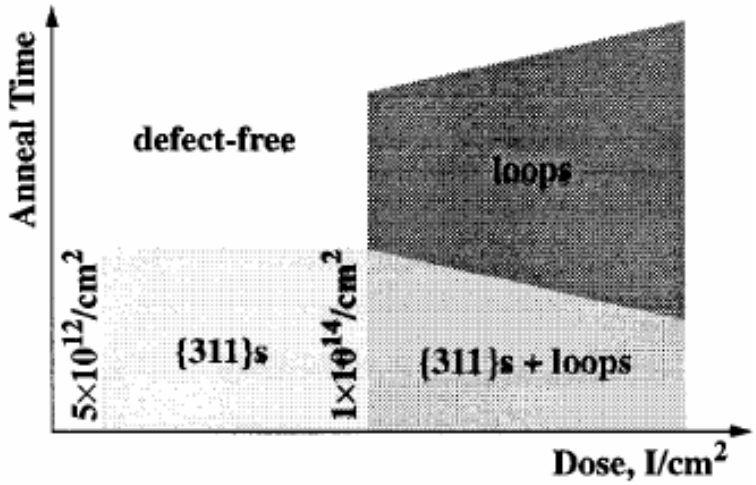

Figure 3.11 Relationship between implantation dose and annealing, on the type of defects formed. From (61).

The driving force for this Ostwald ripening process is the decrease in formation energy. Interstitials to di-interstitials have an energy of formation of 1.3 eV. The formation of clusters tends towards 0.8 eV. {113}'s have an energy of formation of 0.65 eV, and dislocation loops have an energy of formation of 0.027 eV (57).

3.4.3 Bubbles

Bubbles can be formed in Si. This section briefly mentions implantation conditions that can lead to bubble formation, relevant to these studies, i.e. with BF_2 and noble gas implants. At high BF_2 doses such as 1×10^{16} cm^{-2}, F bubble formation may occur upon annealing. During SPER these bubbles are swept ahead of the advancing interface. Bubble size increases for higher anneal temperatures (47, 48). At lower implant BF_2 doses that still result in amorphisation (5×10^{14} cm^{-2}), bubble formation was not seen (46). Previous implantation and annealing studies of noble gas ion implantation into Si and metals have shown that implanted ions tend to agglomerate in clusters or form bubbles depending on the implant dose (62-65). For doses above 6×10^{15} cm^{-2}, Ar bubbles are formed during implantation and grow upon annealing. For lower doses bubble formation occurs during annealing (63). For Kr bubble formation does not occur during implantation but during SPER at temperatures from 550 °C upwards (64). Xe, similarly, has been shown to form bubbles in Si during annealing (65).

3.5 Dopant movement and Diffusion

3.5.1 Introduction

To produce layers with sufficiently high levels of dopant activation and to remove the most stable defects requires annealing temperatures in excess of 1000 °C. At high temperatures dopant diffusion occurs which can have a dramatic effect on the depth of the junction. Diffusion of dopants has been considered a potential "showstopper" in the production of future devices with the need for shallower junctions. It has been observed that atoms migrate in interactions with defects. The dissolution of extended defects introduces an influx of interstitials that can be responsible for a dramatic enhancement, of many orders of magnitude, of the diffusion compared with standard Fickian diffusion. As this enhancement is relatively short lived and decreases with time it is known as transient enhanced diffusion (TED). A more detailed review of diffusion is given in (9, 66).

3.5.2 Models of diffusion

Before describing diffusion models some notation must first be defined. When the dopant atom occupies a substitutional site, surrounded only by Si atoms it is referred to as A_s. When a vacancy V, resides next to a substitutional dopant atom it is known as a dopant vacancy pair and designated AV. If one of the atoms in an interstitialcy defect is a dopant atom then it will be called a dopant interstitialcy pair, AI. If the dopant atom occupies an interstitial position, it will be referred to as an interstitial dopant and written as A_i (9, 67). The diffusion of mainly interstitially dissolved small atoms (A_i) like hydrogen or the 3d transition elements proceeds via interstitial lattice sites, as shown in Figure 3.12 a). Direct diffusion of atoms on substitutional sites (A_s) may occur by direct exchange or a ring mechanism, Figure 3.12 b) but this is rare and no experimental evidence has been found (9, 67). Diffusion by indirect mechanisms involving point defects is usually more favourable and can be expressed by the following point defect reactions.

$$A_s + V \leftrightarrow AV \quad (3.4)$$

$$A_s + I \leftrightarrow AI \quad (3.5)$$

$$A_s + I \leftrightarrow A_i \quad (3.6)$$

$$A_s \leftrightarrow A_i + V \quad (3.7)$$

The first equation describes a vacancy mechanism for dopant diffusion and the second equation describes an interstitialcy mechanism for dopant diffusion. Isolated intrinsic defects approach substitutional impurities and form next – nearest AV and AI

defect pairs due to Coulomb attraction and/or minimisation of local strain. For long range migration of A_s the AV pair partially dissociates and the vacancy diffuses to at least a third nearest – neighbour site in the lattice before returning along a different path. The dopant diffusion via the interstitialcy mechanism only occurs if the AI pair does not dissociate. The third reaction is the "kick – out" mechanism, and the fourth reaction is the dissociative or Frank – Turnbull mechanism. They describe the behaviour of elements that are mainly dissolved on substitutional sites but move as interstitial defects (9, 67). These mechanisms are shown in Figure 3.13 below.

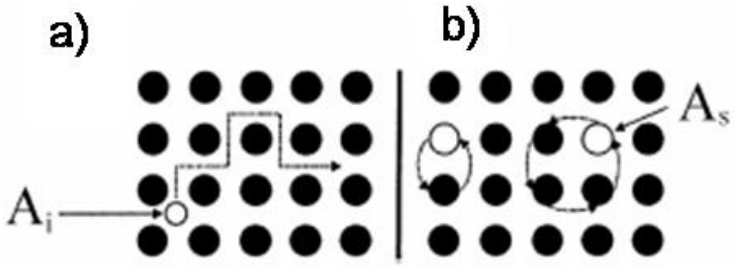

Figure 3.12 Schematic two-dimensional representations of direct diffusion mechanisms of an element A in a solid, via a) interstitial lattice sites and b) substitutional lattice sites. From (67).

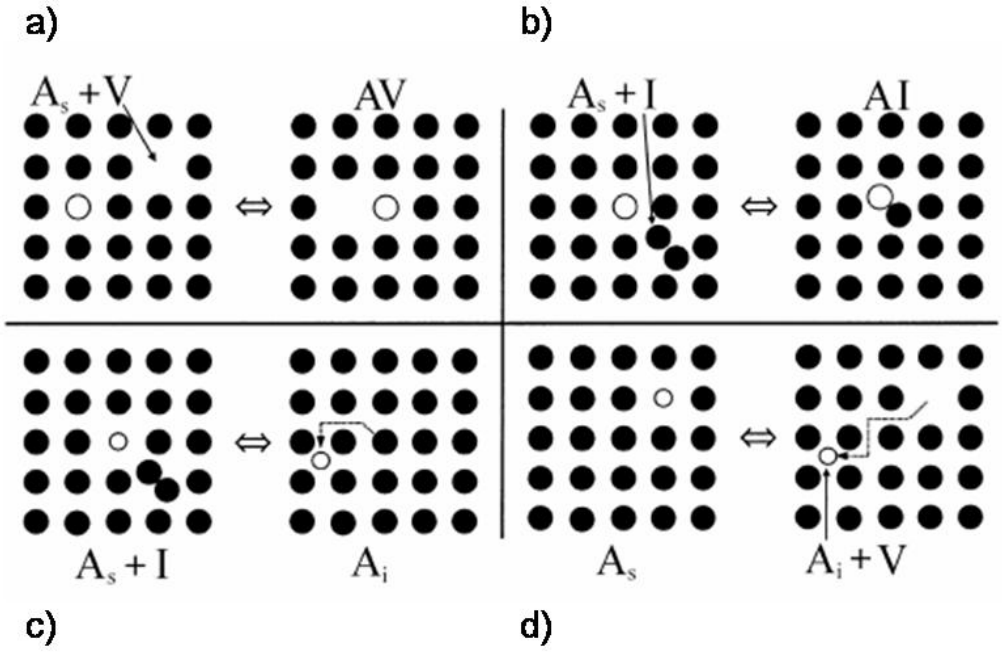

Figure 3.13 Schematic two-dimensional representation of indirect diffusion mechanisms of an element A in a solid. Ai, As, V, and I denote interstitially and substitutionally dissolved foreign atoms, vacancies, and silicon self-interstitials, respectively. AV and AI are defect pairs of the corresponding defects. From (67).

3.5.2.1 Standard Fickian diffusion

When atomic concentration gradients exist, atoms are able to move by taking the form of point defects, to a region where they can reside at an equilibrium level. Interstitial or vacancy mediated diffusion can occur in crystalline material. For low impurity concentrations, i.e. when the dopant concentration is less than the intrinsic carrier concentration, the diffusion is best described by Fickian diffusion. The rate of transfer of solute atoms per unit area (at/cc) is proportional to the concentration gradient of the solute.

$$J_x = -D\frac{\partial C(x,t)}{\partial x} \tag{3.8}$$

where J_x is the diffusion flux in one dimension, C is the solute concentration and D is a diffusion coefficient which is equal to

$$D = D_0 \exp^{-E_{act}/kT} \tag{3.9}$$

where D_0 is a frequency factor, that is dependent upon the atomic jump frequency and distance and in As implanted Si is given by 22.9 cm^2/s (68), E_{act} is the activation energy for diffusion (for interstitial diffusion E_{act} = 0.6 – 1 eV, and vacancy diffusion E_{act} = 3 – 4 eV), and k is the Boltzmann constant.

From the law of conservation of matter, the change in the solute concentration equals the decrease in the diffusion flux.

$$\frac{\partial C}{\partial t} = -\frac{\partial J_x}{\partial x} \tag{3.10}$$

combining 3.8 and 3.10 leads to

$$\frac{\partial C}{\partial t} = D\left[\frac{\partial^2 C}{\partial x^2}\right] \tag{3.11}$$

Equation 3.8 is known as Ficks first law and 3.11 is known as Ficks second law of diffusion. For low concentration of dopants, i.e. near the intrinsic levels of doping, and using appropriate boundary conditions there can be a good match with experimental results (69).

For implantations the concentration is usually too high for Fickian diffusion. At high concentrations the diffusion profiles show a dependence upon the defect concentration. For high concentration diffusion the impurities migrate as impurity point defect complexes. At the temperatures where diffusion occurs, most implanted dopants will be expected to have taken up substitutional sites. The diffusivity of dopant atoms in Si is governed by the local concentration of point defects according to

$$D = D_I\left(\frac{\langle C_I\rangle}{C_I^*}\right) + D_V\left(\frac{\langle C_V\rangle}{C_V^*}\right) \qquad (3.12)$$

where D_I and D_V are the intrinsic diffusivities due to interactions with self interstitials (I) and vacancies (V) and $<C_x> / C_x^*$ and the local / equilibrium concentration of point defects (70). B is known to diffuse by interstitial mechanisms, Sb by vacancy mechanisms and As is thought to diffuse by both interstitial and vacancy mechanisms (71).

3.5.2.2 Transient enhanced diffusion

Anomalous diffusion of dopants has been observed where the diffusivity can be increased by several orders of magnitude from that calculated for normal diffusion. This enhancement was first attributed to the release of Si interstitials during the dissolution of {113} defects during annealing at temperatures from 670 °C to 815 °C (58, 61). However it has since been shown that it is not just the {113} defects that cause TED (59). TED occurred in samples where the implant dose was too low to form {113} defects. In this instance the activation energy for TED was in close agreement with the dissolution of very small clusters of interstitials or the activation energy of migration of free self Si interstitials. Additional experiments had also shown that the maximum diffusivity occurred in timescales before the dissolution of {113} defects starts. Therefore the dissolution of several defect types causes an injection of interstitials responsible for TED.

A model to describe TED in PAI Si assumes a surface interstitial concentration which increases with depth to the EOR region where there is a constant concentration of interstitials which decreases with time (72). Essentially all of the emitted interstitials arrive by diffusion at the Si surface where they are trapped. The flux to the surface is inversely related to the depth of the EOR band, so can be beneficial to separate EOR from dopant implant. TED causes the segregated As buried underneath the oxide to diffuse to greater depths.

References

1 S.M. Sze, Physics of Semiconductor devices, Second edition, John Wiley and Sons, New York, 1981.

2 C. Kittel, Introduction to solid state physics, Seventh Edition, John Wiley and Sons, New York, 1996.

3 P.Pichler, Intrinsic point defects, impurities, and their diffusion in silicon, Springer – Verlag/Wien, 2004.
4 L. Pelaz, L.A. Marqués, J. Barbolla. Appl. Phys. Rev. **96** Dec. 2004, p5947.
5 Introductory Semiconductor Device Physics. G. Parker, Prentice Hall, 1994.
6 E.P.Gusev, H.C. Lu, T. Gustafsson, E. Garfunkel, Phys. Rev. B 52 (1995) 1759.
7 G. H. Kinchin and R.S.Pease, Rep. Prog. Phys.18 (1955) 1.
8 J. Linnros, R.G. Elliman, W.L. Brown. Journal of Materials Research 3(6):1208 (1988).
9 P.M. Fahey, P.B. Griffin, J.D. Plummer, Rev Mod Phys vol 61 No 2 April 1989 p289.
10 P. M. Rousseau, P. B. Griffin, W. T. Fang and J D Plummer, J. Appl. Phys. 84, 1998. pp. 3593-3601.
11 M.D. Giles. J. Electrochem. Soc. 138 (1991) 1160.
12 G.D. Watkins. Mat. Sci in Semiconductor Processing. 3 (2000) 227.
13 J.F. Gibbons Ion implantation in Semiconductors – Part II: Damage Production and Annealing. Proceedings of the IEEE, 60(9):1062, 1972.
14 J Williams Solid Phase Recrystallisation Processes in Silicon, Chapter 5 of Surface Modification and alloying by laser ion and electron Beams. Eds, J.M. Poate, G. Foti and O.C. Jacobson. Plenum (1983).
15 F. Priolo and E. Rimini, Mat. Sci. Rep. 5 (1990) 319.
16 R. G. Elliman, J. S. Williams, W. L.Brown, A. Leiberich, D. H. Maher, and R. V. Knoell, Nucl Instr. Meth. B19/20 (1987) 435.
17 B.C. Johnson, Studies on ion beam induced damage accumulation and crystal recovery by solid phase epitaxy in silicon. PhD thesis, The University of Melbourne, 2003.
18 G. Carter, W.A. Grant, Ion Implantation of Semiconductors, Arnold, 1976.
19 F. F. Morehead and B. L. Crowder, Radiat. Eff. **6**, 27 (1970).
20 J. R. Dennis and E. B. Hale, J. Appl. Phys. **49**, 1119 (1978).
21 J. R. Dennis and E. B. Hale, Appl. Phys. Lett. **29**, 523 (1976).
22 F. L. Vook, in Radiation Damage and Defects in Semiconductors, Inst. Phys. Conf. Ser. No. 16, edited by J. E. Whitehouse (Institute of Physics, London, 1973).
23 M. L. Swanson, J. R. Parsons, and C. W. Hoelke, Radiat. Eff. **9**, 249, (1971).
24 L. T. Chadderton and F. H. Eisen, Radiat. Eff. **7**, 129 (1971).
25 F. L.Vook and H. J. Stein, Radiat. Eff. 2(1969) 23.
26 A. Battaglia, F. Priolo, and E. Rimini, Appl. Phys. Lett. **56**, 2622 (1990).

27 R.D. Goldberg, J. S. Williams, and R. G. Elliman, Nucl Instrum Meth. B106 (1995) 242.

28 J. Linnross, R. G. Elliman and W. Brown, J. Mater. Res. 3 (1988) 1208.

29 R. D. Goldberg, R. G. Elliman, and J. S. Williams, Nucl. Instrum. Meth. B **80/81**, 596 (1993).

30 R.D. Goldberg, J. S. Williams, and R. G. Elliman, Mat. Res. Soc. Symp. Proc. 316 (1994) 259.

31 M. Avrami, J. Chem. Phys. **9**, 177 (1941).

32 G. H. Kinchin and R.S.Pease. J. Nucl. Energy 1 (1955) 200.

33 P. Sigmund, Appl. Phys. Letts. 14 (1969) 114.

34 J.M. Poate, J.W. Williams. Amorphisation and Crystallisation of Semiconductors. in J.W. Williams and J.M. Poate, editors, Ion implantation and Beam Processing, chapter 2, Academic Press, 1984.

35 Ziegler, J. F. SRIM – The Stopping and Range of Ions in Matter. <http://www.srim.org/> (Accessed 07/04)

36 V. E. Borisenko, P. Hesketh. Rapid Thermal Processing of Semiconductors. Plenum Press, 1997.

37 http://public.itrs.net/ (accessed 02/06).

38 G.L. Olsen, J.A. Roth, Kinetics of Solid Phase Crystallisation in Amorphous Silicon. Materials Science Reports 3 (1978) p1-78.

39 P. Pichler, Solid Phase Epitaxy, 2002. (Unpublished).

40 L. Csepregi, J. W. Mayer, T. W. Sigmon, Phys. Lett., Vol. 54A, No. 2, 157-158, (1975).

41 K.S. Jones, S. Prussin, E.R. Weber. A Systematic Analysis of Defects in Ion – Implanted Silicon. Appl. Phys. A 45, 1 – 34 (1988).

42 L. Csepregi, E.F. Kennedy, T.J. Gallagher, J. W. Mayer, T. W. Sigmon. J. Appl. Phys. 48 (1977) 4234.

43 E.F. Kennedy, L. Csepregi, J. W. Mayer, T. W. Sigmon. J. Appl. Phys. 48 (1977) 4241.

44 F.A.Trumbore, Solid solubilities of impurity elements in germanium and silicon, Bell Syst. Tech. J. **39** (1960) 205 – 233.

45 M. Werner, J. A. van den Berg, D. G. Armour, G. Carter, T. Feudel and M. Herden, M. Bersani and D. Giubertoni, P. Bailey and T. C. Q. Noakes. Mat. Sci. Eng. B, 114–115 (2004) 198–202.

46 M. Tamura, Y. Hiroyama and A. Nishida. Mat. Chem. and Phys. **54,** 23 (1998).

47 C. W. Nieh and L. J. Chen, Appl. Phys. Lett. **48,** 1528 (1986).

48 C. H. Chu and L. J. Chen, Nucl. Instr. Methods Phys. Res. **59/60,** 391 (1991).

49 J.S. Williams, R.G. Elliman, Nucl. Instr. Methods 182/183 (1981) 389.

50 F. Spaepen, Acta Metall. 26 (1978) 1167.

51 T. Saito, I. Ohdomari. Phil. Mag. B 43 (1981) 673.

52 F. Spaepen, D. Turnbull, in: Laser Annealing of Semiconductors, eds. J.M. Poate, and J.W. Mayer, Academic Press, New semiconductors, eds. J.M. Poate, and J.W. Mayer, Academic Press, New York, (1982), pp 15 – 42.

53 L. Csepregi, E.F. Kennedy, J. W. Mayer, T. W. Sigmon. J. Appl. Phys. 49 (1978) 3906.

54 J.W. Corbett, J.P.Karins, T.Y. Tan, Nucl. Inst. Meth. 182/183, 1981, p457

55 N. E. B. Cowern, G. Mannino, P.A. Stolk, F. Roozeboom, H. G. A. Huizing, J. G. M. van Berkum, F. Cristiano, A. Claverie, M. Jaraíz, Phys. Rev. Lett., **82**, 4460 (1999).

56 N. Cowern, B Colombeau, A. Claverie, C. Bonofas, B. de Maudit, F. Cristiano, E. Scheid. Presentation at Applied Materials University collaborations Workshop. October 2002.

57 F. Cristiano, N. Cherkashin, X. Hebras, P.Calvo, Y. Lamrani, E. Scheid, B. de Mauduit, B. Colombea, W. Lerch, S. Paul, A. Claverie, Nucl. Inst. Meth. B 216 (2004) 46.

58 D.J. Eaglesham, P.A. Stolk, H.-J. Gossmann, J.M. Poate, Appl. Phys. Lett. 65 (1994) 2305.

59 A.Claverie, L.F. Giles, M. Omri, B. de Mauduit, G. Ben Assayag, D. Mathiot Nucl. Inst. Meth. B 147 (1999) 1.

60 L. Capello, PhD thesis. Structural investigation of silicon after ion-implantation using combined x-ray scattering methods. University of Lyon (France) and Torino (Italy), 2005.

61 P.A. Stolk, H.-J. Gossmann, D.J. Eaglesham, D.C. Jacobson, C.S. Rafferty, G.H. Gilmer, M. Jaraiz, J.M. Poate, J. Appl. Phys. 81 (1997) 6031.

62 G. Faraci, A.R. Pennisi, A. Terrasi and S. Mobilio, Phys. Rev B **38,** 13 468 (1988)

63 P. Resesz, M. Wittmer, J. Roth and J. W. Mayer, J. Appl. Phys. **49,** 5199 (1978).

64 M. Wittmer, J. Roth, P. Resesz, and J. W. Mayer, J. Appl. Phys. **49,** 5207 (1978).

65 A. G. Cullis, T. E. Seidel and R. L. Meek, J. Appl. Phys. **49,** 5188 (1978).

66 S.M. Hu. Mat. Sci. Eng. R13 (1994) 105 – 192.

67 H. Bracht. Diffusion Mechanism and Intrinsic Point-defect properties in Si. MRS bulletin June 2000.

68 R.B. Fair. Concentration profiles of diffused dopants in Si. Chapter 7 in Impurity Doping processes in Si, North-Holland, New York, 1981.

69 S. Whelan. PhD thesis, University of Salford, 2001

70 W. Lerch. M.Glück, N.A. Stolwijk, H. Walk, M. Schäfer, S.D. Marcus, D.F. Downey, J.W. Chow, H. Marquardt, Proc. Mat. Res. Soc. Vol 525 (1998).

71 H.-J. Gossmann, T.E. Hayes, P.A. Stolk, D.C. Jacobson, G.H. Gilmer, J.M. Poate, H.S. Luftman, T.K. Mogi, M.O. Thompson, Appl. Phys. Lett. 71 (1997) 3862.

72 N.E.B. Cowern, D. Alquier, M. Omri, A. Claverie, A. Nejim, Nucl. Inst. Meth. B 148 (1999) 257.

73 C. Bonafos, D. Mathiot, A. Claverie, J. Appl. Phys. 83 (1998) 3008.

Chapter 4 Experimental Techniques and sample preparation

4.1 Introduction

Throughout this study several techniques have been used to characterise the samples. The principal technique applied was medium energy ion scattering (MEIS) (1, 2), which was carried out at CCLRC Daresbury laboratory (UK) (3).

MEIS is a refinement of Rutherford Backscattering Spectrometry (RBS), which has been in common use since the 1960s for studying a variety of applications such as ion implantation of semiconductors, surfaces and thin films (4, 5). The underlying principle behind RBS and MEIS is essentially the same, with modification to the detailed experimental conditions and some differences with the equipment. MEIS is capable of producing quantitative depth profiles of implanted heavy ions and capable of simultaneously detecting displaced Si atoms, surface oxide atoms and any surface contaminant. This enables the experiments to provide information on the crystal lattice damage caused by the implantation, the regrowth of the damaged Si crystal and movement of dopant following annealing. Occasional RBS experiments were carried out at Salford University to confirm findings from MEIS.

Secondary ion mass spectrometry (SIMS) (2, 5, 6) was used to compliment the MEIS analysis. SIMS was carried out at ITC-IRST, Trento, Italy and at IMEC in Leuven, Belgium. The combination of MEIS and SIMS allows, for instance, information regarding substitutional dopants to be obtained. SIMS is also useful for profiling light elements such as B, for which ion scattering techniques have a very much reduced sensitivity.

Other techniques have been used to characterise a small number of samples. Various X-ray studies have been performed at beamline ID01 at the European Synchrotron Radiation Facility (ESRF), France (10). Some of the findings of these experiments are reported in this thesis and elsewhere (9, 41), where the comparison with MEIS has been instrumental in their interpretation. Combined information has provided further information on the segregation of As and details of the regrowth of Si. The techniques are not explained in any detail in this thesis and further information on these experiments and techniques can be found elsewhere (9, 10, 46, 47). Cross sectional transmission electron microscopy (XTEM) (49) was performed at The University of Salford to investigate damage following annealing, and the result is in Chapter 6. Energy filtered transmission electron microscopy (EFTEM) carried out at CNR, Catania, Italy, has been used to image specific elements and the results are used in Chapter 7.

Hall effect measurements were carried out at the University of Surrey using the van der Pauw technique (7, 8, 45).

The implants used for the study reported in Chapter 5 of this thesis, were performed either at the University of Salford using the Salford ultra low energy (ULE) implanter (11), or at Applied Materials, Horsham (UK) using an Applied Materials Quantum implanter (12). The samples reported on in section 6.2.2 were also implanted at the University of Salford. All other implants were performed at AMD, Dresden (Germany), using Applied Materials Quantum implanters (12). Annealing was carried out at Salford using a Steag AST10 rapid thermal processor, or at AMD using an Applied Materials RTP Radiance system.

In this chapter the MEIS technique is described in most detail, since it is the main technique used, in section 4.2. SIMS is briefly described in section 4.3. Information regarding all other analysis techniques is given in section 4.4. Sample preparation, including information on implantation and annealing equipment, is described in section 4.5.

4.2 MEIS

4.2.1 MEIS Introduction and basic principles

The predominant use of MEIS is “perhaps” for surface crystallography studies and a review of the application of MEIS to these types of studies is given in (1). Typical studies include determination of the surface structure of reconstructed surfaces and alloy phases, and layer-by-layer compositional analysis (13, 14, 15). On the other hand MEIS can also be used very effectively for depth profiling (16, 17, 18, 19), as is the case in these studies. The application of MEIS relating to depth profiling is described in this section.

In MEIS samples are bombarded with a monoenergetic, collimated H^+ or He^+ beam with an energy in the range from 50 to 400 keV. The incident ions are scattered elastically by single collisions with atoms in the sample and this results in a spread of energies and scattering angles depending on the details of each collision. The energy of a scattered particle leaving the sample depends on the elastic and inelastic energy loss processes that have taken place within the sample. Elastic energy loss is due to the collision between the nuclei, which depends on the mass ratio of the incident ion to target atom and the scattering angle. This is described in section 2.2 and the implications for MEIS are given in section 4.2.1.1.

Inelastic energy loss is due to ionisation and excitation processes in interactions with the electrons in the target, the rate of which varies as a function of ion energy as described in sections 2.3 and 4.2.1.2. The amount of energy lost inelastically by an ion will depend upon the path length travelled through the sample. The scattering yield vs. ion energy and scattering angle is measured using a toroidial electrostatic energy analyser and a two-dimensional position sensitive detector. Consideration of the ion yield vs. ion energy spectrum, for a known scattering angle, allows quantitative compositional and damage depth profiles to be extracted.

4.2.1.1 Mass sensitivity – elastic collisions

In a hard collision between an ion and a target atom, the ion is scattered and loses energy elastically as described in section 2.2. The ion energy after the collision is related to the energy before ($E_1=KE_0$) by the kinematic factor, K, given in equation 2.10. i.e.:

$$K = \left[\frac{\left(M_2^2 - M_1^2 \sin^2\theta\right)^{\frac{1}{2}} + M_1 \cos\theta}{M_2 + M_1} \right]^2 \qquad (2.10)$$

where M_1 is the mass of the incident ion, M_2 is the mass of the target atom and θ is the scattering angle. The scattering angle is dependant on the impact parameter. Note that in some texts (2) K is given as the term in []'s and hence the kinematic factor is then quoted as K^2.

In a MEIS experiment, the mass of the ion M_1 is known from the choice of ion species. For a fixed scattering angle, which is a given experimental parameter, the energy for scattering from the surface of the sample, can be calculated from the kinematic factor and the beam energy. This gives MEIS the potential to distinguish between scattering off different elements. Some care needs to be taken in the interpretation, as isotopes of different elements can have the same mass, within the resolving power of the system, however in practice the elements contained within a sample are often known.

4.2.1.2 Depth sensitivity and inelastic energy loss

The inelastic energy loss of a moving ion due to interaction with target electrons, as described in section 2.3, provides the basis for depth analysis. An ion scattered from some unknown depth within the sample will have lost energy inelastically on its way in and on its way out of the sample and therefore will have less

energy than one scattered from an atom of the same element at the surface, for the same scattering angle. Comparison of the additional energy lost and knowledge of the rate of inelastic energy loss allows the depth at which scattering occurred to be determined.

The rate of inelastic energy loss (dE/dx), is most conveniently expressed in units of eV/Å, and is dependent on the ion, the target material and the ion energy. The accuracy of the depth scale calibration is obviously limited by the accuracy of the stopping powers used. Work has been done by Andersen and Ziegler to average the best available experimental and theoretical stopping power values and these stopping power values can be obtained from the SRIM 2003 program (20). The appropriateness of the values used is discussed in section 4.2.3.1 later. Values of the inelastic energy loss for H and He ions in Si are shown in Figure 4.1 for the energy range 0 to 400 keV.

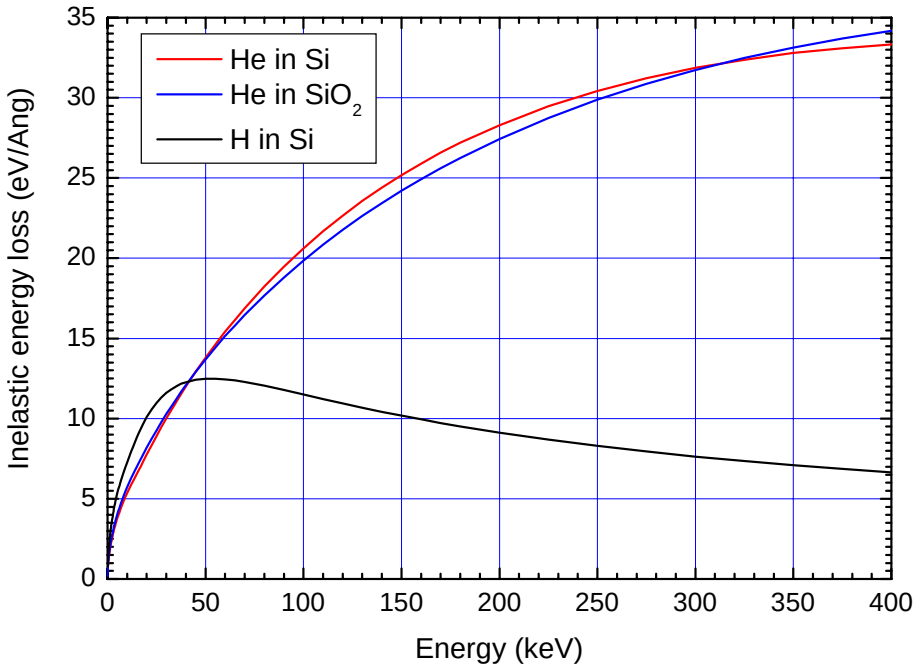

Figure 4.1 Inelastic energy loss rates as a function of energy for H in Si and He in Si and SiO_2.

Deviations in the stopping powers from pure Si targets may arise when a sufficient amount of another element is present. In these studies however, the samples do not have a high enough concentration of any element other than Si to significantly alter the energy loss rates and hence the depth scales. For the case of an extremely high concentration of another element present the stopping of a compound may be estimated by the linear combination of the stopping powers of individual elements, known as

Bragg's rule (21). Although this rule is reasonably accurate, measured values of stopping of ions in compounds can deviate from this, usually by less than 20%. Bragg's rule ignores changes in orbital and excitation structure between elements and compounds. Any bonding changes may alter the charge density, thus changing the strength of the interaction of the ion with the target medium (20). Data outputs from SRIM are available for many compounds based on measurements and theory.

In every sample studied in this thesis there was an oxide layer on the surface of the sample. The stopping power of He in SiO_2, as obtained from SRIM, is also shown in Figure 4.1. The stopping power is approximately 1 eV/Å lower than that in Si for the beam energies used. Oxide layer widths are usually 1.5 – 2 nm which equates to a 0.1-0.2 nm depth deviation in the depths scale from using the values of pure Si.

A small deviation arises of the stopping powers in an open channel compared to that in a random direction (22, 23, 24, 25). The level of deviation depends on the orientation and energy, e.g. for the <110> direction the channels are more open than the <111> channel and hence the stopping powers are ~ 20% lower (22). For He in Si in the <111> direction the stopping powers have been found to be ~ 93% of that of the random direction (22). For the experiments in this thesis most work is primarily concerned with damaged or amorphous layers and hence changes in stopping powers do not need correcting for.

4.2.1.3 Conversion of energy scale to depth

Different methods can be applied to calculate the depth scales in MEIS (4). Two approaches have been used in this project and these are described in section 4.2.1.4 and later in section 4.2.3.3. The first method uses a constant value for the inelastic stopping power along the inward path and a different constant value along the outward path following scattering. There are several places to choose the stopping power values and in this project values were chosen at the surface and directly after scattering. This method is termed the surface approximation. Variations on this method also exist, choosing for example, some average value of the stopping power at some depth within the sample. These types of method are valid as the changes in stopping powers are small over the depths used in MEIS. They are convenient and provide the easiest starting point to explain how the depth scale may be calibrated.

The other approach used in this project is the use of a numerical solution using a computer program, and this was written as part of the project. In this method the instantaneous rate of inelastic energy loss is recalculated along the ion path. It

represents a small improvement over the surface approximation method as it closer describes the physically occurring situation. A variation of 2-3% over a depth of 10nm has been observed between the two methods.

Other ways to calculate the depth scale are based on analytical methods. These are based around solving equations for the distance based on expressions for dE/dx (4) but were not used in this project.

4.2.1.4 Surface Approximation method

A schematic of the MEIS scattering configuration is shown in Figure 4.2. An ion of energy E_0, scattered at the surface loses energy elastically and has a resulting energy KE_0. An ion scattered from a depth of Δz inside the sample travels a path length of $\Delta z/\cos\theta_1$ through the sample before an elastic collision and travels a distance of $\Delta z/\cos\theta_2$ on the exit path, losing energy inelastically along both paths in addition to the energy lost in the collision.

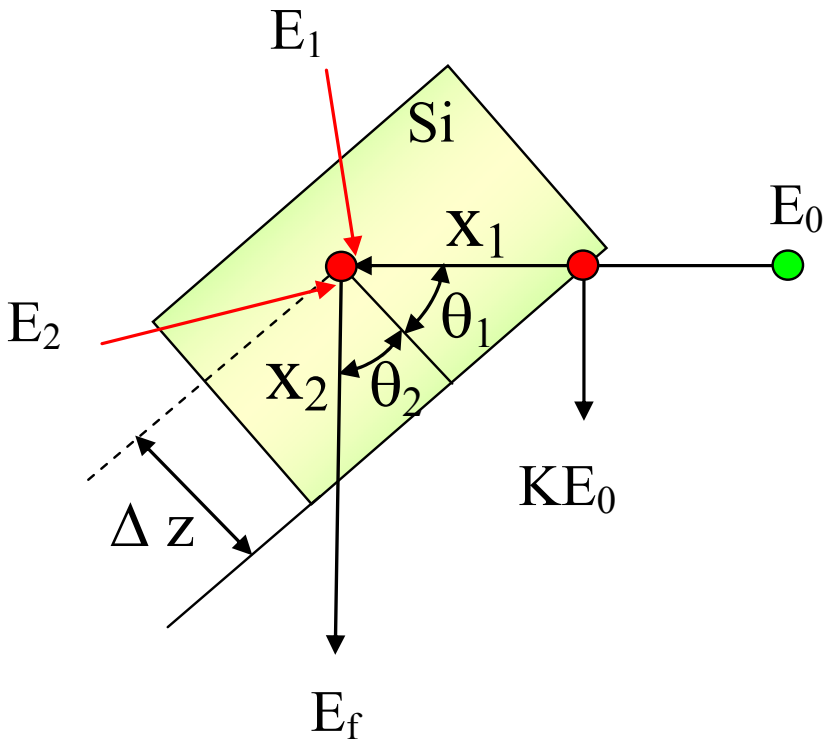

Figure 4.2 MEIS scattering configuration.

Over the small depth range used in MEIS, the variation in the rate of inelastic energy loss per distance is comparably small and as an approximation can be assumed to be constant along each path (4). In the collision with a lattice atom the ion undergoes an elastic energy loss and therefore the rate of inelastic energy loss takes a different

constant value along the exit path compared to the inward path. Using the surface approximation method, the two constant values of the stopping powers are taken as the value that would occur at the surface and immediately after scattering, i.e. the value of dE/dx corresponding to the beam energy and corresponding to the beam energy multiplied by the kinematic factor.

The value of the inelastic energy loss can be read off an inelastic energy loss curve or calculated from a function of the curve. In Figure 4.3 a plot of the inelastic energy loss of He in Si is given, with the constant values of the stopping power on the inward and exit paths indicated for scattering off Si following scattering through 70.5°. The constant value does deviate slightly from the instantaneous stopping power. Despite these simplifications the surface approximation is reasonably accurate over small depths.

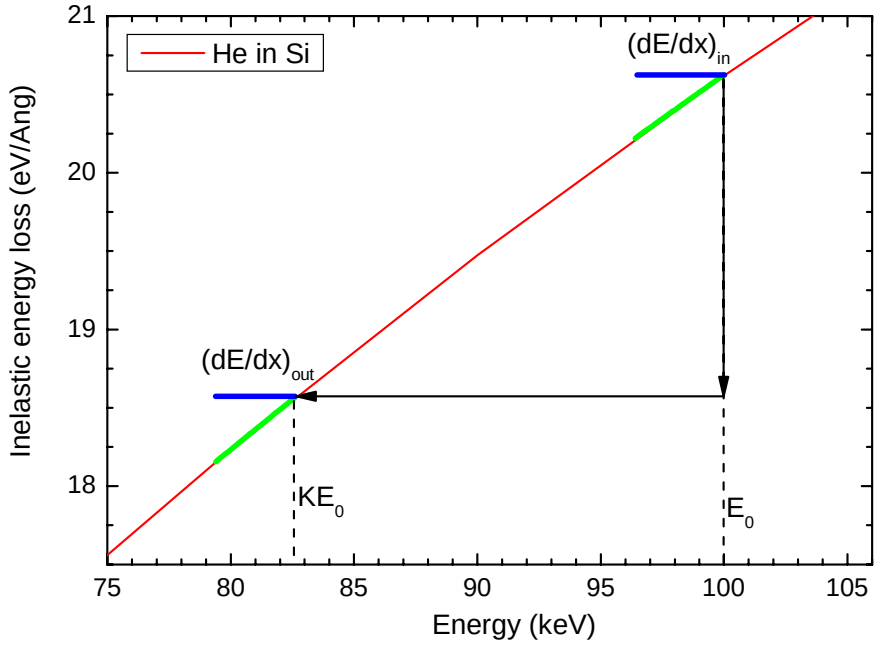

Figure 4.3 Graph of the inelastic energy loss rates, indicating how the energy loss values used in the surface approximation (blue lines) differs slightly from reality (green lines).

The final energy of an ion after scattering from a depth Δz inside the sample is given by accounting for all the inelastic and elastic energy loss processes. Using $(dE/dx)_{in}$ as the rate of inelastic energy loss on the way in, the energy lost on the inward path is simply $(dE/dx)_{in}$ multiplied by the path length $(\Delta z/\cos\theta_1)$. Before a scattering event the ion has energy E_1, which is E_0 minus the energy lost along the inward path. E_1 is multiplied by the kinematic factor K, to give the energy after the collision E_2. On the outward path the amount of energy lost inelastically is the rate of inelastic energy loss

$(dE/dx)_{out}$ multiplied by the path length ($\Delta z/\cos\theta_2$). This leads to an expression for the final energy after scattering at a depth:

$$E_{f\,depth} = K\left(E_0 - \frac{\Delta z}{\cos\theta_1}\left(\frac{dE}{dx}\right)_{in}\right) - \frac{\Delta z}{\cos\theta_2}\left(\frac{dE}{dx}\right)_{out} \quad (4.1)$$

In comparison the energy after scattering from the surface is simply:

$$E_{f\,surface} = KE_0 \quad (4.2)$$

Setting ΔE as the energy difference due to the effects of scattering from a depth Δz:

$$\Delta E = E_{f\,surface} - E_{f\,depth} \quad (4.3)$$

After combining these equations and rearranging, this leads to an expression relating the depth of scattering of an ion to the additional energy lost compared with scattering off surface atoms.

$$\Delta z = \frac{\Delta E}{\left(\frac{K}{\cos\theta_1}\left(\frac{dE}{dx}\right)_{in} + \frac{1}{\cos\theta_2}\left(\frac{dE}{dx}\right)_{out}\right)} \quad (4.4)$$

The depth an ion was scattered from can be determined using the measured energy loss compared to the energy of ions scattered by surface atoms. For example, for a 100 keV He beam and the [$\bar{1}$11] direction inwards and the [111] direction outwards, with a scattering angle of 70.5º, the kinematic factor K is 0.9313 for As. The energy of ions scattered from surface atoms would be 93.13 keV. Applying equation 4.4 gives a depth of 15.7nm for a 10 keV energy loss, i.e. an energy of 83.13 keV. This produces a depth scale where the relation between the energy and depth is a linear scaling factor.

4.2.1.5 Dose and concentration calculations

It is possible in principle to calculate the number of target atoms per unit area. The scattering yield Y is given by

$$Y = Q_d = d\sigma/d\Omega\,\Omega QNt \quad (4.5)$$

where $d\sigma/d\Omega$ is the scattering cross section which describes a probability for scattering, described in more detail in section 2.2.1, Q_d is the number of detected particles, Q is the number of incident particles, Ω is the acceptance solid angle of the detector and Nt is the areal density. The differential scattering cross section can be calculated from the interaction potential V(r). For $M_1 << M_2$.

$$\frac{d\sigma}{d\Omega} = F \cdot \left(\frac{Z_1 Z_2 e^2}{4E}\right)^2 \cdot g(\theta, M_1, M_2) \quad (4.6)$$

For interactions at the energies used in MEIS the nuclear events occur at distances of the order of the screening length, so the scattering is not purely Coulombic and a screening factor F, has to be applied. Screening functions are described in more detail in section 2.2. For MEIS it is generally accepted that a function derived from the Molière potential (26) is best (1, 2). Then F is given by,

$$F = 1 - \frac{0.042 Z_1 Z_2^{4/3}}{E} \qquad (4.7)$$

for $M_1 << M_2$. The screening term lies typically in the range $0.85 \leq F \leq 1$ (1). For a 100 keV He beam there is a 3% deviation in the potential from the case of the purely repulsive Coulombic Rutherford scattering. The implications are small and only have a minor affect with the MEIS scattering yield. The function $g(\theta, M_1, M_2)$ is a transformation factor from the centre of mass to the lab frame of reference, for $M_1 << M_2$ given by:

$$g(\theta, M_1, M_2) \approx 1 - 2(M_1 / M_2)^2 \sin^{-4}(\theta / 2) \qquad (4.8)$$

Equations 4.5 and 4.6 have important implications for the choice of experimental parameters and the ability of MEIS to detect different elements. Since $d\sigma/d\Omega$ is a function of Z_1^2 then the scattering yield is four times higher for He^+ than H^+ and similarly as $d\sigma/d\Omega$ is a function of Z_2^2 then there is a considerably higher scattering yield from heavier elements, eg As, compared to light elements, eg B. Using a lower energy beam gives a higher scattering yield. A smaller scattering angle gives a rapid rise in the scattering yield because of the $\sin^{-4}(\theta/2)$ dependence. The requirements for the experimental set up are discussed more in section 4.2.2.2.

Returning to the calculation of implantation dose, in practice equations 4.5, 4.6 and 4.7 are not used since the acceptance angle of the detector and the detection efficiency are not normally known with sufficient accuracy (1). The yield will also be varied by the neutral fraction. Instead results obtained are compared with the result from a randomly oriented (amorphous) sample or an ion implanted sample with a well known amount of a heavy dopant (4). Data was frequently taken from amorphous Si samples therefore the random level was the preferred concentration reference. It is expected that doses can be calculated to within 5% using this method (1). The density of an amorphous Si sample is known to within 5%, and therefore the number of Si atoms represented by each backscattering count can be determined. This value can be converted for dopant ions by accounting for the difference in scattering cross sections between Si and the dopant ion. The number of atoms per count has to be multiplied by $(Z_{Si}/Z_{atom})^2$. It is largely justifiable to ignore the differences in the screening function as

they are small compared to the differences due to the scattering cross sections. With the random yield typically 375 counts, representing a concentration of $5 \times 10^{22} cm^{-3}$ Si atoms, then displaced Si can be detected down to ~ 1×10^{20} cm^{-3} and As to 1×10^{19} cm^{-3}. A correction has to be applied to account for the different energy widths that peaks of the different elements have on the energy scale. The heavier the element, the greater energy range that equates to a fixed depth. Stated differently $\Delta E/\Delta z$ is larger for higher masses and hence energies. The variation is usually less than 10% but needs to be accounted for (4). It can be most convenient to calculate the number of dopant atoms on the basis of the depth scale.

The effect of neutralisation should be considered when using an electrostatic analyser, as neutrals cannot be detected (1). Analysis of data taken at the MEIS facility at the FOM institute (NL), carried out at Daresbury Laboratory, would suggest that there was little variation in neutral fraction for different elements at the energies used in MEIS (48), which was contrary to other findings (44). The measured results showed that the neutral fraction varied with the velocity of the ion leaving the sample, being lower at lower energies. The amount of variation was small over the energy range of a MEIS spectrum (48). The implications for the dose calculation would therefore appear to be not particularly significant. This is supported by a comparison of the results of MEIS dose calibration with results of RBS measurements carried out at the University of Salford, using a surface barrier detector, which detects neutrals. Good agreement to within 3% was obtained.

4.2.1.6 Crystallography – Channelling, shadowing, blocking and dechannelling

By changing the orientation of a Si crystal the number of atoms "visible" to the beam can be altered. Alignment along crystallographic planes produces so called open channels. Atoms deeper within the crystal effectively become invisible, as illustrated in Figure 4.4. The number of visible atoms is reduced from the initial random orientation, to a planar alignment, and further reduction as the model is axially aligned along the [110] direction on the right.

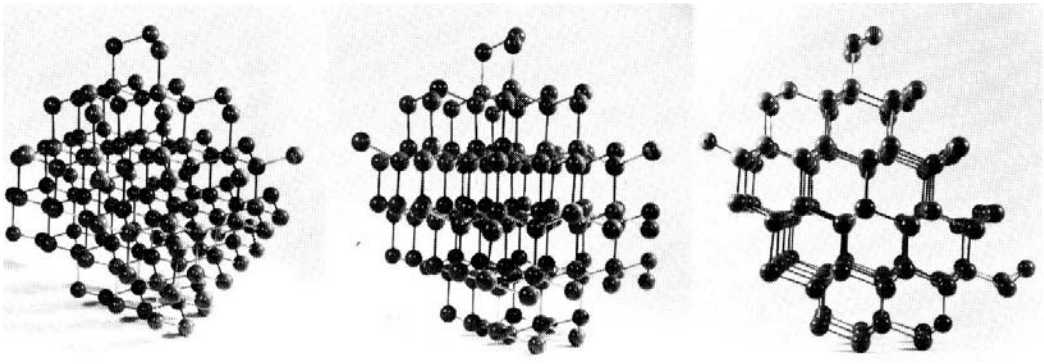

Figure 4.4 Different orientations of a Si Crystal. Randomly oriented, planar aligned, and aligned along the [110] direction. From (4).

When a crystalline sample is aligned to the beam along a crystallographic direction, the open channels are produced and the beam "sees" only the surface atoms. Ions undergo large angle scattering from the first layer atoms but the second and subsequent layer atoms in regular lattice positions are located within the so called shadow cone, and give rise to no scattering as illustrated in Figure 4.5a). The shadow cone radius R_c, can be calculated by (4):

$$R_c = \left(\frac{Z_1 Z_2 e^2 d}{E_0} \right)^{1/2} \tag{4.9}$$

where d is the distance between atoms. Ions that enter the channel can undergo small angle defections with the strings of atoms as shown in Figure 4.5b). There is a critical angle for channelling, and with 100 keV He^+ in Si it is ~ 2.5° (1).

When aligned, the scattering yield from deeper atoms is considerably reduced, by as much as a factor of around 100 compared to scattering from a randomly orientated sample, greatly increasing sensitivity in the near surface region (25). Less than 5% of the incoming ions will undergo a hard collision, these ions will be scattered through large angles with a spread of directions. The rest of the ions will be gently steered into the open channels, with small angle deflections due to interactions with the channel walls (1, 5).

If the lattice atoms were stationary then the beam would only see 1 atom per row. Because of lattice vibrations this is not strictly the case. The lattice vibration time is much lower than the transit time of an ion so the ion effectively sees atoms frozen in their thermally displaced positions during its passage (1). The work of Stensgaard shows that effectively 1.3 – 1.4 atoms per row are left visible to the beam, the net effect is any atom displaced from a regular lattice site by 0.1 – 0.2 Å gives rise to

backscattering (27). This fact forms the basis of the sensitivity of MEIS to lattice damage and implanted dopants in non lattice sites.

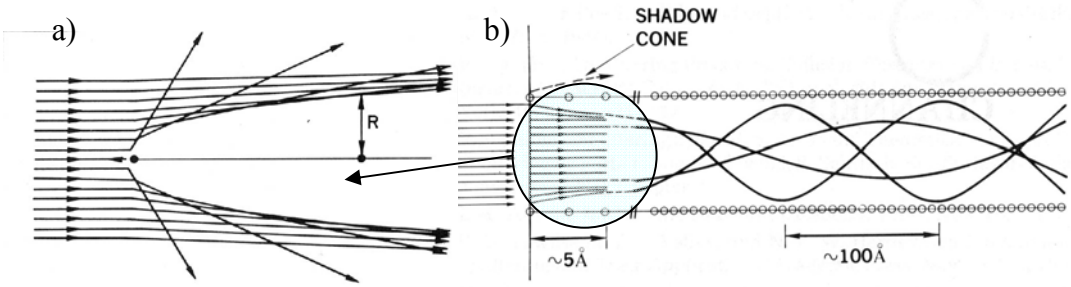

Figure 4.5 a) Shadow cone produced by a surface atom. b) Ions steered into the open channel. From (5).

If the sample is aligned to the beam on its inward path, this situation is called shadowing. Additionally data can be recorded along a direction of a crystallographic axis on the exit path and this is called blocking, it gives a further increase in surface sensitivity. The configuration of combined shadowing and blocking is known as double alignment.

Channelled particles can become dechannelled when undergoing deflections larger than the critical angle. Displaced atoms within a channel, e.g. point defects, stacking faults, dislocation loops and amorphous zones, can cause such deflections of the ions (forward scattering), which then cause the ion to be backscattered from deeper within the sample. Figure 4.6a) illustrates dechannelling, in comparison to channelling and backscattering. Amorphous layers cause dechannelling of the collimated beam, as illustrated in Figure 4.6b). Dechannelling results in a higher background scattering yield.

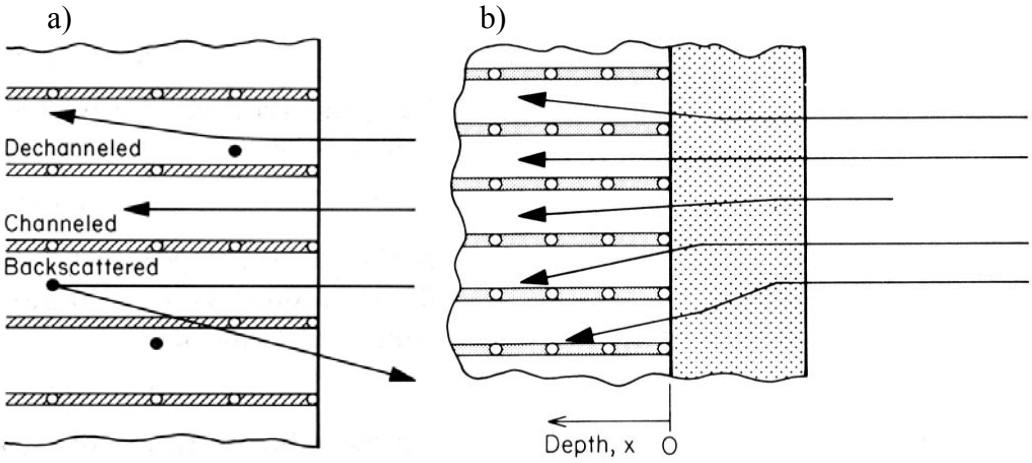

Figure 4.6 a) Schematic illustrations of particles undergoing dechannelling, channelling and backscattering. b) Illustration of the divergence of a collimated beam through an amorphous layer, which results in a high level of dechannelling. From (4).

4.2.1.7 Energy straggling and system resolution, resulting in a convolution of the peaks with Gaussian distributions

MEIS energy spectra are modified from idealised profiles by two unavoidable effects, i.e. energy straggling and the system resolution, causing the idealised profiles to become convoluted with error functions.

As an energetic particle moves through a sample it loses energy through many individual encounters. These encounters are subject to statistical fluctuations. Two ions with an identical initial energy are unlikely to have the same energy after passing through the same thickness of a sample. This effect is called energy straggling, (Ω_s), and this places a finite limit on the accuracy of the energy losses and hence the depths that can be resolved.

It is difficult to calculate the exact amount of straggling, but a theoretical expression that estimates the amount of energy straggling was derived by Bohr and extended by Lindhard and Scharff:

$$\Omega_B{}^2 = 4\pi\left(z_1 e^2\right)^2 N z_2 t \qquad (4.10)$$

where N is the density and t is the layer thickness. This indicates that the energy straggling is proportional to the square root of the layer thickness. Energy straggling also varies with atomic species and the electron density but not the beam energy (4). Theory predicts that the straggling produces approximately a Gaussian distribution from a mono energetic incident beam. Backscattering spectra most often display the integral of the Gaussian distribution (error function) rather than the Gaussian distribution as shown in Figure 4.7 b) and a) respectively. The full width half maximum (FWHM) of a Gaussian corresponds to the 12% to 88% range of the error function and the ±Ω corresponds to the 16% to 84% range. The FWHM is equal to 2.355 times Ω (4).

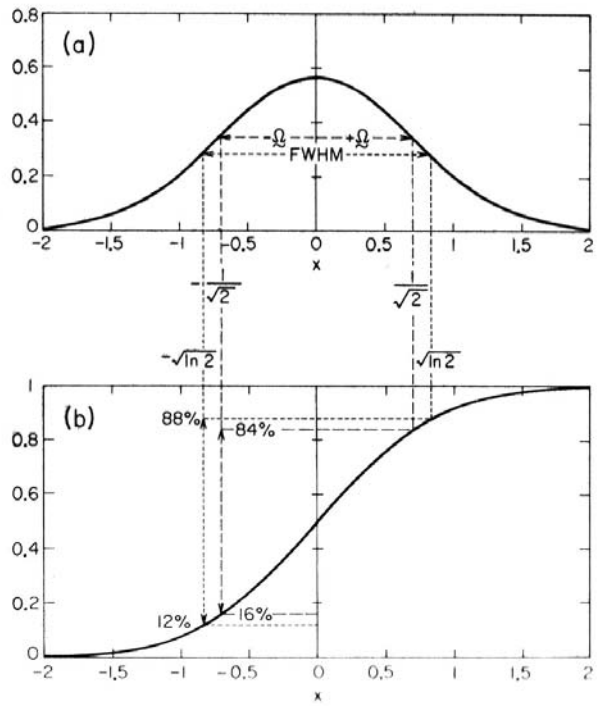

Figure 4.7 a) Plot of a Gaussian distribution b) The error function in MEIS spectra is typically of the form of the integral of the Gaussian distribution. The standard deviation is indicated. From (4).

The second effect referred to earlier is the system resolution. Many parts of the system are subject to statistical fluctuations of some kind. It is convenient to lump together the fluctuations from the major experimental causes. This is close to a Gaussian distribution and can be characterised by the standard deviation Ω_r, commonly referred to as the system resolution. The main contribution to the system resolution is the energy resolution of the detector. At the Daresbury facility $\Delta E/E$ is ~ 0.35%. Other contributions to the system resolution include the energy spread in the analysing beam, the acceptance angle of the detector and the width of the beam. The energy resolution is the most significant contributor.

In the same way as the depth scale is calculated, the depth resolution can be calculated by applying the energy error of the analyser. The resolution is dependent on the scattering configuration but a depth resolution of 0.6 nm is typical (17). To improve the overall depth resolution, scattering configurations that result in long pathways through the sample are used. Using a beam energy where the rate of energy loss is high also improves the resolution. This means that better resolution is achieved with He compared to H. The absolute error of the detector is reduced using lower beam energies, and hence lower beam energies can improve the resolution.

For an idealised peak, shown in Figure 4.8a), the effect of the energy straggling is to broaden the low energy edge of the peak, as is shown in Figure 4.8 b). The effect of the system resolution is to broaden both the leading edge and the low energy edges, as shown in Figure 4.8c). The overall effect is to convolute the ideal peak with the Gaussian distributions. Note that Ω's add together quadratically, i.e. $\Omega_{s+r} = \sqrt{(\Omega_s^2 + \Omega_r^2)}$.

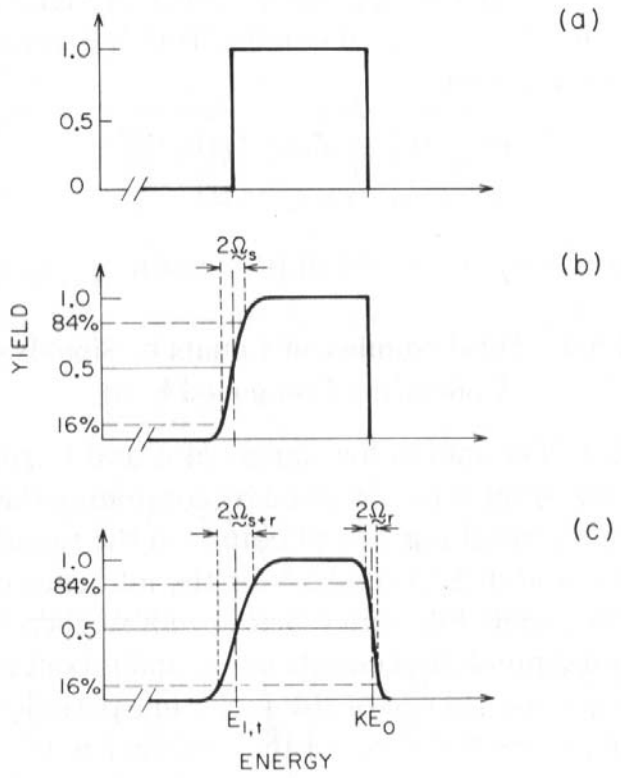

Figure 4.8 The effects of energy straggling and the system resolution. For an ideal profile a), energy straggling causes a broadening of the low energy edge b). The system resolution causes a broadening of both the leading and low energy edges c). From (4).

The impact of the convolution depends on the details of the layers being studied. In Figure 4.9 various ideal peak shapes have been convoluted with a single Gaussian to illustrate the effects. If the width of the layer is wide compared to the convoluting Gaussian, then the layer width can be taken as the FWHM of the convoluted spectrum, as shown in Figure 4.9a). The low and high energy edges are broadened however. The interface sharpness cannot be measured to exceed that determined by the limit imposed by the energy straggling and resolution limit. If a layer is thin compared to the convoluting Gaussian, then the resulting peak will take the form of the Gaussian. The true position of the signal on the energy axis is given by the energy where the Gaussian has its maximum, as in Figure 4.9b). If the real layer width is some intermediate value

similar to the width of the error function, then the resulting convoluted peak will have a FWHM that will be subject to some broadening, as shown in Figure 4.9c). If the slope of an interface is broad compared to the limits imposed due to the convoluting Gaussian, then the resulting convoluted spectra will closely follow the shape of the interface, as shown for the interface at low energy in Figure 4.9d).

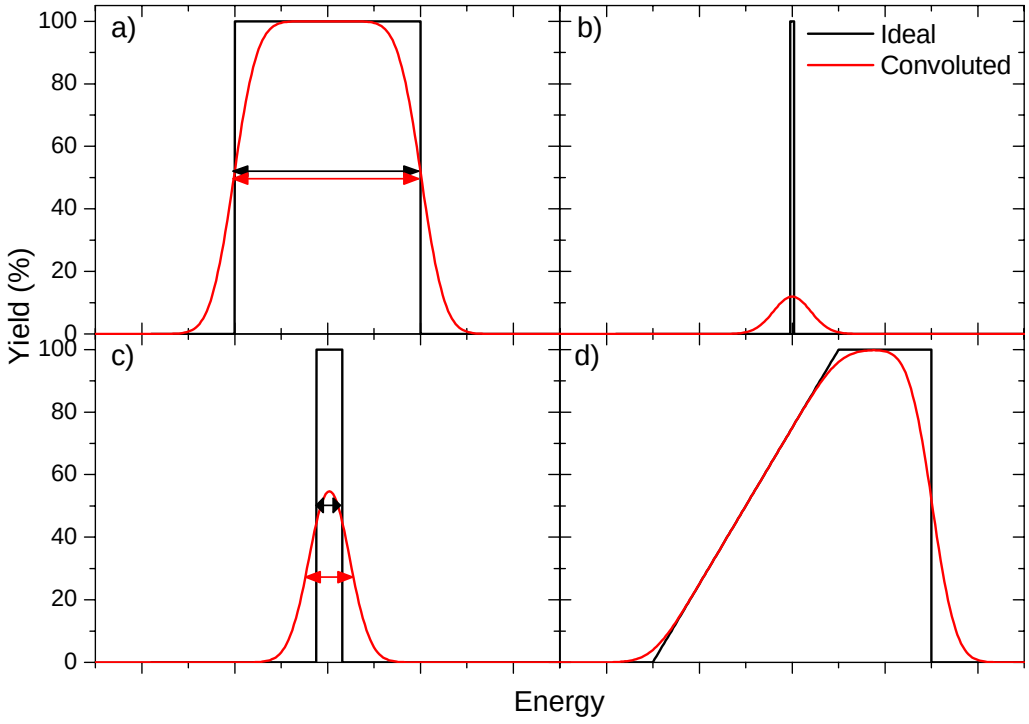

Figure 4.9 The effect of convoluting different ideal peak shapes with a single Gaussian function. a) A layer that is wide compared to the width of the Gaussian. b) A very thin layer. c) A layer with a width similar to the Gaussian. d) An interface with a broad energy distribution.

4.2.2 Experimental

4.2.2.1 MEIS system

A diagram of the Daresbury MEIS facility (3) is shown in Figure 4.10 and the system is also described in (43). The ion source platform houses a duoplasmatron ion source. He^+ or H^+ ions are accelerated with an energy of 20 keV from the source and then the ions are then accelerated again to the required energy with a second power supply. Originally a 500 kV power supply was used but this was replaced with a 250 kV supply, with better voltage stability and which could be set with more accuracy.

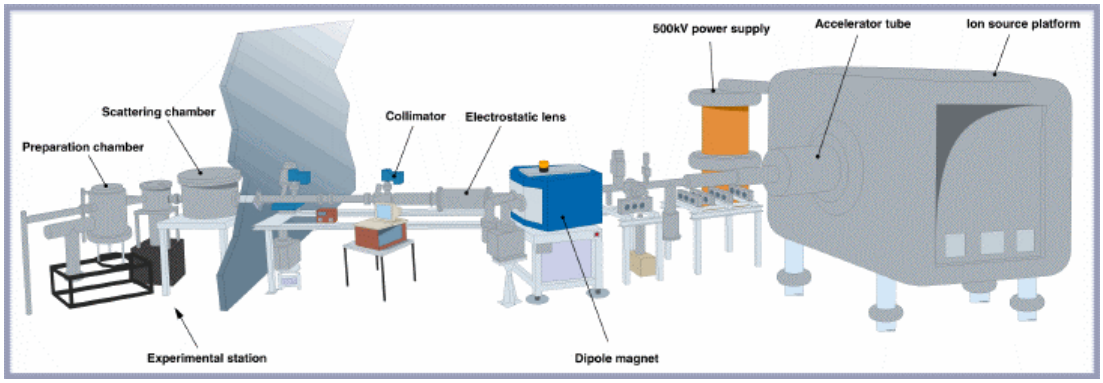

Figure 4.10 Illustration of the Daresbury MEIS facility, from (3).

The beamline is pumped to high vacuum and consists of a bending magnet, several electrostatic lenses, and beam steerers. Collimating slits at various locations along the beamline are used to produce a beam with a divergence of 0.1° and a standard spot size of 1mm wide by 0.5 mm height on target. Most beam parameters can be controlled from a control room next to the experimental station, allowing the beam to be focused or defocused during the course of an experiment to optimise conditions for an experiment.

The beam current is monitored using a thin wire grid placed in the beam. This allows the beam current on target to be known. A current integrator monitors the beam current to ensure a reproducible beam dose on target.

The experimental station contains three ultra high vacuum (UHV) chambers and a loadlock that is set up for rapid pumping to allow samples to be changed over quickly. Samples are mounted on holders that can be transferred from one chamber to the next on transfer arms. The scattering chamber houses a goniometer that can hold a sample holder and position the sample into the beam. The goniometer has three translational degrees of freedom, so that the position of the beam on the sample can be moved and three rotational degrees of freedom that allow the sample to be aligned to the beam. These axes are named the rotation, spin and tilt axes, as designated in Figure 4.11. Each axis can be moved by a stepper motor controlled by the computer in the control room.

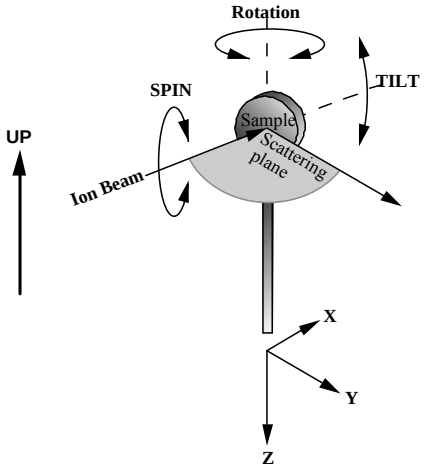

Figure 4.11 MEIS Azimuthal alignment axes.

The toroidal energy analyser equipped with a 2-D detector (28, 29, 30) is also housed in this chamber. These form one unit that can be moved around the goniometer / sample in the plane of the beam. The analyser has a 27° acceptance angle and ions entering the analyser are deflected in an electric field due to the voltage applied to the plates. The position that the ion strikes the detector is thus dependant on its scattering angle and energy. The yield of ions striking each position on the detector is recorded on a computer. The angular resolution of the detector is 0.3° and the energy resolution dE/E is 3.5E-3. The energy window of the analyser is 2% of the pass energy. The analyser /detector configuration is shown in Figure 4.12 in relation to the sample and beam.

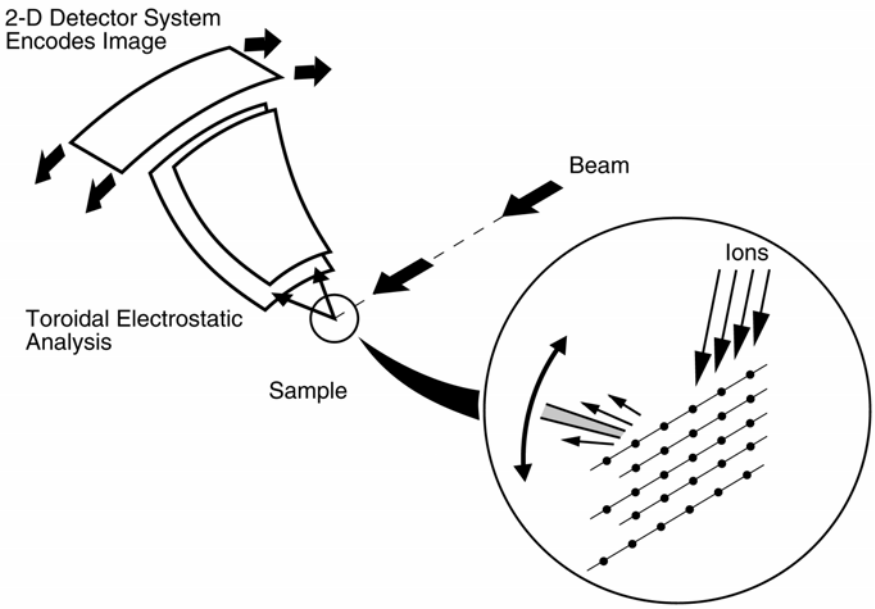

Figure 4.12 MEIS analyser and detector scattering configuration.

Taking data creates a data tile, i.e. a 2D plot of the yield at each point on the analyser. By stepping the pass energy down, and joining together the individual tiles, a continuous energy spectrum can be produced. Further data processing information is given in section 4.2.2.3.

4.2.2.2 Experimental Parameters

Before explaining the MEIS output data, the choice of experimental parameters needs to be discussed. The main experimental parameters to consider are the scattering angle, which is determined by the crystallographic directions in and out, the beam energy and the choice of projectile mass. Changes to these parameters produce a variety of effects and often a compromise is needed to find the best overall conditions.

It is useful to avoid overlap of peaks from different elements (masses) to make analysing the data more straightforward and to avoid ambiguity of the results. This may be achieved by choosing conditions with a sufficiently large variation in the kinematic factors (equation 2.10) for all the different elements present in a sample. The kinematic factor varies with scattering angle and with mass ratio of the atom and incident ion. Plots of the kinematic factor for various atom / ion combinations are shown in Figure 4.13, for He ions on the left and H ions on the right. There are several important observations. As the scattering angle is increased, there is an increased variation in K between the different masses hence there is less likelihood of peak overlap at larger scattering angles. There is less variation for high masses than light elements. Comparison between He and H shows a much larger spread of K values achieved with He.

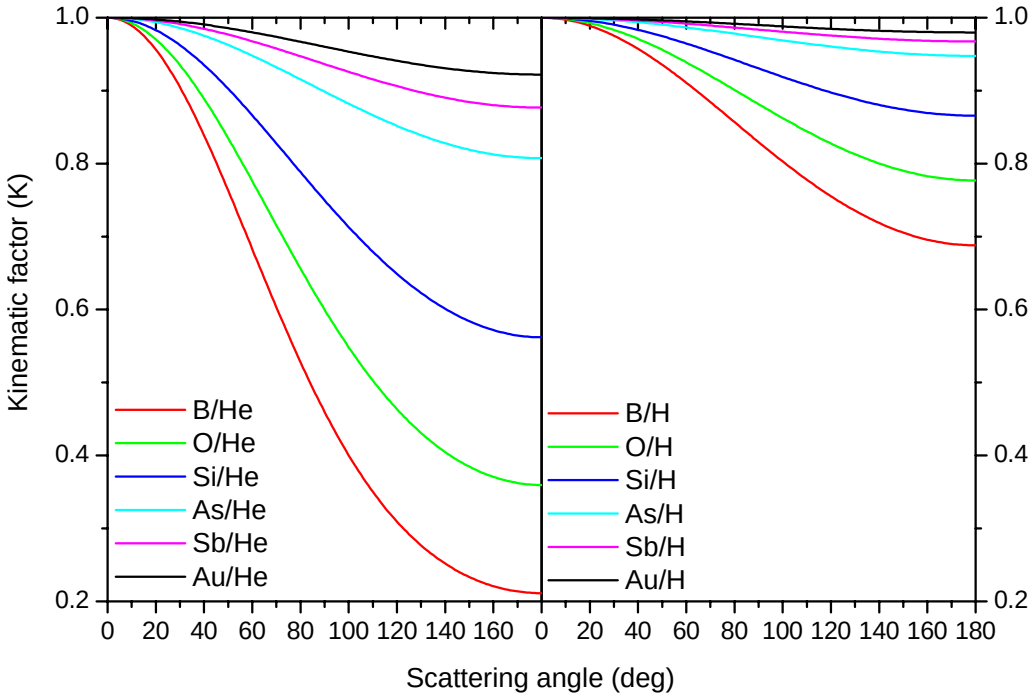

Figure 4.13 Variation in the kinematic factor K with scattering angle, for different atom / He or H combinations.

The depth resolution can be varied with scattering angle. Increasing the path lengths of an ion in a sample produces an improvement in depth resolution; therefore using small scattering angles produces an enhancement of the depth resolution. This is evident in Table 4.1, shown later, where the depth resolutions obtained for different scattering angles is given. Once an appropriate scattering angle is chosen, to satisfy the requirements of peak overlap and depth resolution, the specific crystallographic directions need to be chosen for the channelling and blocking. More open channels produce better blocking dips which makes the set up of the double alignment up more sensitive to the surface and also makes sample alignment easier. He ions have a wider shadow cone compared to H and this means the shadowing and blocking will be more effective and hence He should give deeper channels. The choice of ion has an effect on the depth resolution, He with its higher stopping power produces better depth resolution than H^+.

A high scattering yield is advantageous to improve the sensitivity for detecting particles. As given in equations 4.5 and 4.6 the Z_1^2 dependence of the scattering cross section shows that the scattering yield would be four times higher for He^+ ions than for H^+ ions. Likewise the Z_2^2 dependence shows there is a much higher scattering yield for scattering off heavy elements such as As than light ones such as B. Since the scattering

cross section has an E^{-2} dependence, the scattering yield is higher for lower beam energies. The $\sin^{-4}(\theta/2)$ dependence shows that for smaller scattering angles there is a sharp increase in yield. The sensitivity of MEIS to detect B and F is such that it has not been possible to profile B or F.

Using a lower beam energy improves the depth resolution because of a smaller absolute energy error of the energy detector / analyser but as the stopping power is higher with higher beam energy over the range used, then peak overlap may be reduced using a higher beam energy. Figure 4.13 shows that higher masses have a higher kinematic factor. This determines the order that any peaks will appear in the energy spectrum, but is not significant in terms of the choice of conditions.

The conditions considered best for these studies was the use of a He^+ beam of either 100 keV or 200 keV. The ions were incident along the $[\bar{1}\bar{1}1]$ channelling direction and the analyser positioned to include the [111] and [332] blocking directions. These directions resulted in scattering angles of 70.5° and 60.5°, respectively, and are illustrated in Figure 4.14. These conditions are an optimum compromise between good energy and hence mass separation between the As and the Si peaks and depth resolution. They all result in sub-nm depth resolution and the detection of clear experimental blocking dips (17, 31). The [332] direction gives a better depth resolution but a decreased mass separation can cause a slight overlap of the silicon and arsenic peaks. With the [111] blocking direction, this peak overlap is often avoided. Values of the kinematic factor for the elements and scattering angles used in this study are given in Table 4.1 along with the depth resolution obtained.

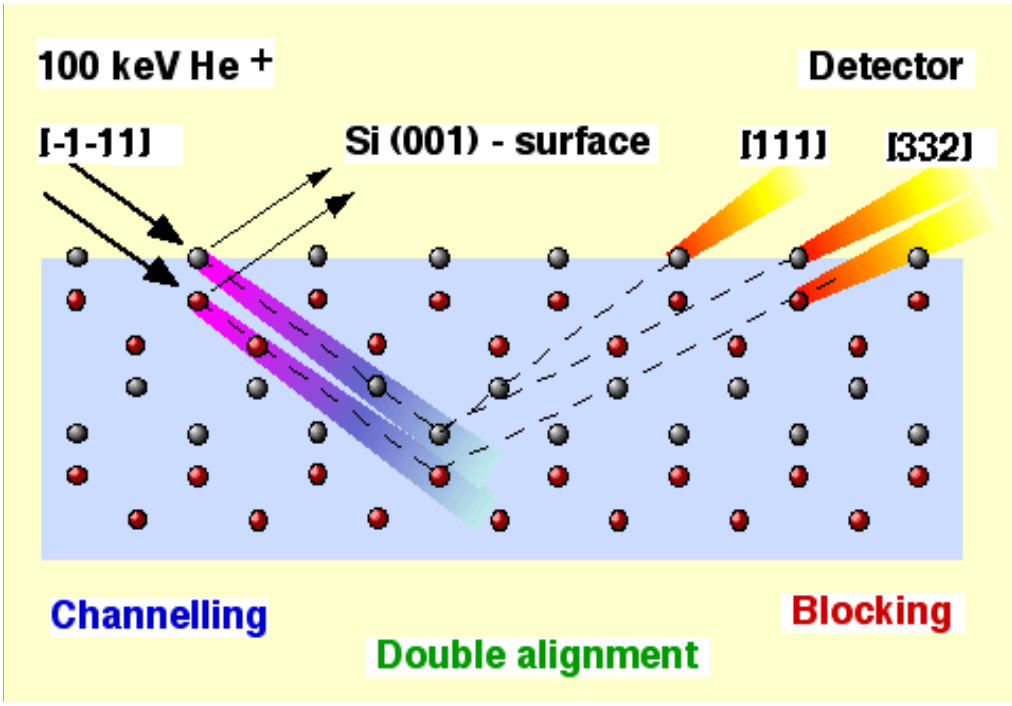

Figure 4.14 Illustration of the double alignment scattering configuration used in the MEIS experiments, showing the shadowing and blocking.

	Kinematic factor		Depth resolution (nm)	
	[332] – 60.5°	[111] – 70.5°	[332]	[111]
Au	0.9796	0.9732	0.42	0.50
Xe	0.9695	0.9602	0.43	0.51
Sb	0.9672	0.9571	0.43	0.51
As	0.9472	0.9312	0.43	0.52
Si	0.8643	0.8255	0.46	0.57
F	0.8059	0.7527	0.49	0.61
O	0.7731	0.7124	0.50	0.64
B	0.6789	0.5991	0.55	0.73

Table 4.1 Values of the kinematic factor for He ions using the [$\bar{1}$1$\bar{1}$] direction on the inward path and the [332] and [111] directions on the outward path. The corresponding depth resolutions are given for a 100 keV He.

To align the sample to the beam along a crystallographic direction, angular scans across the three rotational axes to find the positions with the minimum scattering yield, have to be performed in a systematic sequential manner.

The dose of the beam has to be chosen as a balance between achieving an adequate signal to noise ratio, and acceptable data collection times of the allocated beam time, so as to allow an adequate number of samples to be carried out. Beam damage to the Si needs to be minimised and so the sample would be moved after a set amount of beam on target, to a fresh spot. For most samples analysed, the current integrator was set to acquire a dose corresponding to 5μC charge.

4.2.2.3 Experimental output

As mentioned previously, by changing the voltage applied to the analyser and piecing together separate data tiles a complete 2D yield with energy and scattering angle spectrum is produced. An example is shown in Figure 4.15 which was taken from an As implanted Si sample. The different colours represent different scattering yields. Taking a cross section of the data along the angular axis produces the yield vs scattering angle spectrum, as shown in the top right graph. There are two dips in the spectrum which correspond to the [332] and [111] blocking directions. There is also a peak corresponding to the O peak. Taking a cross section along the energy axis at the angles of these blocking directions produces energy spectra of the [332] and [111] directions as shown in the bottom graph.

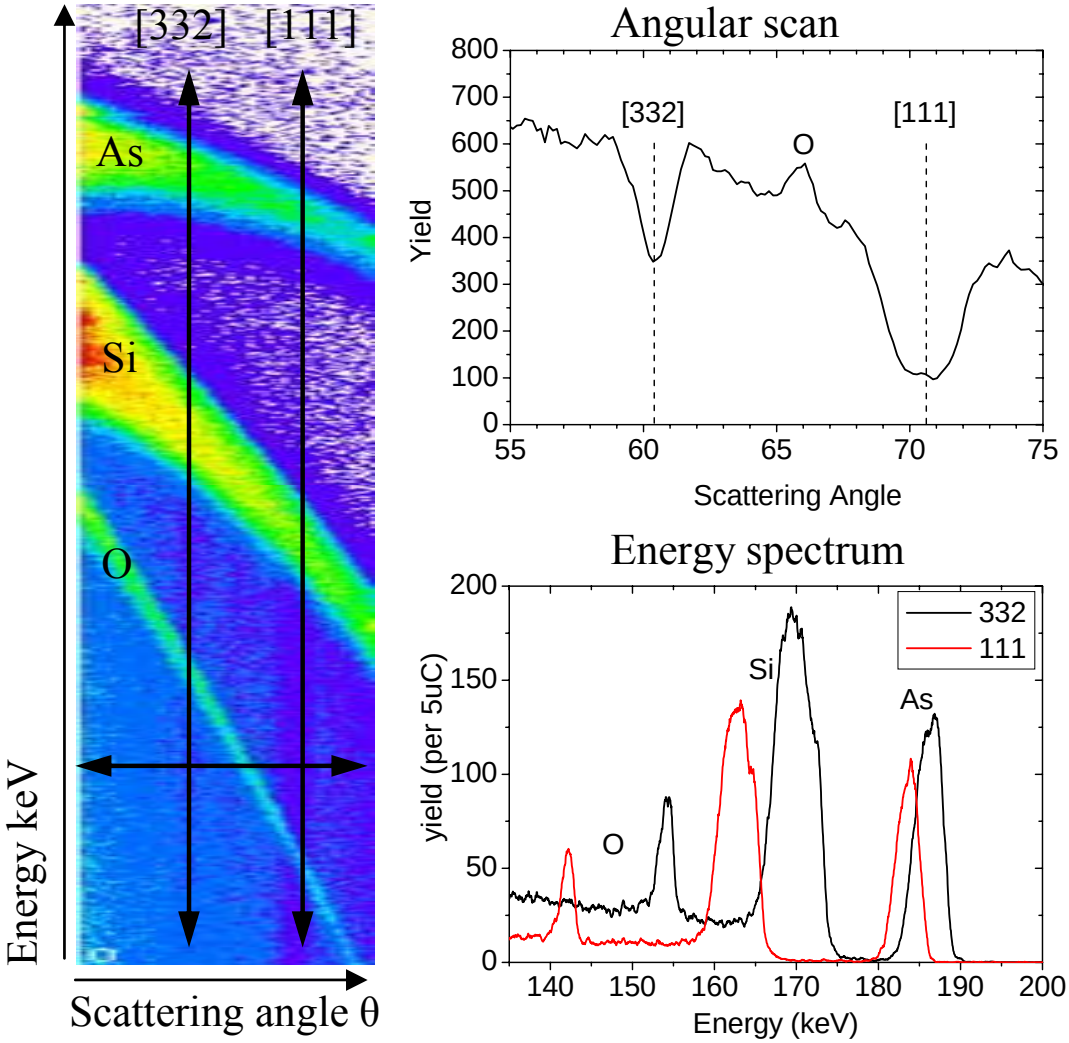

Figure 4.15 MEIS 2D data output (left) of an As implanted Si sample. Indicated is the position of the angular cut and the two cuts along the energy axis of the [332] and [111] blocking dips. The corresponding angular spectrum is plotted in the top right of the figure and the corresponding energy spectra are given in the bottom right of the figure.

4.2.2.4 Interpretation of spectra

An example set of MEIS spectra is shown in Figure 4.16. These are taken with a nominally 100 keV He beam. The samples were aligned along the [$\bar{1}1$1] axis and the data is taken from the [111] blocking direction. Data is taken for a virgin sample, an amorphous sample (random), a sample implanted with 3 keV As to a fluence of 2E15 and a sample with the same implant that has been annealed to 550 °C for 200s.

Using the kinematic factors enables the energy for scattering off surface As, Si and O to be determined. The corresponding extra energy loss with respect to these reference energies with scattering depth, have been calculated and the resulting depth scales have been added to the figure.

Considering first the data from the virgin Si sample, two peaks are present. These correspond to scattering off surface Si and O atoms. The Si peak consists mainly of scattering off Si atoms in the amorphous SiO_2 layer. Deeper atoms in crystalline positions do not give rise to backscattering because of shadowing. A small background yield is due to dechannelling. The O peak is superimposed on this background yield.

The effects, on the shape of the peaks, of the system resolution and energy straggling can be seen. System resolution is responsible for the slope of the high energy leading edge. A combination of the system resolution and energy straggling is largely responsible for the low energy downslope.

Isotopes of Si cause a small extension of the peak in the energy 84 – 85 keV. This occurs for all samples and convolution causes it to become a small tail.

The random spectrum is modified considerably compared with the virgin, as can be seen with the dramatically higher scattering yield of the Si peak. Because the atoms are not on regular lattice sites there is scattering off deeper atoms, giving rise to the high scattering yield. The O peak is on top of this Si signal.

The as-implanted sample shows that the implant causes the Si to be amorphised, as evidenced by the height of the Si peak reaching the random yield. The width of this amorphous layer is taken at the FWHM and is approximately 11 nm. The As peak is also visible in the spectrum at higher energy.

Annealing of the sample causes SPER. This reduces the width of the amorphous layer. The As profile is also modified. This shows how MEIS is able to profile Si damage and dopant profiles simultaneously. Annealing studies are contained in chapter 6 of this thesis.

The effect of the amorphous layer on the dechannelling level is clearly visible for the implanted and annealed samples. An increase in amorphous layer thickness causes a substantial increase in the dechannelling yield. The energy spread of the low energy edges becomes wider for increasing amorphous thickness as can be seen. The energy straggling increases as a function of the square root of the amorphous layer width, as described in equation 4.10.

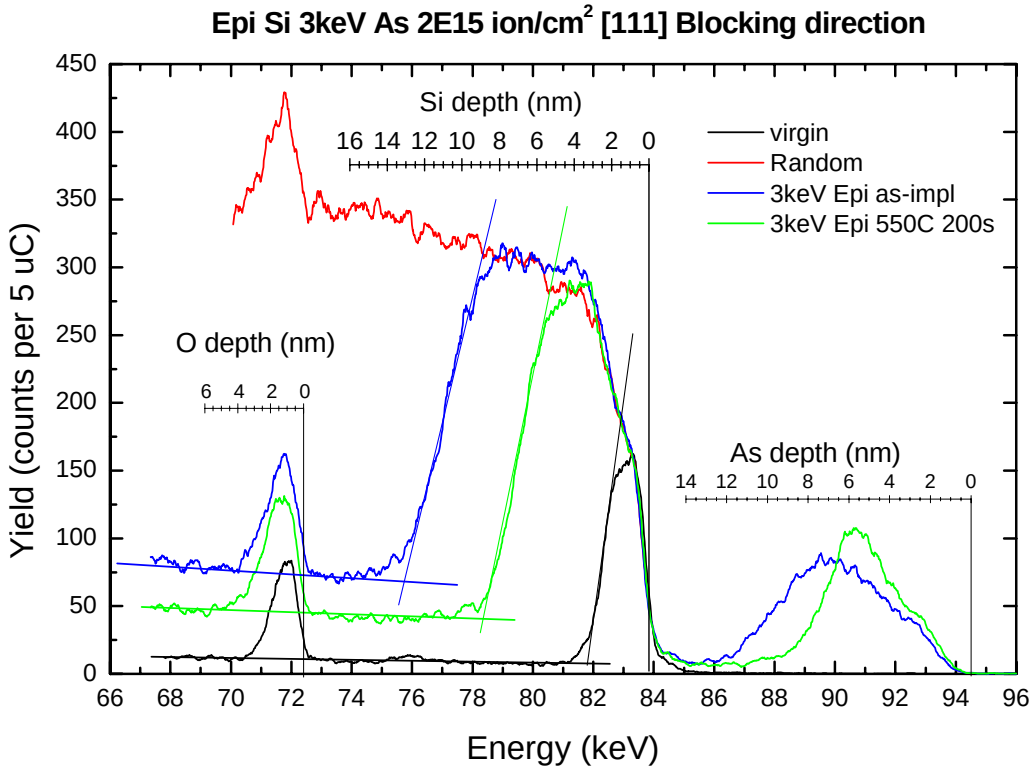

Figure 4.16 Typical MEIS spectra for different samples with a 100 keV He beam and using the [$\bar{1}$11] channelling and [111] blocking directions. The effect of energy straggling and system resolution on the gradient of the low energy edge of the peaks and differences in dechannelling level for different amorphous layer widths are highlighted.

4.2.3 Improvements to methodology

Throughout the project improvements to the MEIS methodology were carried out and its validity checked. The main aim was to be able to produce depth scales as accurate as possible. The work has followed three main strands: 1) finding stopping powers that produce reliable depth scales, 2) determining the beam energy / accounting for beam energy differences from day to day of operation, 3) improving the method of depth scale conversion. The improvements in the accuracy that this section is concerned

with are comparatively small, ~ 0.5 nm, but effort was put into this area in an effort to maximise the high resolution potential of the technique.

4.2.3.1 Stopping powers

At an early stage it was observed that a variation of up to 9 % existed between depth profiles converted from MEIS spectra taken on the same sample using 100 keV or 200 keV He^+ beam energies. An example of these depth profiles is shown in the top of Figure 4.17, including data taken using a 150 keV beam. The discrepancy in the peak centres is indicated with dashed lines. The cause of this discrepancy was an incorrect slope of the inelastic loss curve. There have recently been a number of studies with the aim to improve the accuracy of stopping powers (32, 33, 34, 35). The solution that produced consistent depth scales was found with the release of the 2003 version of SRIM. The stopping powers have been significantly improved from the last major update in SRIM 1998 (20). The updated energy loss rates are compared with those of the SRIM 2000 version in Figure 4.18. The use of the new inelastic loss data largely eliminated the discrepancy at the two energies as demonstrated in the depth profiles in the bottom of Figure 4.17.

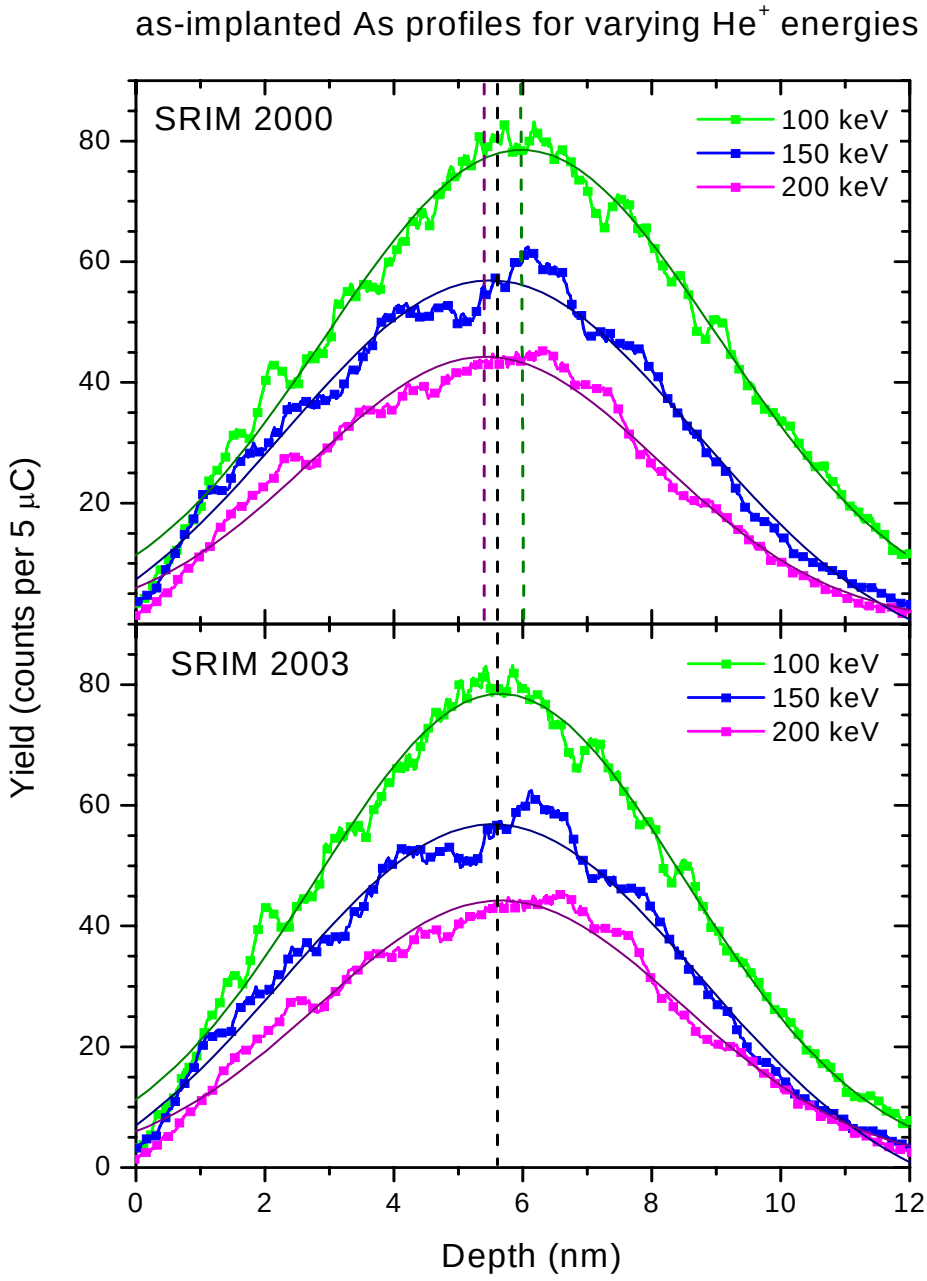

Figure 4.17 Comparison of depth scales calibrated using inelastic energy loss rates from SRIM 2000 (top) and SRIM 2003 (bottom). Gaussian distributions have been fitted to the peaks and dashed lines have been placed through the centre for clarity.

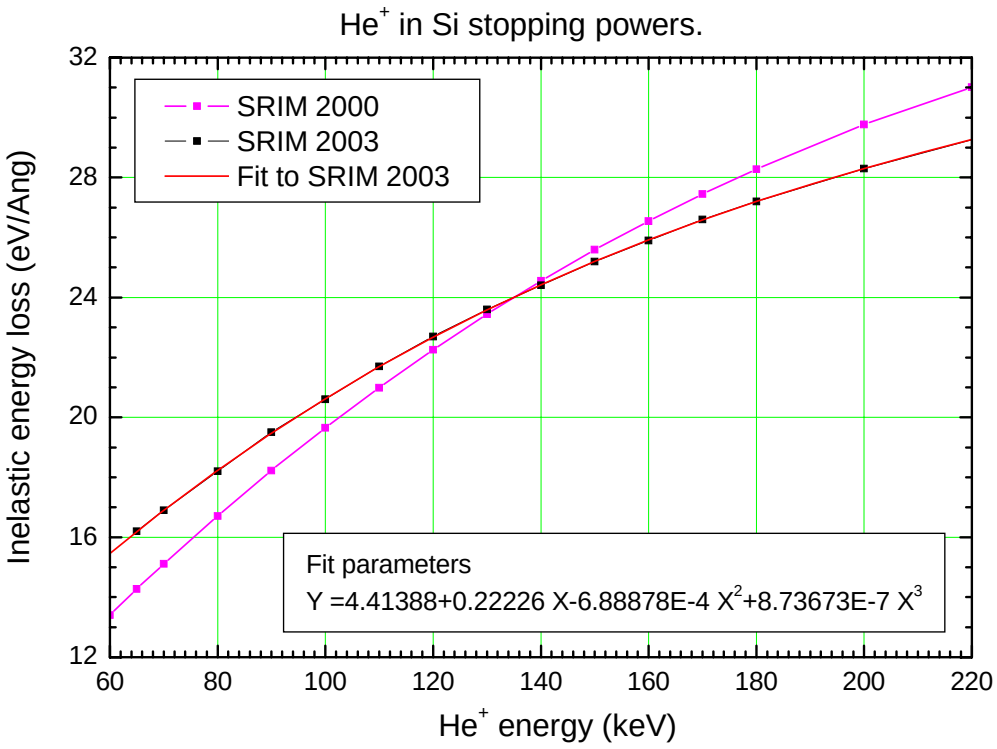

Figure 4.18 He inelastic energy loss rates in Si as a function of energy, taken from SRIM 2000 and SRIM 2003. The function, of a best fit to the values from SRIM 2003 is given.

4.2.3.2 Determination of beam energy

With the MEIS system it is not possible to set the beam energy to a reproducible energy with sufficient accuracy so that any minor energy differences occurring from one day to another would not be noticeable on the energy and hence depth scales. A difference of approximately a few hundred volts would cause a difference around 0.5 nm on a depth scale, depending on scattering conditions and element. With the original power supply used earlier in the project this level of variation was common and despite an improvement later on in the project with a new power supply, beam energy variations still needed to be accounted for.

The original approach for this was to align the Si peaks of all data sets, to the Si peak on the spectra from a reference virgin Si sample, using a multiplication factor of the energy scales. All the samples could be compared with the "same" beam energy. This alignment approach is in theory reasonable in view of the fact that the energy for scattering at the surface is dependant on the kinematic factor and the beam energy only. Complications with this alignment method arose however. The most significant problem was the lack of a perfectly definable position on each spectrum to align to the virgin. A

broadening of the Si peak at the base occurs due to Si isotopes, the system resolution, and any overlap of the Si peak with the dopant peak. This prevented the base of the Si peak from being used as a reference point for alignment. The gradient of the leading edge of Si peaks varies between samples, primarily because of a dilution for different oxide layer widths, causing a marginal error if a set height on the peaks was chosen. The best point on the spectra to align the peaks to was near the base but above the isotope tail. Even so there was a lack of reproducibility in this method and an error, estimated to be of up to 0.2 nm could be introduced.

A fitting routine developed at Daresbury laboratory that attempted to find the best fit of beam energy to the peaks was trialled but did not give sufficient reliability to be used routinely.

Finally it was concluded that the best solution was to deposit a very small amount of Au onto the surface of each sample using a k-cell evaporator. This was used as a reference to determine the beam energy, from the kinematic factor and the energy at the centre of the Au peak. The presence of considerably less than a monolayer of Au would have no appreciable affect on the rest of the spectrum. Using the k-cell could produce a consistent Au layer on each sample. Knowing the beam energy accurately for each sample meant that the relationship between the energy scale and scattering depth could be calculated, referenced to the actual beam energy used for each sample.

4.2.3.3 Numerical solution to depth scale

In order to utilise the knowledge of the beam energy a method of calculating the depth scales quickly was needed. A computer program was written to calculate these depth scales using numerical methods. There are important differences in principle compared to the surface approximation method, which uses a fixed rate of energy loss. The numerical method calculates the depth scale in a manner which mirrors the actual situation. Within the program the instantaneous rate of energy loss is calculated. The stopping power is given as a function of the beam energy by a third order polynomial (given in Figure 4.18) which gives an accurate fit to the values obtained from SRIM. Given the starting energy of the incident beam, the instantaneous rate of inelastic energy loss is calculated. After travelling a fixed distance (set at 0.1 nm), a reduced “beam energy” is calculated from the inelastic energy lost, and from this “beam energy” a new rate of inelastic energy loss is determined. From the path length the number of repeat cycles in the calculations is determined. Once at the scattering depth, the reduced “beam energy” is multiplied by the kinematic factor, to account for scattering. The same

iterative procedure is carried out on the exit path. This produces a final energy for scattering from some depth x. The program tabulates values of final energy against x, from x = 0 to a user defined value. A least squares fit of these values gives the relationship between energy and scattering depth. This method produces a relationship between energy and depth that is slightly non linear and the scattering depth is expressed as a second order polynomial function of the energy. A screen shot of the program and an example of an output file is given in Figures 4.19a) and b), respectively. The program can calculate the depth scale for any chosen scattering angles, mass of ion or target atom, and the beam energy specific to a particular data set. Depth profiles can be produced by applying the calculated conversion factor, in the bottom of Figure 4.19b), to the energy scale. An example of this conversion is given in Figure 4.20. The top of the figure contains an energy spectrum, which contains scattering off the Au marker, the implanted As, as well as off Si and O. Applying the conversion factor, which in this example is correct for As, gives the profile in the bottom of the figure. Obviously this is only appropriate for scattering off the As atoms, and this range of the profile is highlighted in red. The rest of the profile, illustrated by a dashed line, is meaningless on this depth scale and is normally removed.

a)

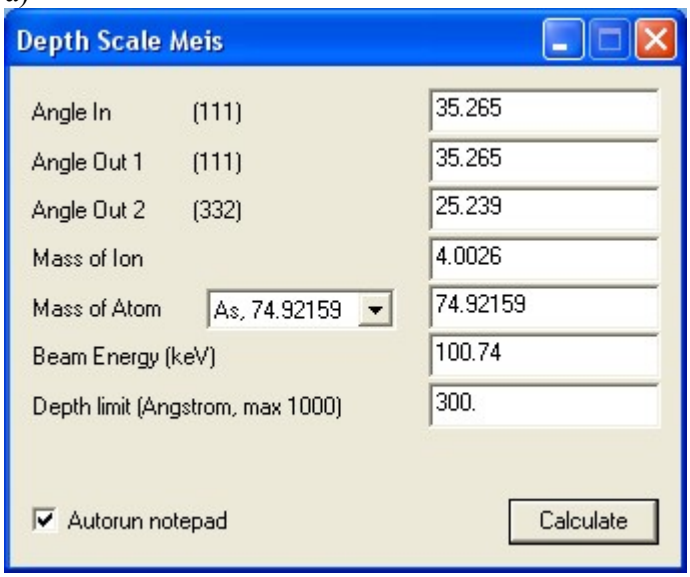

b)

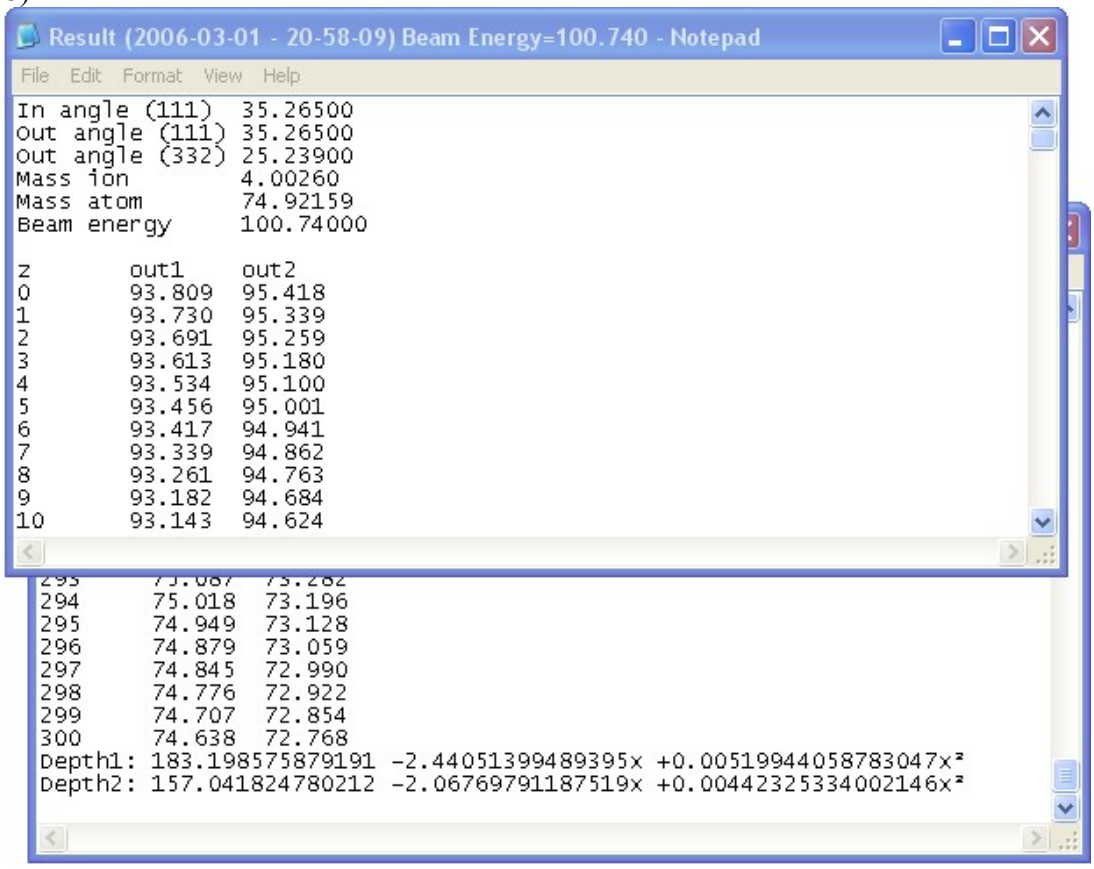

Figure 4.19 a) Screen shot of the depth scale program showing the variable input parameters. b) An example of the result of a calculation. The relationship between scattering depth and energy (x) for the two scattering angles is given at the bottom.

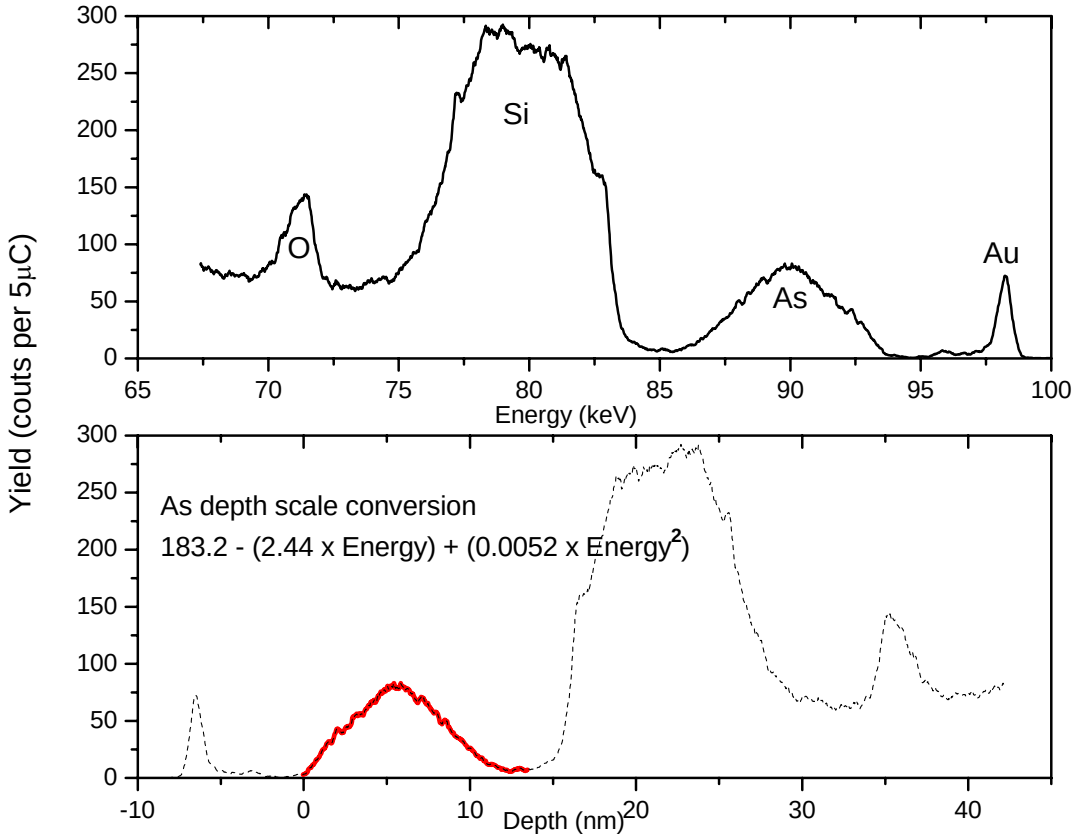

Figure 4.20 Example of conversion from an energy scale (top) to a depth scale (bottom). Depth scales are specific to individual elements. For this example only the As peak (in red) is correctly converted. The rest of the spectrum (dashed line) is effectively meaningless.

This depth scale calibration method matches the physical reality more closely than the surface approximation method. For that reason it represents an improvement over the surface approximation method. However the level of difference between the two methods was seen to vary only by about 2-3% over a depth of 10 nm and this confirms the validity of the surface approximation method. A plot of a 3 keV As as-implanted is shown in Figure 4.21 calibrated by the surface approximation and depth scale program showing the comparatively small difference between the methods.

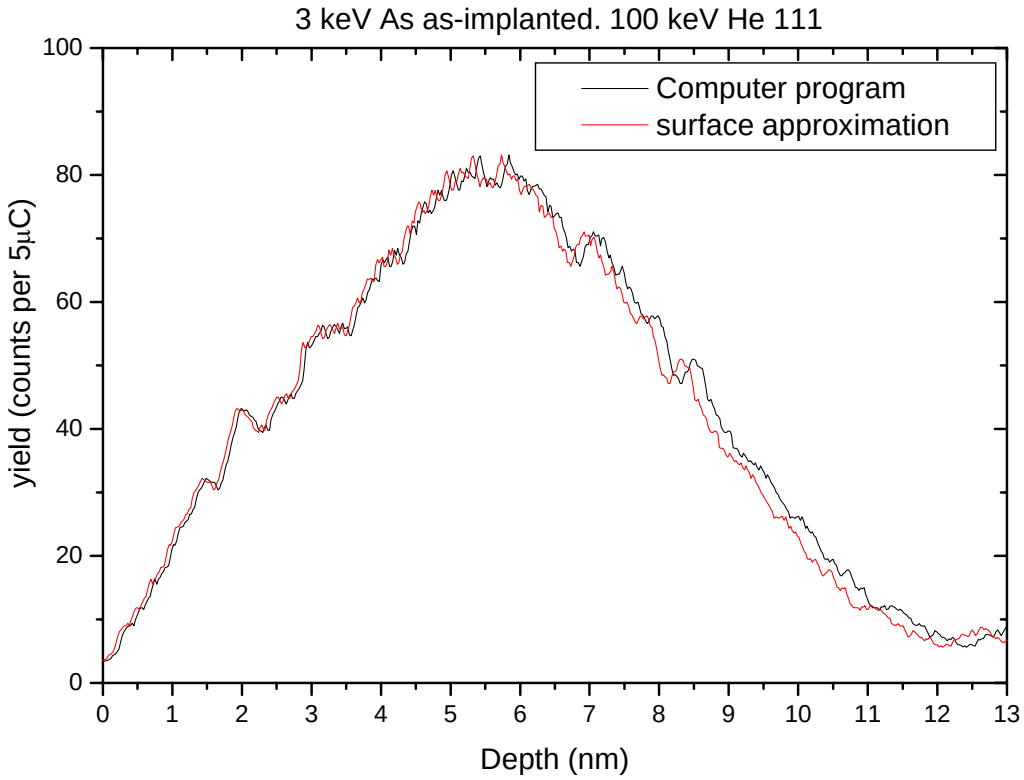

Figure 4.21 Example of the difference between depth spectra calibrated using the surface approximation method and the computer program for a 3 keV As as-implanted sample.

4.2.3.4 Changes to the data acquisition

It is worth noting that during the course of the project changes were made to the data acquisition system. The detection efficiency has been altered at different stages of the project. For this reason some of the random levels differ over time and are not directly comparable. An appropriate random level for the operating set up is used with all data in this thesis.

4.3 SIMS introduction and basic principles

SIMS is a surface analytical technique used in a wide range of experiments. This section contains a brief explanation of depth profiling using dynamic SIMS with particular attention to unusual aspects that cause deviations from the ideal profiles, referred to as SIMS artefacts. The technique operates by bombardment of the sample surface with a primary ion beam causing sputtering of particles, followed by mass spectrometry of the emitted secondary ions. Much of the SIMS used in this thesis was carried out at ITC – IRST, Trento, using a Cameca Wf SC Ultra instrument (36, 37).

SIMS experiments were also carried out at IMEC, Belgium, using an Atomika 4500 instrument in each case conditions for these experiments are described. Unless otherwise stated, the SIMS measurements presented in this thesis were carried out at ITC – IRST.

In a SIMS instrument an ion source is used to produce primary ions that are formed into a beam by an ion optical column. Often instruments have several different sources to allow a range of ions to be used. The most common primary beams to use are O_2^+, O^-, Ar^+, and Cs^+. Oxygen ion bombardment enhances the secondary ion yields of electropositive elements and produces more uniform erosion of the sample than inert gas bombardment. O_2^+ is the general purpose primary beam for semiconductor samples where sample charging is not a problem. For insulating samples when sample charging is a problem an electron flood gun can be used to neutralise the sample and sample charging can also be reduced using an O^- beam. A beam of Cs^+ ions is generally used for optimum sensitivity with electronegative elements (6). In the present studies Cs^+ has been used to profile As and F, while O_2^+ was used for profiling B (38, 39).

Ion optics allows the ions to be accelerated and focused into a small beam that can be rastered over an area of the sample. In these experiments a beam energy of around 4 – 6 keV was used, but the sample was biased to create an impact energy of 0.25 – 1 keV. The beam was rastered over an area of typically around 200 μm^2 and data recorded over an area of around 70 μm^2 depending on the particular experiment. Incidence angles of 44 – 76° were obtained in the Cameca, which depended on the impact energy. Normal incidence was used in the Atomika. Erosion rates of 0.2 – 0.9 Å/s were obtained (38, 39). Sputtered secondary ions are energy filtered. This is useful for removing interference of molecular species from an atomic species with the same mass. Secondary ions can then be mass analysed in a mass spectrometer before being detected. Either magnetic sector spectrometers or quadrupole analysers are used. Either positive or negative secondary ions can be monitored (6). Negative As and F ions and positive B ions were collected (38, 39).

The number of ions sputtered from the surface of the sample provides a means for measuring the composition of the sample. The sputtering yield is not linearly related to the concentration of an element present in a sample since the secondary ion yield varies with element (e.g. As or B), with changes to the matrix, (such as going from SiO_2 to Si) and varies with the primary bombarding species (6). The erosion rate is also not constant during the first couple of nm. Depth scales are often calibrated on the basis of the final crater depth measurement and assuming a constant erosion rate. The use of a

laser profilometer, for a dynamic depth scale assessment, i.e. at every stage of the developing depth profile the instantaneous actual depth is being determined, can in principle improve this situation. The non constant erosion rate leads to SIMS analysis being unreliable in terms of the concentration quantification and the depth scale in the first couple of nm. (6, 38, 39). These effects are evident with samples spectra shown in this thesis.

The collision cascade produces atomic mixing of the species within the subsurface region. Consequently when species are sputtered from the surface they may not have been occupying the sites at depths that they originally occupied in the unsputtered sample. Once an equilibrium situation is established, the implanted primary ions and collision cascade region are always present and move through the sample ahead of the analysed surface (6). This collisional mixing causes a broadening of the profile and limits the depth resolution obtainable. Using a lower impact energy produces a smaller collision cascade and this can improve the resolution. A reasonable agreement of the downslope of SIMS and MEIS profiles of As as-implanted samples has been found using the Cameca instrument for low impact energies (0.25 – 0.5 keV) and impact angles of around 45° suggesting that for these conditions collisional mixing effects were not appreciable (38, 39).

Comparison of SIMS results with MEIS results have been carried out to try and understand the best methods to quantify the SIMS data accounting for SIMS artefacts (40, 42). This took the form of optimising the calibration of the SIMS profiles. Dopant profiles were calibrated to different monitoring matrix species, and it was found that the SIMS profiles which were calibrated to the $^{29}Si_2^-$ monitoring species gave profiles with the best agreement between MEIS and SIMS. Even so, discrepancies occurred in the first 3 nm. It has been suggested that a shift to the depth scale needs to be applied to align the SIMS profiles to the MEIS ones. Work is continuing in this area.

In spite of the weakness of SIMS, the technique has significant strengths and offers useful comparisons with the MEIS results. SIMS can profile light elements for which the MEIS sensitivity is too low. The sensitivity to detect atoms of the order of 10^{16} at/cm^3 is much greater than MEIS. SIMS registers all of the atoms, whereas in MEIS, in the double alignment configuration, atoms in substitutional lattice sites are invisible to the analysing beam. This provides an interesting comparison of the techniques and gives information as to the fraction of dopant atoms that have taken up substitutional positions. The depth range is also much greater with SIMS than that of

MEIS, using the scattering conditions typical in this project, and this again is useful for studying the diffusion of dopant deeper into a sample.

4.4 Other analysis techniques used

4.4.1 X-ray techniques

A variety of X-ray techniques have been used at the ID01 beamline at the ESRF in comparison with the MEIS and SIMS studies, providing interesting additional information. The techniques are described in more detail in (9, 41, 46, 47) and are only briefly covered here.

Conventional X-ray diffraction (XRD) is sensitive to the strain distribution of the crystalline part of the Si wafer in the direction perpendicular to the sample surface. The scattering contrast is obtained from the interference of the scattering amplitudes from the stack of deformed crystalline layers in the sample. The interference fringes appear on both sides of the Bragg peak. The position, periodicity and contrast of such fringes are determined by their strain and thickness (9, 46). In this project XRD was used to study solid phase epitaxially regrown layers (9, 41).

X-ray specular reflectivity (SR) measurements, are sensitive to the electron density distribution, perpendicular to the sample surface, independent of the sample being crystalline or amorphous (9, 47). SR measurements have been used to study the distribution of As, including segregation under the oxide (9).

4.4.2 TEM

A small amount of cross sectional transmission electron microscopy (XTEM) was carried out. TEM utilises the wave-like nature of electrons to view the internal structure of samples in a manner akin to that of an optical light microscope, yet with a resolution several orders of magnitude higher than that of the optical microscope (49). Through the use of cross-sectional TEM (XTEM), it is possible to image and characterise the damage following ion implantation and annealing. XTEM was carried out on a sample at the University of Salford. The sample was prepared by creating a glued, sandwiched stack of silicon, with two pieces of the sample to be imaged at the centre of the stack and the surfaces of interest glued together. From this stack, a long cylindrical stack was cut and glued into a copper cylinder which was then in turn cut into thin disks. Both sides of a disk were polished and dimpled using finer and finer grades of diamond paste until the centre of the disk was thinned to a thickness of approximately 15-20 μm. The sample was ion beam milled using Ar ions at an energy

of 3.5 keV until the sample was electron transparent. The sample was imaged in a JEOL 3010 TEM, operating at 300 keV. Images were taken in down-zone bright-field conditions. Additionally energy filtered transmission electron microscopy (EFTEM) was carried out on selected samples at CNR-IMM Catania (Italy). In EFTEM, transmitted electrons are subject to energy filtering, providing the possibility of elemental specific contrast.

4.4.3 Electrical measurements

Some Hall effect electrical measurements were carried out, using the van der Pauw technique (7, 8, 45). From this technique, the sheet resistance R_s, the sheet carrier density n_s, and the mobility μ, can be determined, using a combination of resistance and Hall effect measurements. A very simple description of the technique is given here.

The sheet resistance of a sample can be determined from several measurements of voltage and current across the sample, in a set up illustrated in Figure 4.22a). A dc current is applied between two terminals on one side and the voltage is measured across the opposite side. This leads to a characteristic Resistance R_A. The same types of measurement are carried out using terminals rotated by 90° rotation, giving resistance R_B. The sheet resistance can be obtained from the equation:

$$\exp\left(-\pi R_A / R_s\right) + \exp\left(-\pi R_B / R_s\right) = 1 \qquad (4.11)$$

To determine the activated concentration, Hall voltage measurements are required. To measure the Hall voltage V_H a current is applied between an opposing pair of contacts and a constant magnetic field is applied perpendicular to the plane of the sample, as shown in Figure 4.22b). The Hall voltage V_H is measured across the remaining pair of contacts. The sheet carrier density n_s can be calculated using:

$$n_s = IB / qV_H \qquad (4.12)$$

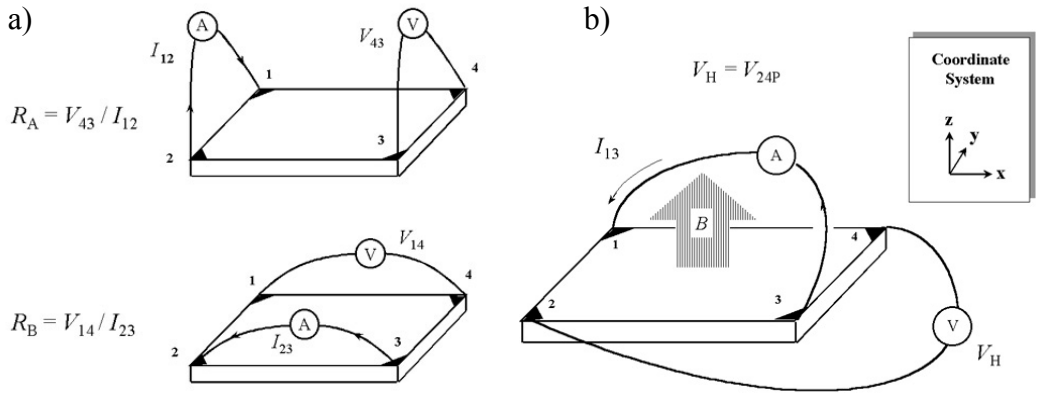

Figure 4.22 Set up for van der Pauw measurements. From (45).

4.5 Sample production

Samples have been implanted using an Applied Materials Quantum LEAP implanter (12) at AMD Dresden and Applied Materials (UK). Some samples and have also been implanted at Salford University using the ultra low energy (ULE) implanter (11). The principle behind the two implanters is the same and the Salford implanter is described here in section 4.5.1. Major differences between them are the size of sample that can be implanted and sample throughput. The implanter at Salford is a research tool and can only implant small samples of approximately 12 × 12 mm. The Applied implanter is a manufacturing tool and hence wafers of 200mm or 300mm diameter were implanted. Unless otherwise stated, the implants used in this thesis were implanted at AMD. Annealing was carried out at Salford University using an Steag AST 10 RTP system, and at AMD using an Applied Materials RTP Radiance system. These are both lamp based tools.

4.5.1 Salford Ultra Low Energy Implanter Laboratory

A schematic of the ULE implanter (11) is shown in Figure 4.23. The beamline consists of three electrically isolated sections; the ion source, beam transport, and target chamber. Two Applied Materials ion source assemblies are located symmetrically about a mass analysing magnet. The ion sources used are the Bernas type, fitted with ovens for solid source materials and also several gas inputs. The sources have a triode extraction system, with adjustable gap and lateral alignment, which can adjust the profile of the beam.

Beams are selected by focusing them through an adjustable mass resolving slit located beyond the mass analysing magnet. Any neutrals present in the beam are removed in a second magnet used to bend the beam through 5 º or 90 º into one of two target chambers. For implantation the target chamber is used. The system comprises of five stages of differential pumping so that pressures of ~ 10^{-8} mbar are maintained in the target chambers while the sources operate at ~ 10^{-4} mbar. In the target chamber used for the implants is a target mount attached to a precision goniometer with one rotational and three directional degrees of freedom. At the final stage a low fill factor deceleration lens is located directly in front of the target. The lens allows beams to be transported at higher energies (5 – 15 keV) before being decelerated at the target to energies as low as 20 eV. This set up is called accel – decel mode, also referred to as retard mode. Alternatively the transport and target sections may be electrically coupled so that ions

remain at the extract ion energy throughout the entire length of the beam line for higher energy implants. This is called the drift mode.

The UHV part of the system comprises of the target chamber, a sample preparation chamber, and a loadlock chamber which can be quickly vented to air allow the vacuum in the target chamber to be maintained while allowing fast transfer of samples. Silicon samples of up to 12 × 12 mm are mounted into sample holders, and are transported between chambers by transfer rods. The preparation chamber and the loadlock both contain a carousel for storing up to six samples. The target chamber is also equipped with X-ray gun, electron gun and electron energy analyser for in situ XPS and AES analysis.

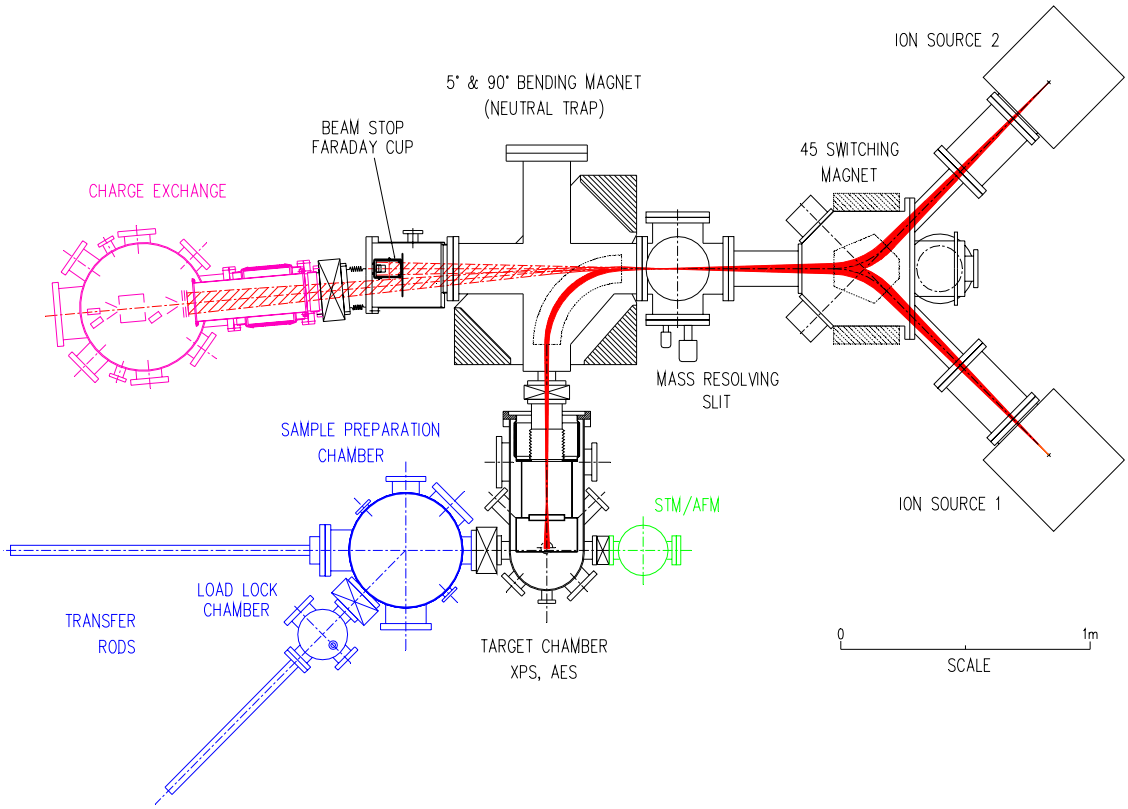

Figure 4.23 – Salford ultra low energy ion beam system.

4.5.2 Annealing equipment

Most samples were annealed in a lamp based RTP system. Halogen lamps mounted above and below were capable of producing ramp rates of typically 25 – 70 °Cs^{-1} Wafers were mounted on a quartz holder. For samples annealed at Salford, small samples were placed onto an 8" wafer in the annealer. Samples were annealed in

an N_2/O_2 environment to maintain an oxide layer to prevent dopant loss. This resulted in some oxide growth for certain annealing conditions.

References

1 J.F. Van der Veen, Surf. Sci. Rep., **5**, Nos. 5/6, 1985.

2 R.M. Tromp, Medium Energy Ion Scattering. In: Briggs D. and Seah P. editors. Practical surface analysis. Volume 2 – Ion and Neutral Spectroscopy. 2nd ed. John Wiley Ltd. 1992.

3 http://www.dl.ac.uk/MEIS/ (accessed 11/2/06).

4 Backscattering Spectrometry, W. K. Chu, J. W. Mayer, M. Nicolet, Academic Press, New York, 1978.

5 Fundamentals of surface and thin film analysis, L.C. Feldman, J. Mayer, North-Holland, 1986.

6 Methods of Surface Analysis. Techniques and Applications. Edited by J.M. Walls. Cambridge University Press, 1989.

7 L.J. van der Pauw. Philips Tech. Rev. Vol 20, (1958), p220.

8 Electronic Materials Science For Integrated Circuits in Si and GaAs. J.W. Mayer, S.S. Lau. Macmillian Publishing Company, 1990.

9 L. Capello, PhD thesis. Structural investigation of silicon after ion-implantation using combined x-ray scattering methods. University of Lyon (France) and Torino (Italy), 2005.

10 http://www.esrf.fr/UsersAndScience/Experiments/SurfaceScience/ID01/ (accessed 11/2/06).

11 R. D. Goldberg, D. G. Armour, J. A. van den Berg, N. Knorr, H. Ohno, S. Whelan, S. Zhang, C. E. A. Cook, and M. A. Foad, Rev. Sci. Instr. 71 (2) (2000) 1032

12 http://www.appliedmaterials.com/products/Quantum.html?menuID=1_10_1 (accessed 11/2/06).

13 P. Bailey, T.C.Q. Noakes, C.J. Baddeley, S.P.Tear, D.P.Woodruff, Nucl. Instr. and Meth. **B** 183 (2001) 62.

14 M. Copel, R.M. Tromp. Surface. Sci. Lett. 337 (1995) L773.

15 D.P.Woodruff, D. Brown, P.D. Quinn, T.C.Q. Noakes, P. Bailey. Nucl. Instr. and Meth. **B** 183 (2001) 128.

16 T. Gustafsson, H.C. Lu, B.W. Busch, W.H. Schulte, E. Garfunkel. Nucl. Instr. and Meth. **B** 183 (2001) 146.

17 J. A. Van den Berg, D. G. Armour, S. Zhang, S. Whelan, and H. Ohno, T.-S. Wang, A. G. Cullis, E. H. J. Collart, R. D. Goldberg, P. Bailey, T. C. Q. Noakes. J. Vac. Sci. Tech. B 20 (2002) 974.

18 J. Kim, W.N. Lennard, C.P. McNorgan, J. Hendriks, I.V. Mitchell, D. Landheer, J. Gredley. Current Appl. Phys. 3 (2003) 75.

19 H.C. Shin, S.K Oh, H.J. Kang, H.I. Lee, D.W. Moon. Current Appl. Phys. 3 (2003) 61.

20 http://www.srim.org/ (accessed 11/2/06)

21 W. H. Bragg and R. Kleeman, Philos. Mag., 10, 318 (1905)

22 F. H. Eisen, G.J. Clark, J. Bøttiger, J.M.Poate, Radiat. Eff. 13 (1972) 93.

23 G. de M. Azevedo, M. Behar, J.F. Dias, P.L. Grande, D.L.da Silva. Phys. Rev. **B** 65 (2002) 075203.

24 F. Cembali, F. Zignani, Radiat. Eff. 31 (1977) 169.

25 D.V. Morgan (editor). Channelling Theory, Observation and Applications, John Wiley and sons, London, 1973.

26 G. Moliere, Z. Naturforsch. 2a, 1947, 133.

27 I. Stensgaard, L.C. Feldman and P.J. Silverman. Surface. Sci. 77 (1978) 513

28 R.G. Smeenk, R.M. Tromp, H.H. Kersten, A.J.H. Boerboom, F.W. Saris. Nucl. Inst. and Meth. 195 (1982) 581.

29 R.M. Tromp, M. Copel, M.C. Reuter, H. Horn von Hoegen, J. Speidell, R. Koujis. Rev. Sci. Instr. 62 (1992) 2679.

30 P.M. Zagwijn, A.M. Molenbroek, J. Vrijmoeth, G.J.Ruwiel, R.M. Uiterlinden, J. ter Horst, J. ter Beek, J.W.M. Frenken. Nucl. Inst. and Meth. B 94 (1994) 137.

31 J.A. van den Berg, S. Zhang, S. Whelan, D.G. Armour, R.D. Goldberg, P. Bailey, T.C.Q. Noakes. Nucl. Inst. and Meth. B 183 (2001) 154.

32 G. Konac, S.Kalbitzer, Ch. Klatt, D. Niemann, R. Stoll. Nucl. Instr. and Meth. B 136 – 138 (1998) 159.

33 W.N. Lennard, G.R. Massoumi, T.W. Simpson, I.V. Mitchell, Nucl. Instr. and Meth. B 152 (1999) 370.

34 N.P. Barradas, C. Jeyes, R.P. Webb, E Wendler. Nucl. Instr. and Meth. B 194 (2002) 15.

35 W.N. Lennard, H. Xia, J.K. Kim. Nucl. Instr. and Meth. B 215 (2004) 297.

36 http://www.itc.it/irst/Renderer.aspx?targetID=185 (accessed 11/2/06).

37 http://www.cameca.fr/ (accessed 11/2/06).

38 M. Anderle, M. Barozzi, M. Bersani, D. Giubertoni, P. Lazzeri, Characterisation and Metrology for ULSI Technology: International Conference. AIP Proceedings 683. (2003) p695.

39 D. Giubertoni, M. Barozzi, M. Anderle, M. Bersani. J. Vac. Sci. Tech. B 22 (2004) 336.

40 D. Giubertoni, M. Bersani , M. Barozzi, S. Pederzoli, E. Iacob, J. A. van den Berg, M. Werner. To be published in Proceeding of SIMS XV conference.

41 L. Capello, T.H. Metzger, M. Werner, J.A. van den Berg, M. Servidori, M. Herden, T. Feudel. Mat. Sci. Eng. B 124-125 (2005) 200.

42 W. Vandervorst, T. Janssens, B. Brijs, T. Conard, C. Huyghebaert, J. Fruühauf, A. Bergmaier, G. Dollinger, T. Buyuklimanli, J.A. VandenBerg, K. Kimura, Appl. Surface. Sci. 231–232 (2004) 618–631.

43 P. Bailey, T.C.Q. Noakes, D.P. Woodruff. Surface. Sci. 426 (1999) 358.

44 Y. Hoshino, S. Semba, T. Okazawa, Y. Kido. Surface. Sci. 515 (1999) 305.

45 http://www.eeel.nist.gov/812/hall.html (accessed 28/02/06).

46 M. Servidori, F. Cembali, S. Milita, Characterisation of lattice defects in ion-implanted Si in X-ray and Neutron dynamical diffraction: Theory and Application, A. Autiers, S. Lagomarsino, B.K. Tanner and R. Colella Editors, (Plenum Press, New York, 1996).

47 U. Pietsch, V. Holý, T. Baumbach, High-Resolution X-ray Scattering from Thin Films and Lateral Nanostructures, (Spinger, Berlin, 2004).

48 Private communication. P Bailey.

49 Transmission Electron Microscopy—A Textbook for Materials Science D. B. Williams and C. B. Carter 1996. Plenum Press, New York and London.

Chapter 5 – Damage accumulation and dopant migration during shallow As and Sb implantation

5.1 Introduction

The studies described in this chapter are concerned with the mode of formation of amorphous layers in As and Sb implanted Si. Above the displacement threshold ion implantation results in the production and build up of disorder or complete amorphisation of the Si lattice in the implant region, depending on implant conditions such as dopant ion mass, flux, fluence and implant temperature (1, 2). The mechanisms responsible for the formation of a continuous amorphous phase have been investigated in considerable detail at medium and high bombardment energies (1-10) and two main types of models based on either homogeneous or heterogeneous nucleation of the amorphous phase have been proposed for different implant conditions (see also sections 3.2.2.4 and 3.2.2.5). Under light ion bombardment its growth is generally well explained in terms of homogeneous nucleation of the amorphous phase, once a critical defect density is exceeded (1, 3-6). On the other hand, for heavy ion bombardment in which the energy deposition rates are much higher, heterogeneous nucleation of the amorphous phase occurs either through disorder accumulation of overlapping collision cascades or within a single collision cascade (1, 7-10).

However, later studies that also used medium and high energy ion beams and were carried out at implant temperatures well above room temperature, for which dynamic annealing becomes significant, have demonstrated the occurrence of amorphisation or recrystallisation depending on the balance between dose rate and bombardment temperature (1,2, 11-13). Under these conditions amorphisation is considered to be nucleation limited and may, for example, be mediated by secondary defects (14). Nucleation of the amorphous phase may also occur at pre-existing amorphous crystalline interfaces and surfaces and results in the planar growth of the amorphous layer (14-16). These processes are thought to involve the migration of mobile defects (e.g. interstitials, vacancies), annihilation and / or trapping at a nucleation centre (17, 18).

Recent studies of the damage formation for low energy (~1 keV) shallow B implants in Si carried out at room temperature, using MEIS (19, 20) have shown that the growth of the damage depth distribution is quite unlike the energy deposition function, as was previously observed for higher energies and elevated temperatures (16). The

damage evolution behaviour observed is strongly influenced by, on the one hand, the proximity of the surface, that acts as a nucleation centre for a fraction of the interstitials produced along the collision cascade and on the other by the operation of dynamic annealing effects even at room temperature. These cause a substantial reduction in the disorder at depths where the interstitial and vacancy distributions, which for low energies are closely overlapping, have their maxima.

The work reported here consists of a detailed MEIS study of the mode of damage evolution as a function of implant dose and its correlation with dopant movement for 2.5 keV As and 2 keV Sb ions implanted into Si at room temperature to doses from a few times 10^{13} cm^{-2} upwards.

It will be seen that for both As and Sb ion implantation, the energy deposition rate is sufficiently high for the Si matrix to become amorphised at room temperature for doses above 10^{14} cm^{-2}. This study exploits the ability of MEIS to provide quantitative information on either the As or Sb implants and the Si damage depth distributions. MEIS shows the operation at room temperature of a damage accumulation process for low doses that is explained in terms of interstitial trapping at pre-existing nucleation sites formed by the oxide / Si crystal interface and the planar growth of the amorphous layer from the surface inwards into the bulk through the accumulation of point defects produced in the collision cascade. In particular, this work shows a novel dopant movement correlated to the growth of the amorphous layer that is driven by differences in the energetics of accommodation of these heavy ions in damaged crystalline and amorphous Si.

5.2 Experimental

Implants of 2.5 keV As ions into Cz, p-type Si (100) samples of resistivity 10 – 20 Ω cm were performed under UHV conditions using the ultra-low energy ion implanter at Salford (21). Sb implants at 2 keV, were carried out in p-type (100) Si wafers of resistivity of 2– 10 Ω.cm at Applied Materials. In all cases the targets were held at room temperature and all implants were performed through the native oxide.

The MEIS studies reported were carried out using a nominally 200 keV He ion beam and the double alignment configuration, in which the $[\bar{1}\,\bar{1}\,1]$ channelling direction was combined with the [332] and [111] blocking directions. Using a 200 keV He beam, sufficient separation of the dopant and Si peaks could be obtained for the [332] blocking direction. Results from the [332] direction only are presented here. The overall depth resolution obtained for these conditions was better than 0.7 nm (20). Energy spectra

acquired were converted into damage depth distributions in terms of number of displaced Si atoms or dopant atoms cm^{-3}, using a standard calibration procedure (22). The backscattered ion yield was referenced to the random level measured on a Si sample, amorphised by high dose self ion bombardment. In addition the energy scales were converted into depth scales using established inelastic energy loss data (23) and applying the surface approximation (22, 24). Implanted As / Sb and displaced Si distributions can be detected down to levels of ~ 1×10^{19} cm^{-3} and 10^{21} cm^{-3}, respectively.

Additional SIMS As profiles were obtained in an Atomika 4500 instrument at IMEC using a 0.5 keV 0_2^+ primary beam at normal incidence. In these measurements a crater size of 250 μm was used and mass Si^{30} was monitored to ensure a better than 1% current stability. Depth scale calibration relied on a constant ion beam current and was performed using the erosion rate obtained on one deep crater in combination the erosion time for each crater. Relative sensitivity factors (RSF, from implant standard) were repeatable within 1%.

5.3 Results and discussion

Considering first the damage evolution during As ion bombardment, a series of Si samples was implanted through the native oxide with 2.5 keV As ions to doses ranging from 3×10^{13} to 1.8×10^{15} cm^{-2}. The dose dependence of the MEIS spectra obtained for these samples is shown in Figure 5.1. Peaks resulting from the As implant, the displaced Si atoms and the oxide, respectively, are indicated in the figure. For comparison Figure 5.1 also contains the spectrum for a virgin Si sample as well as a random spectrum. The virgin Si sample shows two peaks due to scattering off Si (edge at 171 keV) and O atoms (edge at 153 keV) both contained in the native oxide. The thickness of the native oxide thickness is calculated as ~1.5 nm. It should be noted however that in the case of the Si peak there is also a contribution from disordered Si atoms at the oxide / Si interface (19, 25). The virgin spectrum is the base against which any additional backscattering from displaced Si atoms that results from the As implant is measured. The figure shows the changes in the energy spectrum in terms of the growth of the As and Si scattering peaks for increasing As implant dose. It is seen that the Si damage peak and also the As peak, spread towards lower energies, i.e. greater depths, although the movement of the latter is less pronounced.

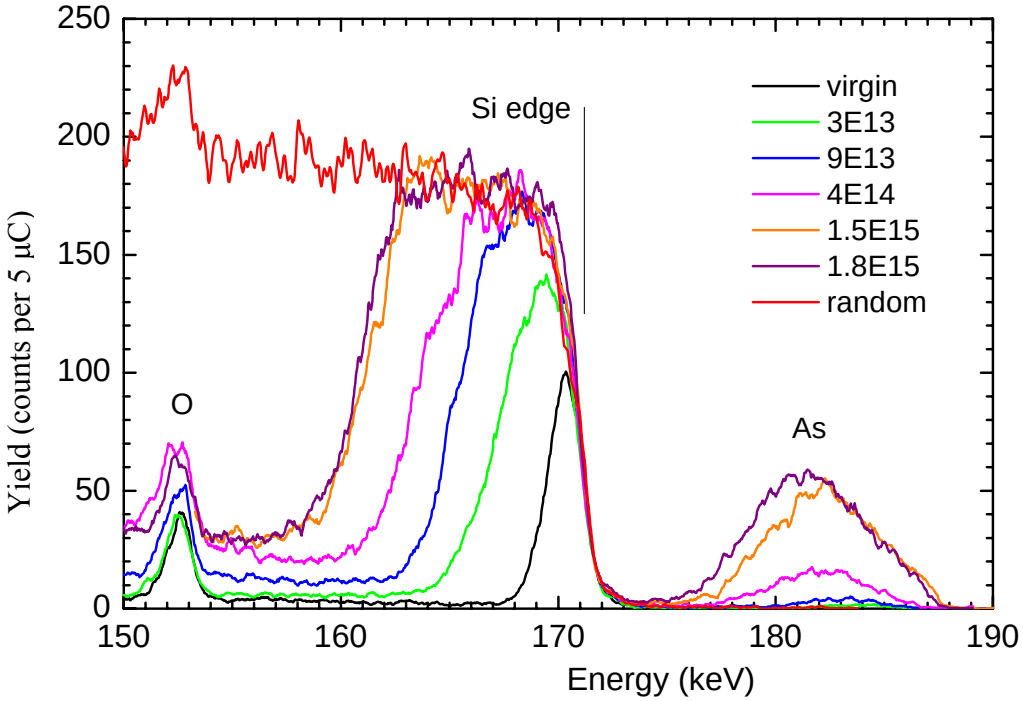

Figure 5.1 MEIS energy spectra showing the growth of the Si damage and As dopant yield as a function of fluence for 2.5 keV As^+ ion implantation into virgin Si at room temperature.

This development of these peaks is more clearly visible after conversion of the spectra to the depth profiles of As and of displaced Si atoms. The results are shown in Figure 5.2. The use of logarithmic concentration scales in these profiles depicts more clearly the effects of the As implant dose changes that cover nearly two decades. The depth profiles of the displaced Si atoms (top) were obtained after subtraction of the virgin surface peak (shown separately in the figure) and hence represent the distributions of the additional damage after each implanted As dose. The common depth scale illustrates the correlation between implant and displaced Si. The evolution of these two sets of peaks shows an unexpected behaviour for both the growth of the damage and the accumulation of the dopant.

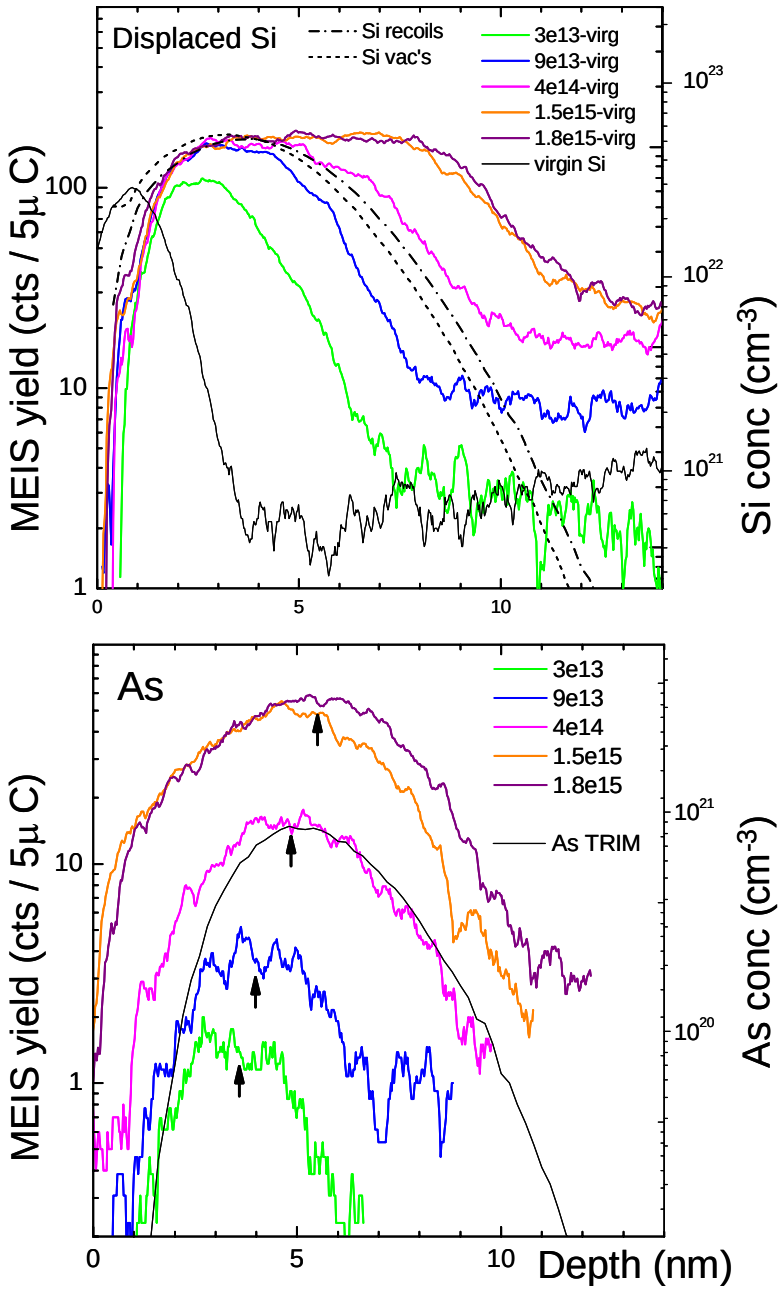

Figure 5.2 Depth profiles of displaced Si and As implant atoms obtained from the MEIS energy spectra in Figure 5.1. TRIM calculated Si vacancy and recoil distributions and the As implant profile are shown for comparison. The dose dependent peak position of the As implant is indicated by arrows.

Starting with the As range distributions (bottom), TRIM (26) calculations show that the maximum of the As profile in a pure Si matrix is expected to occur at a depth of approximately 5 nm (R_p = 5.5 nm) and hence its maximum range (~3 × R_p,) and associated damage might extend to ~16 nm. The TRIM calculated profile is shown adjacent to that measured by MEIS after an As dose of 4 × 10^{14} cm^{-2}. At or above this dose the agreement is very good for depths greater than R_p. Since TRIM provides

essentially a "zero dose" profile in a randomised solid, agreement with a low dose implant profile may be expected, provided that the Si matrix is amorphised. Figure 5.1 shows that this is the case for doses above 9×10^{13} cm^{-2}, as evidenced by the Si damage peak reaching random level close to the surface, however this is not the case for the lowest dose investigated of 3×10^{13} cm^{-2}.

The development of depth profiles of displaced Si in Figure 5.2 suggests that the Si damage build up involves two distinct phases that partly overlap, i.e. an initial growth of disorder near to the oxide /Si interface until a ~4 nm wide amorphous layer centred at a depth of ~3.5 nm is completed, followed by the planar growth of the amorphous layer from the surface inwards, until for doses above 1.5×10^{15} cm^{-2} the amorphous layer approaches a saturation depth of ~10 nm. The increase in the thickness of the amorphous layer also causes the dechannelling level to rise, as is seen in Figure 5.1. The observed damage evolution behaviour cannot be explained in terms of the heterogeneous nucleation model of amorphous phase formation at room temperature (7-10). In this model the energy deposition in the collision cascade is sufficiently dense to produce small amorphous zones (either in a single collision cascade or via cascade overlap) and these zones once they spatially overlap at a certain dose, effect a lattice phase change. Accordingly, the build up of displaced atoms would be expected to follow the shape of the energy deposition function as is given by vacancy and interstitial profiles produced by the implant ion. These profiles, again calculated by TRIM, are added to the top of Figure 5.2 showing the Si damage distributions, using arbitrary units but the same logarithmic scale. The two profiles are spatially close together and have their maxima at shallower depths than the TRIM calculated As profile in the bottom of Figure 5.2, as expected. It is clear that the growth of the disordered / amorphous Si layer does not coincide with the maximum in the energy deposition rate; in fact the damage profile for the lowest As implant dose is appreciably shallower than the calculated profiles. It appears that for a shallow As implant, initially at low doses, a highly damaged/amorphous 4 nm wide (FWHM) near-surface layer builds up, nucleated at the oxide/Si interface. No deeper damage is observed at this stage and this suggests that a fraction of the point defects produced at greater depths annihilate in dynamic annealing processes during the cascade. This behaviour is similar to that observed in previous MEIS studies for ULE B^+ implants into Si (19, 20) which showed the development of a 3–4 nm wide near-surface, highly damaged/amorphised layer, independent of implant energy up to 2 keV at room temperature. The formation of this layer was ascribed to the action of the oxide / Si interface as a sink for interstitials that are generated along the

collision cascade and are mobile at room temperature, in combination with the operation of dynamic annealing. The migration and trapping of these point defects at the oxide interface is the origin of the formation of the amorphous, near-surface damage layer. A similar process in which the surface represents a trap capturing interstitials (of which there is an excess over vacancies (27)), can also explain the formation of the damage layer observed for the case of the low dose, low energy As implants. In this early stage amorphisation will be nucleation limited (14, 16). At a later stage in the process, the planar growth of the amorphous layer into the underlying bulk material is observed. This phenomenon is due not only to the accumulation of mobile interstitials originating from greater depths at the advancing amorphous/crystalline interface, but also to the expansion of disordered regions due to the increasing density of coverage of the Si crystal matrix by the growing number of collision cascades that ultimately overlap. The type of planar growth seen here at room temperature has also been observed at elevated temperatures in studies of amorphisation / recrystallisation of the Si matrix under higher energy ion bombardment (11, 14-16). Similar processes to those described above were considered to be responsible for the planar growth.

Considering next the development of the As profile and its correlation with the displaced Si distribution, Figure 5.2 shows that at doses below 1×10^{14} cm^{-2} the implanted As profile is significantly shallower than the TRIM calculated one which is also drawn in the figure. However for increasing doses the As profile peak shifts to greater depths, from 3.6 nm at 4×10^{14} cm^{-2} to 5.5 nm for 1.8×10^{15} cm^{-2}, as indicated by the arrows in the figure. At the same time the As profile broadens towards the surface, as is clearly visible for doses of 4×10^{14} cm^{-2} and above. The latter behaviour can be explained on the basis of range shortening due to the changing composition of the matrix through As accumulation, collisional redistribution and / or collective mass flows to take account of the accommodation of the implanted ions. Sputtering can be largely ignored, as a TRIM calculation shows that 2.5 keV implanted to a dose of 1.8×10^{15} cm^{-2} causes the removal of less than 0.3 nm oxide. The incident ions will of course cause disorder to the native oxide which remains unnoticed by MEIS. Figure 5.2 clearly shows that the movement of As to greater depth with increasing dose occurs in parallel with the planar growth of the amorphous layer. This indicates that the two effects are closely related. On the basis of ballistics arguments, there is no doubt that a substantial fraction of the As is initially stopped beyond the amorphous /crystalline interface.

Since MEIS does not detect any clear presence of As at these depths, the possibility of the dopant having moved into substitutional positions and therefore being

no longer "visible" in MEIS has to be considered. This was checked in a control experiment using SIMS in which all As present is detected. Figure 5.3 shows the SIMS depth profiles, all taken under identical sputter erosion conditions, for As implanted to a dose of 8×10^{13} cm^{-2} into a virgin Si crystalline sample and to doses of 5×10^{13} cm^{-2} and 1×10^{14} cm^{-2} into a self-ion pre-amorphised Si sample. Although for shallow implants SIMS may give rise to small peak shifts, these will be the same in all these cases. The TRIM calculated As profile is again included for reference. The approximate peak positions for the two cases are indicated by arrows. It is clear that there is a good agreement between the As implant and the TRIM calculated profile, as would be expected. Significantly however, the SIMS results shows a clear shift "inwards" by ~1 nm of the maximum of the distribution, for the implant into the crystalline compared to the ones into the pre-amorphised Si sample. This corroborates the MEIS evidence and confirms that the shallower As peak observed for low implant doses for which the Si matrix is not yet fully amorphised is real. The effect of ion beam mixing limited resolution of SIMS is likely to cause the tail on the SIMS profiles in Figure 5.3 beyond the TRIM profile.

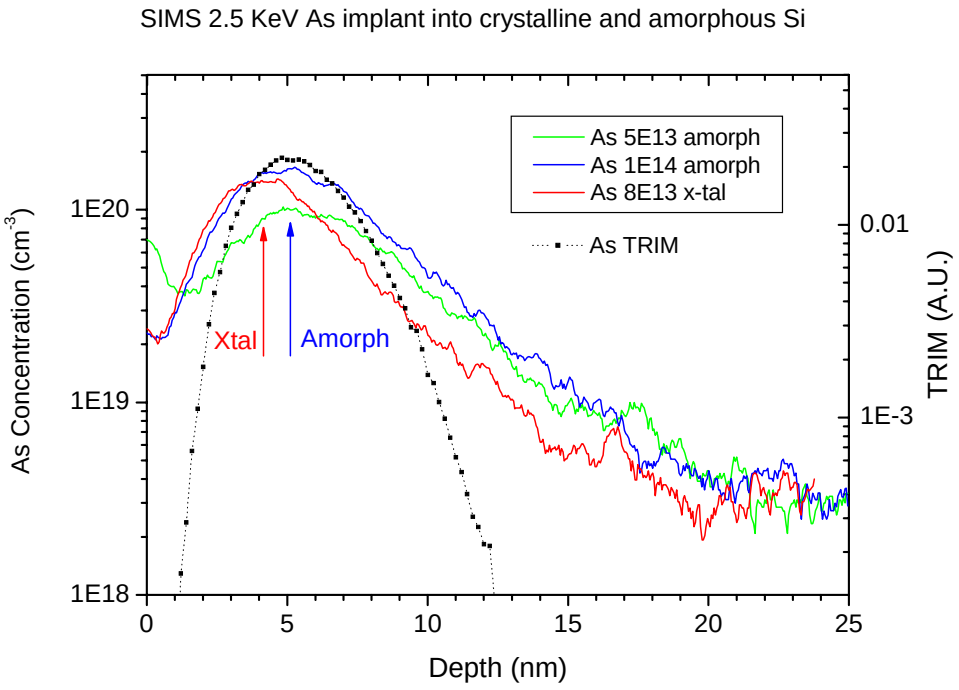

Figure 5.3 SIMS depth profiles taken under identical sputter erosion conditions, for As implanted to a dose of 8×10^{13} cm^{-2} into a virgin Si crystalline sample and to doses of 5×10^{13} cm^{-2} and 1×10^{14} cm^{-2} into a self-ion pre-amorphised Si sample. The TRIM calculated As profile is shown for comparison

The above observation by MEIS of the correlation between the planar growth of the amorphous layer and the movement of the As peak to greater depth with increasing dose, implies that most of the dopant that initially came to rest beyond R_p, migrates towards, on average, shallower depths, back into the growing, highly disordered/ amorphous layer in which it is more readily accommodated than in the still crystalline material. This movement is possibly initiated or occurs during the quenching stage of the cascade and is likely to be point defect mediated.

The combined damage evolution and dopant movement behaviour observed for shallow As implants is, in most respects, replicated for the even heavier Sb ion, implanted at 2 keV into Si at room temperature. Sb with a mass of 121 amu compared to As 75 amu, is expected to show reduced straggle and should in principle give better defined implant profiles. Whereas As is believed to diffuse either through an interstitial or vacancy assisted mechanism, Sb diffuses exclusively through the latter (28).

Figure 5.4 shows the dependence of the MEIS spectra on the Sb dose, over the range from 1×10^{14} cm^{-2} to 5×10^{15} cm^{-2}. All implants were again carried out at room temperature. As before the spectrum for the virgin Si surface and the random spectrum are shown for reference and the peaks due to scattering off implanted Sb, surface Si and O are marked. The expected reduced straggling shows itself in the steeper down slope of the deep edge of the Sb implant profile compared to the equivalent region of the As profile shown in Figure 5.1. The development of the Sb scattering peak as a function of dose indicates a peak shift to greater depths, similar to that seen for As. The lowest implanted Sb dose of 1×10^{14} cm^{-2} has already produced a fully amorphised near surface layer as demonstrated by attainment of the Si random level in the MEIS peaks. For increasing Sb dose this layer shows a planar growth to greater depth, again akin to that found above for As. The growth in width of the near-surface amorphous layer also causes the increased dechanneling level seen in the spectra for high Sb doses. For the highest dose of 5×10^{15} cm^{-2} a dilution of the Si peak is observed that manifests itself in a dip in the displaced Si signal. This is caused by the unusual growth of the oxide thickness, in combination with the high Sb concentration. The oxide layer grows from a width of 2 nm at a dose of 3×10^{15} cm^{-2} to 4 nm at 5×10^{15} cm^{-2}. This observation and other MEIS results (not shown) appear to indicate that a high Sb implant concentration at shallow depths promotes the growth of the oxide layer to depths well beyond that of the native oxide.

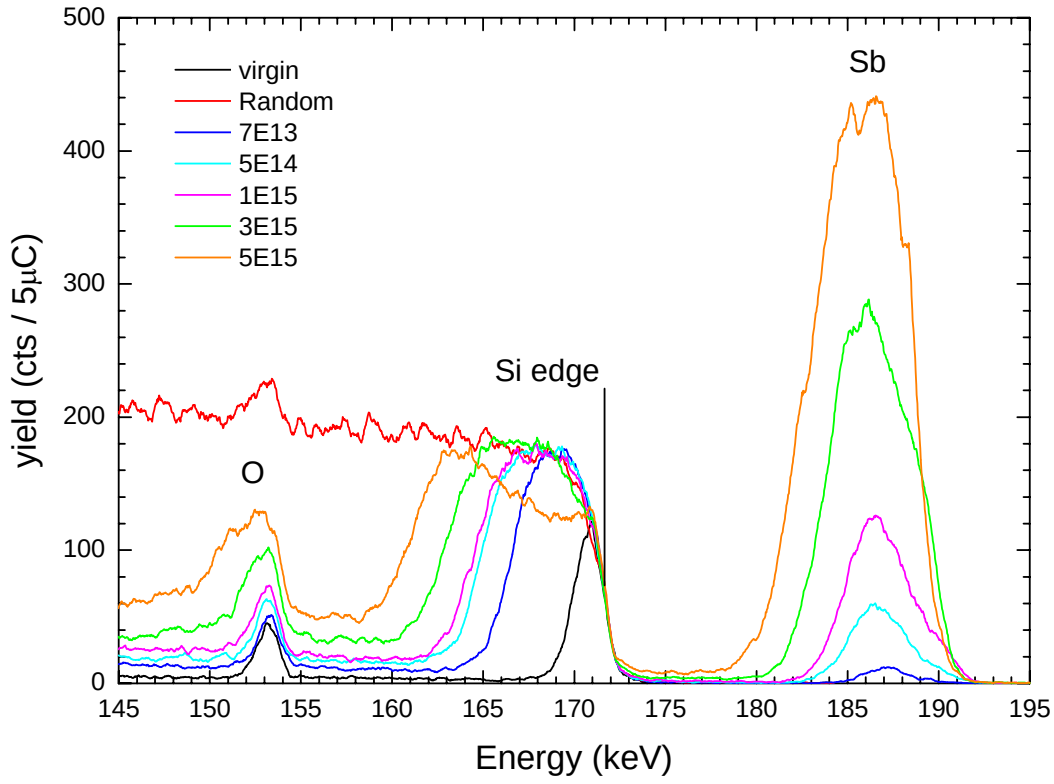

Figure 5.4 MEIS energy spectra showing the growth of the Si damage and Sb dopant yield as a function of fluence for 2 keV Sb^+ ion implantation into virgin Si at room temperature.

The combined behaviour of the displaced Si and the implanted Sb dopant depth profiles is shown in Figure 5.5, as before using a common depth scale and logarithmic concentration scales. Here too the displaced Si profiles are those obtained after subtraction of the virgin Si spectrum and hence represent the additional disorder generated by the Sb implant at each dose indicated. The TRIM calculated vacancy distribution has been added to the top part of the figure as a representation of the energy deposition function. Equally the calculated Sb implant profile is added to the bottom of the figure, adjusted to the height of the profile for the dose of 5×10^{14} cm^{-2}. The amorphous layer produced for the lowest implant dose investigated of 1×10^{14} cm^{-2}, extends to a depth of ~5 nm (half height) and the shape of the disordered layer produced at this stage, not surprisingly, coincides with the energy deposition profile for depths beyond R_p. The half height of the down slope of the Sb distribution for this implanted dose also occurs approximately at this depth. Yet the actual implanted Sb distribution should extend to a greater depth as shown by the TRIM calculated Sb profile. Just as was seen for the As, Sb ions implanted with a R_p of 5 nm having a maximum range of at least twice that figure, migrate out of the as yet not amorphised deeper layer in which

they are stopped into the amorphised layer nearer the surface, where they are more readily accommodated. The correlation between the amorphous layer that grows in a planar fashion to greater depths and the "movement" of the Sb profile to greater depths, as indicated by arrows, is evident. Although for the Sb implant, the lowest dose of 1×10^{14} cm^{-2} shows a later stage in the development of the combined disorder / dopant profile behaviour, in essence the observations for the two heavy ion dopants are commensurate and both scenarios present evidence of an intricately combined damage evolution-dopant migration mechanism.

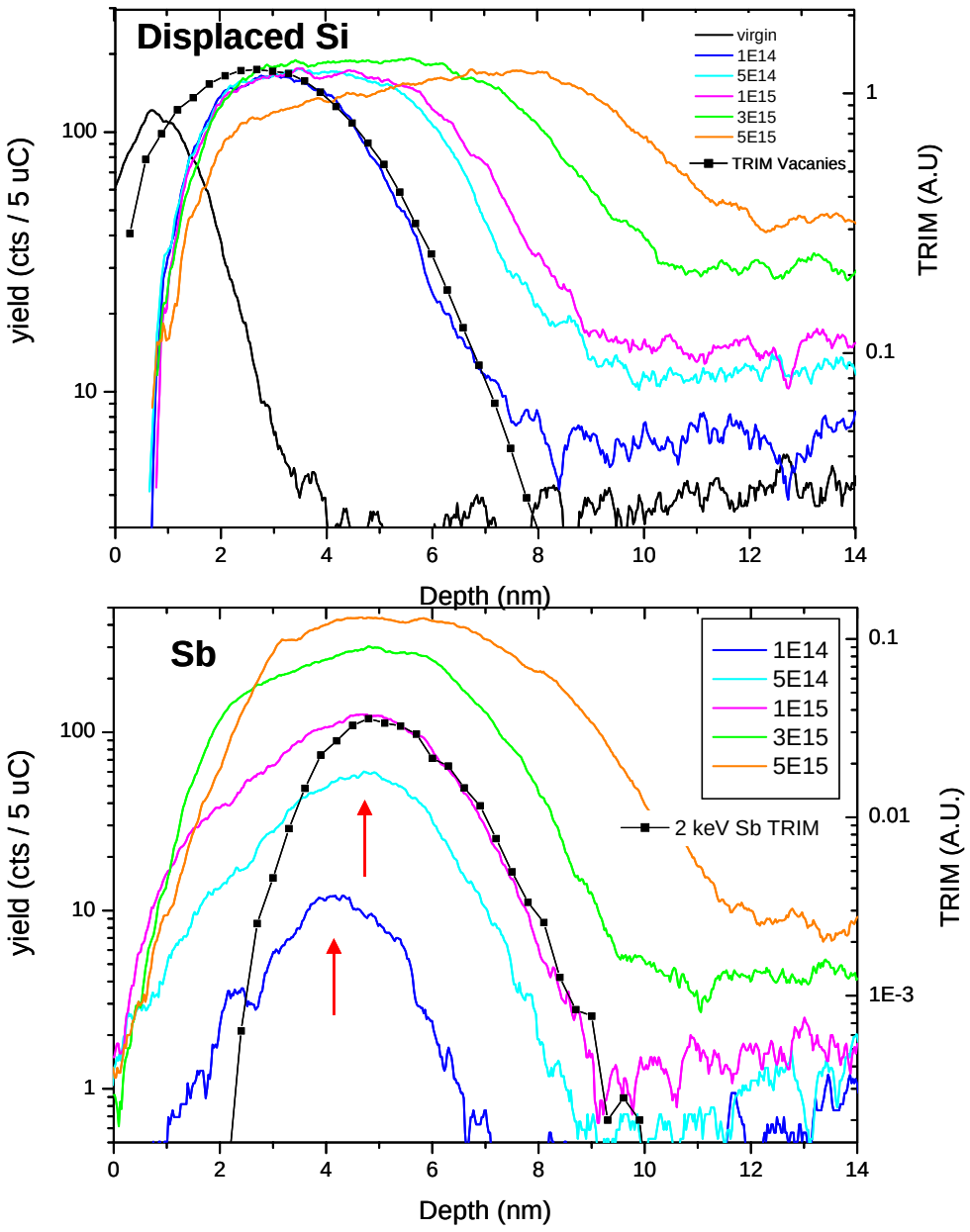

Figure 5.5 Depth profiles of displaced Si and As implant atoms obtained from the MEIS energy spectra in Figure 5.4. The TRIM calculated Si vacancy distribution and As implant profile are shown for comparison. The dose dependent peak position of the Sb implant is indicated by arrows.

5.4 Conclusion

MEIS analysis with additional SIMS depth profiling has been used to investigate the growth mode of the amorphous layer as well as the relationship between disorder formation and dopant redistribution for shallow As and Sb implants into Si performed at room temperature. MEIS studies show that damage evolution caused by these heavy ions for doses from 3×10^{13} cm^{-2} upwards does not follow the profile of the energy deposition function, but proceeds from the surface where an initial 4 nm wide amorphous layer developed, and then grows inwards in a planar fashion as the dose is increased. It is proposed that a fraction of the generated interstitials migrate towards the surface, and are captured by the oxide or amorphous /crystal Si interface, where their trapping nucleates the growth of a shallow amorphous layer and the subsequent planar growth inwards of the damage layer. The observed build up of the As profile, the maximum of which moves from a depth of 3.5 nm to 5.5 nm over the dose range studied is related to this process: Arsenic that is stopped in the as yet not amorphised layer, moves out into the growing disordered layer, in which it is more easily accommodated. SIMS studies have confirmed this dopant segregation effect. Low dose, shallow Sb implants also exhibit this novel damage evolution / dopant movement effect.

References

1 L. Pelaz, L.A. Marqués, J. Barbolla. Appl. Phys. Rev. **96** Dec. 2004, p5947.

2 F. Priolo and E. Rimini, Materials Science Reports 5 (1990) 319.

3 F. L.Vook and H. J. Stein, Radiat. Eff. 2(1969) 23.

4 L. A. Christel, J. F Gibbons and T. W. Sigmon, J. Appl. Phys. 52 (1981) 7143.

5 M. L. Swanson, J. R. Parsons, and C. W. Hoelke, Radiat. Eff. **9**, 249, (1971).

6 L. T. Chadderton and F. H. Eisen, Radiat. Eff. **7**, 129 (1971).

7 F. F. Morehead, Jr. and B. L. Crowther, Radiat. Eff. 6 (1970) 27.

8 J. R. Dennis and E.B Hale, J. Appl. Phys. 49(3) (1978) 1119.

9 J. R. Dennis and E. B. Hale, Appl. Phys. Lett. **29**, 523 (1976).

10 L. M. Howe and M. H. Rainville, Nucl. Instrum Meth B 19/20 (1987) 61

11 R. G. Elliman, J. S. Williams, W. L.Brown, A. Leiberich, D. H. Maher, and R. V. Knoell, Nucl Instrum Meth. B19/20 (1987) 435.

12 R. D. Goldberg, R. G. Elliman, and J. S. Williams, Nucl. Instrum. Meth. B **80/81**, 596 (1993).

13 M. Avrami, J. Chem. Phys. **9**, 177 (1941).

14 R.D. Goldberg, J. S. Williams, and R. G. Elliman, Nucl Instrum Meth. B106 (1995) 242.

15 J. Linnross, R. G. Elliman and W. Brown, J. Mater. Res. 3 (1988) 1208.

16 R.D. Goldberg, J. S. Williams, and R. G. Elliman, Mat. Res. Soc. Symp. Proc. 316 (1994) 259.

17 J. S. Williams, H. H. Tan, R.D. Goldberg, R. A. Brown, and C Jagadish, Mat. Res. Soc. Proc. 316 (1994) 15.

18 T. Henkel, V. Heera, R. Koegler, W Skorupa and M Seibt, J. Appl. Phys. 82 (1997) 5360.

19 J A van den Berg, S. Zhang, D. G. Armour, S. Whelan R.D. Goldberg, E. J. H. Collart, P. Bailey and T. C. Q. Noakes., Nucl. Instrum. Methods B 183 (2001) 154.

20 J. A. van den Berg, D. G. Armour, S Zhang and S Whelan, L.Wang and A. G. Cullis, E. H. J. Collart, R. D. Goldberg, P. Bailey and T. C. Q. Noakes, J Vac. Sci. Technol. B 20 (2002), 974.

21 R. D. Goldberg, D. G. Armour, J. A. van den Berg, N. Knorr, H. Ohno, S. Whelan, S. Zhang, C. E. A. Cook, and M. A. Foad, Rev. Sci. Instr. 71 (2) (2000) 1032

22 W. K. Chu, J. W. Mayer, M. Nicolet, Backscattering Spectrometry, (Academic Press, New York, 1978).

23 J. F. Ziegler, J. P. Biersack, and U. Littmark, The Stopping and Range of Ions in Solids (Pergamon Press, New York, 1985).

24 R.M. Tromp, in Practical Surface Analysis, Vol. 2: Ion and Neutral Spectroscopy, D. Briggs and M.P. Seah (eds.), 1992, Wiley, p.577.

25 A H Al-Bayati, K Ormannn- Rossiter, J A van den Berg and D G Armour, Surface Sci 241 (1991) 91.

26 http://www.srim.org/ (accessed 02/06).

27 M D Giles, J Electrochem. Soc. 138 (1991) 1160.

28 H.-J. Gossmann, T. E. Hayes, P. A. Stolk, D,C. Jacobson, G. H. Gilmer, J. M. Poate, H. S. Luftman, T. K. Mogi, M. O. Thompson, Appl. Phys. Letts.71 (1997) 3862.

Chapter 6 Annealing studies

6.1 Introduction

In this chapter the results of a range of annealing studies are described and discussed, most of which were carried out within the IMPULSE project and as such are highly relevant to current technologies and possible solutions for future devices. The studies in this chapter fall into three general categories.

The first category in section 6.2 focuses on implantation and annealing conditions that are similar to those used in device production. This is based on annealing predominantly using RTA and spike annealing, at temperatures above 1000 °C. Comparisons with lower temperatures are also included. The effects of reduced implant energy are discussed. The predominant feature with these conditions is that diffusion of the dopant will be the limiting factor in reducing the junction depth.

The second category in this chapter is in section 6.3, concerning studies of SPER at lower annealing temperatures, in the region of 550 °C to 700 °C. This annealing range has been identified as a possible solution for 65 and 45 nm nodes, as the problem of diffusion would be minimal (1-3). Note that in the semiconductor industry the terminology SPER often refers to annealing at lower temperatures, approximately 550 – 800 °C. From a physical point of view, regrowth at higher temperatures still occurs by the SPER process but is more commonly referred to as RTA/RTP, spike annealing, flash etc, based on the annealing equipment used rather than the physical process that occur.

The final category, in section 6.4, is the regrowth behaviour of SOI wafers, which are currently being implemented in production. Differences in annealing behaviour were observed in SOI compared to bulk Si.

One of the features of the IMPULSE project was to further develop analytical techniques for USJ characterisation. Dispersed throughout this chapter are some of the interesting comparisons with various X-ray techniques carried out at the ESRF. As well as providing additional information on the samples, these highlight the potential of these techniques for future studies.

6.2 Studies involving RTA of implanted samples, conditions similar to current device production

6.2.1 Introduction

In this section there is a discussion of the results of several studies involving RTA of As implanted samples. The first study is used to introduce the way in which phenomena such as SPER, the segregation of As, As moving into substitutional positions and diffusion of dopant can be studied with MEIS and SIMS. The two techniques provide complementary information and form the backbone of these studies.

Similar studies were carried out in which pre-amorphising with a Xe implant was introduced and the effects of changing the implantation energy are studied. These are coupled with studies using X-ray techniques.

6.2.2 RTA of 2.5 keV As implanted samples

This first set of samples has no pre-amorphisation and uses an As implant that is similar in energy and dose to those used in current technology. The samples are annealed with a range of temperatures and times to illustrate different aspects of the annealing behaviour, including a > 1000 °C spike anneal which is typical of device production. Results of these studies are also presented in (4,5).

6.2.2.1 Experimental

2.5 keV As^+ ion implants into Cz grown Si(100) samples of resistivity 10 – 20 Ω.cm were performed at room temperature, under UHV conditions using the ultra-low energy ion implanter at Salford to a dose of 1.8×10^{15} cm^{-2}. All implants were executed through the native oxide using dose rates of up to 1×10^{14} ions sec^{-1} cm^{-2}. Samples were annealed in a Steag AST10 rapid thermal processor at Salford to temperatures of up to 1050 °C, using ramp rates of 25 °C s^{-1} in a N_2/6% O_2 ambient to avoid dose loss.

MEIS analysis was carried out using a nominally 200 keV He^+ beam and the double alignment configuration, in which the [$\bar{1}\,\bar{1}\,1$] channelling direction was combined with the [332] blocking direction. Implanted As and displaced Si profiles can be detected down to levels of 1×10^{19} cm^{-3} and 2×10^{20} cm^{-3}, respectively.

SIMS analysis of the As profiles was carried out in an Atomika 4500 instrument at IMEC using a 0.5 keV 0_2^+ primary beam at normal incidence. Crater size was 250 μm and Si^{30} was monitored to ascertain a better than 1% current stability. The depth scale calibration relied on a constant ion current. Relative sensitivity factors (RSF, from an implant standard) were repeatable to within 1%.

6.2.2.2 Results and Discussion

Figure 6.1 shows the MEIS energy spectra for 2.5 keV As ions, as-implanted at 1.8×10^{15} cm^{-2} and after RTA at 600 °C for 10 s, 700 °C for 10 s, 900 °C for 10 s and 1050 °C spike annealing. Depth scales have been added to the figure for As, Si and O. The as-implanted sample shows that the 2.5 keV As implant amorphises the Si to ~ 9.5 nm, (half height of the back edge of the damage peak). The As profile is centred around 5 – 6 nm. Note that all the Si damage peaks include a contribution from the surface peak (FWHM 2 nm).

The annealing behaviour is best introduced by first considering the sample annealed at 600 °C for 10s. The annealing produces a reduction in the width of the amorphous layer, from 9.5 nm to 6.5 nm (FWHM), due to solid phase epitaxial regrowth (SPER). An average regrowth rate of ~ 0.3 nm s^{-1} is obtained in this region in which the interface moved through a region with a high As concentration. This value compares to a value of 1 nms^{-1} found for intrinsic Si (6, 7). It is known that regrowth rate is dopant concentration dependent and that a high As concentration causes a reduction in the regrowth rate (6, 7, 28). Regrowth rates with a changing of As concentration are examined in more detail in section 6.3.2.1.

MEIS shows that during annealing there is a close correlation between the reduction in the width of the Si damage peak and the movement of the As implant. The 600 °C anneal has also caused a distinct change in the As distribution. The half height of the back edge has moved to a depth of 6.5 nm which coincides with the depth of the crystalline/amorphous interface. It also shows that the As yield in front of this interface has increased by about 20%. This increase is due to As atoms that apparently could not be accommodated in the regrown layer, and therefore segregates out and are "snowploughed" in front of the advancing interface (7). Overall the As peak area measured by MEIS is reduced by 12 %. SIMS measurements, discussed later, show the retention of all the implanted As atoms. Hence the "missing" As atoms have moved into substitutional positions where they are no longer visible to the analysing MEIS beam.

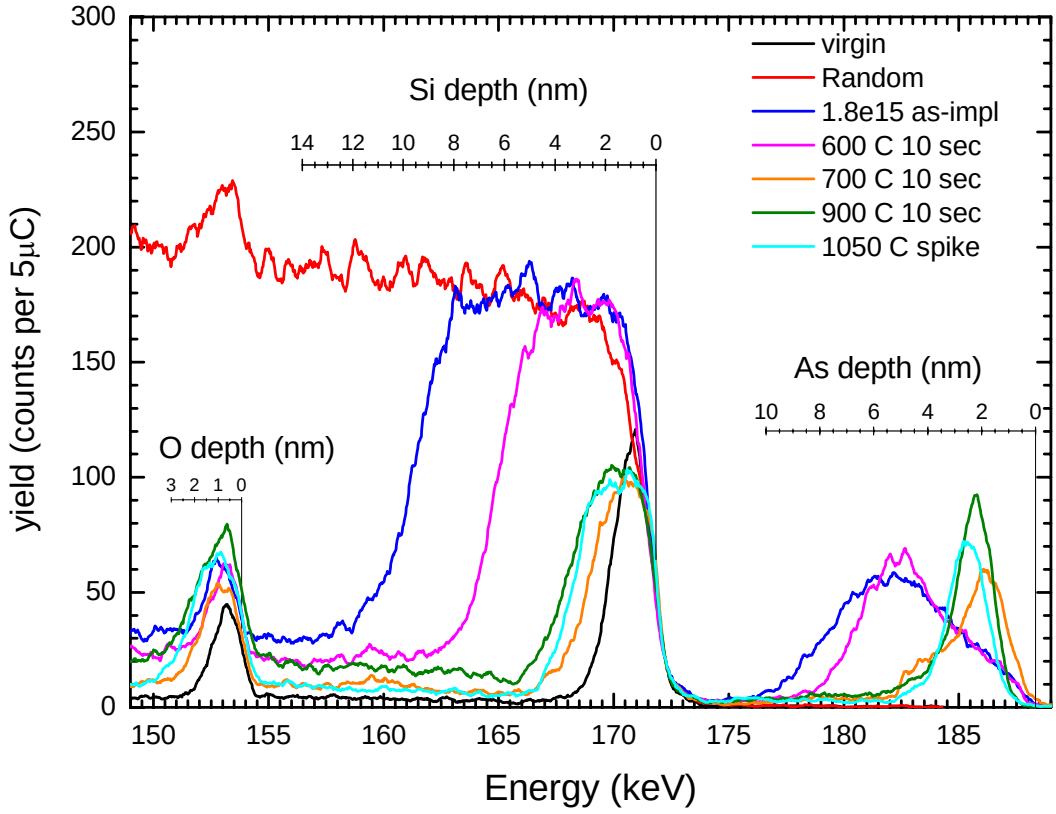

Figure 6.1 200 keV He MEIS energy spectra for 2.5 keV 1.8E15 As implants, for various anneal temperatures.

RTA at 700 °C causes a substantial change in the spectrum indicating the completion of the SPER process. The depth of the Si damage peak reduces to 2.8 nm, which is still somewhat greater than that of the virgin Si peak (2 nm). This larger width is in part accounted for by the growth of the oxide layer from 1.5 nm (for virgin Si) to 1.8 nm (after 700 °C RTA), also shown in the spectrum. A second reason is given below. The SPER of the amorphous layer has produced a segregated layer of As, which has been pushed out of the regrown layer and has piled up at the interface. MEIS unambiguously shows that this pileup occurs at the interface with the now 1.8 nm thick oxide (10). This As yield accounts for about 40 % of the implanted dose. Apart from a visible As profile tail, the remainder has moved into substitutional lattice positions and is no longer visible to the He^+ beam. The tail of the As profile indicates that the regrowth is not perfect and that the layer still contains some non-substitutional As atoms. RTA at 900 °C causes some further reduction in the visible As profile tail and a corresponding growth in the segregated As peak to 47 % of the implanted As dose. Taking the system energy resolution into account, the FWHM width of this peak may be below 1 nm and in fact the peak may actually be 1 ML thick in agreement with certain

theory predictions and X-ray fluorescence (XRF) studies (8, 9). Broadening of the MEIS peak may also occur since MEIS samples a large area of the samples over which there may be a distribution of depths of the SiO_2 layer. The small shift of the As peak to increased depth is consistent with a small growth in the thickness of the oxide layer during annealing at higher temperatures which pushes the segregated As layer in. Spike annealing at 1050 °C finally, results in the highest level of damage annealing as indicated by the lowest dechannelling level. The increase in the width of the damage peak compared to the 700 °C anneal is entirely accounted for by the growth of the oxide layer to 2.4 nm. Spike annealing also leads to the highest fraction of substitutional As atoms being accommodated in the regrown layer, leaving only 40 % of the implanted As, the amount that can be contained in one monolayer (ML) i.e. 7E14 cm^{-2}, visible in the segregated layer. Observations of such high levels of segregated As dopant in a very shallow layer have been reported previously (10).

Returning briefly to the movement of As atoms into substitutional sites upon SPER regrowth, this observation is consistent with activation and/or the formation of an inactive As-vacancy cluster, As_nV ($n \leq 4$) (11). For n = 4 the cluster consists of four substitutional As atoms tetragonaly clustered around a vacancy that accommodates the larger dopant size. The formation of As_nV clusters is accompanied by the ejection of Si interstitials (10) that migrate and are trapped at the oxide/Si interface sink (12), and their accumulation contributes to the growth in depth of an amorphous layer and thus, the width of the surface peak. This is the second effect, referred to above that may explain the increase in width of this peak upon RTA.

The annealing and segregation behaviour described above in Figure 6.1 is confirmed by SIMS depth profiling measurements. The results are given in Figure 6.2 which shows the profiles using both logarithmic and linear concentration scales. The Si^{30} signal (3.09% abundance, multiplied by 32 to give ~ 100 % Si) is shown in Figure 6.2 for the as-implanted profile only. It was monitored in all cases and found to coincide to within 1 %, confirming the current stability of the measurements. The excellent quality of SIMS profile of the as implanted sample may be judged in comparison with the MEIS result also shown in the bottom part of the figure. Only the marginally increased FWHM (~ 10 %) in the SIMS profile and minor shift (< 0.5 nm) towards the surface reflect collisional mixing effects and sputter rate changes in the transient region, respectively. The development of the SIMS profiles following annealing wholly confirms the MEIS observations. Integration of the profiles shows no As dose loss and hence the As invisible in MEIS can only represent dopant atoms that have moved into

substitutional sites. The formation of the segregated peak, is clearly visible after the high temperature anneals at the depth indicated by MEIS (1.5– 2 nm). The SIMS results finally show the onset of As diffusion after 900 °C RTA, and after 1050 °C spike annealing.

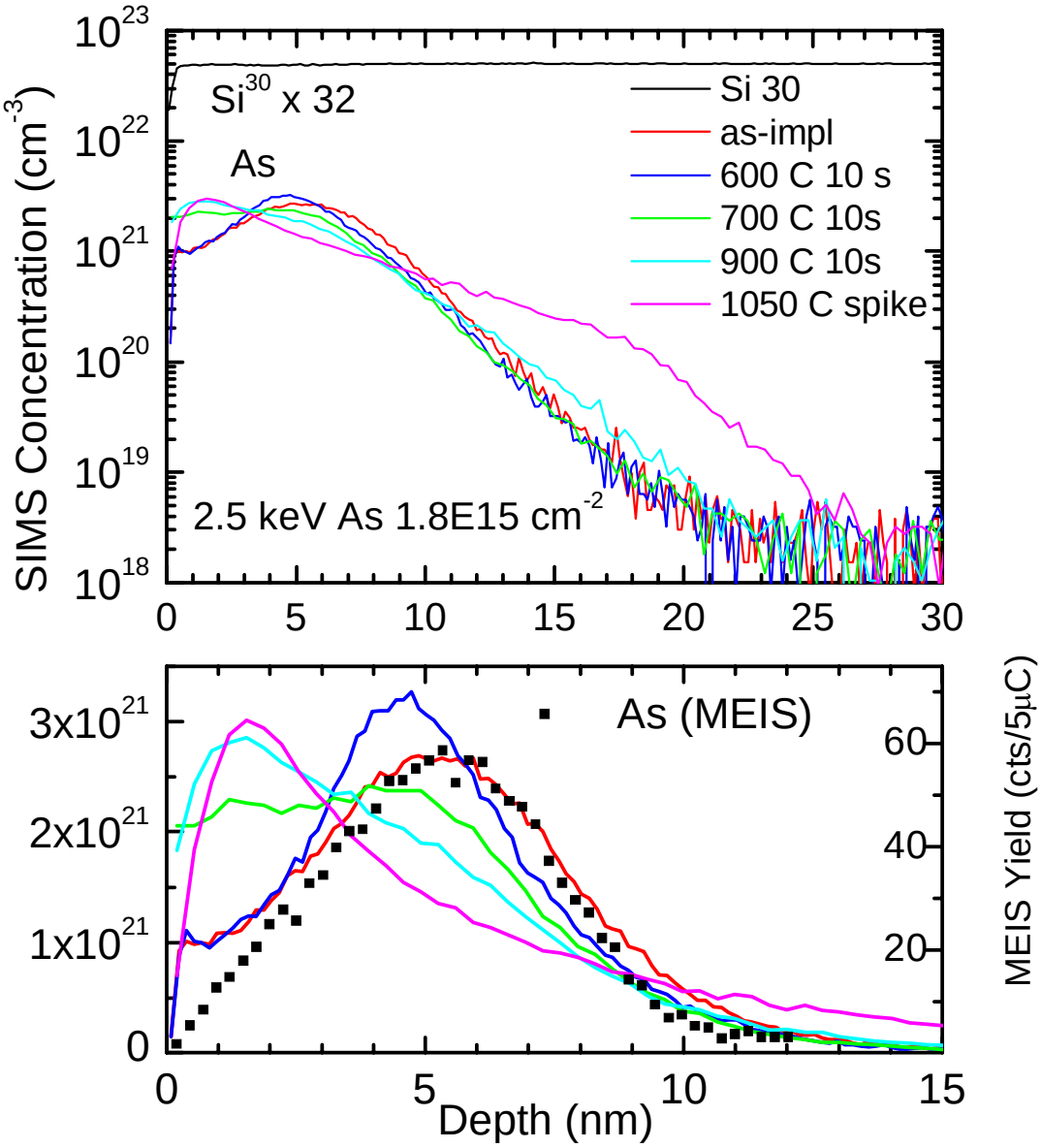

Figure 6.2 (Top) SIMS As depth profiles for 2.5 keV 1.8E15 As implants, for various anneal temperatures. (Bottom) The same profiles are plotted with a linear concentration scale and smaller depth range. The MEIS profile from the as-implanted sample is included in the figure for comparison.

6.2.3 PAI 3keV As implanted samples

Experiments with comparable implantation and annealing conditions using Xe-PAI samples were also carried out and results of selected samples are presented here. They include a comparison with specular reflectivity (SR) measurements. The dopant

implantation conditions are those used for device manufacturing, i.e. a 3 keV As^+ implant to a fluence of 2E15 cm^{-2}. These implants have been carried out into crystalline Si (No PAI), and Si pre-amorphised with a 130 keV Xe^+ implant to a fluence of 2E14 cm^{-2} (PAI). This results in a Si amorphisation depth of 100 nm as measured with XTEM (13). The results obtained for two annealing conditions are presented here, these are furnace annealing at 600 °C for 20 minutes and spike annealing to 1130 °C. The sample after high temperature spike anneal is representative of current manufacturing methods. The results following the low temperature furnace anneal are included primarily for comparison with SR results.

6.2.3.1 MEIS results

The MEIS analysis conditions used were a nominally 100 keV He^+ beam with the samples aligned along the [$\bar{1}$11] channelling direction relative to the beam. The analyser was positioned to record data along the [111] and [332] blocking directions. MEIS energy spectra from along the [111] blocking direction, for both PAI and NoPAI sample series, are shown in Figure 6.3. Also included in the figure for reference is a spectrum from a virgin Si sample and a random spectrum taken from an amorphous Si sample.

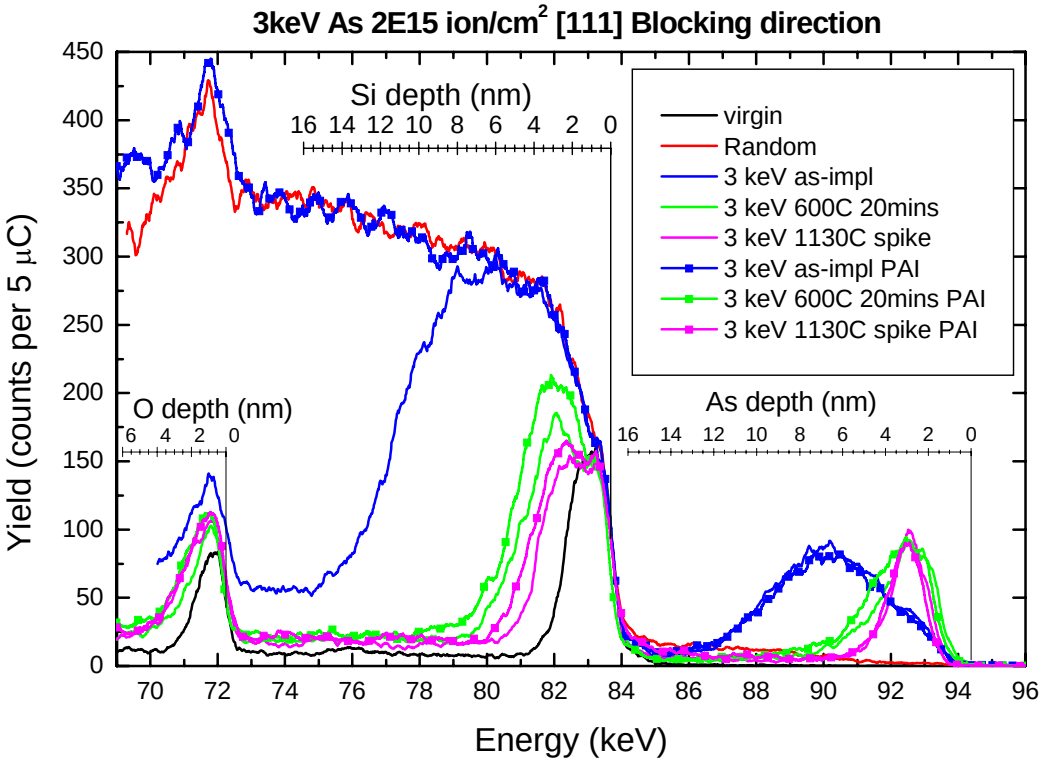

Figure 6.3 MEIS spectra collected along the [111] blocking direction. The non-implanted Si sample and a random amorphous Si spectrum are shown for comparison.

The energy spectra have been converted into depth profiles. The profiles for both the NoPAI and PAI samples are shown in Figure 6.4a) and 6.4b) for As and Si, respectively. Figure 6.4 b) shows that the 3 keV As implant produces a ~11 nm deep amorphous layer, as evidenced by the extra Si scattering yield behind the surface peak that reaches the random level and extends to a depth of ~11 nm (half height). Arsenic implant profiles for the PAI and NoPAI implants are in close agreement. This is expected since Si is amorphised after a As dose of 10^{14} cm^{-2} (14, chapter 5). MEIS shows that the peak of the As distribution is at 6.3 nm depth, in close agreement with TRIM calculations that yield an R_p = 6.4 nm (profiles not shown). Following a 600 °C 20 min anneal the amorphous layer has recrystallised by SPER. The regrowth is not perfect, leaving a surface damage peak of greater width (5 nm) than the surface peak width of the virgin sample (2.5 nm) and greater height. The As profile too has undergone considerable change with the disappearance from " beam view" of most of the As in the implanted profile and the appearance of a narrow, segregated As peak with a maximum at a depth of 3 nm. The former is due to As taking up substitutional positions within the regrown Si, where it is no longer visible to the beam. The latter is due to the As concentration that exceeds the solid solubility and cannot be accommodated in the regrown layer due to solid solubility restrictions, although the operation of a simple activated segregation process cannot be excluded. In either case it is "snowploughed" ahead of the advancing amorphous/ crystalline interface and forms the segregated surface peak (7).

a)

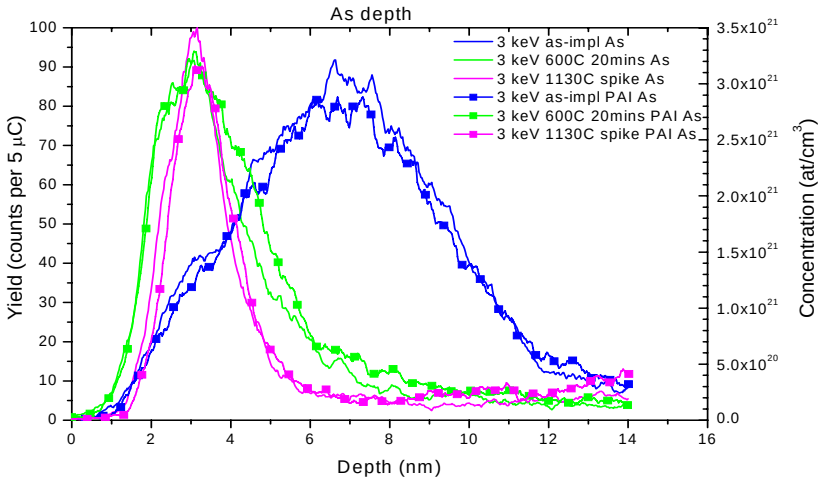

b)

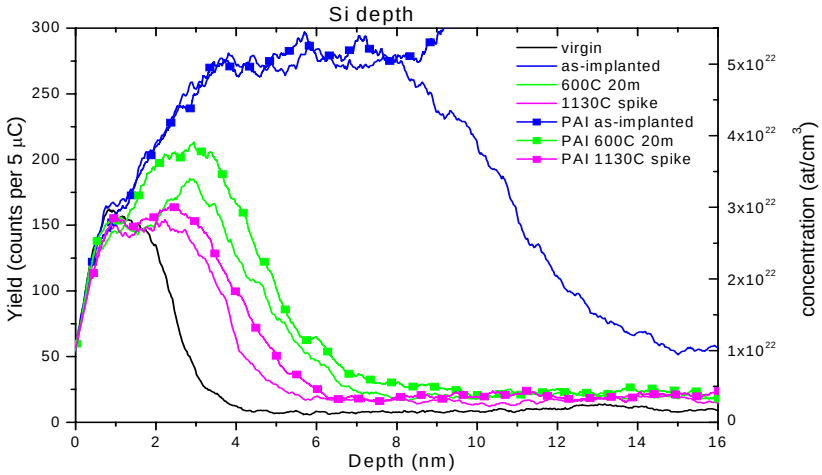

c)

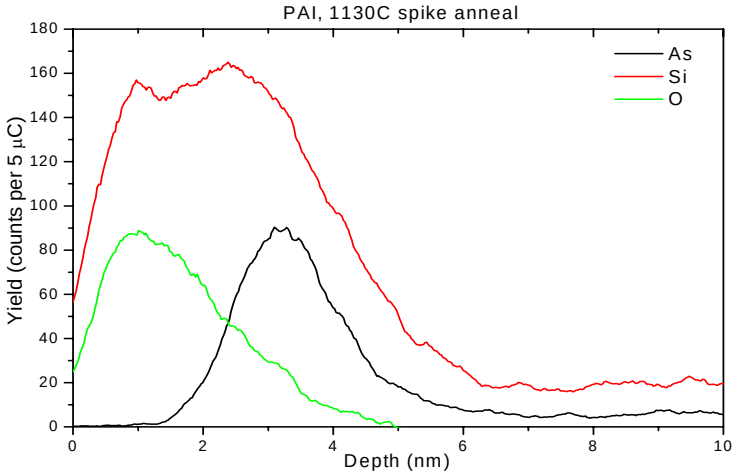

Figure 6.4 MEIS depth profiles along the [111] blocking direction a) As depth profiles for all the annealed samples. b) Si depth profiles for all the annealed samples. c) Combined depth profile of As, Si and O for the PAI 1130 °C spike annealed sample.

Integration of the peak and calibration of the ion yield shows that 40 - 46 % of the dopant is no longer visible to the beam. From SIMS studies it is known that no As has been lost from the matrix, which is consistent with the previous studies (4).

Spike annealing to 1130°C produces more perfect regrowth. The segregated As peak is sharper and the surface damage layer for these anneal conditions is reduced to ~ 4 nm. The latter includes a substantial component from the silicon contained in the oxide layer, which as a result of the RTA has grown in thickness to ~ 3 nm. The anneal conditions also affect the percentage of the dopant atoms taking up substitutional positions. The 1130 °C spike anneal produces the highest substitutional fraction with ~ 60 % of the implanted ions accommodated in substitutional lattice positions which is consistent with the spike annealing results from section 6.2.2.

A comparison of MEIS spectra for implants in the PAI samples with the NoPAI samples shows the general annealing behaviour remains similar for both. However the PAI samples show a higher amount of damage after annealing, as evidenced by the slightly wider Si peak and the marginally higher background level, caused by dechannelled particles. The slightly better regrowth for the NoPAI samples could be due to the fact that there is less distance to regrow. i.e. 11 nm compared to the 100 nm wide amorphous layer. If the regrowth rate at 600 °C is ~1 nm/s for intrinsic Si, then the NoPAI sample could reach the point of high As concentration, where it slows down, about 90s before the PAI sample. In addition Xe incorporation could affect the regrowth rate. Slightly thicker oxide layers for the PAI As implant are also seen.

The detail of the distribution of the oxide layer and the snowploughed As layer is more clearly seen by overlaying the Si, As and O depth profiles, as presented in Figure 6.4c) The dechannelling background has been removed from under the O peak only, since at these energies they become significant. Although the effects of energy resolution (& energy straggling) broaden the peaks it is clear that the segregated As is situated under the SiO_2. The downslope of the oxide peak indicates the existence of suboxides, as indicated in (15) which maybe mixed in with the segregated As layer. The Si depth profile shown in the figure further demonstrates the fact that the Si surface peak contains scattering off Si in the oxide layer and disordered Si at the depth of the segregated As peak.

6.2.3.2 Comparison with SIMS

SIMS results for this set of samples are shown in Figure 6.5. These were produced using a 0.5 keV Cs^+ primary beam. The sensitivity of SIMS to detect As is

greater than MEIS. SIMS is not sensitive to the lattice position of the dopant and so sees all of the As present. In combination with MEIS depth profiles SIMS allows the substitutional As fraction to be implied.

For the as-implanted samples there is virtually no difference between the PAI and NoPAI samples. The only difference is that there is a small amount of As channelled to greater depths that accounts for the slightly higher level in the depth range 20 – 40 nm in the NoPAI sample. MEIS does not have the sensitivity or depth range to observe this.

The changes in the depth profile following annealing at 600 °C for 20 minutes in the SIMS profile are far less dramatic than in the MEIS profile. The pile up of segregated As at the surface is visible, with a small reduction in concentration in the depth range 5-10 nm to account for this, otherwise the profile is largely the same. In combination with MEIS this suggests that As has become substitutional. As has not diffused deeper into the sample for the 600 °C anneals.

Spike annealing causes a dramatic change in the SIMS profile and shows the diffusion of As deeper into the bulk. Taking the junction depth to occur at a concentration of nominally 1E18 cm^{-3} this would result in a junction depth of 43.6 nm for the PAI sample and 45.9 nm for the NoPAI sample. SIMS suffers from inaccuracies in the depth scale in the first few nm and although the segregated As peak can be observed, the accuracy of the concentration and depth scale in this region is limited. MEIS results are considered much more quantitative. The combined results suggests that all the As has been retained, based on the integration of the SIMS profile at depths beyond the segregated peak, and using the MEIS results to determine the dose contained within the segregated peak.

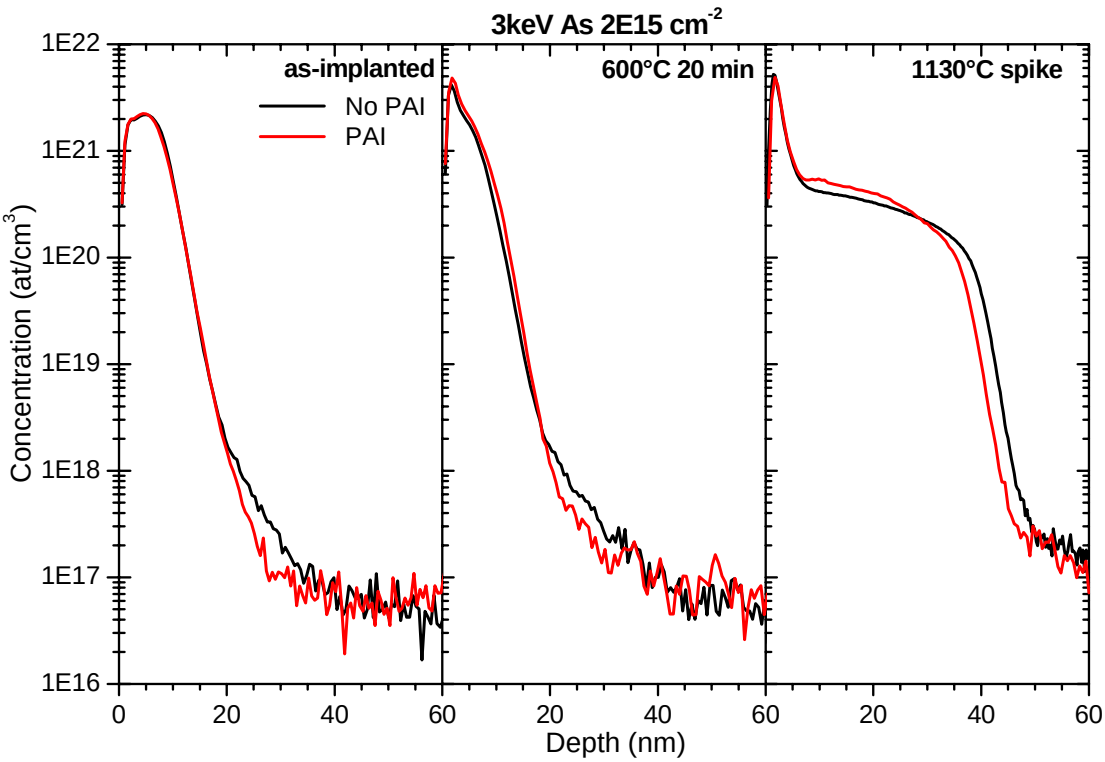

Figure 6.5 SIMS As depth profiles of the 3keV 2E15 samples, with and without PAI, as-implanted, and after 600C annealing and 1130C spike annealing.

6.2.3.3 Specular reflectivity (SR) results – comparison with MEIS

These samples were also analysed with several X-ray techniques at beamline ID01 at the ERSF, Grenoble (Fr) (16). Results obtained from specular reflectivity (SR) experiments provide an interesting and valuable comparison with the MEIS results and as such are briefly discussed here. The strengths of the two techniques, notably the ability of MEIS to produce depth profiles specific to individual elements and the superior depth resolution of SR, have been exploited. The SR results of the PAI and NoPAI series are almost identical, hence only the results of the PAI samples are reported here. A full explanation of the SR technique and more information on the results are given elsewhere (17-20). It should be mentioned that SR measurements are sensitive to the electron density perpendicular to the sample surface, independent of whether the sample is crystalline or amorphous (18, 19).

The SR results from the PAI samples are shown in Figure 6.6a) together with the measurement of a non-implanted (virgin) sample. These are plots of the measured reflected intensity vs z in reciprocal space. The resulting profiles show oscillations, which are most pronounced after spike annealing. The period of the oscillations is

attributed to the interference between the air/SiO_2 surface and the interface at the high density, subsurface layer to which the As and any Si interstitials are swept by the regrowing crystalline front. For the as-implanted sample the As depth distribution is broad without sharp interfaces, as can be seen by the MEIS results shown in Figure 6.3 and 6.4a). As a consequence SR reflectivity appears to be quite similar as the non-implanted wafer where only one long-period oscillation is observed resulting from the thin native oxide. The resulting electron density profiles from a fit of the data are given in Figure 6.6 b).

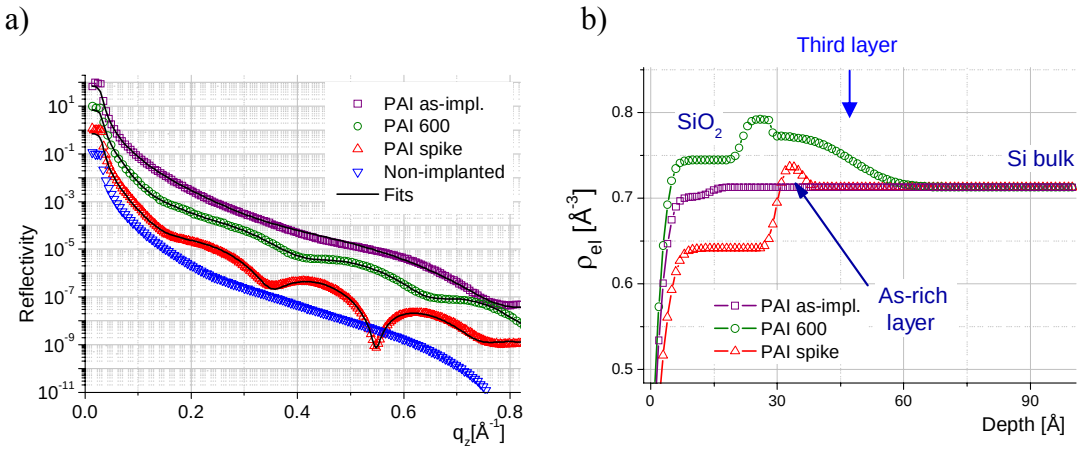

Figure 6.6 a) Specular reflectivity curves for the PAI sample series and non-implanted Si with corresponding fits. b) Depth profile of the density as derived from the fits. From (19, 20).

SR does not possess specific mass sensitivity, unlike MEIS which can unambiguously distinguish between scattering off different masses. Through a comparison with the MEIS profiles (Figure 6.3 and 6.4), regions in the SR density profiles (Figure 6.6b) can be attributed to the different layers and features of the samples, i.e. the SiO_2 layer and the As rich segregated layer, these are indicated in Figure 6.6b). A contribution to the As rich peak from Si interstitials swept in front of the a/c interface during SPER may also occur. An advantage of the SR measurements is that in some instances the thickness of layers may be inferred with more accuracy than with MEIS. With MEIS it is unavoidable that for very thin layers some broadening occurs due to the system energy resolution and energy straggling.

Returning to the results and considering first the spike annealed sample, the SR density depth profile shows a segregated As rich peak with a width of 0.7 nm. The SR result of 0.7 nm agrees well with the theoretical result of 1ML segregated As (8). This shows up a significant difference in the As layer thickness between MEIS and SR, with

a width of 0.7nm from SR and of 1.7nm from MEIS as given in Table 6.1 below. The MEIS determined value is affected by the system resolution broadening and as MEIS samples an area on the sample of 1×0.5 mm, any undulation in the layer over that area will also result in a broadening of the peak. When the broadening of the MEIS peak is considered it would be a fairly good agreement between the techniques. This highlights a use of SR to compensate for a weakness in MEIS. The SR result for the depth of the As-rich layer in the spike sample, in Figure 6.6 b), is in excellent agreement with the MEIS result, in Figure 6.4, both are centred around a depth of 3.2 nm. From MEIS the As segregated layer is found to be unambiguously below the oxide layer (Figure 6.4c)).

	As atoms in peak (%) by MEIS	As peak FWHM (nm) by MEIS	"As rich layer thickness (nm) by SR	"Third layer" thickness (nm) by SR	Oxide thickness (nm) by MEIS	SiO_2 thickness (nm) by SR
PAI as-impl	100	5.5[i]	–	–	1.8	1.4
PAI 600C	60	2.8	0.7	1.94	2.3	2.2
PAI spike	46	1.7	0.7	–	2.4	2.9

i As distribution is actually wider than this value based on FWHM. FWHM is not a good criterion to describe as-implanted profiles.

Table 6.1 Comparison of layer thicknesses between MEIS and SR on the PAI samples.

For the sample annealed at 600 °C, the density fit indicates the presence of an additional "third layer", as indicated in Figure 6.6b), with high density characterised by a thickness of 1.9 nm, as well as the SiO_2 and As rich segregated layer. This "third layer" contains a decaying density profile of As atoms. The As peak in the MEIS depth profile does not show any distinction between the segregated peak and the "third layer" as seen by SR but includes both. Taking into account both the As-rich and the "third layer" agreement on the As layer thickness between the techniques is good for the sample annealed at 600 °C being 2.8nm for MEIS and 0.7+1.94=2.64nm for SR. A detailed physical description of the "third layer" cannot yet be given (18-20) but what can be said is that it is clearly an area of high As concentration.

The as-implanted sample, with a broad As distribution (seen from MEIS), does not provide sufficient density contrast to be visible in SR.

In terms of the behaviour of the oxide layer, both MEIS and SR show the SiO_2 layer growing in thickness with increasing thermal budget. The measurements of the width of the SiO_2 are in reasonable agreement, within the experimental accuracy and are given in Table 6.1. The small differences may be simply due to different measurement criteria. MEIS shows that the oxide peaks appear to contain a region of suboxide (Figure 6.4c), which are not included in the oxide widths in Table 6.1, based on FWHM. It is not clear how the SiO_2 layer is defined in the SR measurements.

To conclude this comparison section, it has been shown that the combined use of MEIS and SR can provided complementary and additional information. MEIS has provided the essential starting point for an unambiguous modelling of the SR curves. SR with the better depth resolution gives the width of the segregated As layer to be 0.7 nm. Within the accuracy of the two techniques they give good agreement on the depth of the segregated peak and the trends in the oxide layer width.

6.2.4 Reduction in implant energy – 1 keV As implantation and annealing

In terms of improvements in junction depth a common trend in manufacturing has been to reduce the implant energy. In this section the results of 1 keV As implantation are presented as a comparison to the 3 keV results described in section 6.2.3. It is shown that diffusion is far more critical in determining the final junction depth than the implantation energy and hence a reduction in beam energy may not necessarily lead to an improvement in junction depth.

6.2.4.1 Experimental

MEIS and SIMS analysis was carried out on a similar batch of samples to the previous set but with a 1 keV implant instead of 3 keV. The dose was again 2E15 cm^{-2}. As with the previous samples, implants were carried out into crystalline (NoPAI) and pre-amorphised (PAI) wafers. The pre-amorphising implant was a 130 keV Xe to a dose of 2E14 cm^{-2}, producing a 100 nm amorphous layer (13). Samples were annealed with a furnace anneal at 600 °C for 20 min, rapid thermal annealed at 1000 °C for 5s and 1025 °C for 10s, and spike annealed at 1050 °C. MEIS analysis was performed using a 100 keV He^+ beam. The results of the [332] blocking direction are presented here. The shallower implantation does not require as large an energy separation of the peaks as in the case of a 3 keV implant and so the [332] direction with its better depth resolution

can be used without the problem of peak overlap. SIMS analysis was carried out using a 0.5 keV Cs^+ primary beam, as previously.

6.2.4.2 Results and Discussion

The MEIS energy spectra for the NoPAI samples are shown in Figure 6.7. Depth scales have been added to the figure to indicate the depth dependence of scattering off arsenic, silicon and oxygen atoms, respectively. Also included in the figures, for reference, are spectra from a virgin Si sample and a random spectrum from an amorphous sample. The energy spectra have also been converted into depth spectra for As, Si and O for NoPAI and PAI samples and they are shown in Figure 6.8a), b) and c), respectively. It can be seen that the results of PAI samples are almost identical to the NoPAI samples.

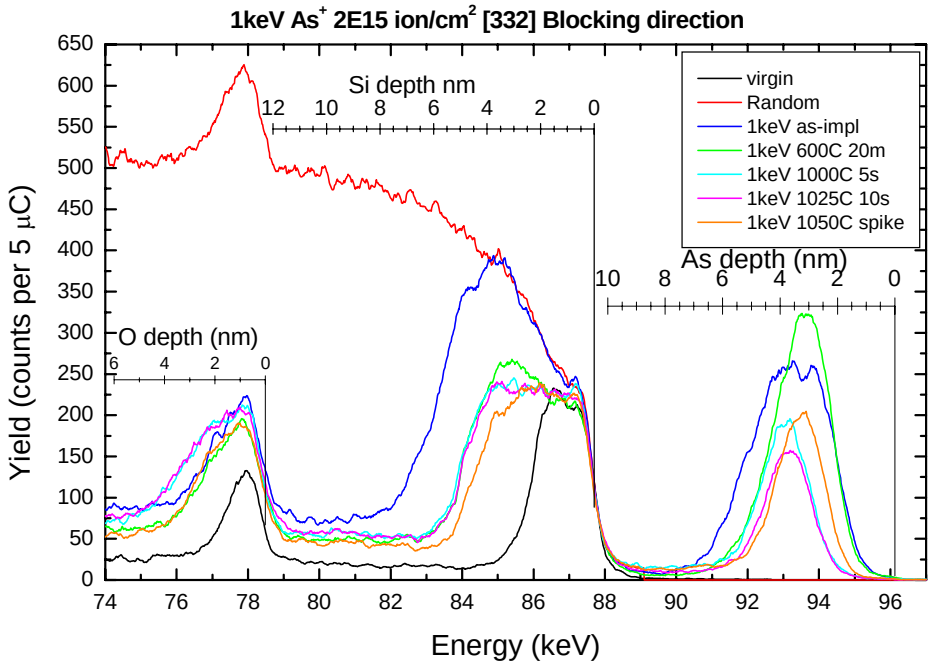

Figure 6.7 MEIS energy spectra for 1 keV As implanted into crystalline Si following various anneals.

a)

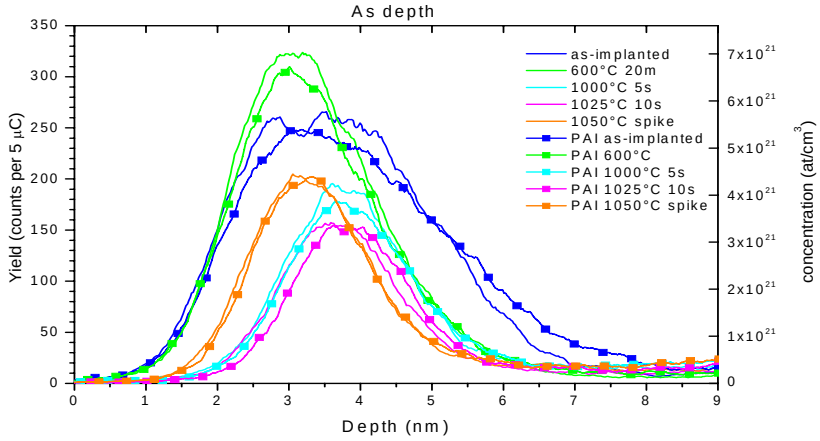

b)

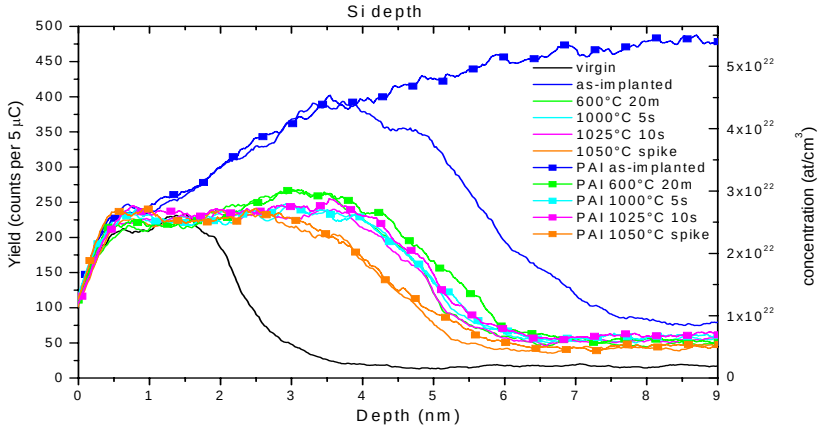

c)

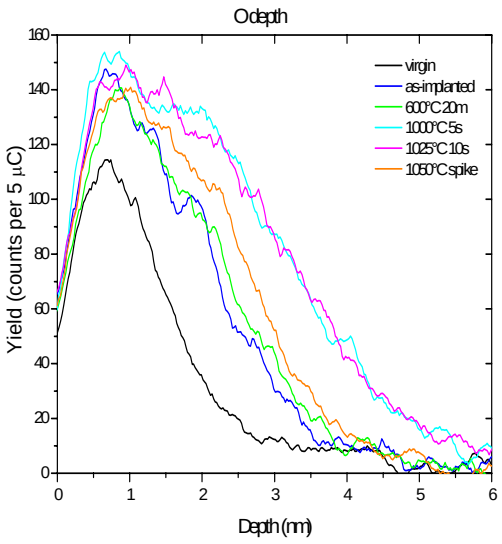

d)

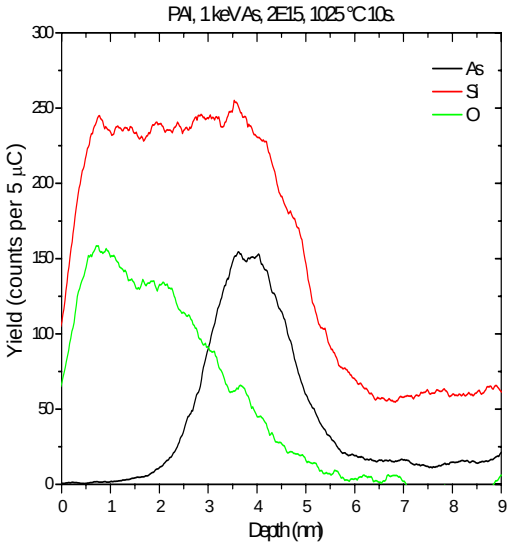

Figure 6.8 Depth profiles for 1 keV As implants, PAI and NoPAI. a) As, b) Si, c) O. d) combined profiles for the PAI 1025 °C 10s annealed sample.

Figure 6.7 and 6.8b) show that the 1 keV implant produces a 5.5 – 6 nm wide amorphous layer (FWHM). The as-implanted As profiles (Figure 6.7 and 6.8a)) have a peak at a depth of around 3.5 nm which corresponds well with TRIM simulation value of R_p = 3.75 nm.

The NoPAI and PAI samples show the same general behaviour after implantation and annealing with only minor differences between the two. Following annealing the samples have largely recrystallised. The extra width of the Si peaks compared to the virgin Si peak with a thickness of 2.5 nm, is mainly a result of the increased oxide layer thickness. It also has a contribution from Si atoms in the distortion around the segregated As (discussed later) and an accumulation of interstitials trapped at the surface sink during annealing.

The 600 °C 20 min annealed samples have a Si surface peak with a thickness of ~ 4.8 nm, including the increased oxide thickness of ~ 2.4 nm. This anneal has the poorest regrowth. The RTA samples of 1000 °C 5 s and 1025 °C 10 s also have a Si peak with a width of 4.8 nm but the higher temperature RTAs produce more oxide growth, to a thickness of ~ 3.4 nm. The spike annealed sample has a Si peak width of 4.4 nm and an oxide layer thickness of just over 2.8 nm. The dechannelling background level (between the Si and O peaks) is consequently lowest for the spike annealed samples, albeit only by a small amount.

In the samples annealed to 600 °C a shoulder, located at 0–2 nm, to the Si peak around 3-4 nm represents the transition point from pure SiO_2 (with concentration 2.3E15 cm^{-2} (30)), to region of suboxides and damaged Si. The damage level in this region in the other samples is lower as a consequence of less distortion around the segregated As.

As seen before, during SPER some of the As takes substitutional positions invisible to the MEIS beam in the regrown layers and the remainder, that exceeds the solubility segregates underneath the oxide layer. In the 600 °C sample only a small amount of As takes up substitutional positions, 94% remains visible to the MEIS beam as indicated in Table 6.2. This amount is significantly higher than for the equivalent 3 keV implant and anneal where 40% of the implanted As became substitutional, (Table 6.1). The reason is as follows, for the 3 keV implant with the deeper implant more amorphous Si layer can regrow, as indicated in Figure 6.4 b). The 1 keV samples with shallower implant depths have a narrower damage region that regrows and hence less As is incorporated within the regrown region. In the 1keV 600 °C annealed sample, only a small amount of As is ‘snowploughed’ in front of the crystalline/amorphous

interface, as evidenced by the higher scattering yield of the 600 °C annealed samples compared to the as-implanted ones at a depth around 2.5-3.5 nm (Figure 6.7 and 6.8a)).

	Crystalline		PAI	
	Visible dose	Visible %	Visible dose	Visible %
as-implanted	2.02e15	100	2.11e15	100
600 °C 20 min	1.90e15	94	1.78e15	84
1000 °C 5 s	1.02e15	50	0.973e15	46
1025 °C 10 s	0.830e15	41	0.825e15	39
1050 °C spike	1.07e15	53	1.05e15	50

Table 6.2 As dose visible in MEIS, for crystalline and PAI samples implanted at 1 keV.

The three higher temperature anneals produce a much higher substitutional fraction, in the region of 50 – 60% substitutional. The 1025 °C 10 s, with the largest thermal budget produces the smallest segregated peak and hence the highest substitutional fraction. For these three temperatures the segregated peak forms a narrow layer underneath the oxide. As with the previous results, it is likely that the system resolution results in some broadening of the peaks. These segregated layers probably cause lattice disorder contributing to the increased width of the silicon peak. Figure 6.8d) clearly illustrates this effect for the 1025 °C 10 s PAI sample in which the As, Si and O peaks are plotted on the same depth scale. In the figure the dechannelling background has been subtracted from the oxygen profile.

For the three high temperature samples the percentage of the implanted As in the segregated peak goes down with increasing anneal duration, i.e. the 1050 °C spike annealed sample has the most segregated As, followed by the 1000 °C 5s and 1025 °C 10s samples. Here the differences in anneal duration are more significant than the differences in anneal temperature. The solubility of As during SPER increases with temperature and if the temperature was the only factor involved here it would be expected that the 1050 °C spike anneal sample would have the lowest amount of segregated As which is not the case. The differences in the amount of segregation observed in the MEIS profiles can easily be understood by examination of the SIMS profiles in Figure 6.9. For all samples annealed at the high temperatures there is diffusion of the As deeper into the bulk, with more diffusion for the longer anneal

durations with higher thermal budgets. The extra amount of diffused As seen in the SIMS profiles accounts for the variation in the amount of segregated As seen in MEIS.

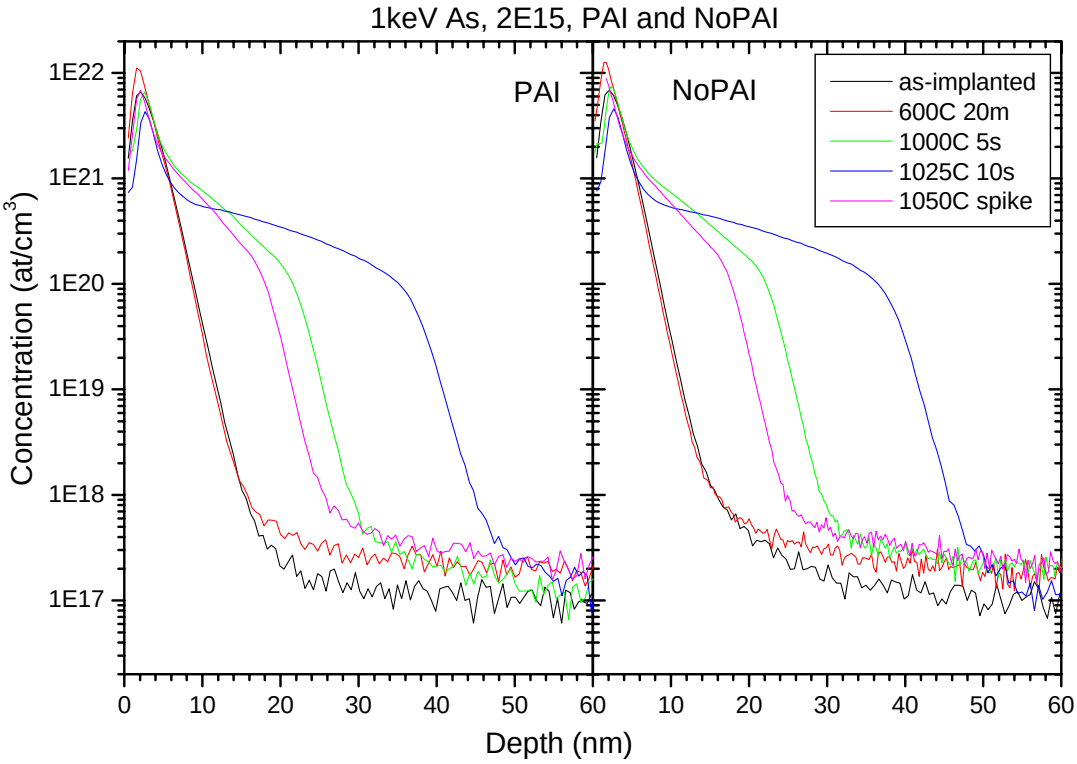

Figure 6.9 SIMS profiles for 1 keV As implanted samples, as-implanted and following various anneals.

With respect to device production this experiment shows that a reduction in beam energy is less important in determining the junction depth than the diffusion. The depths of the 3 and 1 keV implants only vary by a few nm. This becomes much less significant when compared to the amount of diffusion, which in some cases was approximately 40nm. Note that the final junction depths of the 1 and 3 keV spike samples are not directly comparable in this study as they are at different temperatures. Using a 1 keV beam could be detrimental from the point of view of lower throughput, since lower beam currents are usually obtained with a 1 keV beam compared with 3keV due to space charge beam blow up effects. Solely changing anneal temperatures for spike annealing may result in less diffusion at the lower temperatures, but this doesn't necessarily lead to an increased device performance due to overall processing effects (3).

Returning to the results discussed in this section, a small growth in the oxide layer thickness to 2 nm occurs following implantation. As with previous experiments, the growth in thickness of the oxide layer, with increasing anneal temperature and/or

duration, is observed. MEIS results have shown that the segregated As is located underneath the oxide layer. Figure 6.8 c) shows the O depth profiles for the NoPAI samples. The 0.6 nm increase in the oxide layer width is exactly replicated in the shift in depths of the As peaks of Figure 6.8a). It is likely from a simple consideration of the shape of the O peaks that the oxide layer contains some suboxides (15). The back edge of the peak is substantially less steep than the front edge and also less steep than the back edge of the corresponding Si peak plotted on the same depth scale in Figure 6.8d). This result again shows that the segregated As clearly sits underneath the SiO_2 layer, although probably in a region of some suboxides. The Si is probably distorted around the segregated As and this is reflected in increased backscattering.

6.2.5 BF_2 implanted samples

Similar sets of experiments have been carried out using BF_2 implanted samples. The regrowth is seen to proceed in the same way. Neither B nor F is visible in MEIS at the concentrations used; therefore the results are not presented here. However a novel effect involving the interaction between Xe, F and the defect structure was identified. This is the subject of chapter 7 of this thesis.

6.3 SPER studies

6.3.1 Introduction

There is interest in studies of low temperature SPER, i.e. ~ 550 °C – 800 °C as this temperature range has been suggested as a possible solution for the formation of USJs in the 65 nm and 45 nm nodes (1-3). These temperatures are currently not used due to problems of lower electrical activation / solubility and a high level of defects left after annealing. However the real strength of this type of annealing is less diffusion, as the results in this section will corroborate.

The first part of this section shows results of annealing a 3 keV As implanted wafer. An isothermal annealing series at 600 °C and an isochronal series for 10 s were carried out. MEIS results show the same effects as discussed before, i.e. segregation of As, with a fraction of As taking up substitutional positions and the movement of the a/c crystalline interface towards the surface in a layer by layer fashion. The As substitutionality is observed to follow the depth of the a/c interface. SIMS measurements show the same movement of As, seen in MEIS, and also show that the As invisible to MEIS is retained and importantly does not diffuse deeper into the bulk.

Hall effect measurements have been carried out on these samples to find their sheet resistance and the activated dose.

The second part of this section uses identical implant conditions and a variety of anneals. This work forms part of a study carried out in a comparison with X-ray techniques at the ESRF to develop X-ray techniques to study defect evolution. The specific techniques used were GI-DXS, SR, and XRD. More information on these techniques and studies can be found in (18-20). MEIS has proved to be particularly useful, providing a basis for the interpretation of some of the X-ray results. It is found that the results obtained from MEIS and XRD are in excellent agreement.

6.3.2 Isothermal and Isochronal series

6.3.2.1 Isothermal series

A crystalline Cz Si (100) wafer was implanted with 3 keV As^+ and a fluence of 2E15 cm^{-2}. These implant conditions are typical in these studies. The wafer was split into small samples which were annealed at the University of Salford at a temperature of 600 °C for different durations from 5s to 120s. MEIS was carried out with a 100 keV He^+ beam using the [$\bar{1}\bar{1}$1] channelling direction and the analyser was positioned to record the [332] and [111] blocking directions. Results presented here were taken from the [111] blocking direction. SIMS analysis was carried out using 0.5 keV and 0.25 keV Cs^+ beams. Additionally Hall effect measurements were carried out on these samples by ITC-IRST staff using the van der Pauw technique and facilities at the University of Surrey.

The MEIS energy spectra for the [111] blocking direction is shown in Figure 6.10. Included in the figure is the spectrum from the as-implanted sample and the random level from an amorphous Si sample. Depth scales are indicated on the figure for scattering off Si and As. Depth profiles of Si and As are shown in the top and bottom of Figure 6.11 respectively.

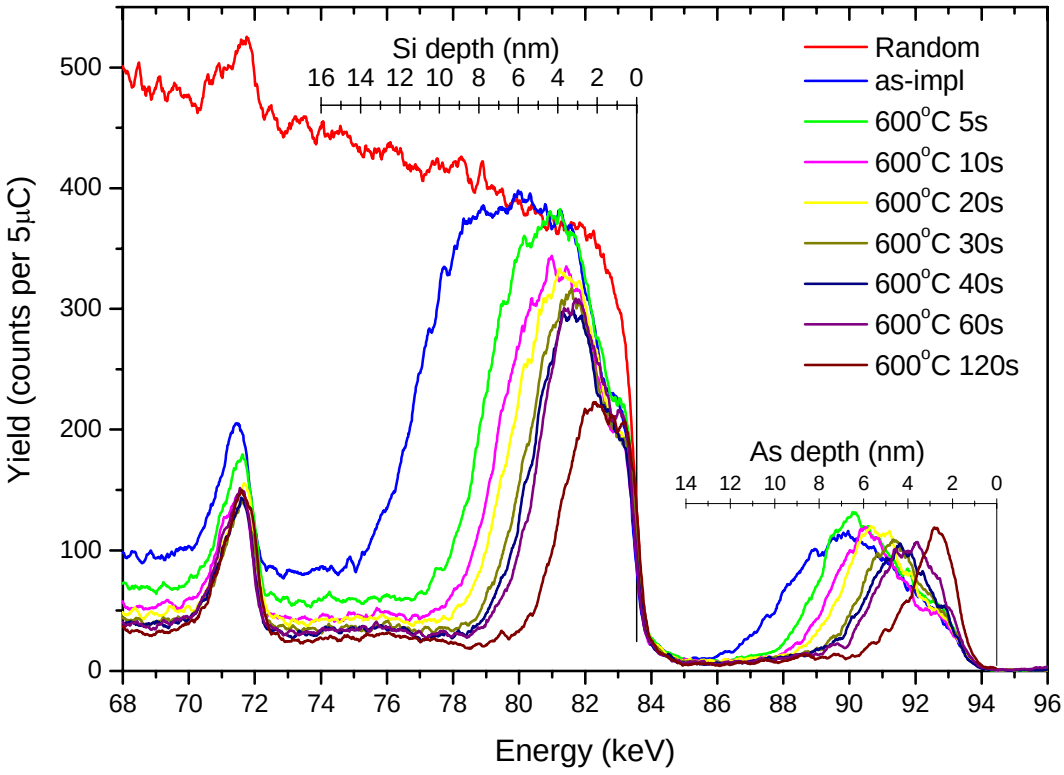

Figure 6.10 MEIS energy spectra for 3 keV As implants, as-implanted and after annealing at 600 °C for various times. A random spectra from an amorphous sample is included in the figure. Depth scales have been added to indicate scattering off As and Si atoms.

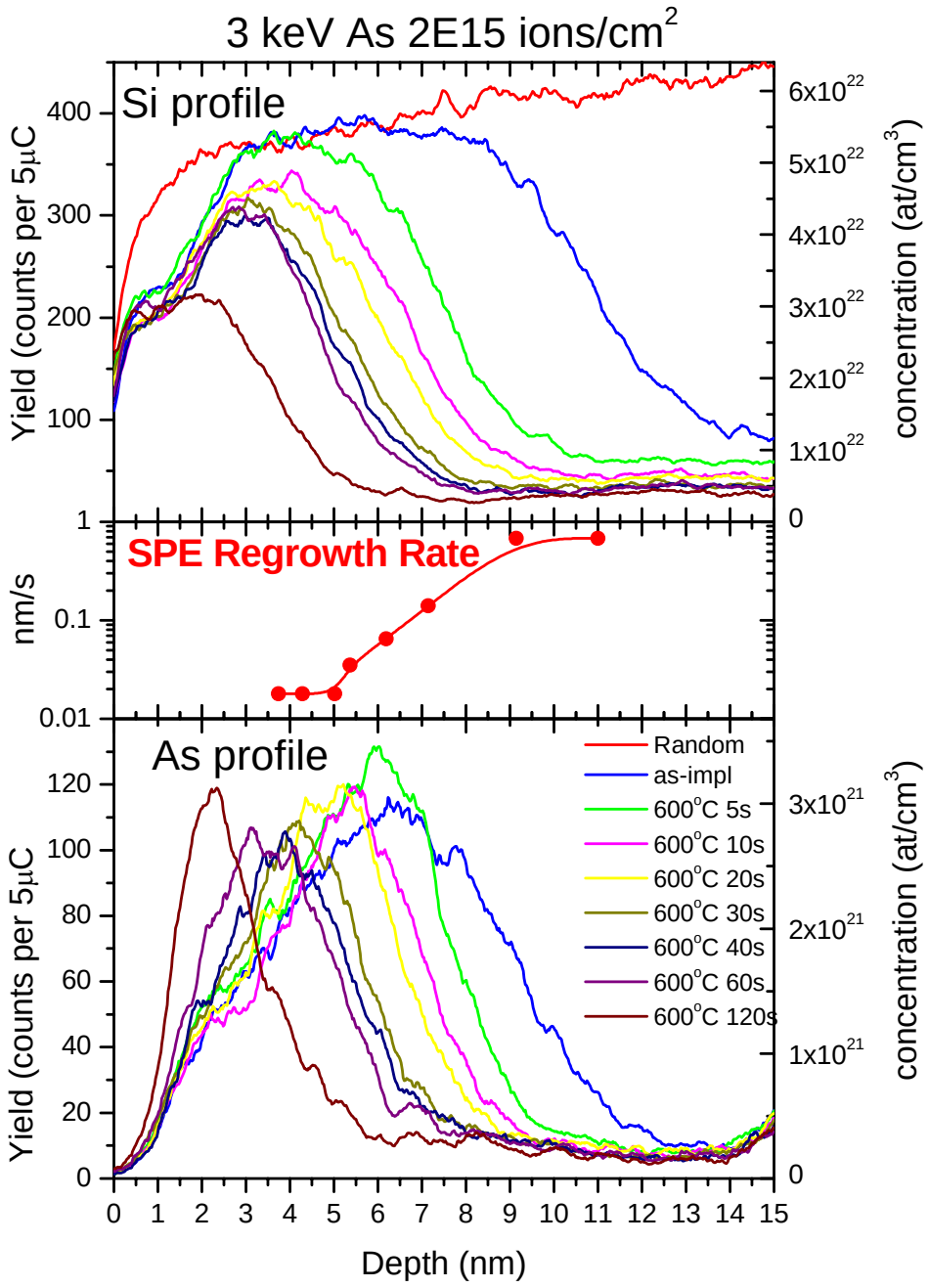

Figure 6.11 MEIS Si depth profiles (top), As depth profiles (bottom) and approximate regrowth rates (centre).

Figure 6.10 and the top of Figure 6.11 shows that the implant produces an ~ 11 nm amorphous layer. The regrowth rate at 600 °C is slow enough to capture various intermediate stages of regrowth for the different durations. The regrowth starts at the amorphous crystalline (a/c) interface and proceeds to the surface in a layer-by-layer fashion as evidenced by the half height of the back edge of the Si peak moving to progressively shallower depths with increasing annealing duration. The slopes of the

back edges of the Si peaks are very similar for all samples. As mentioned previously this slope is mainly caused by a combination of the energy resolution of the MEIS system and energy straggling. Their similarity supports the layer-by-layer regrowth since deviations from this behaviour would result in a change in width of the a/c interface and hence the slope of the back edge. This aspect of the MEIS spectra and SPER will be discussed in more detail in section 6.4 in relation to the regrowth of SOI wafers. The depths of the a/c interfaces are tabulated in Table 6.3.

The behaviour of the As can also be observed very clearly with this series of samples. The As profiles, in the bottom of Figure 6.11, show the original As peak disappearing from "view" of the analysing beam and the As becoming substitutional. The segregation of excess As can be clearly observed as discussed before. Both of these effects are seen most clearly with the longer anneal durations. A comparison of the Si and the As profiles shows that they are closely related. After any of the anneals, the depth of the half height of the back edge of the Si peak, representing the a/c interface, has moved in a similar fashion to the half height of the back edge of the As peaks. The As no longer visible has taken up substitutional positions after the a/c interface has swept past. The amount of As visible is shown in Table 6.3 and is also expressed as a percentage of the implant. For the sample annealed for 120s the regrowth appears to be almost complete. The amount of visible As is also low at 40%. This value is close to the values observed for high anneal temperatures (< 1000 °C) seen in section 6.2.3. However the As peak is not quite as sharp as those observed for high temperature spike anneals and appears to have a "tail" at around 3-5 nm, suggesting imperfect regrowth in this region. Figure 6.10 shows that the variation in oxide thickness with anneal temperature is comparatively small in this experimental series.

	a/c interface depth.	Amount of visible As	% of implant visible.
as-impl	10.9	2.0E15	100
5s	7.4	1.74E15	87
10s	6.8	1.38E15	69
20s	6.2	1.35E15	68
30s	5.5	1.14E15	57
40s	5.2	1.07E15	54
60s	4.8	1.01E15	50
120	3.7	8.0E14	40

Table 6.3 Depths of the a/c interfaces and the amount of As visible in MEIS for the isothermal anneal series.

In the centre section of Figure 6.11 is a graph showing the approximate regrowth rate inferred from these results. A simple consideration of the results reveals that the regrowth rate falls dramatically from its initial value as the concentration of the As peak increases and as the a/c interface reaches the surface. The regrowth rates are taken as an average value based on the distance between successive Si peaks and the time differences between them. The accuracy of this method is limited due to the changing time intervals, the instantaneous rate may vary quite quickly but this method assumes a constant regrowth rate over a period of 5s or longer. There may also be some acceleration of rate in a region of low As concentration (4, 23) which inevitably is averaged out. Additionally the ramping up and down introduces a small error in the timing which is obviously more pronounced with shorter durations. Nonetheless the trend seen provides a good illustration of the slowing down of the regrowth around the high As concentration and surface. From an initial estimated value in the region of 0.7 nms^{-1} (which will be < $1nm^{-1}$ for intrinsic Si (6), due to the overlapping over some depth in which the As concentration increases), it drops to ~ 0.065 nm s^{-1} where the local As concentration has its maximum concentration of ~ $3E21cm^{-3}$. It slows down further in the region of the surface to ~ 0.02 nms^{-1}.

The relation between regrowth, segregation effects and substitutional behaviour can be illustrated by plotting the As, Si and O peaks on the same depth scale as shown in Figure 6.12 for the as-implanted, 10s, 60s and 120s samples. The O peaks have had the Si dechannelling level subtracted. It clearly shows the following observations already made, i) that the Si peak contains scattering from the Si atoms in the oxide layer and scattering of Si atoms around the As peak, ii) the segregated As peak is located

underneath the SiO_2 layer, iii) it appears that some suboxides exists around the segregated As peak.

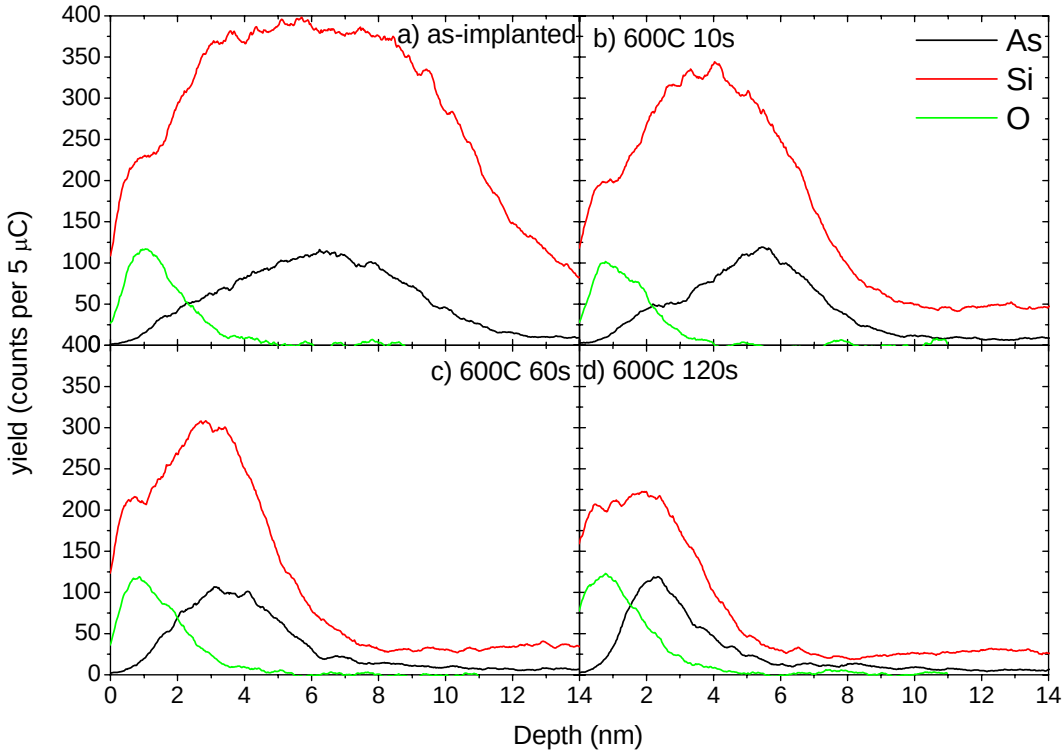

Figure 6.12 As, Si and O depth profiles for the 3 keV As implanted samples, as-implanted and following 600 °C annealing for different durations.

SIMS analysis was carried out at with 0.5 keV and 0.25 keV Cs^+ primary beams and no appreciable difference was observed between the two energies. The SIMS profiles for some of the annealed samples are shown in Figure 6.13a) using a logarithmic concentration scale and in Figure 6.13b) using a linear concentration scale. Note that the depth range is different in the two figures. A profile from an equivalent as-implanted sample is included in Figure 6.13a). Only minor differences are observed between the profiles of the annealed samples and this as-implanted case beyond the near surface, i.e. deeper diffusion does not occur. The lack of diffusion to greater depths is crucially important in determining the usefulness of this type of annealing for the production of shallow junctions. Figure 6.13 shows clearly that the As profiles are changed little upon annealing for concentrations below ~2E21 cm^{-3}. This concentration is of the order of the maximum solid solubility (21, 22). However clear changes for concentrations higher than 2E21 cm^{-3} do occur, which are most clearly seen in Figure 6.13b) which has a reduced depth range. SIMS profiles agree with the trend of the MEIS results in terms of the segregation of As that cannot be accommodated in the

regrown layers. It should be noted that the depth and concentration accuracy of the MEIS profiles in the near surface region is better than the SIMS profiles.

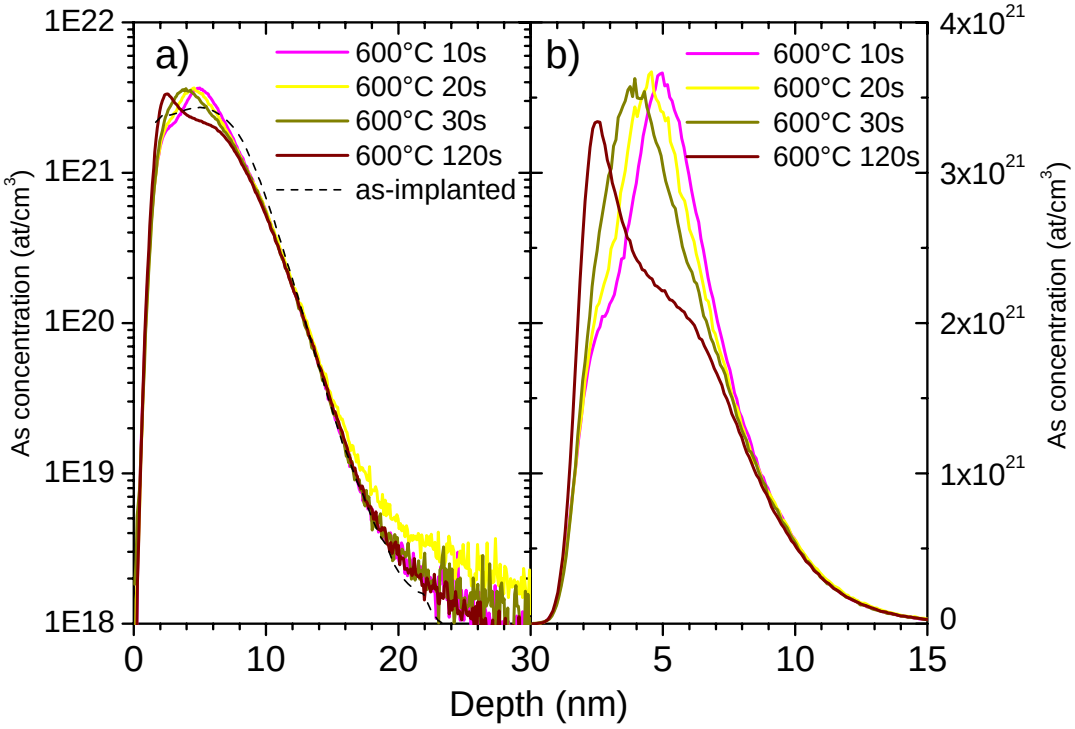

Figure 6.13 SIMS results for samples annealed at 600 °C for different durations.

In terms of the electrical activation, Hall effect measurements using the van der Pauw technique have been carried out on these samples, the sheet resistance and activated dose results are shown in Figure 6.14. For the samples that have regrown the sheet resistance is around 750 Ω/□. This value is higher than the requirements currently predicted in the ITRS.

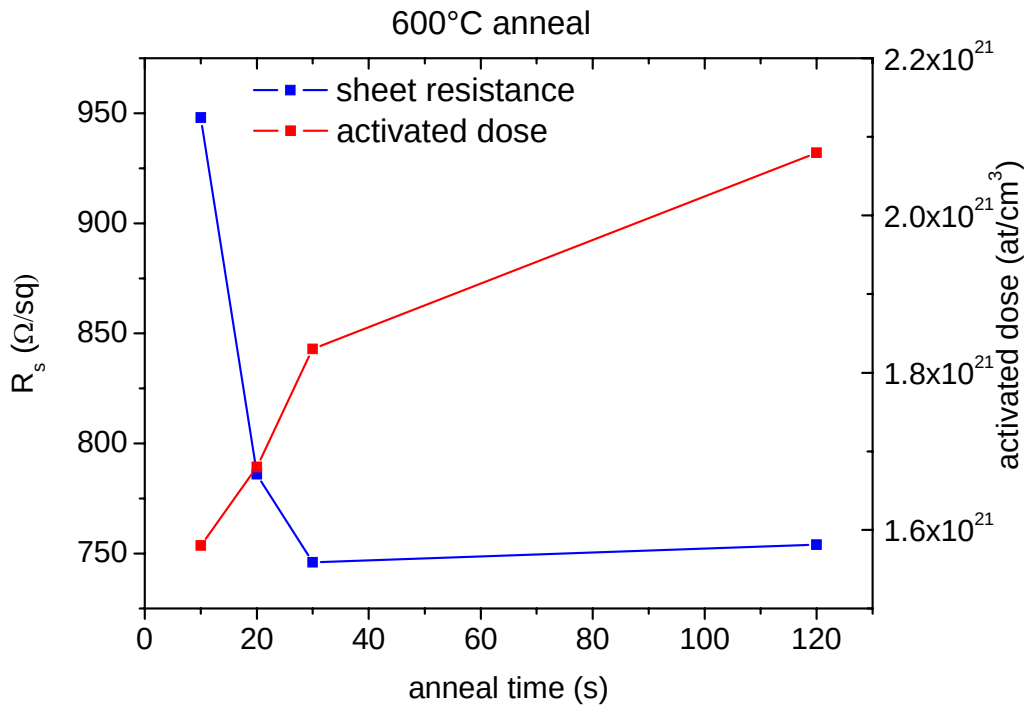

Figure 6.14 Sheet resistance and activated dose for a 600 °C anneal with different anneal durations.

6.3.2.2 Isochronal series

An isochronal anneal series was produced from the same wafer as the isothermal series. Anneals for 10s duration were carried out at 600 °C, 650 °C and 700 °C. MEIS, SIMS and Hall effect measurements were carried out on these samples with the same conditions as used for the isothermal series. MEIS energy spectra are shown in Figure 6.15. Included in the figure is the random spectrum from an amorphous Si sample and an as-implanted spectrum. Depth scales have been added to the figure for scattering off As and Si. The differences in regrowth rates with temperatures are reflected in the level of regrowth of these samples. The higher anneal temperatures with faster regrowth rates have produced a much fuller regrowth. An interesting feature in the 700 °C sample is a small bump in the Si background level at an energy of 76 keV, equivalent to a depth beyond 12 nm, with the yield scale blown up in the inset. This may correspond to a distortion of the Si lattice around defects in the EOR region. As with all samples the shape of the As peaks is related to the depth of the regrown Si layer. The sample annealed at 700 °C produces a quite well regrown layer, with a small segregated As peak. In fact the spectrum from sample annealed at 700 °C for 10s is very similar to that from the sample annealed at 600 °C for 120s.

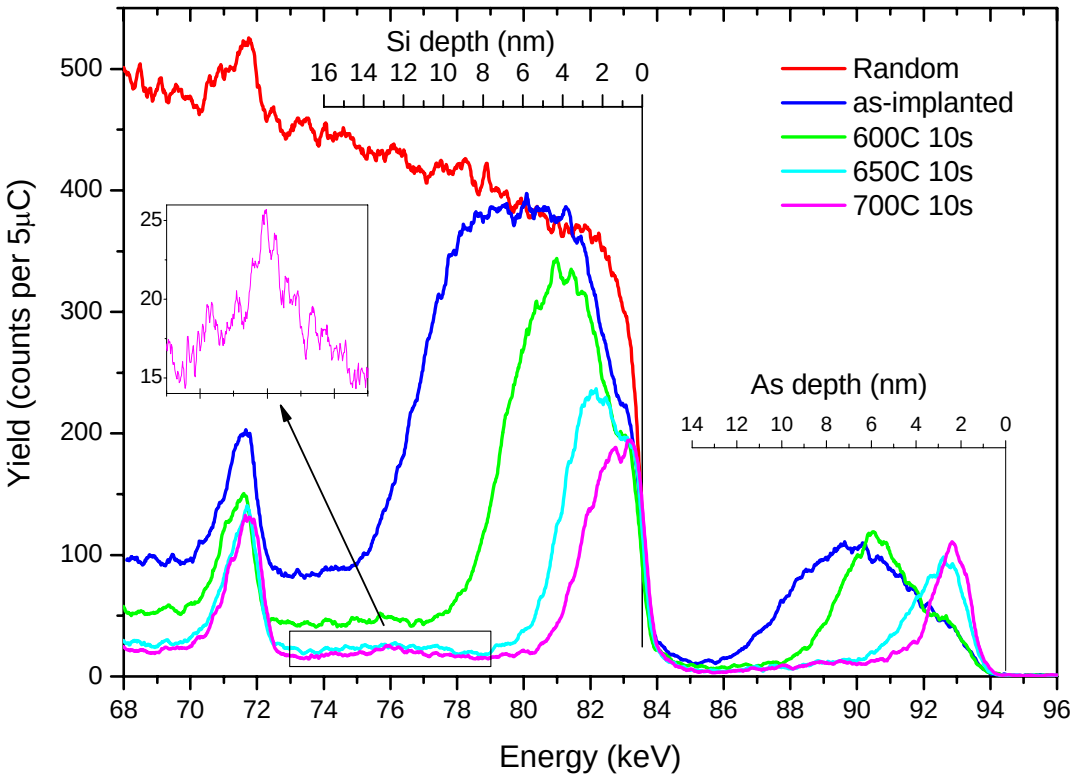

Figure 6.15 100keV He MEIS energy spectra for the [111] blocking direction, for 3keV As 2E15 implanted samples annealed for 10s at 600 °C, 650 °C, and 700 °C.

SIMS profiles for these samples are shown in Figure 6.16 a) and b). The two graphs contain the same data set but are plotted with different scales on the axes, as before. There has not been diffusion deeper into the bulk following these anneals (Figure 6.16a)). The segregation behaviour of As observed in MEIS is again seen in SIMS, (Figure 6.16b)).

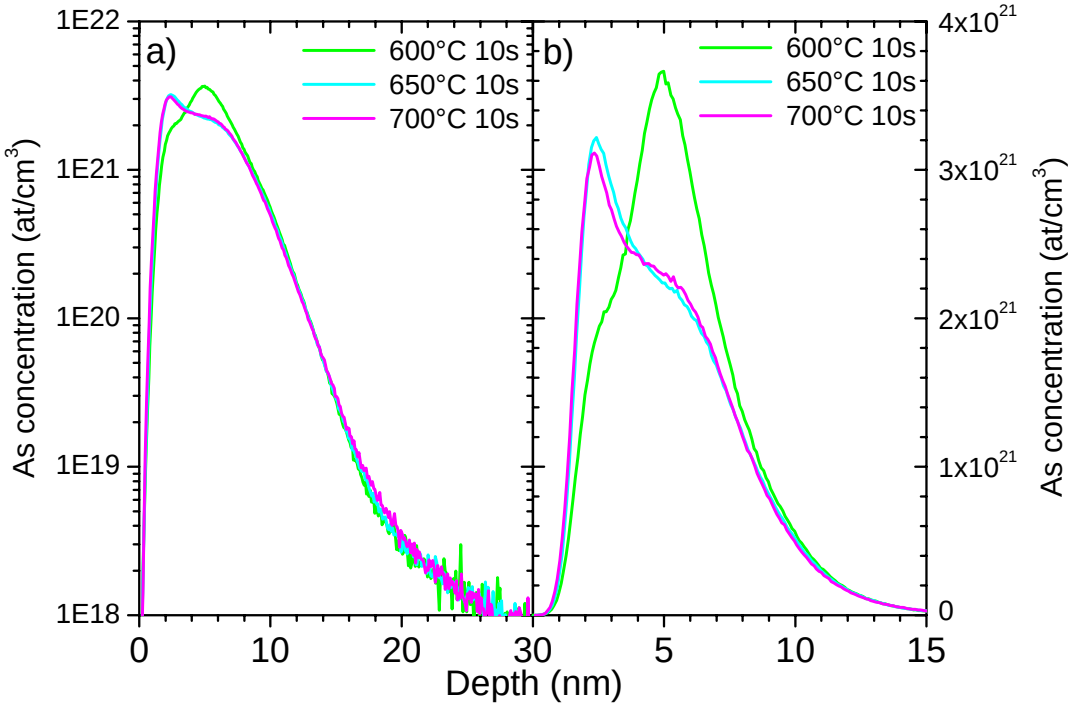

Figure 6.16 0.5 keV Cs^+ SIMS As depth profiles for the 3 keV implanted samples annealed for 10s at 600 °C, 650 °C and 700 °C.

A direct comparison of the MEIS and SIMS depth profiles for these samples is shown in Figure 6.17 using the same depth scales for a) 600 °C, b) 650 °C and c) 700 °C. The MEIS spectra have been converted into As concentration profiles to enable proper comparison with the SIMS profiles. As previously mentioned SIMS has some inherent problems in calibration of the first couple of nanometres in terms of depth and concentration, which does mean that the SIMS results have limited accuracy and this must always be born in mind. MEIS (in the double alignment mode) is sensitive only to non substitutional As atoms. SIMS however sees all of the As, and so the substitutional fraction can be inferred.

In Figure 6.17a) the profiles for the sample annealed at 600 °C for 10s is given. From the MEIS results in Figure 6.15 it can be seen that for this sample there has been some regrowth at a depth of 8 – 10 nm (As peak), including a small amount of segregation visible between (5 – 6 nm) and only a small amount of As has taken up substitutional positions in the regrown layers (8 – 10 nm). In view of this, the MEIS and SIMS profiles would be expected to be similar, as is the case. The SIMS profile contains some extra As compared to MEIS in the region of 8-10 nm, at a depth where there is some substitutional As. Extra As observed in the SIMS profile in the region of 0 - 4 nm is likely to be caused by inaccuracies in the SIMS calibration.

For the sample annealed at 650 °C, where there is a major change in the MEIS profile the differences between the results from the two techniques are clearly visible. The SIMS profile shows a great deal of extra As from a depth of 4 – 12 nm and this, as argued above, must represent substitutional As. For the 0 – 4 nm depth range the SIMS profile is higher than the MEIS profile. This is most likely due to the comparatively large uncertainty in the calibration of the concentration in SIMS. A similar picture is seen with the sample annealed at 700 °C. The segregated peak has tightened up as seen in both MEIS and SIMS, and again SIMS probably overestimates the segregated peak concentration. However the substitutional fraction from 4 – 12 nm can be clearly seen.

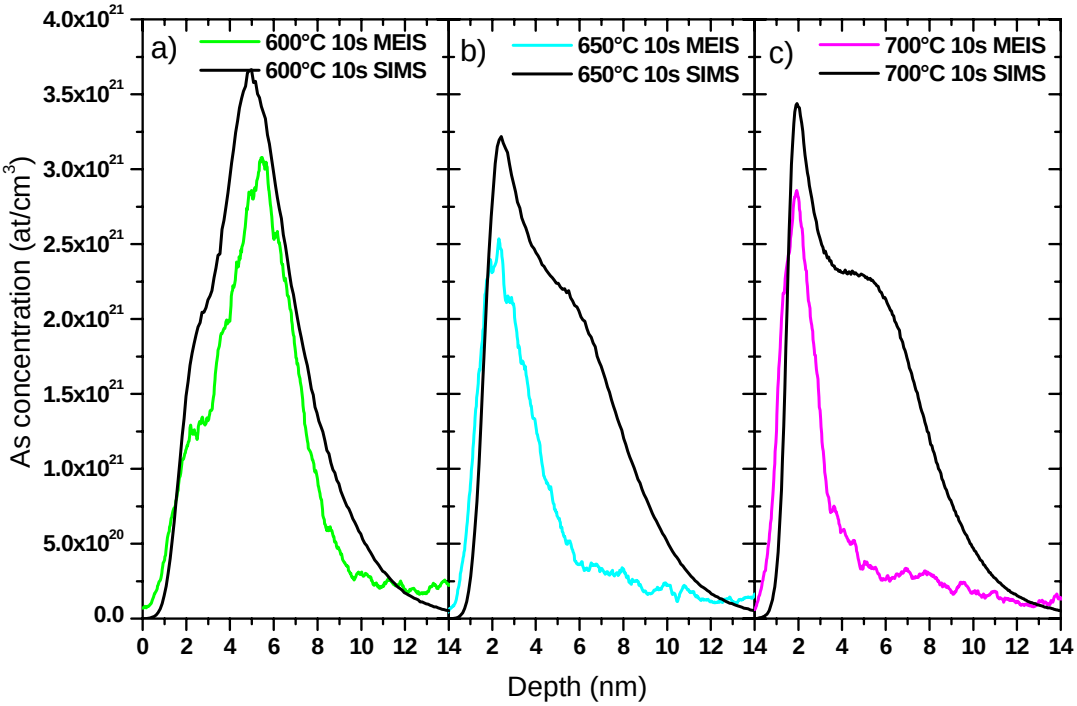

Figure 6.17 MEIS and SIMS combined depth profiles.

Hall effect measurements were carried out on these samples, and the results are given in Figure 6.18. The sheet resistance was as low as 610 Ω/□ for the sample annealed at 650 °C for 10s. The 700 °C had a slightly higher R_s value of 684 Ω/□. It is suggested that this could be due to As clustering at the higher temperature. From these measurements the activated dose can be obtained and this was found to be in the region of 2.2E14 -2.4E14 cm^{-2} which is in reasonably good agreement with the values that could be obtained from the shoulder height in the SIMS comparison in Figure 6.17, which lends support to the validity of the comparisons.

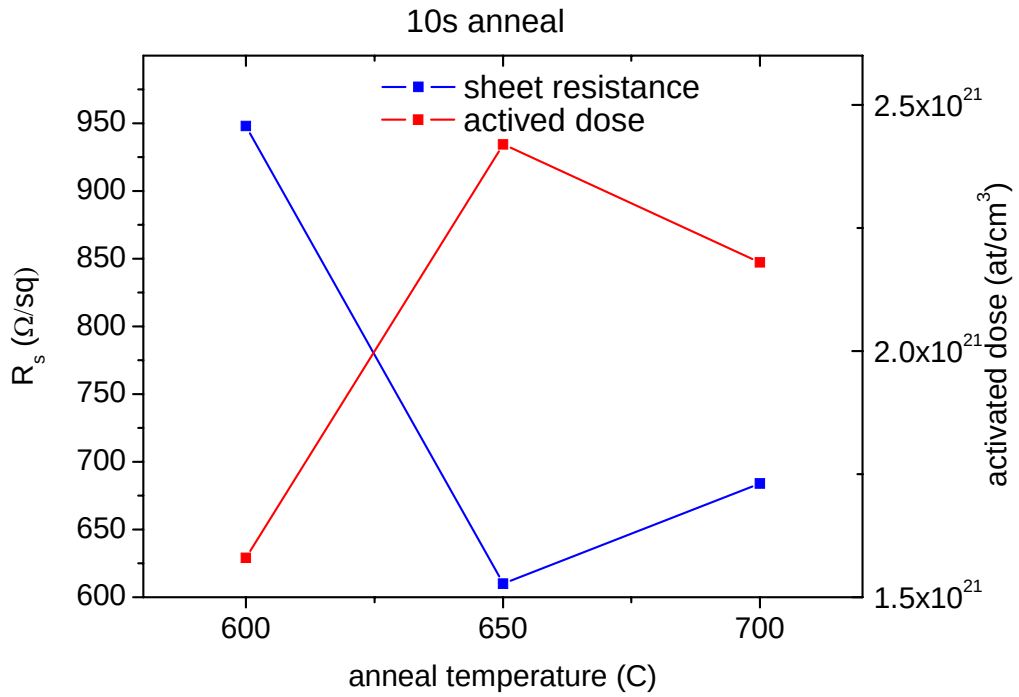

Figure 6.18 Sheet resistance and activated dose for 10 s annealing at different anneal temperatures.

6.3.3 MEIS and XRD study of SPER on Cz and Epi 3 keV As – Comparison of the two techniques

A set of samples using the same implant conditions as discussed with the previous section, i.e. 3 keV As^+ 2E15 cm^{-2}, were produced. Implants were carried out into both Cz and Epi Si wafers. Several different anneals were used to capture different stages of the SPER. The samples were studied with X-ray techniques (XRD, SR and GI-DXS), reported in more detail elsewhere (19). A comparison of the results from MEIS and XRD studies are presented in this section.

Samples were implanted with 3 keV As ions, to a dose of 2E15 ions/cm^2, into crystalline Cz and Epi Si wafers. Cz and Epi samples then underwent simultaneous anneals with temperatures and times of 550 °C: 200 s; 600 °C: 20 s; 650 °C: 10 s; and 700 °C: 10 s were chosen based on the requirements of the defect studies.

6.3.3.1 MEIS

MEIS was carried out using 100 keV He^+ ions, with the samples aligned to the beam along the [$\bar{1}$11] channelling direction and the analyser positioned to collect data along the [111] blocking direction. The MEIS energy spectra of the as-implanted and

annealed samples are shown in Figure 6.19. A random spectrum, from an amorphous sample and a spectrum from a virgin Si sample are included in the figure for reference. Approximate depth scales, for scattering off As, Si and O atoms have been added to the figure.

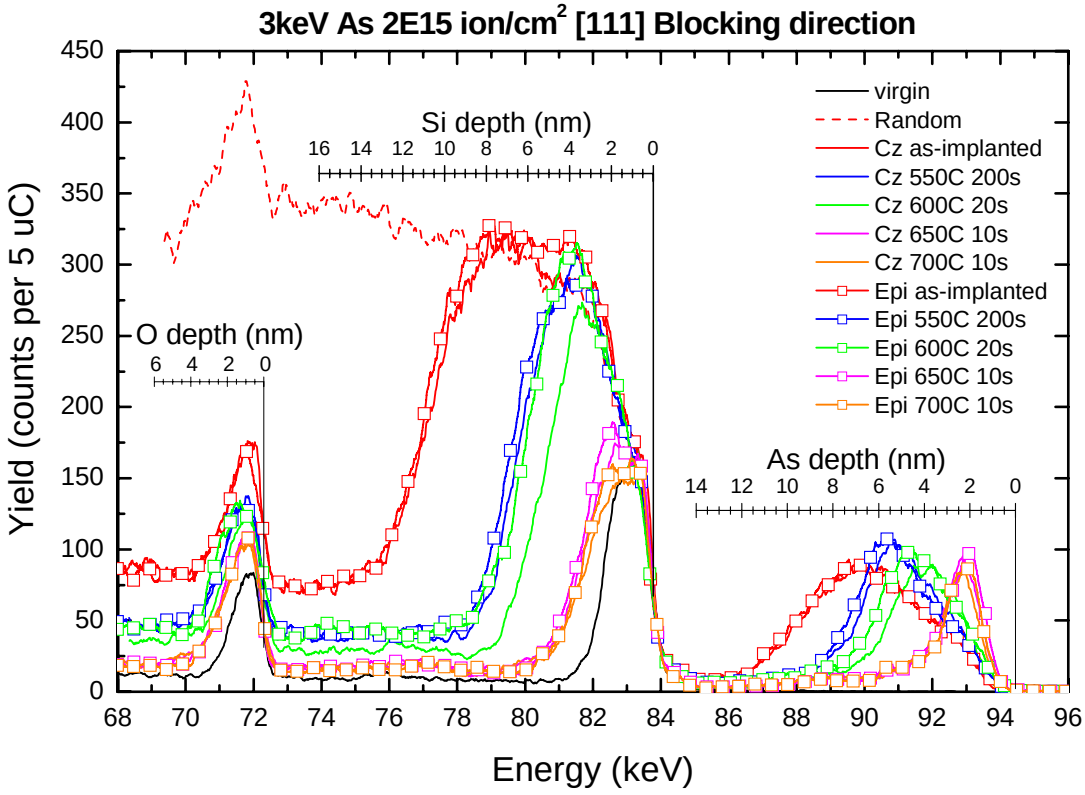

Figure 6.19 MEIS energy spectra for the Epi and Cz Si samples, implanted with 3 keV As, as-implanted and following various anneals.

The spectra of both the Cz and Epi as-implanted samples show that there are no observable differences using MEIS between the Cz or Epi implanted silicon wafers. None are expected in view of the rapid amorphisation rates in Si for As ions. The arsenic peaks coincide and the depths of the back edges of the amorphous layer to are within 0.2 nm.

Although the temperatures and times do not follow a systematic isothermal or isochronal series, the different anneals have captured various stages of regrowth along the way to fully regrown crystalline Si. The 550 °C 200 s annealed Si sample has regrown to a depth of ~ 7 nm, and the 600 °C 20 s anneal to a depth of ~ 6 nm. For the samples annealed at 650 °C 10 s and 700 °C 10 s the regrowth process is almost complete. Any minor differences with the previous set of samples (section 6.3.2.2) can be ascribed to small differences between the anneals.

Following annealing it was observed that at the lowest temperatures used, the regrowth was marginally slower in the Epi silicon than the Cz silicon. With the 550 °C Epi sample the depth of the half height of the silicon damage peak is at 7.3 nm, while the Cz sample is ~ 0.4 nm closer to the surface. This behaviour is replicated in the position of the half height of the back edge of the arsenic peaks, which are at the same depth as the corresponding silicon damage layer. A small amount of segregation has occurred, as shown by the additional build-up of arsenic in front of the as-implanted peak, (at a depth of 4 to 7 nm). The 600 °C 20 s anneal also does not produce a fully regrown layer. Here the difference between Cz and Epi silicon appears to be the starkest, with the Epi sample regrown to a depth of 6.4 nm and the Cz has regrown by a further 0.9 nm to a depth of 5.5 nm. This is repeated in a similar fashion for the back edges of the arsenic peak, which appears to be contained within the depth of the silicon damage layer. The higher temperature anneals at 650 °C and 700 °C produce a much better crystal regrowth. All have a silicon surface peak extending to a depth of 3.5 – 3.8 nm. Again the Epi samples are marginally thicker than Cz ones.

6.3.3.2 X-ray Techniques

Both the Epi and Cz sample series were studied using combined x-ray scattering methods (18-20). A summary of GI-DXS and SR findings reported in (19, 20), is given. GI-DXS results showed that the EOR region contained point defects, and that the depth of the EOR region is the same for all samples. The signal from the EOR region was weakest in the 700 °C annealed sample. The segregated As peak provides enough electron density to produce an oscillation in the SR spectra for the 650 °C and 700 °C samples in the same way as for the RTA samples described in section 6.2.3.3. However this contrast is weaker than for the spike annealed sample, and does not provide any new information. The results are not presented here.

XRD results provide an interesting comparison with MEIS. Before this comparison is made in section 6.3.3.3, the XRD results are briefly summarised. XRD measurements have been carried out on the (004) Bragg peak for both the Epi and Cz series. The two series give very similar results, as was also observed with MEIS. Only the data for the Epi series is shown in Figure 6.20. They show an oscillation with a period getting shorter with increasing annealing temperature. The slope of the intensity is associated with disorder and/or roughness at the a/c interface, while the oscillation is related to the interference between this interface and the EOR defects region.

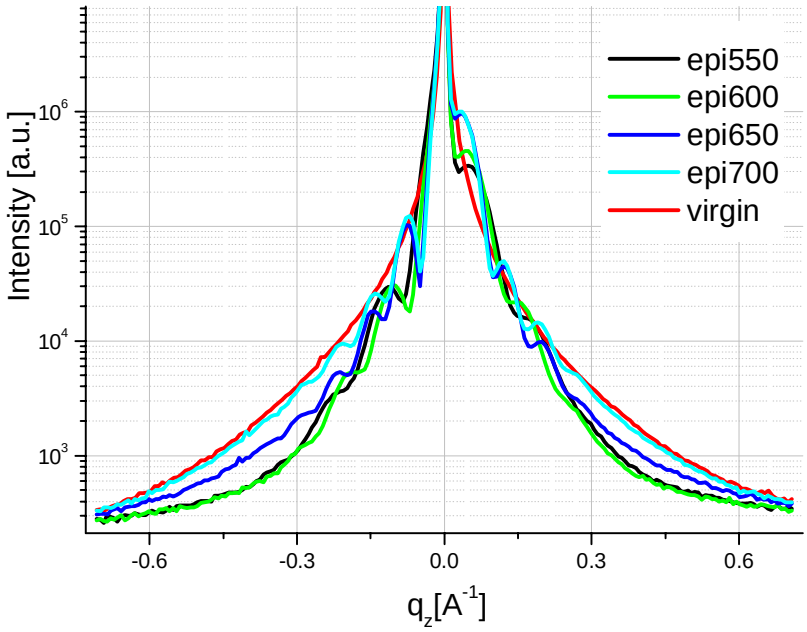

Figure 6.20 Radial scan through (004) Bragg reflection for the Epi series and a virgin sample. From (18, 19).

These XRD curves have been simulated and the strain profiles and static disorder parameter L_h resulting from the best fits are shown in Figure 6.21 a) and b) respectively. Three regions are observed and are indicated in the figure. 1) A layer at and just below zero depth with positive strain and high static disorder. 2) A central area with no or negative strain accompanied by no static disorder, 3) a deeper layer with high positive strain and low static disorder. The three layers are attributed to the region at the a/c interface, the regrown, electrically active layer and the EOR region respectively. The main features to note with these results are the increases in the width of the recrystallised region in between the EOR region and the surface with increasing anneal temperature. Also after annealing to 650 °C and 700 °C the onset of the negative strain at depths between 1 and 10 nm, is attributed to the As occupying substitutional sites or forming inactive As_nV clusters.

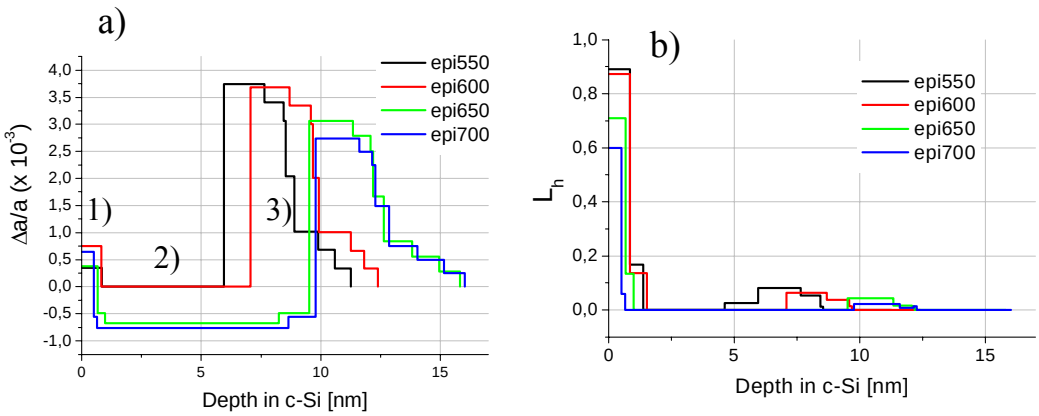

Figure 6.21 a) Lattice parameter strain profile in the growth direction resulting from the best fit. b) Static disorder depth profile resulting from the best fit. From (18, 19).

6.3.3.3 Comparison between MEIS and x-ray scattering results

Both XRD and MEIS techniques are sensitive to the regrowth of the amorphised Si during the annealing but in different ways. While MEIS measures the disordered Si, XRD is sensitive to the crystalline part of the sample. Figure 6.22 shows a plot of the width of the SPER layer measured by MEIS against that by XRD. There is a linear relationship with a constant offset between the results from the two measurement techniques. It follows that the definition of the reference points, which the regrown layer thickness is measured between, is different for the two techniques but otherwise the results tell the same story. The differences become evident when the details of the measurements are considered.

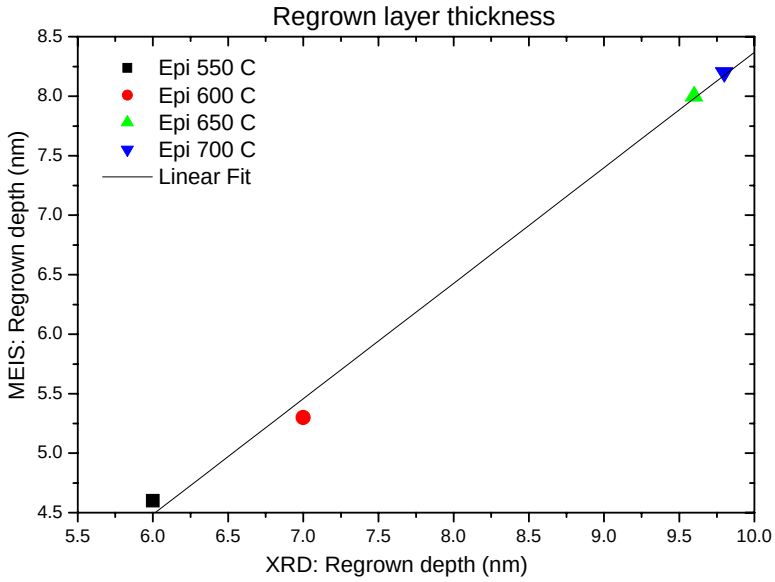

Figure 6.22 Thickness of the regrown layer: comparison between MEIS and XRD results. The constant off-set is due to the different definitions of the start and points for the two techniques.

The “zero” depth point in the MEIS depth profiles is always taken at the sample surface, and the depth of the a/c interface is measured in relation to the surface. XRD however takes the “zero” point of the depth scale at some depth in the region of the amorphous to crystalline interface as it is only sensitive to the crystalline material and hence does not “see” the amorphous Si. Obviously this point is at a different depth for each sample. The other difference between the techniques that affects the recrystallisation depth measured, results from differences in criteria for the end point. The depths in MEIS are based upon the a/c interfaces and as such the regrown layer thickness is determined by subtracting the depth of the a/c interface following annealing from the depth of the original a/c interface. In XRD the end point is the strained region around the EOR defects. This would be deeper than the a/c interface. The regrown layer thickness is given from the distance between this point and the region of strain near to the zero depth point below the a/c interface, i.e. the distance between region 1 and 3 shown in Figure 6.21a).

In Figure 6.23 the strain profiles obtained from XRD measurements (Figure 6.21a)) have been rescaled by a shift of each profile for direct comparison to the MEIS spectra in the following way. The EOR damage region, which causes the strongest contrast in XRD curves, has been arbitrarily located at the back edge of the as-implanted Si amorphous layer and its position has been kept fixed during the annealing, as would be expected for EOR defects in this temperature range. The peak is located at a depth of 13.5 – 16.5 nm. As a result of this rescaling of the depth, Figure 6.23 shows the disordered Si profile from MEIS superimposed by the lattice strain profile from the fits of the XRD curves. The a/c interface from XRD always aligns with the back edge of the Si peak in MEIS (i.e. area of strong lattice disorder).

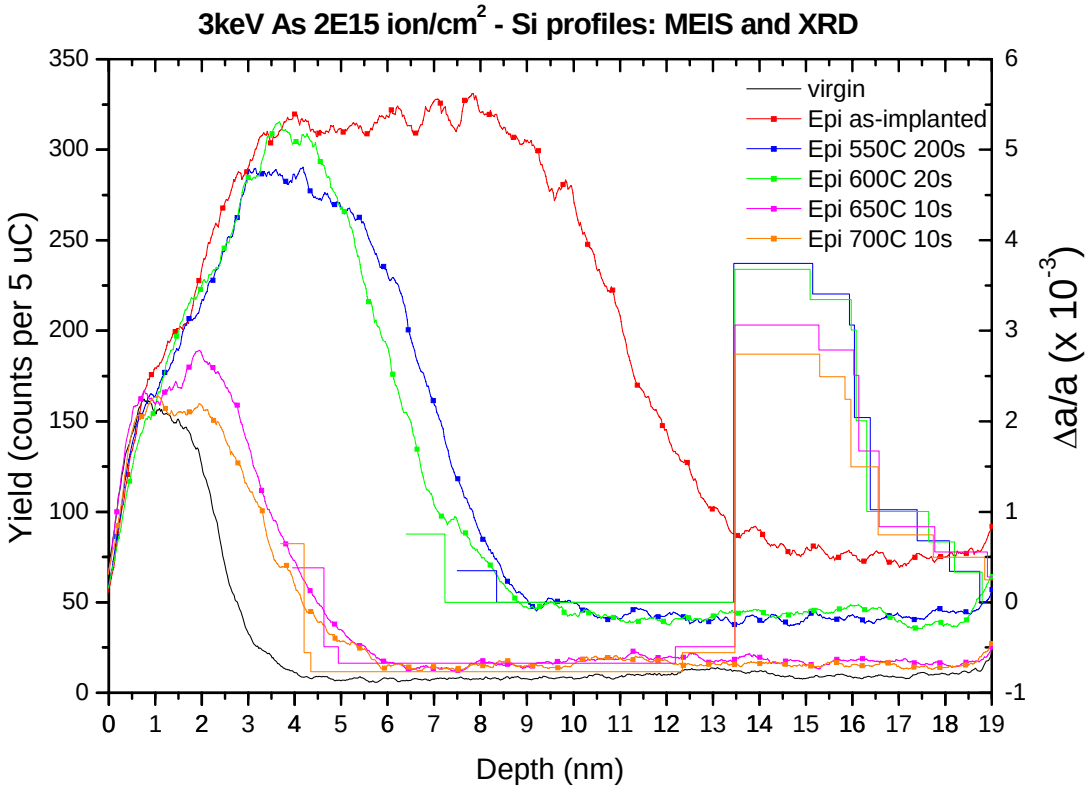

Figure 6.23 Comparison of MEIS depth profiles with the strain profile from XRD after rescaling of the depth.

This procedure demonstrates the excellent agreement of the SPER thickness measured by the two techniques. In fact both of the comparisons of MEIS with X-ray studies (section 6.2.3.3 and 6.3.3.3) give corroborative results. It has again been shown how MEIS can be used as a starting point in the interpretation of the results of the X-ray studies, which could become increasingly useful for future defect studies.

6.4 SOI regrowth

6.4.1 Introduction

Annealing studies have been carried out to investigate the regrowth behaviour of silicon on insulator (SOI). SOI wafers are produced from two bulk Si wafers. An oxide layer is grown on one of the wafers, which subsequently forms the buried oxide layer. Hydrogen ions are implanted through the oxide into the underlying silicon and form a damage layer containing H bubbles at the end of the ions range. The two wafers are then bonded together using Van der Waals forces. The implanted wafer is then cut across the damage plane leaving a thin layer of Si, which is then polished, on top of a buried oxide layer (23). The process is called Smart Cut (24, 25). The wafers used in these studies have either a 60 nm, 88 nm or 100 nm Si layer on top of a buried SiO_2 layer

approximately 200 nm wide. Implants have been carried out similar to the ones used previously. Annealing conditions used have been predominantly in the low temperature range (550 °C to 700 °C) in order to capture intermediate stages of regrowth, rather than using higher anneal temperatures typical of device production for which the regrowth occurs too quickly. It will be seen that for PAI implant energies which are sufficiently high for some damage to extend to the buried oxide (BOX) interface, regrowth is different from the normally layer-by-layer regrowth, probably through changed seed conditions at the start of the regrowth.

6.4.2 Experimental

A range of samples were produced to compare the regrowth of 60 nm, 88 nm and 100 nm SOI wafers with bulk Si wafers. Implantation was carried out using conditions typical for As and BF_2 extension implants into crystalline and Xe pre-amorphised wafers, (3 keV As, to fluences of 2E15 cm^{-2} and 1E15 cm^{-2}, 3 keV and 1 keV BF_2 implants to a fluence of 7E14cm^{-2}). For the PAI samples 40 keV Xe was implanted to a fluence of 1E14cm^{-2}. Anneals were carried out at the University of Salford. MEIS was carried out with 100 keV He^+ and the samples were aligned along the [$\overline{1}$11] direction and the analyser positioned to record the [332] and [111] blocking directions. The results from the [111] direction are presented.

6.4.3 Results

Results of several experimental series are presented in the next few subsections and an overall discussion, based on all the results, is given in section 6.4.4.

6.4.3.1 No – PAI samples

MEIS energy spectra for samples implanted with 3 keV As ions to a dose of 2E15 ions/cm^2 into crystalline bulk Si, 60 nm SOI and 100 nm SOI, respectively, are shown in Figure 6.24, for as-implanted samples and following annealing at 600 °C for 30 s. Also included in the figure is a spectrum from a virgin Si sample and a random spectrum taken from an amorphous Si sample. Depth scales have been added to the figure to give an indication of the depth of scattering from As, Si and O atoms, respectively. The implantation, as is typical, produces an ~ 11 nm wide amorphous layer. For the as-implanted samples there are no major differences observed between the different wafer types. Following annealing all samples have undergone SPER of part of the amorphous layers, with the surface damage peaks extending to a depth of ~ 7 nm

(FWHM). Concomitantly, As in the regrown region has taken up substitutional positions invisible to the analysing beam. A small amount of As segregation has occurred, as evidenced by the slight As yield increase at a depth around 5 nm. These findings are entirely similar to those described in section 6.3. No major differences between the different materials are observed. With these shallow implants the implant is well away from the BOX. In this instance the SOI materials would be expected to behave as bulk material, as observed.

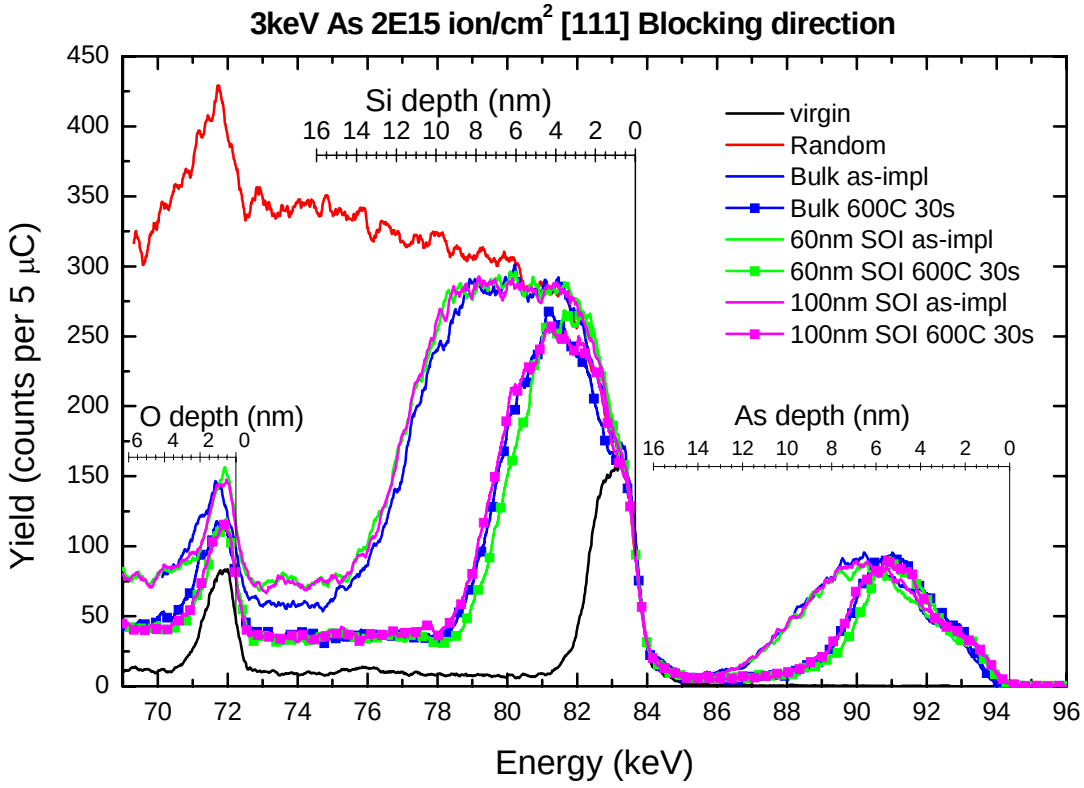

Figure 6.24 MEIS energy spectra from bulk Si, 60 nm SOI and 100 nm SOI samples, implanted with 3 keV As to a dose of 2E15 ions/cm^2, as-implanted and following annealing at 600 °C for 30s.

6.4.3.2 60nm SOI PAI (40 keV Xe) 3 keV As 1E15

A 60 nm SOI wafer was pre-amorphised with 40 keV Xe^+ (PAI) to a dose of 1E14 ions/cm^2. XTEM results (not shown) reveal that the PAI produces an amorphous layer to a depth of approximately 35 nm (13). The PAI was followed by a 3 keV As implant to a dose of 1E15 ion/cm^2. Note that the As dose was half that of the As implants previously used in this project, (in section 6.2 and 6.3). This would not be expected to fundamentally affect the regrowth mechanism, but probably the regrowth

rate. Samples were annealed at temperatures of 550 °C, 600 °C and 650 °C, respectively, for different durations and several higher temperature anneals were carried out.

The MEIS energy spectra for samples annealed at 550 °C for 200 s, 500 s and 600 s are shown in Figure 6.25a). For all samples the regrowth is clearly not "standard" SPER as seen on bulk Si samples. The back edge of the Si damage peaks is stretched and distributed over a greater depth than would be expected for standard layer-by-layer SPER, even accounting for energy straggling. For example Figure 6.24 is typical for a sharp amorphous crystalline interface. The broad amorphous / crystalline interface, of ~13 nm, is most pronounced in the sample annealed for 600s, where a lower dechannelling level and less overlap with the O peak allows more of the a/c interface profile to be visible. This broad a/c interface profile is unusual and has not been observed in our previous MEIS studies on bulk Si (4, 5). There is no single clearly definable depth for the location of the amorphous / crystalline interface.

The As profiles have not changed compared to the as-implanted profile in Figure 6.25 following any of the anneals at 550 °C. For the sample annealed for 200s this should be expected, regrowth has not passed the depth of the As. For the sample annealed for 500s, again this is not too surprising. Regrowth has not come closer to the surface than 12 nm, which is close to the depth of the end of the As profile. For the sample annealed for 600s however, clearly some Si recrystallisation has occurred at depths between 6 and 14 nm but the As present at those depths has not taken up substitutional positions or become segregated. This behaviour has not been seen with the bulk Si samples.

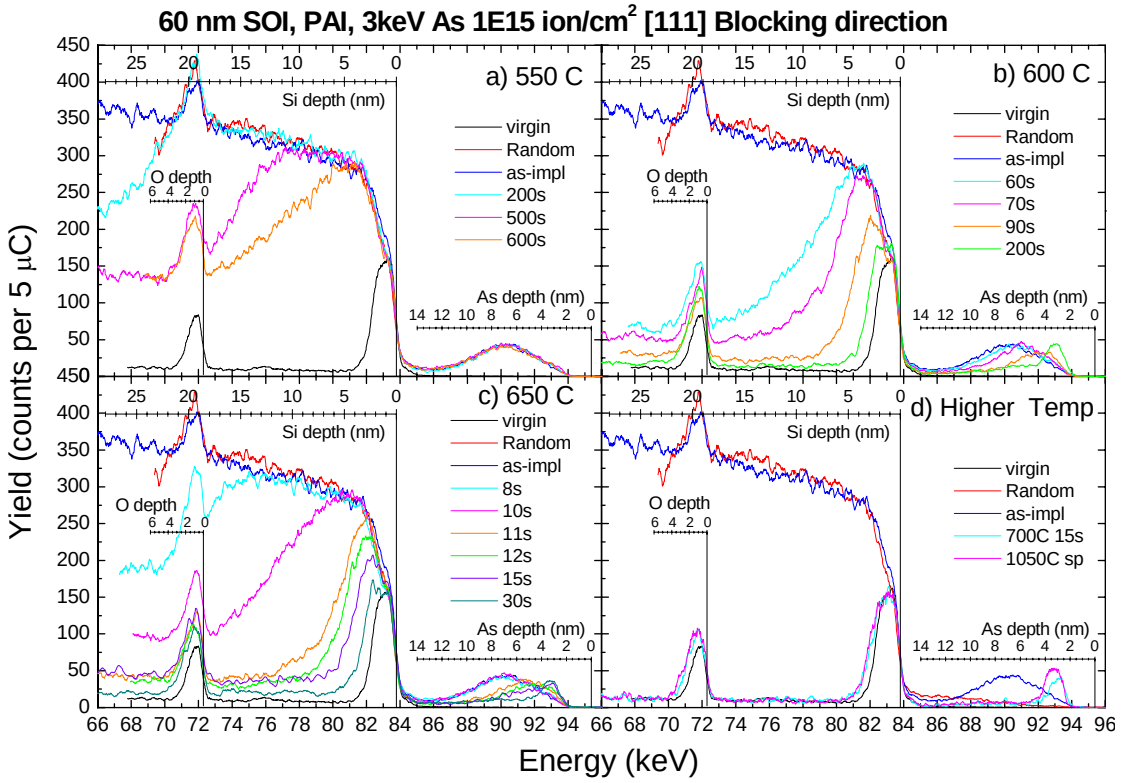

Figure 6.25 MEIS energy spectra from 60 nm SOI samples, pre amorphised with 40 keV Xe 1E14 cm^{-2} and implanted with 3 keV As to 1E15 cm^{-2}, annealed at a) 550 °C, b) 600 °C, c) 650 °C, and d) higher temperatures.

Results from the samples annealed at 600 °C are shown in Figure 6.25b. The anneal times used, appear to have captured stages in the regrowth process that follow on from the sample annealed at 550 °C for 600s. The sample annealed for 60 s shows a profile that could be thought to consist of different damage regions. There is an ~ 7 nm wide fully amorphous layer beyond which there is region, at depth from 7 to 16 nm, with a high level of residual damage, as evidenced by a scattering yield substantially above the dechannelling level of around 75 counts. For the sample annealed for 70 s the amorphous layer has reduced to ~ 5 nm and is accompanied by a considerable, but not complete, regrowth of the residual damage region seen with the 60 s anneal. Annealing for 90 s produces a further reduction in the width of the surface peak and a substantial reduction in the residual damage. Annealing for 200 s produces an almost completely regrown layer. Here the additional width of the Si peak relative to the virgin spectra is to some extent accounted for by the increased oxide layer thickness. However the height of the Si peak is greater than that of the virgin sample suggesting that the layer is still not quite fully regrown. For this series of samples a general sharpening-up of the a/c

interface around the depth of the As peak and surface occurs. With regards to the As profiles, for the sample annealed for 60 s, where there is more regrowth than in the case of the 550 °C 600 s sample, there is a marginal change in the As peak relative to the as-implanted spectra, consisting of a small but detectable reduction of the As peak at a depth between 6 and 12 nm. Considering there is considerable recrystallisation of areas of the Si within this depth region, the change in the Si shape at those depths is remarkably small. A small amount of segregation has occurred, as seen by the slightly increased As yield between 3 and 6 nm. Overall, integration of the peak shows a reduction in the peak area of only 3.5 % compared to the area of the as-implanted sample. For increasing anneal durations (≥70s) there is a greater amount of substitutional As, as well as As segregation. During SPER on bulk Si, there is normally very little or no As left visible in regrown layers, however this is not the case with these samples. The sample annealed for 200s gives the clearest example of this, 58% of the implanted As is still visible with the MEIS beam, 32% is within the segregated peak but 26% of the implanted As remains visible within the regrown layers at a depth between 4-12 nm. From this it must be concluded that the unusual regrowth behaviour also appears to affect the perfection of the regrowth and the As moving into substitutional positions. In view of the fact that for a 3 keV 2E15 As implant, ≥ 50% segregation is found (4) only a small segregation effect would ever be expected for these conditions for full regrowth, assuming that segregation is driven by solid solubility limitations.

The samples annealed at 650 °C go through the same stages of regrowth, albeit achieved with shorter anneal durations, as seen in Figure 6.25c). The level of regrowth of the sample annealed at 650 °C for 8s falls somewhere between those annealed at 550 °C for 200 s and 500 s. The sample annealed at 650 °C for 10 s is similar to the sample annealed at 550 °C for 600 s. In both cases a wide a/c interface is present. With longer anneal durations the level of the residual damage layers comes down with increasing time and result in narrower surface peaks as the interface straightens around the depth of the high As concentration. The redistributed As peak is related to the shape of the regrown Si layer, however there is still As visible in regrown areas. For example the 30s anneal causes a segregated As peak as well as visible As in the regrown layers between 4 and 10 nm depth, similar to that observed after a 200s anneal at 600 °C. As with the SPER studies discussed in section 6.3 the rate of regrowth slows down in the As rich regions and may also be affected by the increasing proximity of the surface.

The higher temperature anneals carried out at 700 °C for 15s and 1050 °C spike anneal, shown in Figure 6.25d) with their faster regrowth rates produced a fully regrown layer, with less As visible in the regrown layer and hence a clear segregated peak.

In summary of these results, the wide amorphous / crystalline transition regions observed in the MEIS spectra following anneals where regrowth is not completed are unique for SOI. The continued visibility of the As in the regrown layer, typical for the regrowth of SOI pre-amorphised samples, is also an unusual feature.

6.4.3.3 Bulk Si, 60, 100 nm SOI, PAI, 3 and 1 keV BF_2

Experiments similar to the ones reported above were carried out using BF_2 implants. Samples were produced from bulk Si, 60 nm, and 100 nm SOI wafers, respectively. All samples were pre-amorphised with 40 keV Xe to a dose of 1E14 ions/cm^2, and implanted with 1 or 3 keV BF_2^+ to a dose of 7E14 ions/cm^2.

MEIS results for the 3 keV BF_2 implants into bulk Si are shown in Figure 6.26a) for anneals at 550 °C for 600s and at 600 °C for 60s. For both samples, the regrowth has proceeded in the conventional SPER manner as is usual for bulk Si. There is no wide transition layer from amorphous to crystalline. The anneals have not produced complete regrowth, since there remains a ~ 4 nm wide Si surface peak after the 550 °C anneal and a ~ 3 nm wide Si surface peak after the 600 °C anneal. The growth of the oxide layer thickness only partially accounts for the width of these layers.

MEIS results for 60 nm SOI samples using identical implant conditions are shown in Figure 6.26b), the only difference with this set of samples is the wafer material, i.e. SOI. Si damage profiles with wide a/c interfaces similar to those in the PAI As implanted samples (section 6.4.3.2) are also seen with these samples. The sample annealed at 550 °C for 600 s has a very broad transition from crystalline to amorphous Si taking place over a depth of ~ 14 nm. The sample annealed at 600 °C for 60 s also has high level of residual damage at a depth from 6 to 16 nm, behind a 6 nm wide highly damaged / amorphous surface peak. The samples annealed at 650 °C and 700 °C for 15 s both show good regrowth. This is in contrast to the As implanted sample annealed at 650 °C for 15s, shown in 6.25c), which is not yet fully regrown, attributed to the effect of the high As concentration slowing down the regrowth.

Lastly the 100 nm SOI wafer was pre-amorphised and then implanted with 1 keV BF_2 to a dose of 7E14 ions/cm^2. An equivalent 3 keV BF_2 implanted sample was not available. It is not likely that the different BF_2 energy will cause a fundamentally different behaviour. The results are shown in Figure 6.26c) and they prove almost

identical to the 60 nm SOI series in Figure 6.26b) using 3 keV BF_2 and hence the same observations apply.

Summarising this section, the unusual regrowth of SOI wafers seen with the PAI As implanted samples is also seen with the PAI BF_2 implanted samples. The most significant feature is the wide a/c interface of up to 14 nm width. Upon continued annealing this proceeds towards the surface, where there is a tightening of the a/c interface. The regrowth on the PAI SOI samples appears to be delayed relative to the rate of regrowth in bulk Si.

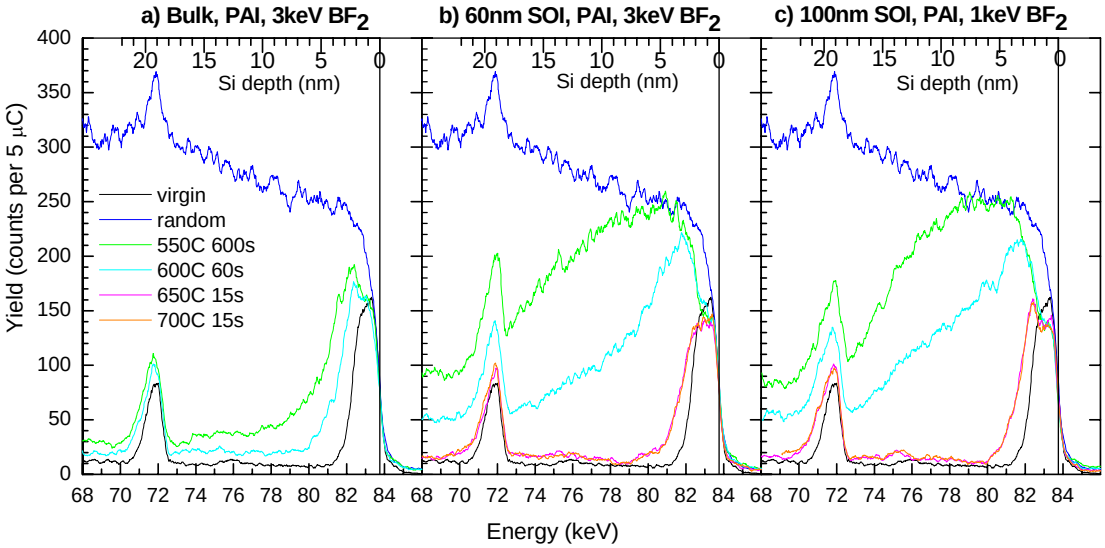

Figure 6.26 MEIS energy spectra from BF_2 samples a) bulk Si, b) 60 nm SOI, and c) 100 nm SOI. In all cases the wafers were pre amorphised with 40 keV Xe to a fluence of 1E14 cm^{-2}. In a) and b) samples were implanted with 3 keV BF_2 and in c) with 1 keV BF_2. Samples were annealed at various temperatures, as indicated.

6.4.3.4 88 nm SOI vs. bulk Si, PAI Xe 40 keV 1E14, As 3 keV 2E15

In order to confirm the differences in regrowth behaviour for bulk Si and SOI, a series of experiments was performed using identical implantations and simultaneous anneals on bulk Si and 88 nm SOI. Both wafers were pre-amorphised with 40 keV Xe to a dose of 1E14 cm^{-2} and implanted with 3 keV As to a fluence of 2E15 cm^{-2}, conditions typically used in this thesis. Samples were annealed at 600 °C for different durations.

Figure 6.27 shows results from 88 nm SOI samples (top) and bulk Si samples (bottom). The SOI samples show the same wider a/c interface as seen with the previous SOI series. The samples annealed for 50s, 60s, and 65s all have downslopes with similar gradients. A linear fit through the slopes illustrates this point more clearly. The slope

becomes steeper for the sample annealed for 70s, around the depth of the high As concentration. In comparison, the bulk samples have downslopes that are generally steeper and become steeper as the thickness of the amorphous layer decreases. This behaviour is as expected for a sharp interface when accounting for energy straggling. As an example to illustrate the differences in amorphous crystalline interfaces between the two wafer types, a comparison of the bulk sample annealed for 30s, that has an amorphous layer thickness of ~ 17 nm, with the SOI sample annealed for 65s, that has an amorphous layer thickness of ~ 11nm (based on FWHM), shows that the SOI sample has a ~ 50% less steep gradient, despite the reduced amorphous layer width.

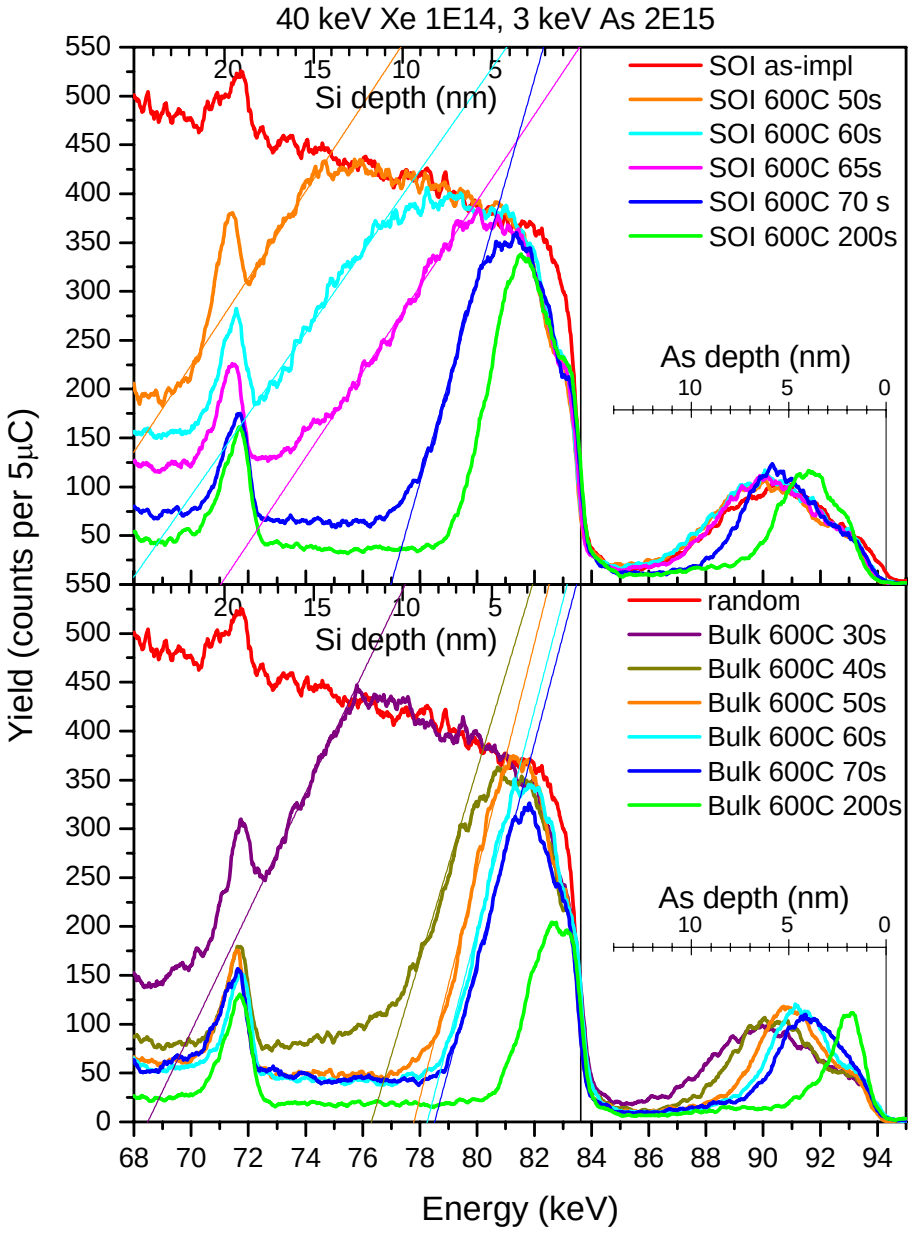

Figure 6.27 MEIS energy spectra for SOI (top) and Bulk Si (bottom) wafers. Samples were pre-amorphised, implanted with 3 keV As to 2E15 and annealed at 600 °C for various times.

The slower, or initially delayed, regrowth on SOI is also apparent with these samples. It is most noticeable with the samples annealed for 50s. For the SOI sample, regrowth to a depth around 20 nm has occurred but the bulk sample has regrown to a depth of approximately 6 nm. The samples annealed for 200s also show a large difference in the amount of damage regrowth between SOI and bulk Si. The samples annealed for 70s appear to show a similar level of regrowth between bulk Si and SOI. However for both samples the a/c interface is at a depth where there is a high As concentration and hence the regrowth rate is very slow. The bulk sample has regrown by an extra 2nm compared to the SOI sample. With the regrowth rate so low in this area this is a significant difference in depth. Indeed the depth of the a/c interface of the bulk Si sample annealed for 70s is close to the depth of the SOI sample annealed for 200s.

6.4.4 Discussion

Before the regrowth mechanisms can be considered it is important to discuss the detail of the a/c interfaces. In Figure 6.28a) and b) are 2D schematic illustrations showing entirely different possible damage scenarios. In these illustrations black represents fully amorphous Si and white represents fully crystalline Si. Different levels of shading of grey represent different levels of damage between amorphous and crystalline. The right hand side of each illustration represents the surface. The approximate shape of the idealised MEIS profile (ignoring energy straggling and system resolution convolution) is given underneath each image. Figure 6.28a) illustrates a situation where there is a gradual transition from the crystalline region with increasing damage until an amorphous layer is reached. In Figure 6.28b) a sharp wavy interface between fully crystalline and fully amorphous Si is presented. Both scenarios would produce a similar shape in a MEIS profile, hence MEIS alone cannot distinguish between them.

To determine the profile XTEM was carried out on the 60 nm SOI sample, pre-amorphised, implanted with 3keV As to 1E15 cm^{-2}, and annealed at 550 °C for 600s (MEIS result Figure 6.25a)). The result is shown in Figure 6.29. It shows that the a/c interface is indeed wavy in an irregular fashion, over a depth range of ~ 14 nm. This in excellent agreement with the depth range of the a/c interface from MEIS results.

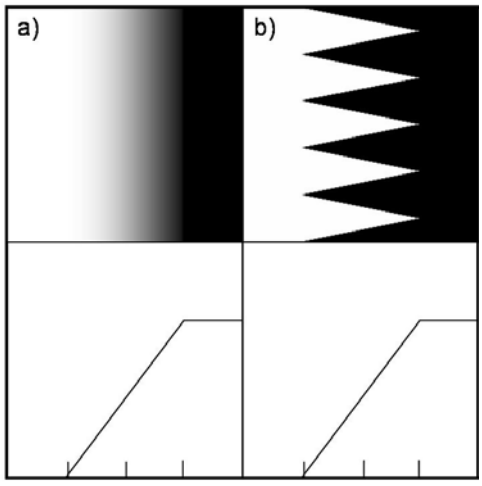

Figure 6.28 Schematic illustrations of possible damage scenarios with the associated idealised MEIS profile.

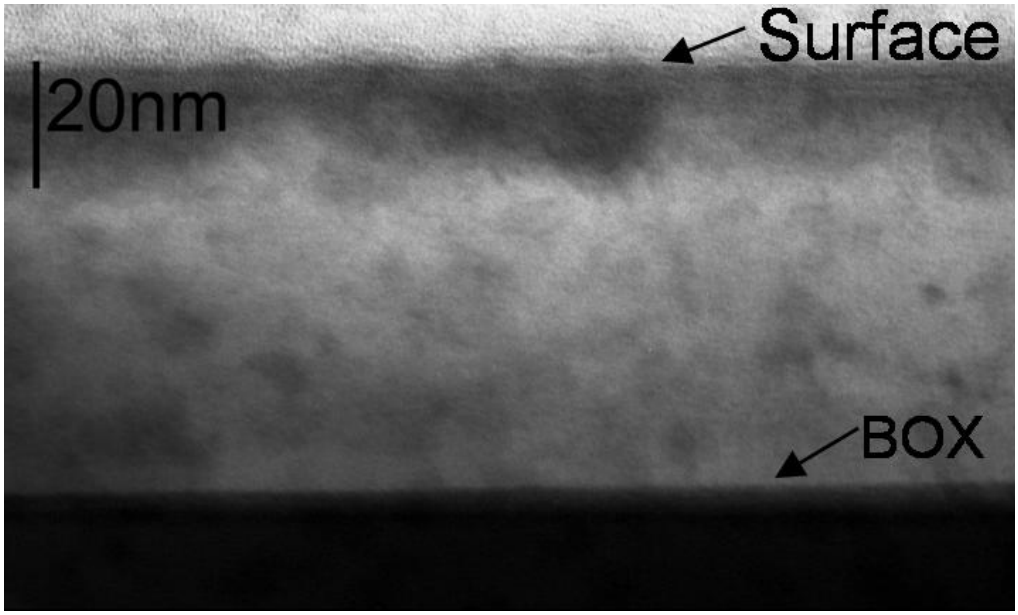

Figure 6.29 TEM image from a sample on 60 nm SOI, PAI, 3 keV As and annealed at 550 °C for 600s.

Analysing the differences observed between the annealing of bulk Si and SOI, the most likely explanation is based on the accumulation of localised damage areas at the buried oxide interface, removing the crystal seed for the regrowth to proceed from in patches. In this section the disorder produced at the BOX is considered for the different studies presented.

TRIM results for a 3 keV As implant are shown in Figure 6.30. The calculated As depth profile along with the vacancy and interstitial depth profiles are shown in Figure 6.30a) whilst a 2D pictorial representation of the calculation is shown in Figure

6.30b). TRIM calculations show the maximum range of the implant and recoil interstitials during a 3 keV As implant does not extend beyond a depth of approximately 20 nm. Therefore any damage from the implant should be well away from the buried oxide interface. MEIS results for the 3 keV As samples showed no significant differences between the bulk, 60 nm and 100 nm SOI samples, (Figure 6.24). Combined with the TRIM results this would lead to the conclusion that when the damage is well away from the BOX and there is a continuous crystalline seed layer the SOI regrowth proceeds in the same fashion as bulk Si, as also seen in (26).

a)

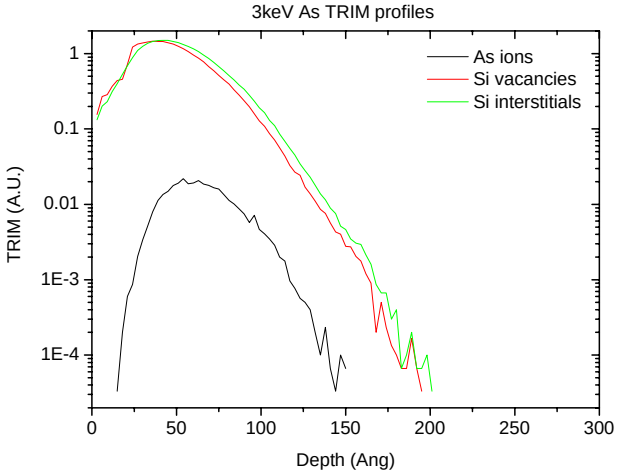

b)

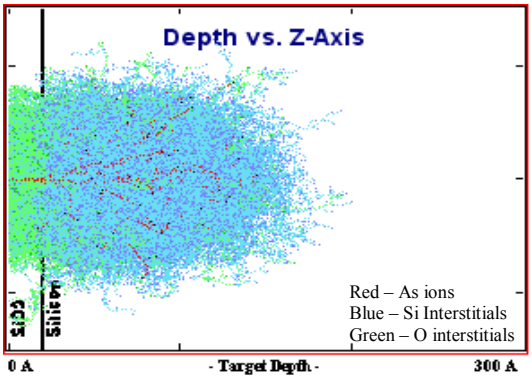

Figure 6.30 a) TRIM results for a 3 keV As implant into Si including vacancy and interstitial profiles. b) Pictorial representation of the TRIM calculation.

Results of TRIM calculations for a 40 keV Xe implant are shown in Figure 6.31, likewise the Xe profile and interstitial and vacancy profiles are plotted in Figure 6.31a)

and the 2D picture in Figure 6.31b). It is clear that for the case of 60 nm SOI some Xe and energetic interstitials will reach the BOX.

a)

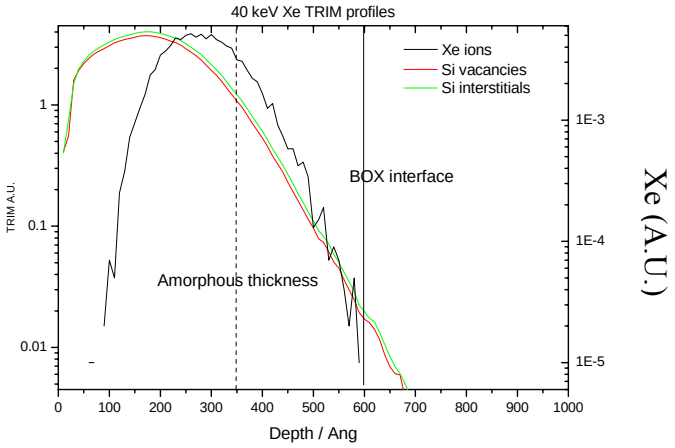

b)

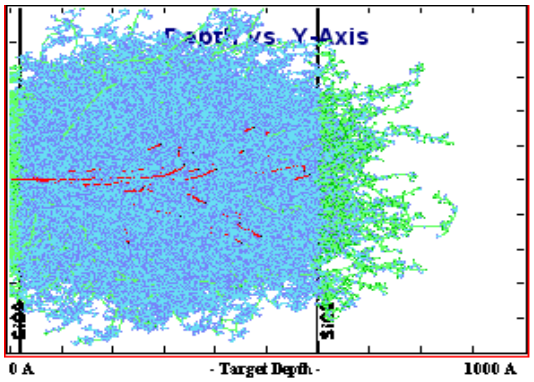

Figure 6.31 a) TRIM results for a 40 keV Xe implant, together with the Si vacancy and interstitial depth profiles. b) Pictorial representation of the calculation.

TRIM results suggest that for the 88 nm and 100 nm SOI wafers the recoiled interstitials will not reach the BOX, but could be within ~ 20 nm. However interstitials produced in the collision cascade are mobile at room temperature and may migrate to and be trapped at the interface, as seen at the surface (14, chapter 5). Excess interstitials at the end of the range of the implant will have a higher chance to be trapped at the BOX than at the surface.

The following model is tentatively put forward. The model assumes that due to the capture of interstitials from the cascade dendrites extending from the main collision cascade envelope towards the SOI interface may be captured in aggregates at the BOX interface. It also assumes that the dendrite region means the amorphous / crystal interface makes the surface form a less than perfect seed for the SPER. Hence locally at these dendrites SPER is retarded and the regrowth interface instead of being flat as in

the bulk Si becomes wavy in the early stages. This wavy-ness is retained for the full regrowth and this may explain the XTEM and MEIS results. This initial formation of the wavy layer is the probable reason for the SOI samples lagging behind the bulk Si in terms of the amount of regrowth that occurs for the same anneal duration. The proposed mechanism is illustrated schematically in Figure 6.32 for one such region.

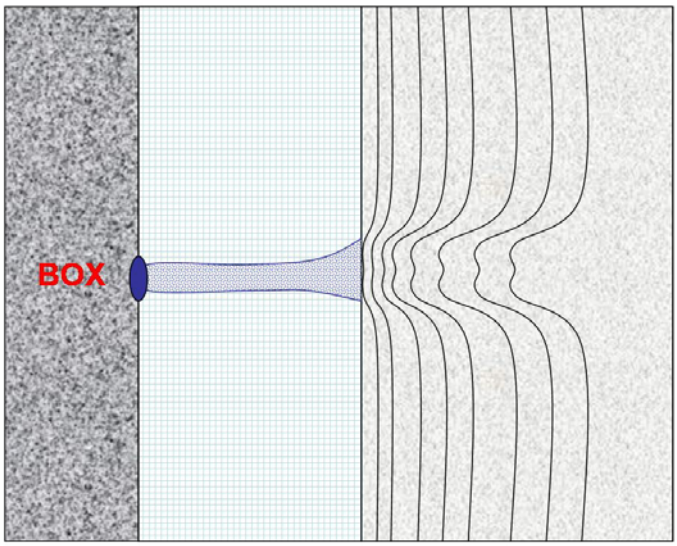

Figure 6.32 Illustration of proposed regrowth mechanism on SOI wafers.

Once the leading edge of the interface reaches a depth where there is a high As concentration, regrowth slows down effectively allowing the back edge to catch up. This causes the straightening up of the interface as is observed by MEIS. Arsenic atoms that cannot be accommodated as areas of the a/c interface pass by are pushed into neighbouring amorphous areas, explaining why there is less modification of the As peak at depths where there has been some recrystallisation.

A previous RBS study of samples where an amorphous Si was deposited on a layer containing at least one atomic layer of native oxide showed that upon annealing the height of the RBS peak from the amorphous Si was reduced but not the width (27). Columnar regrowth of the Si above regions where at isolated points crystal growth centres occur, most likely at gaps of the oxide layer, was suggested (27). This is consistent with the proposed mechanism in the sense that regrowth could occur selectively above small areas of seed and not above other areas without seed. If an implant produced an amorphous layer to the BOX, then random nucleation and growth would be expected (28, 29).

6.5 Conclusion

In summary, in this chapter a range of studies of the effects of annealing on As implanted Si are presented. In the first section results are presented for annealing conditions similar to those currently used for device manufacturing, e.g. > 1000 °C spike annealing. MEIS results shows the effect of annealing causing recrystallisation of the implanted layers. The effect of As segregation is visible in the MEIS spectra. MEIS was used as the starting point for the interpretation of specular reflectivity results, the results of which suggested that the segregated As is narrower than that measured in MEIS. MEIS results showed that the segregated As is located underneath the oxide layer. SIMS measurements showed that As which becomes invisible in the MEIS spectra following annealing is retained and hence must represent As atoms in substitutional lattice positions. SIMS also shows that diffusion of As deeper into the bulk is a feature of this type of annealing. It was shown that diffusion played a more significant role in determining the final junction depth than the implant energy.

Studies of the effect of using lower annealing temperatures have been carried out. Layer-by-layer SPER regrowth has been observed. During SPER, As takes up substitutional lattice sites and any that can't be accommodated segregates in front of the advancing amorphous / crystalline interface. Importantly, diffusion deeper into the bulk was not observed with this annealing temperature range. Comparisons between MEIS and XRD have shown how MEIS can be used to interpret XRD results. The results of the two techniques in terms of the measured regrown layer thickness are in excellent agreement.

Finally unusual regrowth of SOI wafers was observed. For conditions where a recoiled interstitials reached, or were close to, the buried oxide interface, a broad amorphous / crystalline interface was observed. This is attributed to the damage causing regions of imperfect crystalline seed for the regrowth to proceed from.

References

1 http://public.itrs.net/ (accessed 12/1.06).

2 R. Lindsay, B.J. Pawlak, P. Stolk, K. Maex. Proceedings of MRS vol 717, p 65

3 T. Feudel, M. Horstmann, M. Gerhardt, M. Herden, L. Herrmann, D. Gehre, Ch. Krueger, D. Greenlaw, M. Raab. Mat. Sci. in Semiconductor Processing **7** (2004) 369–374.

4 J.A. van den Berg, D. G. Armour, M. Werner, S. Whelan, W. Vandervorst, T. Clarysse, E. H. J. Collart, R. D. Goldberg, P Bailey, T. C. Q. Noakes. Proc Int Conf. on Ion Implantation Technology (ITT 2002), (Sept 2002), IEEE Operations Center, Piscataway, NJ 08855-1331. p. 597 (2003)

5 J.A. van den Berg, D Armour, S Zhang, S Whelan, M Werner, E.H.J. Collart, R.D. Goldberg, P. Bailey, T.C.Q. Noakes. P303 – 308. Materials Research Society proceeding (MRS) vol 717, Si front end junction formation technologies, San Francisco Ca April 2 – 4 2002. Published MRS, Pennsylvania, USA.

6 P.Pichler, Solid Phase Epitaxy. Unpublished.

7 Solid phase recrystallization processes in silicon,in Surface modification and alloying by laser, ion and electron beams, J. S. Williams, J. M. Poate, G. Foti and D. C. Jacobson, Eds. Plenum, 1983, p. 133-163.

8 J. Dabrowski, H.-J. Mussig, V. Zavodinsky, R. Baierle and, M. J. Caldas, Phys. Rev. B, **65**, 245305 (2002)

9 Private communication. P.Pichler.

10 R. Kasnavi, Y. Sun, P. Pianetta, P.G. Griffin, J.D. Plummer. J. Appl. Phys. 87, 2000, p 2255–2260.

11 P. M. Rousseau, P. B. Griffin, W. T. Fang and J D Plummer. J. Appl. Phys. 84, 1998. p. 3593-3601

12 J. A. van den Berg, S. Zhang, S. Whelan, D.G. Armour, R.D. Goldberg, P.Bailey, T.C.Q. Noakes. Nucl. Instr. Methods B. 183 (2001) 154-165.

13 Private communication. T. Feudal, AMD.

14 M. Werner, J. A. van den Berg, D. G. Armour, W. Vandervorst, E. H. J. Collart, R. D. Goldberg, P. Bailey, T. C. Q. Noakes. Nucl. Instr. And Meth B **216** (2004) 67.

15 A H Al-Bayati, K Ormannn- Rossiter, J A van den Berg and D G Armour, Surface Sci 241 (1991) 91.

16 http://www.esrf.fr/UsersAndScience/Experiments/SurfaceScience/ID01/ (accessed 12/1/06).

17 U. Pietsch, V. Holý, T. Baumbach, High-Resolution X-ray Scattering from Thin Films and Lateral Nanostructures, (Spinger, Berlin, 2004).

18 L. Capello, T.H. Metzger, M. Werner, J.A. van den Berg, M. Servidori, M. Herden, T. Feudel. Mat. Sci. and Eng. B **124-125** (2005) 200 – 204.

19 L. Capello, PhD thesis. Structural investigation of silicon after ion-implantation using combined x-ray scattering methods. University of Lyon (France) and Torino (Italy), 2005.

20 L. Capello, T. H. Metzger, M. Werner, J. A. van den Berg, M. Servidori, L. Ottaviano, C. Spinella, G. Mannino, T. Feudel, M. Herden. Influence of pre-amorphization on the structural properties of ultra-shallow arsenic implants in silicon. (To be published).

21 F. A. Trumbore, Bell Syst. Tech. J. 39 (1960) 205.

22 Rapid Thermal Processing of Semiconductors. V. E. Borisenko, P. Hesketh. Plenum Press, 1997.

23 http://www.elecdesign.com/Articles/ArticleID/3400/3400.html (accessed 12/1/06)

24 M. Bruel. Nucl. Instr. and Meth. B 108 (1996) 313.

25 http://www.soitec.com/ (accessed 12/1/06)

26 J.J. Hamilton, E.J.H. Collart, B. Colombea, C. Jeynes, M. Bersani, D. Giubertoni, J.A. Sharp, N.E.B. Cowern, K.J. Kirkby. Nucl. Instr. and Meth. B 237, (2005) 107.

27 M. von Allmen, S.S. Lau, J.W.Mayer, Appl. Phys. Lett. **35** (1979) 280.

28 G.L. Olsen, J.A. Roth, Kinetics of Solid Phase Crystallisation in Amorphous Silicon. Mat. Sci. Rep. 3 (1978) p1-78.

29 D.A. Williams, R.A. McMahon, H. Ahmed. Mat. Sci. and Eng. 4 (1989) 423.

30 Handbook of Semiconductor Silicon Technology. W.C. O'Mara, R.B. Herring, L.P. Hunt, Noyes Publications, New Jersey, 1990.

Chapter 7 Interaction between Xe, F and B

7.1 Introduction

The study reported in this final results chapter formed part of a much wider investigation within the IMPULSE project to characterise the behaviour of B and find optimum implantation and annealing conditions for CMOS devices. This was a parallel study to the study of As implants, parts of which are reported in section 6.2.3 and 6.2.4. B doped source/drain and extension regions in Si CMOS devices are usually produced using BF_2 ions, for reasons of higher beam and hence wafer throughput. As with the As studies, 1 and 3 keV BF_2 implants were carried out. The energy deposition rate of BF_2 is sufficient to amorphise the Si matrix at comparatively low doses, unlike B, however the use of deeper pre-amorphising implants (PAI) is preferred, as discussed elsewhere in this thesis. The benefits of pre-amorphising include suppression of channelling effects and the enabling of a good spatial separation of the end-of-range defects and the junction depth. Pre-amorphising implants using Xe were carried out instead of Ge, which is the most commonly used PAI dopant. Xe offers several advantages, for example it forms a sharper amorphous / crystalline interface, which can lead to a lower concentration of hairpin dislocations (25). Other manufacturing and transistor device advantages exist. The study in this chapter is concerned with the collective behaviour of the Xe, F, and the implanted B.

Many previous studies have been carried out with ion implanted F in Si (1-11). These have shown that F becomes mobile at temperatures above 550 °C and is swept in front of the a/c interface during SPER. Other studies have shown that when BF_2 implants amorphise Si, upon annealing, a small fraction of F migrates in deeper into the bulk and is gettered in low concentrations at defects beyond the original a/c interface (4,8,6). For non – amorphising BF_2 implants, only F segregation to the surface and out diffusion was observed (2). With high dose BF_2 implants (1E16 cm^{-2}), bubble formation, as described in section 3.4.3, was observed, (9,10). F has also been found to exert an influence on retarding the diffusion of B (3, 7), form interstitial and vacancy complexes (1) and retard SPER. These studies have not been carried out with the added complication of the presence of Xe. Earlier studies of Si implanted with only Xe have shown that Xe bubbles can be formed during annealing (12). Bubble formation has also been observed with other noble gases (13-15).

MEIS results presented in this chapter have revealed an unexpected behaviour of the implanted Xe. While brief comments regarding Si regrowth and information

regarding B profiles relevant to the formation of junctions are included in this chapter, the main focus is on this unusual Xe behaviour and the observed associated interaction with F and B.

Following annealing, MEIS studies showed that approximately half of the implanted Xe accumulated, surprisingly at a depth defined by the end of range of the B and F within amorphous Si. SIMS showed that in the pre-amorphised samples, approximately 10 % of the F migrated deeper into the bulk and was trapped at the same depth in a ~ 1:1 ratio to Xe (23, 24). A small fraction of the implanted B was also trapped. EFTEM micrographs suggest the development of Xe agglomerates that are stabilised by F and the defect structure at the depths determined by MEIS (24).

7.2 Experimental

Implants of 1 and 3 keV BF_2^+ ions to a dose of 7×10^{14} cm^{-2} were carried out at room temperature into pre-amorphised and, for comparison, crystalline Cz, p-type Si(100). PAI was carried out with 20 keV Xe to a dose of 2×10^{14} cm^{-2}. Following implantation various anneals were carried out, including furnace annealing at 600 °C for 20 minutes, rapid thermal annealing from 950 °C to 1025 °C, and spike annealing at temperatures of 1050 °C and 1130 °C. All anneals were performed in a N_2/O_2 5% ambient to reduce dopant loss.

Medium-energy ion scattering (MEIS) studies were, as previously, carried out using a nominally 100 keV He^+ ion beam and the double alignment configuration. The channelling direction was along the $[\bar{1}\,\bar{1}\,1]$ direction and the blocking direction reported is along [111] direction. The overall depth resolution for these conditions was better than 0.6 nm. SIMS F depth profiles were obtained using a Cs^+ primary beam with an impact energy of 0.5 keV or 1 keV and an incidence angle of 45 ° (21). Negative secondary ions were collected and depth scales calibrated by use of the final crater depth measured by a mechanical stylus profilometer (22). B depth profiles were obtained using a 0.5 keV O_2^+ beam and collecting secondary positive ions, the depth scale was calibrated by a laser interferometer that measures the in-situ depth in order to minimise depth scale distortion (22). Energy filtered transmission electron microscopy (EFTEM) images of the Xe distribution were obtained at CNR-IMM in Catania by detecting the energy filtered image of electrons that had undergone ~670 and ~65 eV energy losses, corresponding to the Xe -M and -N excitation edges, respectively.

7.3 Results and discussion

Figure 7.1 shows the MEIS energy spectrum of an as-implanted, PAI, 3 keV BF_2^+ implanted sample, as well as spectra taken after 10 s annealing at 1025 °C for both 1 and 3 keV BF_2^+ implants. The spectrum of the Xe pre-amorphised, 1 keV BF_2 implanted sample is identical to the 3 keV implanted one, as should be expected, and hence is not shown. A virgin Si sample showing scattering from the surface Si and O atoms, at energies of 84 keV and 72 keV, respectively, is included as a reference. The increased random yield between 70 and 84 keV for the pre-amorphised, as-implanted sample is caused by scattering off deeper atoms in the amorphised layer. Spectra obtained after annealing show that SPER has restored the Si crystalline state. The observed increase of the width of the Si peak compared to the virgin sample is largely accounted for by the growth in oxide thickness following implantation and annealing. For all of the anneals investigated here the SPER process was completed.

The behaviour of the Xe implant after annealing forms the main interest in this chapter. The Xe is visible in the spectrum between 84 and 95 keV and shown in the inset with the yield multiplied by a factor 10 and the Xe depth scale added. The as-implanted Xe profile extends from ~ 94 keV, down in energy until it merges with the Si surface peak at ~ 84 keV. The TRIM calculated Xe profile, added in the inset, shows good agreement with the as-implanted shape. Approximately half of the Xe profile is visible for energies above the Si peak. TRIM calculations give a mean projected range (R_p) of 18 nm for 20 keV Xe.

Following the 1025 °C 10 s anneals, some of the Xe has migrated to a shallower depth where it is trapped, in a relatively narrow distribution, the depths of which are dependant on the BF_2 implant energy. For the 1 keV BF_2 implanted sample the peak centre is at ~ 7 nm, and for 3 keV BF_2 it is at ~ 13 nm, as indicated with arrows. The Si regrowth at all other anneal conditions used is very similar to that shown in Figure 7.1.

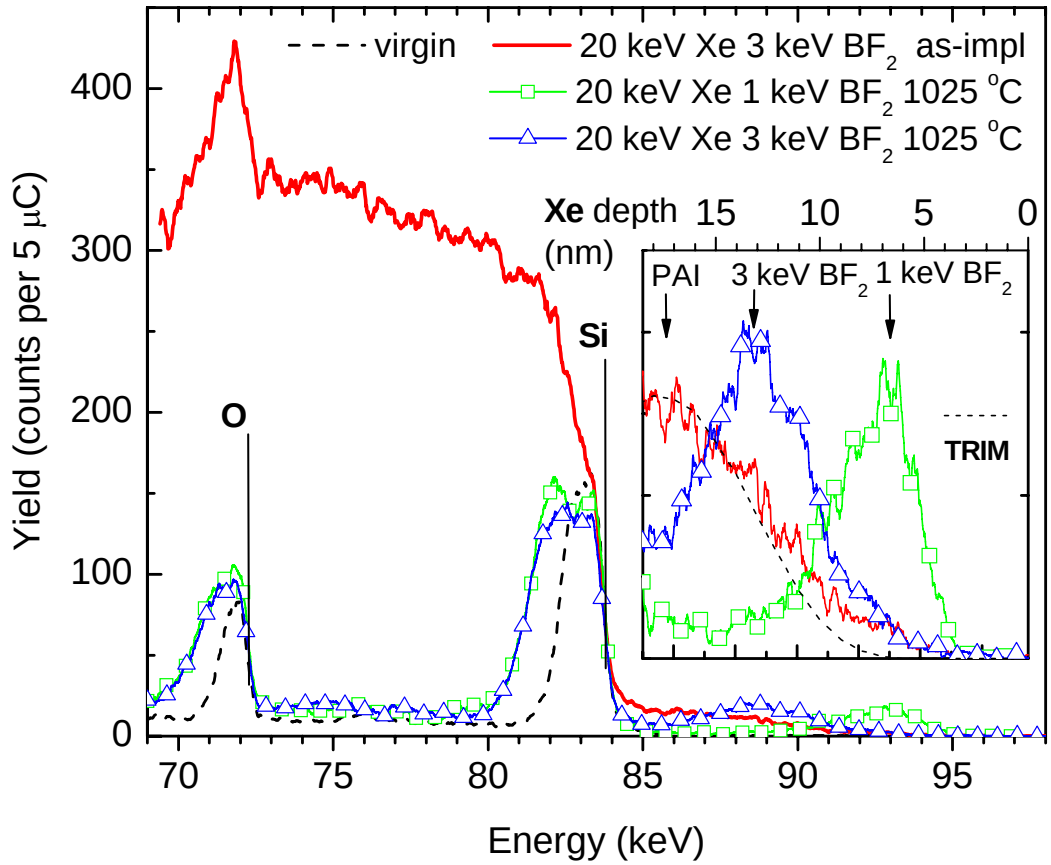

Figure 7.1 MEIS energy spectra of Xe pre-amorphised Si samples, implanted with 1 and 3 keV BF_2, before and after annealing at 1025 °C for 10s. The inset shows the depth Xe depth profiles before and after annealing.

Figure 7.2 shows Xe depth profiles before and after SPER for different anneals. Note that here the depth scale is plotted in the opposite direction to the energy scale in Figure 7.1. The Xe concentration scale is also included on the right hand side of the figure. The top of the figure contains Xe profiles for 3 keV samples and the bottom contains those for the 1 keV samples. Both include profiles from as-implanted, 600 °C 20 minutes furnace anneal, 1000 °C 5 s RTA and a high temperature spike annealed sample. As is observed for the 1025 °C 10s sample in Figure 7.1, for all anneals following SPER, Xe has migrated closer to the surface and is trapped in a 5-6 nm wide layer (FWHM). For the 1 keV BF_2 implanted samples this is centred at approximately 7 nm, and for 3 keV BF_2 at around 13 nm.

The location of the Xe is consistent for all anneal conditions used. The different anneals affect the sharpness of the profile but not the depths of the peaks. Lower temperatures generally produced a broader Xe distribution. By referencing the integrated peak areas to the random Si yield, the Xe dose could be calculated.

Approximately half of the nominal 2×10^{14} cm^{-2} implanted Xe appears to be contained within the peak. The remainder is assumed to have diffused out.

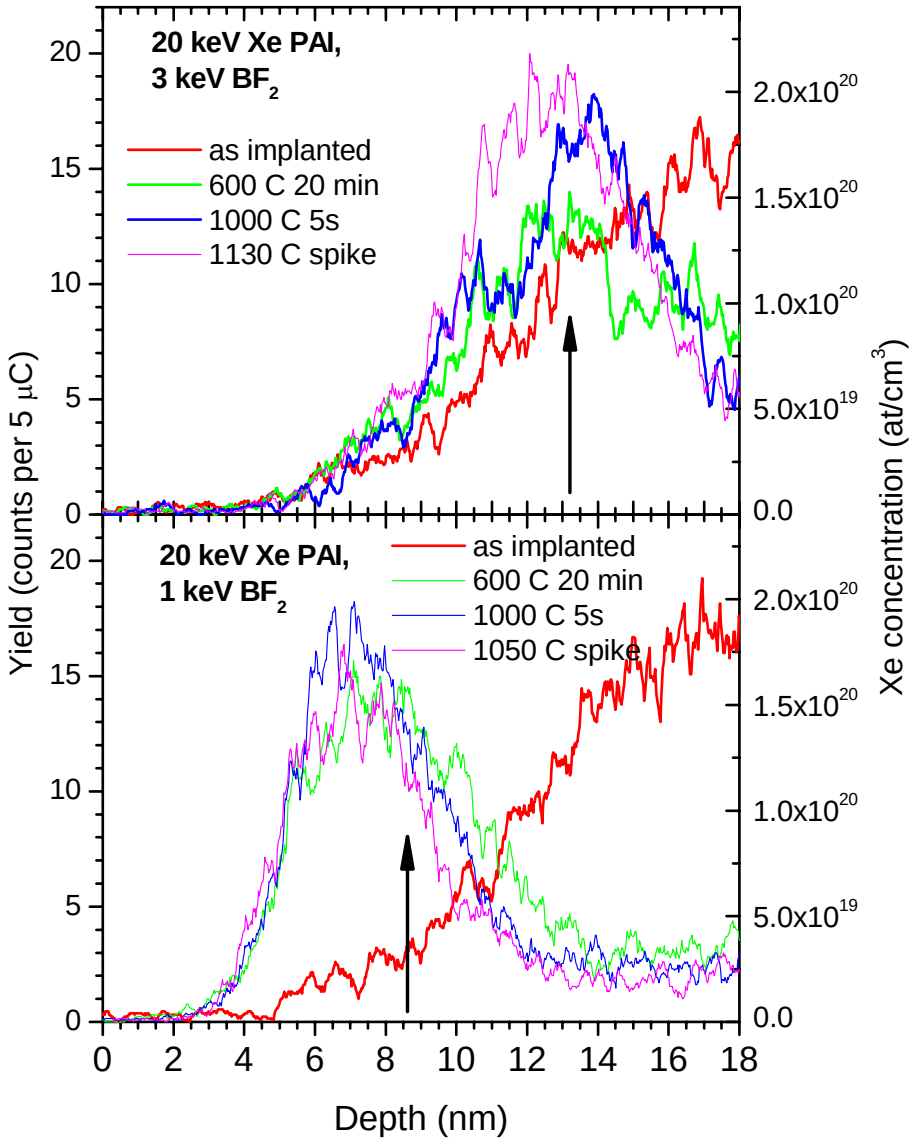

Figure 7.2 MEIS Xe depth profiles for Xe pre-amorphised Si samples, implanted with 3 keV BF_2 (top) and 1 keV BF_2 (bottom), as-implanted and after different anneals.

Since the depth of the Xe accumulation is closely related to the energy (hence depth) of the BF_2^+ implant into the amorphous Si, it was also interesting to study the behaviour of the F and B. TRIM calculations show that for the low BF_2 implant energies used in this study, B and F projectiles have similar ranges. The depth profiles of 1.16 keV F, 0.67 keV B, 0.39 keV F and 0.22 keV B, corresponding to 3 and 1 keV BF_2 implants, respectively, are shown in Figure 7.3. For 3 keV BF_2^+ the mean projected range (R_p) of F is ~ 4.7 nm, and for 1 keV ~ 2.3 nm. The depth of the Xe accumulation is close to 3 × R_p i.e. towards the end of the B and F ranges.

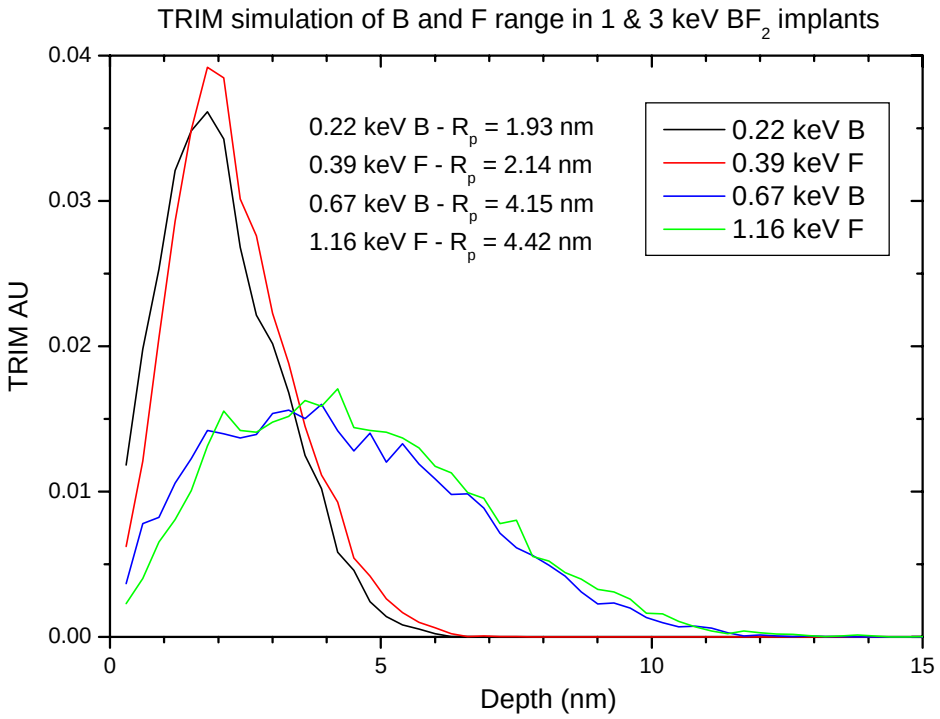

Figure 7.3 TRIM depth profiles for B and F from 1 and 3 keV BF_2 implants.

SIMS analysis was used for detecting F and B since the sensitivity of MEIS for low Z elements is relatively small and any scattering at the F and B concentrations present would be contained within the noise level of the Si background. Figure 7.4a) shows SIMS depth profiles for F, from pre-amorphised samples, as-implanted and after various anneals. Figure 7.4b) shows F depth profiles from the non pre-amorphised samples. The BF_2 implant energy was 3 keV. Note that the use of SIMS for ultra shallow junction profiling has some inherent difficulties in the first few nanometres, caused by changing sputtering rates until an equilibrium erosion rate has been reached. This can cause some inaccuracies to the depth scale and concentration calibration in the first couple of nanometres (22). Disregarding a sharp spike within the first 2 nm that is probably a SIMS surface artefact, the as-implanted samples shows profiles with maxima that are in close agreement with the TRIM calculation.

The PAI samples are considered first. After annealing there has been F migration to the surface, yielding a F surface peak within the first 3 – 4 nm. (The concentration these may be partially influenced by SIMS artefacts). For the pre-amorphised samples there is the additional migration of some of the F deeper in, forming a second peak. An ~6 nm wide peak (FWHM) centred around 12 – 13 nm is found. This depth recurs for all the anneal conditions, with a slightly wider distribution for the 600 °C sample compared to the higher temperatures. Integration of the second

peak gives a dose of 1.2E14 cm^{-2} – 1.7E14 cm^{-2} which is between 9 - 12 % of the implanted F. The dose measured by SIMS suggests total dose retention. F appears to be trapped at the oxide interface.

For the non-PAI samples in Figure 7.4b), the as-implanted sample displays a slight channelling tail and is otherwise the same as the PAI sample. For samples annealed at high temperatures the F migration to the surface is also observed. However the deeper migration observed with PAI samples does not occur in non PAI samples. The only variation is with the sample annealed at 600 °C, in which a double peak is observed. The second peak is centred around a depth of 7-8 nm. This behaviour is not too unusual and can be attributed to trapping of some F around the original a/c interface which is consistent with previous studies (4). The MEIS profile in Figure 7.4c) indicates the depth of the original a/c interface around 7 – 8 nm which is indeed consistent with the F trapping result. Returning to the PAI samples in figure 7.4a), it is worth mentioning that the second deeper damage peak at 12 – 13 nm cannot be attributed to trapping at the original a/c interface, which is much deeper in the PAI samples.

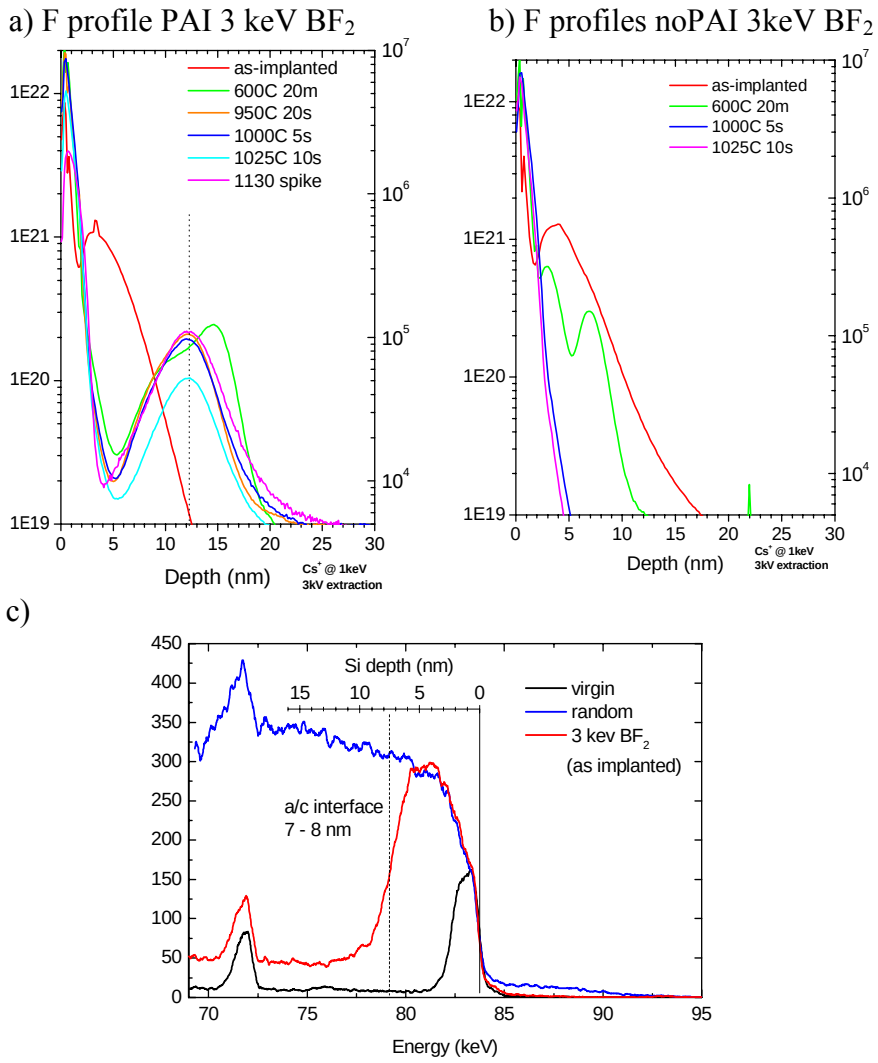

Figure 7.4 SIMS F depth profiles for 3 keV BF_2 samples, as-implanted and after a variety of anneals in a) PAI samples and b) non-PAI samples. The MEIS profile in c) shows the non-PAI, 3 keV BF_2 as-implanted profile.

For 1 keV BF_2 samples the general behaviour is like that of the 3 keV samples and the results are shown in Figure 7.5. For the PAI samples in Figure 7.5a) deeper migration of F occurs forming a second peak centred around 7 nm, as well as the migration to the surface. For non PAI samples, shown in Figure 7.5b), there is no second peak and only migration to the surface occurs. The trapping of F at the depth of the original a/c interface, seen with the 600 °C 3 keV non PAI sample in Figure 7.4b), has not occurred with the 1 keV samples.

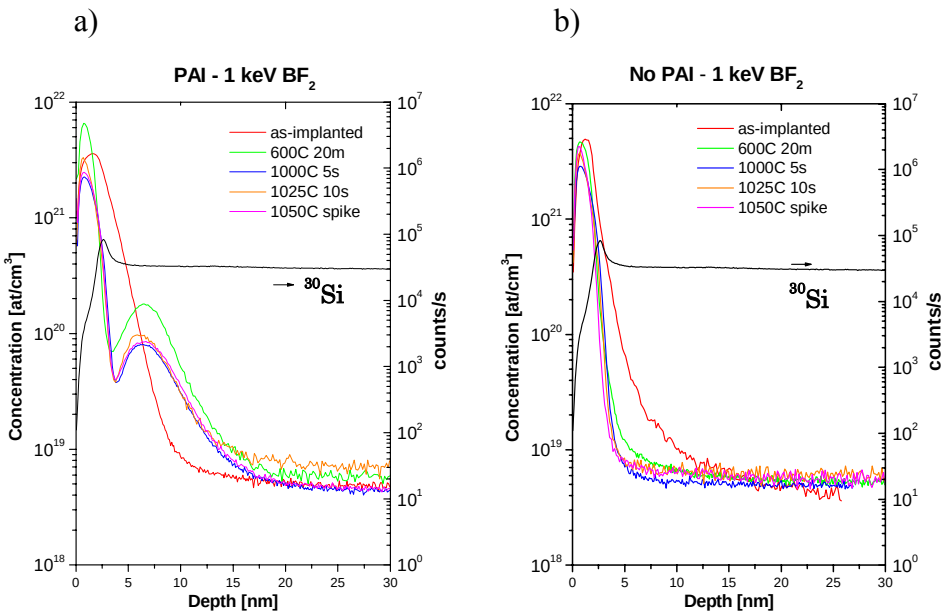

Figure 7.5 1 keV SIMS profiles for a) PAI samples and b) non-PAI samples.

Figure 7.6 shows combined depth profiles of Xe (from MEIS) and F (from SIMS), for as-implanted, 600 °C 20 min, 1000 °C 5 s and spike annealed at 1130 °C or 1050 °C sample, for both 3 keV and 1 keV BF_2 implants. The figure illustrates the close link between the Xe and F. For some anneal conditions (e.g. 3keV BF_2^+ 1130 °C) the relative concentrations of Xe to F would appear to be ~ 1:1, but there are some minor deviations with different samples, notably the high temperature 1 keV samples.

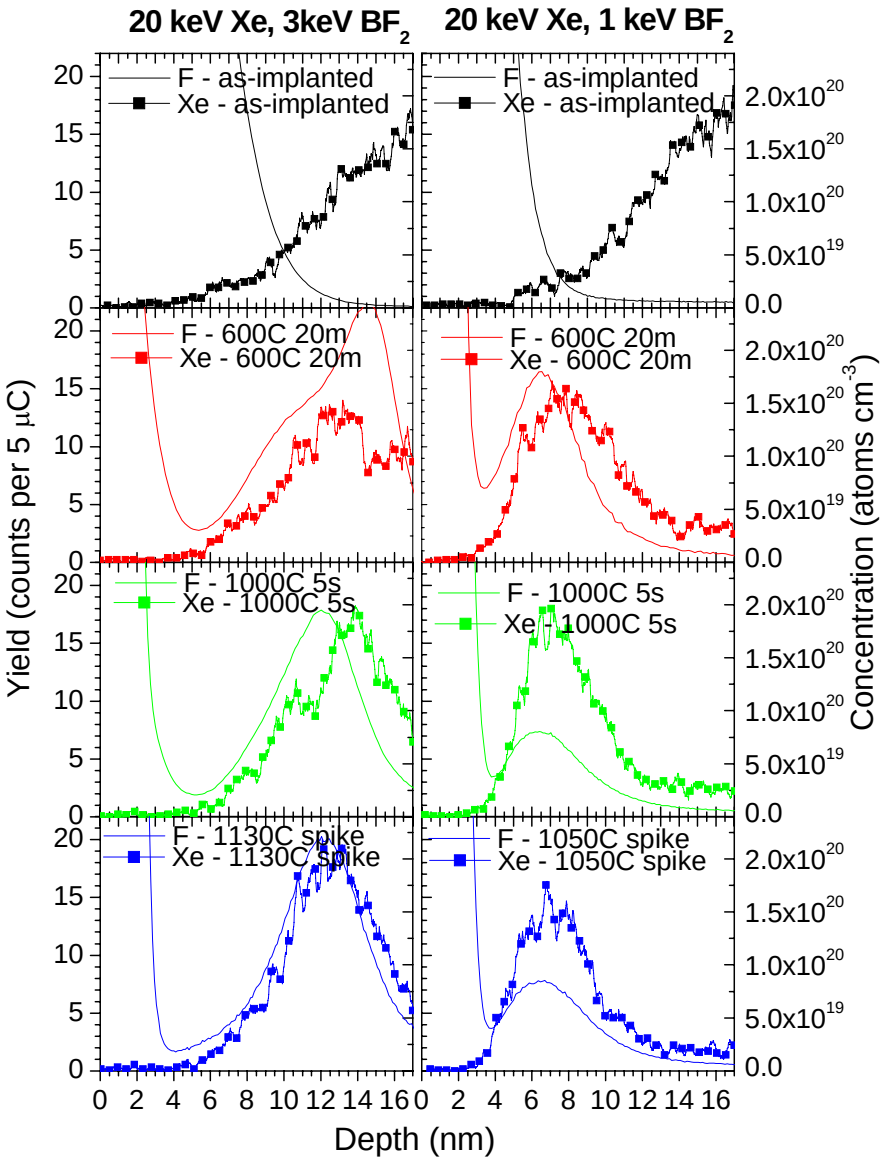

Figure 7.6 Combined MEIS Xe depth profiles and SIMS F depth profiles for Xe pre-amorphised samples implanted with 3 keV BF_2^+ (left) and 1 keV BF_2 (right), as-implanted and after various anneals.

Figure 7.7a) shows SIMS B depth profiles for the 3 keV BF_2 implants into crystalline and pre-amorphised Si, as-implanted, after 600 °C 20m, 1000 °C 5s RTA, and 1130 °C spike annealing. For the as-implanted sample the effect of channelling is visible at depths greater than 10 nm. Annealing causes several effects. Segregation of B to the surface occurs in all samples. Diffusion deeper into the bulk occurs for the 1000 °C and 1130 °C samples, the higher temperature causing a greater amount of diffusion. Using 1E18cm^{-3} as a reference concentration for the junction depth gives a junction at 43 nm and around 60 nm for the 1000 °C and 1130 °C samples respectively.

a)

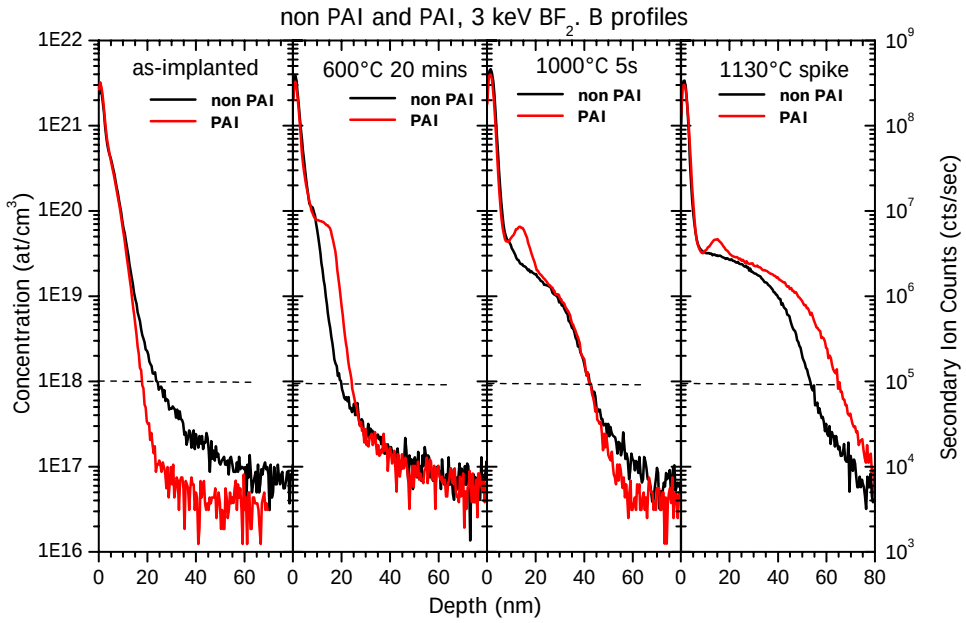

b)

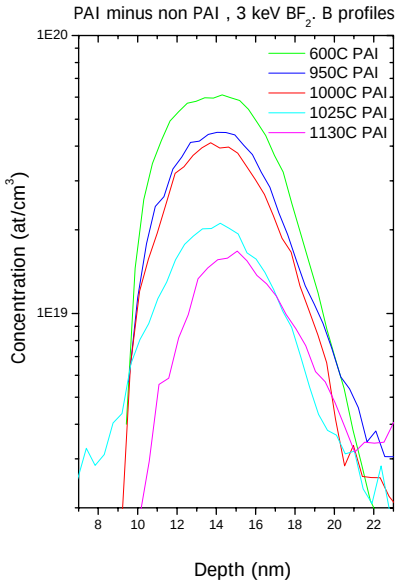

Figure 7.7 a) SIMS B depth profiles for Si implanted with 3 keV BF_2 with and without Xe pre-amorphisation, as-implanted, and after anneals of 600 °C 20mins, 1000 °C 5s and 1130 °C spike. b) B profiles from PAI samples with the corresponding non PAI profiles subtracted, showing the trapped B.

Returning to the interaction between implanted species, in the pre amorphised annealed samples there is an additional B peak formed, centred around 13 – 14 nm, Figure 7.7a). This is not present in the non pre-amorphised samples. B is trapped at roughly the same depth as the trapped Xe and F. This occurs for all anneals. The 600 °C PAI has the B peak superimposed on the back edge of the main peak, making it appear to be a broader layer and not a separate peak. Subtraction of the non PAI spectra from

the corresponding PAI sample, yields a clear peak shape similar to the rest of the anneals, as shown in Figure 7.7b). Integration of the B peaks in Figure 7.7b) shows that the amount of B in the trapped peak goes down with increasing annealing temperature. Starting from 4E20 cm^{-3} for the 600 °C sample, the amount falls to 3.03E20 cm^{-3} for 950 °C, 2.63E20 cm^{-3} for 1000 °C, 1.46E20 cm^{-3} for 1025 °C and 1E20 cm^{-3} for the sample annealed at 1130 °C. As a B peak is formed with the 600 °C sample it is clear that some B has to have moved in deeper to form the trapped peak during SPER. The B peak formation is therefore not associated with trapping during B diffusion. In fact the amount of trapped B, shown in Figure 7.7b) goes down in the samples where there is more diffusion and so it would indicate that some of the trapped B dissolves during high temperature annealing.

Comparison with the amount of accumulated F at the same depth shows that initially there is four times the amount of trapped F to B. The amount of F trapped has less variation with temperature than B and so for the 1130 °C sample there is approximately 14 times more trapped F than B. The combined behaviour is shown in Figure 7.8, with the SIMS F and B profile overlaid on top of the MEIS Xe profile, for the 3 keV 1000 °C 5s and 1130 °C spike samples.

a) b)

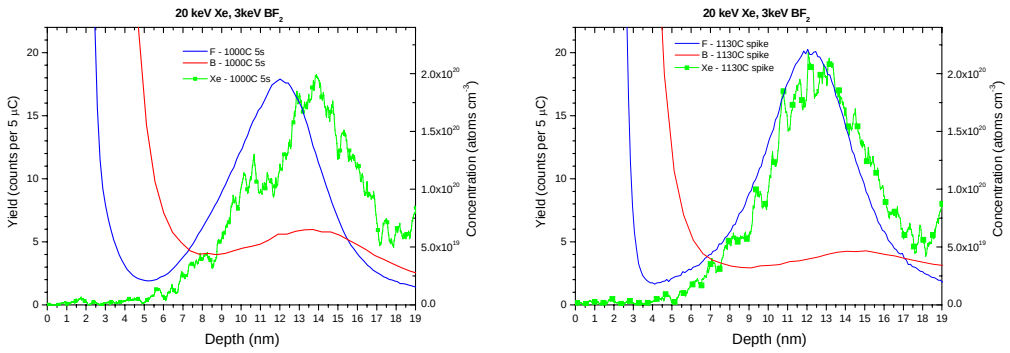

Figure 7.8 Combined MEIS Xe depth profiles with SIMS F and B depth profiles overlaid, for a) 1000 °C 5s and b) 1130 °C spike samples.

Since noble gases, including Xe have previously been observed to form bubbles in Si (12-15), the possible formation of Xe agglomerates or bubbles was checked using EFTEM experiments. Figure 7.9a) shows cross sectional EFTEM images using electrons that have undergone a ~ 670 eV loss (M excitation edge of Xe) for a Xe PAI, 3 keV BF_2 implanted sample, annealed to 1025 °C. Any Xe present appears as a bright area. To check that the areas indeed represent Xe, an image using N excitation edge electrons (~65 eV loss) was taken and is shown in Figure 7.9b). Both figures show the

existence of Xe agglomerates at depth between 10 and 15 nm, in agreement with the MEIS peak observed at ~13 nm for the 3 keV BF_2 implant. The size of these agglomerates was seen to grow with increasing anneal temperature, in a ripening process. It is likely that the agglomerated Xe is in bubbles.

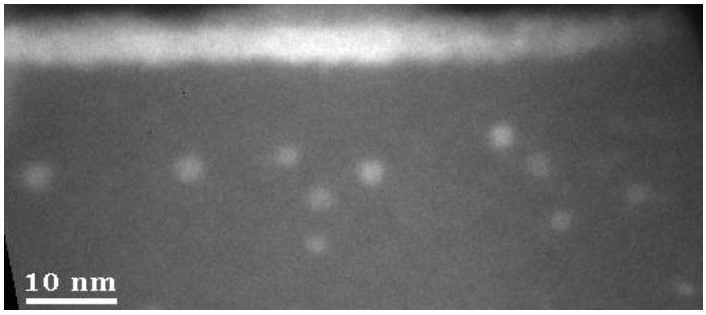

a) Xe M-edge, ~ 670 eV energy loss electrons

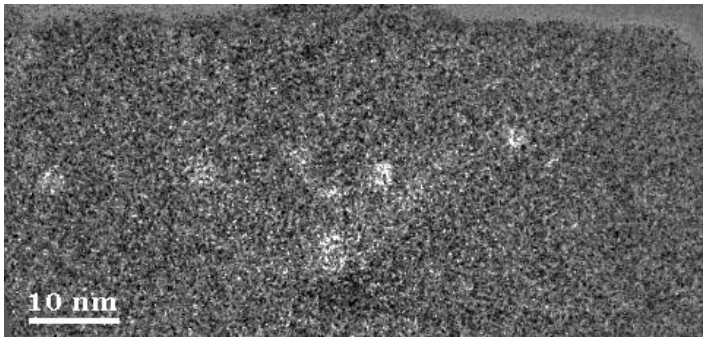

b) Xe N-edge, ~ 65 eV energy loss electrons

Figure 7.9 EFTEM images of a Xe PAI, 3keV BF_2 implanted Si sample after annealing to 1025 °C for 10 s using electrons with an energy loss corresponding to (a) the M ionisation edge and (b) from the N ionisation edge of Xe.

Summarising the above observations and considering the results from literature it appears that during SPER most F migrates, probably in front of the moving a/c interface to the surface where it is trapped. The rest of the implanted F, approximately 10 %, moves in deeper, to a depth surrounding the EOR of the BF_2^+ implant. Xe equally moves to the surface and ~ 50 % is trapped at a depth that coincides with the depth of the deeper F peak. The remainder of the Xe is assumed to diffuse out. During SPER a small amount of B is trapped at the same depth.

The precise details of the interaction, i.e. the exact sequence of events, are not known, nor the reasons for the interaction. Trapping of some F at a depth of the EOR of the BF_2 has been observed before (4), but in these cases the samples were not pre-amorphised and so there would be a clear defect structure in the damaged crystalline Si to act as a gettering site. In this set of experiments, the end of range of the BF_2, was located in amorphous Si. It is known that defect structures can exist within an

amorphous matrix, (16) i.e. local changes in density, sometimes referred to as volume defects. The depth of the Xe, F and B accumulation at the depth of the EOR of the BF_2 implant may indicate that the implant accumulation observed is related to this type of defect structure.

MEIS and SIMS studies (not shown) of Ge PAI samples, with similar implant and anneal conditions, do not show any accumulation effect of F, B or Ge. The accumulation effect of Xe F and B may therefore be related to a chemical interaction, possibly forming a Xe-F compound, since for Si pre-amorphised with Ge such an accumulation is not seen. The damage structure still plays a role however.

As both Xe and F are known to form bubbles under certain conditions it is suggested that F mediated and/or stabilised Xe bubbles may be formed. The EFTEM images showing round agglomerates of Xe may support the formation of bubbles. An alternative argument is that it may also be that it may be energetically favourable to accommodate Xe, F and B together in crystalline Si to reduce lattice strain.

7.4 Conclusion

To conclude, it has been observed that following SPER half the Xe from the PAI is trapped in a ~ 6 nm wide peak, at a depth that is dependant on the energy of the subsequent BF_2 implant, during SPER. The depth of the trapped Xe is $3 \times R_p$ of the post PAI BF_2 implanted species. After annealing, 9 – 12% of the implanted F had accumulated at the same depth, in peaks of similar width and of similar concentration to Xe. The remainder of the F is segregated at the surface. A small amount of B is also trapped around the same depth during SPER. This effect is attributed to the formation of F mediated and/or stabilised Xe bubbles / agglomerates, or possibly even a Xe-F compound. It appears to be closely related to a defect structure within an amorphous matrix, and as well as some chemical interaction between the Xe, F and B.

This interaction does not directly have an effect on the operation of current devices as its depth of occurrence is well above the junction depth. It could, however, have an effect on the sheet resistance of the conductive layer. It was observed that, upon activation/anneal, Xe pre-amorphised samples had a ~40% higher sheet resistance than non pre-amorphised ones (results not shown). The explanation for the higher sheet resistance is not clear at this stage.

References

1 X. D. Pi, C. P. Burrows and P.G Coleman, Phys. Rev. Lett **90,** 1555901(2003).

2 S. P.Jeng, T. P. Ma, R. Canteri, M. Anderle and G. W. Rubloff, Appl. Phys. Lett. **61,** 1310 (1992).

3 D. F. Downey, J. W. Chow, E. Ishida and K. S. Jones, Appl. Phys. Lett. **73,** 1263 (1998).

4 M. Y. Tsai, D. S. Day, B. D. Streetman, P. Williams and C. A. Evans, Jr, J. Appl. Phys. **50,** 188 (1979).

5 F. Boussaid, M. Benzohra, F. Olivie, D. Alquier and A. Martinez Nucl. Instr. Methods Phys. Res. B **134,** 195 (1998).

6 M. Tamura, Y. Hiroyama and A. Nishida. Mat. Chem. and Phys. **54,** 23 (1998).

7 A. Mokhberi, R. Kasnavi, P. B. Griffin and J. D. Plummer, Appl. Phys. Lett. **80,** 3530 (2002).

8 N. Ohno, T. Hara, Y. Matsunaga, M. Current and M. Inoue. Mat. Sci. in Semicond. Processing **3,** 221 (2000).

9 C. W. Nieh and L. J. Chen, Appl. Phys. Lett. **48,** 1528 (1986).

10 C. H. Chu and L. J. Chen, Nucl. Instr. Methods Phys. Res. **59/60,** 391 (1991).

11 C. H. Chu, J. J. Yang and L. J. Chen, Nucl. Instr. Methods Phys. Res. B **74,** 138 (1993).

12 G. Faraci, A.R. Pennisi, A. Terrasi and S. Mobilio, Phys. Rev B **38,** 13 468 (1988)

13 P. Resesz, M. Wittmer, J. Roth and J. W. Mayer, J. Appl. Phys. **49,** 5199 (1978).

14 M. Wittmer, J. Roth, P. Resesz, and J. W. Mayer, J. Appl. Phys. **49,** 5207 (1978).

15 A. G. Cullis, T. E. Seidel and R. L. Meek, J. Appl. Phys. **49,** 5188 (1978).

16 S. Roorda, J. S. Custer, W. C. Sinke, J. M. Poate, D. C. Jacobson, A. Polman and F. Spaepen, Nucl. Instr. Methods Phys. Res. B **59/60,** 344 (1991).

17 J. A. van den Berg, D. G. Armour, S Zhang and S Whelan, L.Wang and A. G. Cullis, E. H. J. Collart, R. D. Goldberg, P. Bailey and T. C. Q. Noakes, J. Vac. Sci. Technol. B **20,** 974 (2002).

18 M. Werner, J. A. van den Berg, D. G. Armour, W. Vandervorst, E. H. J. Collart, R. D. Goldberg, P. Bailey, T. C. Q. Noakes. Nucl. Instr. Methods Phys. Res. B **216,** 67 (2004).

19 J. F. Ziegler, J. P. Biersack, and U. Littmark, The Stopping and Range of Ions in Solids (Pergamon Press, New York, 1985).

20 W. K. Chu, J. W. Mayer, M. Nicolet, Backscattering Spectrometry, (Academic Press, New York, 1978).

21 M. Anderle, M. Bersani, D. Giubertoni, P. Lazzeri. Characterisation and Metrology for ULSI Technology: 2003 International Conference Proceedings 683, NY (2003), p.695.

22 D. Giubertoni, M. Barozzi, M. Anderle and M. Bersani, J. Vac. Sci. Technol. B 22(1), 336 ((2004) 2004).

23 M. Werner, J. A. van den Berg, D. G. Armour, G. Carter, T. Feudel and M. Herden, M. Bersani and D. Giubertoni, P. Bailey and T. C. Q. Noakes. Mat. Sci. Eng. B, 114–115 (2004) 198–202.

24 M. Werner, J. A. van den Berg, D. G. Armour, G. Carter, T. Feudel, M. Herden, M. Bersani, D. Giubertoni, L. Ottaviano, C. Bongiorno, G. Mannino, P. Bailey and T. C. Q. Noakes. Appl. Phys. Lett. **86**, (2005) 151904.

25 P. Pichler, Solid Phase Epitaxy, 2002. (Unpublished).

Chapter 8 Conclusion

The studies presented in this thesis are concerned with issues relating to formation of damage during low energy ion implantation into Si and its subsequent annealing. The focus is on those implant conditions that are typical of source/drain and extensions, for current and future CMOS devices.

The primary analysis technique used has been MEIS and to a lesser extent SIMS. Work has been carried out to improve the methodologies of both MEIS and SIMS. For MEIS the object has been to remove inaccuracies in the methodology that caused small depth scale errors, of the order of up to 0.5 nm, to occur. These are notably: i) the use of consistent stopping power data for different beam energies, ii) the accurate determination of the beam energy from experimental data, iii) the use of a recursive depth scale calibration instead of using the surface approximation method. MEIS results have also been used as a reference to determine the optimum way of processing experimental SIMS profiles through ratio-ing these to bulk monitoring species to correct for the effects of SIMS artefacts that are the cause of unreliable depth profiles in the first few nm. Comparisons have also been made between MEIS results of As implants into Si and results of various X-ray techniques applied to these samples. These were useful for several reasons. Firstly they provided a basis for the interpretation of the X-ray results, to help develop the application of these techniques to study low energy ion implants. Potentially these techniques can monitor and provide an understanding of defect evolution. These measurements can also be carried out with a greater depth resolution than that of MEIS. For example, specular reflectivity measurements were useful for measuring segregated As peaks following annealing. Good agreement between the results of X-ray diffraction and MEIS was found in studies of SPER.

The damage build up during implantation, with increasing implantation dose, has been studied for As and Sb implants and these studies identified an unusual damage evolution and dopant migration effect. For both species it was found that the damage evolution does not follow the energy deposition function and that initially, implantation causes the formation of a narrow, 4 nm wide, damaged / amorphous layer under the surface oxide. For increasing dose the amorphous layer then grows to a greater depth in a layer-by-layer fashion. This implies that mobile interstitials are trapped at a surface SiO_2 sink causing the build up of the damaged / amorphous layer. The location of the implanted ions follows a similar trend, in that they were initially found to be located at a similar depth as the narrow damaged layer, although a fraction of the implant was

stopped at depths beyond the observed profiles. This implies a movement of dopant species back to a depth closer to the surface and indicates that As and Sb is more readily accommodated in the amorphous layer than the damaged crystalline layer. Implantation carried out into an amorphous matrix does not show this movement of the dopant back towards the surface, in agreement with the proposed mechanism.

A range of annealing studies was performed using As implants. The first strand focused on implantation and annealing conditions that are similar to current device manufacturing conditions, i.e. using predominantly spike annealing above 1000 °C. MEIS results showed that for many anneals, complete regrowth of damaged layers was achieved. For temperatures of 700 °C and above, the regrowth rate was sufficient to complete regrowth within a timeframe of several seconds. Segregation of As occurred, as did the disappearance of the dopant from view of the He^+ beam. Combined SIMS studies showed the full retention of the As, and hence the As lost from view is equated to As taking up substitutional positions. For higher temperature anneals, i.e. > 900 °C diffusion of the As to greater depths was observed. Any improvements in depth using a 1 keV implant compared to a 3 keV implant, which lead to shallower implant depths, were found to be negated by the greater effect of diffusion during subsequent annealing.

Diffusion, which is influenced by the level and nature of the implant damage, has been identified as a limiting factor in reducing the junction depth in future devices. Further SPER annealing studies were carried out using low anneal temperatures (550 °C – 700 °C). MEIS results captured various stages of regrowth within these samples. This highlighted the layer-by-layer nature of the regrowth process. Changes in the As profiles were observed that matched the depth of the amorphous / crystalline interface, showing how As became substitutional or segregated out with the movement of the interface. With these low anneal temperatures, importantly, deeper As diffusion was not observed. A reduction in the regrowth rate was observed with increasing As concentration and proximity to the surface.

Finally annealing studies using SOI wafers were carried out. For samples where the implant damage was well away from the buried oxide layer, MEIS results showed that the regrowth behaviour of SOI samples was the same as for bulk Si samples. For samples where a small amount of implantation damage extended to the depth of the buried oxide layer, or a depth close to the buried oxide, MEIS results showed that the amorphous / crystalline interface of annealed samples could be much wider than those observed for bulk Si samples. In SOI samples the interface was observed to be distributed over a depth of approximately 14 nm. This unusual behaviour was attributed

to the accumulation of small pockets of damage at the buried oxide interface, due to interstitial trapping and this resulted in the local absence of a seed for the damaged Si to rearrange upon. For the cases where the range of the implantation was not sufficient to reach the buried oxide, this effect was attributed to the accumulation of mobile interstitials that were trapped at the buried oxide interface. TEM micrographs showed that the amorphous / crystalline interface was wavy over the same depth range as observed with MEIS. It is proposed that locally, where there is no seed, regrowth is initially delayed. The initial delay is responsible for producing the wavy interface. The regrowth of SOI samples was observed to either proceed with a slower rate, or be initially delayed compared to bulk Si samples. This observation fits in with the proposed explanation.

MEIS studies also demonstrated an interaction between Xe, used to pre – amorphise the samples, and F and B, from a subsequent BF_2 implantation following annealing. It was observed that approximately half of the Xe became trapped at a depth that was dependent on the energy of the BF_2 implant, which corresponded to $\sim 3 \times R_p$ of the F and B atoms. SIMS analysis showed that following annealing most of the implanted F had segregated to the surface, but a small fraction had moved in deeper and was trapped at the same depth as the Xe in an ~ 1:1 ratio. B similarly was observed to be trapped at the same depth albeit with a concentration of around a quarter or lower of the other species. EFTEM studies showed that the Xe was present in spherical agglomerates or bubbles. It was proposed that this interaction is caused by some defect structure (e.g. a density variation or volume defect) at the EOR of the F and B implant within amorphous Si, and some chemical interaction between F and Xe. The possibility of the formation of a Xe F compound cannot be excluded either.

Further studies may be carried out in several areas. In terms of improvement of the techniques, there is scope for further experiments to compare the results between MEIS, SIMS and the X-ray methods with the aim of a better understanding of the effects studied and a further optimisation of the techniques.

There is also scope for further studies regarding the regrowth behaviour in SOI. It would of interest to carry out more experiments directly comparing bulk Si with SOI samples and to vary systematically the depths of implantation damage. This area of study would also benefit from more TEM experiments.

In order to understand the Xe F and B interaction better, experiments should be carried out with individual B and F implantations rather than BF_2 to try to understand

the role of each individual element. Such studies are expected to provide further information on the mechanisms of the agglomeration at the particular depths observed.